Toward the Comprehension of the Infrared to Submillimeter View of the Interstellar Medium of Nearby Galaxies

Maud Galametz

▶ **To cite this version:**

Maud Galametz. Toward the Comprehension of the Infrared to Submillimeter View of the Interstellar Medium of Nearby Galaxies. Astrophysics [astro-ph]. Université Paris-Diderot - Paris VII, 2010. English. NNT : . tel-00555151

HAL Id: tel-00555151
https://theses.hal.science/tel-00555151

Submitted on 12 Jan 2011

Thèse de Doctorat de l'Université de Paris Diderot (Paris 7)

Ecole Doctorale d'Astronomie et d'Astrophysique d'Ile de France

présentée par :

Maud Galametz

pour obtenir le grade de

Docteur ès sciences de l'Universite Paris 7.

Toward the Comprehension of the Infrared to Submillimeter View of the Interstellar Medium of Nearby Galaxies

---

Thèse conduite sous la supervision de Suzanne Madden

Réalisée au sein du Laboratoire AIM / CEA , Paris Saclay

Soutenue le 30 Septembre 2010

Membres du Jury:

Dr. Alessandro BOSELLI .... rapporteur

Dr. Caroline BOT .... examinateur

Prof. Elias BRINKS .... rapporteur

Dr. Eli DWEK .... examinateur

Prof. Rob KENNICUTT .... examinateur

Dr. Daniel KUNTH .... examinateur

Dr. Jacques LE BOURLOT .... examinateur, président du jury

Dr. Suzanne MADDEN .... directeur de thèse

In Genesis it is recounted that God said "Let there be light" and there was light. Being an uplifting text, it does not go on to say "and then there was dust to muck things up."

P.G. Martin, "Astrophysics of Dust", 2004

Acknowledgements

Abstract

This thesis aims to study the interstellar medium (ISM) of nearby galaxies to characterize the physical properties of the gas and dust. We especially focus our study on low-metallicity galaxies of the Local Universe, ideal candidates to study the influence of metal enrichment on the ISM properties of galaxies. Previous studies have shown that the Spectral Energy Distributions (SEDs) of low metallicity galaxies differ significantly from those of massive galaxies and that the dust-to-gas mass ratio (D/G) of the galaxy could be dependent of the metallicity. Observations of low-metallicity galaxies also often led to the detection of an excess at submillimeter (submm) wavelengths not always accounted for in usual SED models. Further studies and observations had to be performed to better cover the far-IR to submm range and probe the coldest phase of dust.

We adopt a multi-wavelength approach to model and analyse the SEDs of 4 low-metallicity galaxies observed with LABOCA at 870 μm. We estimated the fraction of cool dust to be significant compared to the total dust mass of the galaxies. Some D/Gs are incompatible compared to what is expected from the current chemical evolution model, revealing possible reservoirs of gas not detected by current HI or CO observations.

I enlarged the first sample to a wider range of metallicities and showed that submm measurements significantly affect the dust mass estimates of galaxies. For dustier galaxies for which the SED usually peaks at longer wavelengths, submm fluxes are crucial to constrain the position of the peak and the Rayleigh-Jeans slope of their SED. For low-metallicity galaxies, the submm wavelength domain harbours an excess that may imply a large amount of very cold dust.

Our results confirm that low-metallicity galaxies can exhibit a submm excess when observed at longer wavelengths. Obtaining a more precise inventory of the cold dust and resolve the main actors of dust evolution in massive star forming regions and molecular clouds was the logical following step. We obtain LABOCA observations of a resolved star forming region of the Large Magellanic Cloud (LMC), the N158/N159/N160 complex, situated in the south of the 30 Doradus complex. The proximity of the LMC enables us to resolve structures of a few parsecs at the LABOCA resolution to model the SEDs of individual and isolated regions across the complex and get a handle on the temperature distribution of the dust (hot, warm, cold). I am also comparing the dust distribution with the HI, CO and Hα observations to spatially quantify the variations of the D/G.

I finally present the first *Herschel* observations of the galaxies NGC 6822 and NGC 1705, two low-metallicity galaxies observed as part of the Science Demonstration phase of the telescope launched in May 2009. In NGC 6822, we model the SEDs of some HII regions and less active regions across the galaxy and find that the SEDs of HII regions show warmer ranges of dust temperatures. We derive very high dust masses when graphite is used in our model to describe carbon dust. Using amorphous carbon, instead, requires less dust mass to account for the same submm emission due to its lower emissivity properties. This indicates that SED models including Herschel constraints may require different dust properties than commonly used.

Résumé (en français)

Cette thèse porte sur l'étude du milieu interstellaire des galaxies proches afin de mieux comprendre les processus physiques de ses composantes de gaz et de poussière. Elle s'est essentiellement concentrée sur les galaxies de faible métallicité. Les galaxies à faible métallicité sont considérées comme les briques de fabrication des galaxies plus larges dans le scénario hiérarchique de formation des structures et pourraient présenter des caractéristiques physiques proches des galaxies de l'Univers primordial. L'Univers Local est riche de ces objets et constitue un laboratoire idéal pour étudier l'influence de l'enrichissement en métaux sur les propriétés du milieu interstellaire.

L'astronomie infrarouge a révolutionné notre connaissance des propriétés des galaxies. Le télescope Spitzer nous a notamment permis d'avoir accès aux bandes des hydrocarbures aromatiques polycycliques, molécules constituées de cycles aromatiques de carbone et d'hydrogène et émettant en infrarouge proche. Les observations couvrent l'intervalle de longueur d'onde [3.5 μm - 160 μm] et permettent d'échantillonner une grande partie de la densité spectrale d'énergie des galaxies observées et donc d'effectuer une étude globale (mais aussi locale pour les galaxies les plus proches) de l'activité de formation d'étoiles ainsi que des propriétés de la poussière.

Les études précédentes ont montré que les densités spectrales d'énergie des galaxies à faible métallicité présentaient des différences notables avec celles des galaxies plus massives. Les bandes des hydrocarbures aromatiques polycycliques sont fortement diminuées, voire absentes lorsque la métallicité diminue fortement. On observe de plus une modification de la distribution de taille des grains, dominée, en énergie, par les grains de très petite taille. Le rapport en masse poussière sur gaz (D/G) semble également dépendre de la métallicité de la galaxie.

L'observation des galaxies à faible métallicité conduit assez souvent à la détection d'un excès submillimétrique qui n'est pas pris en compte dans la modélisation des densités spectrales d'énergie en raison notamment du faible nombre de contraintes disponibles dans ce régime de longueurs d'onde. Les données en submillimétrique de galaxies à faible métallicité pourraient donc révéler une très grande quantité de poussière jusqu'alors non détectée par les observations infrarouge. Des études complémentaires étaient nécessaires pour comprendre les phénomènes physiques liés aux différentes populations de grains responsables de l'émission infrarouge/submillimétrique, sonder les composantes les plus froides de la poussière, quantifier la masse de poussière pour la comparer aux différents traceurs du gas (hydrogène atomique, moleculaire etc.), étudier la distribution en température des grains et les propriétés telles que leur émissivité.

J'ai, pour ce faire, adopté une approche multi-longueur d'onde afin d'échantillonner et de modéliser les densités spectrales d'énergie de galaxies de l'infrarouge proche aux longueurs d'onde submillimétriques. Le modèle de densité spectrale d'énergie que j'ai choisi d'utiliser dans cette étude possède deux niveaux. Le premier niveau concerne les choix des propriétés intrinsèques (leur composition ainsi que leur distribution en taille) des grains. J'ai utilisé pour cela le modèle standard et actualisé de Zubko et al. (2004). Le second niveau concerne la forme analytique de la distribution en température des grains, déterminante pour la quantification de la masse de poussière du

milieu. J'ai utilisé la paramétrisation proposée par Dale et al. (2001), approche qui a été, par la suite, énormément utilisée. Le champ de radiation interstellaire est la source d'excitation des grains. Des études précédentes ont mis en évidence que ce champ de radiation variait en fonction de la métallicité. Néanmoins, la dureté du champ de radiation affecte majoritairement les grains hors équilibre et n'influence donc pas l'estimation de la masse totale de poussière, paramètre sur lequel nous nous concentrons majoritairement dans cette étude. J'ai choisi d'utiliser la forme standard du champ de radiation de la Galaxie définie par Mathis et al. (1983). L'absence d'information, sur les distributions de grains entre autres, ne nous permet pas de réaliser un modèle complet de transfert de rayonnement. Le modèle que nous appliquons ici est donc une approche simplifiée mais néanmoins basée sur des propriétés physiques réelles de grains et suffisamment complexe pour étudier des propriétés globales sans sur-interpréter les contraintes dont nous disposons.

Notre premier échantillon est constitué de quatre galaxies à faible métallicité observées avec l'instrument submillimétrique LABOCA sur le télescope APEX au Chili et observant à 870 μm. La fraction de poussière froide de ces galaxies peut être significative au regard de leur masse totale. L'addition de la contrainte à 870 μm conduit à la détection d'un excès submillimétrique pour deux d'entre elles, venant compléter l'échantillon encore faible de galaxies où cet excès est détecté. J'ai choisi de modéliser cet excès par une composante de poussière froide indépendante afin d'étudier les conséquences de cette hypothèse sur les propriétés de nos galaxies. Néanmoins, la nature de cet excès reste incertaine et sujet à débat. L'une des galaxies de l'échantillon, Haro 11, présente des caractéristiques très intéressantes. C'est une galaxie lumineuse en IR (LIRG) située à une distance de 92 Mpc qui présente un excès submillimétrique et pour laquelle très peu de gaz, atomique comme moléculaire, a été détecté. Son rapport D/G ne correspond pas aux prédictions des modèles d'évolution chimique actuels. Haro 11 ne semble pas, de plus, suivre la relation de Schmidt-Kennicutt. La masse de gaz non détecté estimée pour obtenir un D/G cohérent avec les prédictions correspond à celle qui serait nécessaire pour ramener la galaxie sur la relation de Schmidt-Kennicutt. Ces résultats pourraient suggérer la présence d'un réservoir de gaz moléculaire non détecté par les observations actuelles en H I et CO.

J'ai ensuite élargi cet échantillon à un intervalle plus large de métallicité et étudié comment les données submillimétriques affectaient l'estimation de la masse de poussière totale de ces environnements. Les barres d'erreur sur les masses sont considérablement diminuées lorsque les contraintes submillimétriques sont utilisées. De la même façon, nous observons un resserrement de la relation liant le rapport D/G à la métallicité lorsque ces données sont utilisées dans la modélisation de la densité spectrale d'énergie. La modélisation des galaxies riches en poussière dont les densités spectrales d'énergie piquent généralement à grande longueur d'onde nécessite des contraintes submillimétriques pour échantillonner à la fois le pic et la pente submillimétrique de leur densité spectrale d'énergie. L'absence de ces contraintes conduit dans la majorité des cas à une surestimation de la masse de poussière totale. Une parade pour éviter cette surestimation est de fixer l'intervalle des intensités du champ de radiation, plus exactement le paramètre U_{min} de notre modèle, comme mentionné dans Draine et al. (2007). Cette technique semble fonctionner dans le cas des galaxies riches en poussières, même si cette solution reste *ad hoc* et que le choix de cette limite reste arbitraire. En revanche, cette technique risque d'entraîner une sous-estimation de la masse de poussière totale dans le cas de galaxies présentant un excès submillimétrique. Neuf galaxies de l'échantillon semblent présenter un excès, majoritairement des galaxies à faible métallicité. Ces galaxies présentent un rapport en flux 160 μm/850 μm plus faible que le reste de l'échantillon. Notons également que les densités spectrales d'énergie des galaxies présentant un excès submillimétrique piquent avant 85 μm. Aucune corrélation claire n'a finalement été trouvée entre le pic de la densité spectrale d'énergie et la métallicité de la galaxie.

Il faut, dans un deuxième temps, faire l'inventaire complet de cette population froide de grains et résoudre les principaux acteurs de l'émission IR et submillimétrique dans les régions massives de formation d'étoiles et dans les nuages moléculaires. Nous avons obtenu des observations LABOCA du complexe N158/N159/N160, une région intense de formation d'étoiles dans le Grand Nuage de Magellan, située au sud de 30 Doradus. La proximité du Nuage de Magellan nous permet de résoudre des structures de quelques parsecs à 870 μm avec LABOCA. Cela permet d'effectuer une étude spatiale de l'évolution des densités spectrales d'énergie à travers le complexe afin d'étudier la distribution en température des grains. Je compare également la distribution IR et submillimétrique avec les observations déjà disponibles en HI, CO et Hα. Le but de ce travail, encore en cours, est de réaliser une étude spatiale du rapport en masse poussière sur hydrogène atomique, ou poussière sur gas total dans les régions où des observations CO sont disponibles pour tracer l'hydrogène moléculaire. Le rapport D/G est-il constant? Peut-on étudier des variations dans le facteur de conversion CO - H$_2$?

Ma dernière année de thèse a enfin été marquée par le lancement de l'observatoire spatial Herschel en mai 2009. Herschel possède le plus grand miroir primaire jamais envoyé dans l'espace. Sa résolution spatiale et la gamme de longueurs d'onde couverte par ses deux instruments PACS et SPIRE en font l'instrument idéal pour étudier la poussière dans ses phases les plus froides ainsi que pour quantifier précisément cette poussière, notamment dans les galaxies proches.

J'ai analysé les premières images *Herschel* des galaxies à faible métallicité NGC 6822 et NGC 1705 observées lors de la phase de Science Demonstration du télescope. La galaxie NGC 6822 est une galaxie étendue présentant des régions isolées plus ou moins intenses de formation d'étoiles baignant dans un milieu diffus. J'ai modélisé les densités spectrales d'énergie de régions HII ainsi que de régions moins actives à travers la galaxie en utilisant notamment les données des cartes SPIRE à 250, 350 et 500 μm. Ces cartes sont dominées par l'émission étendue et non-homogène de cirrus Galactiques qu'il a fallu au préalable modéliser et supprimer des cartes. Les densités spectrales d'énergie des régions HII présentent des intervalles de températures plus chaudes que dans les régions diffuses.

J'ai également mis en évidence une corrélation entre le rapport 250 / 500 μm, rapport qui caractérise la distribution en température des grains les plus froids avec la brillance de surface à 24 μm, liant ici les processus de chauffage des grains à l'activité de formation d'étoiles. J'ai enfin obtenu des masses de poussières significatives lorsque les graphites sont utilisés pour décrire la poussière carbonnée (modèle standard). Certaines études récentes nous mettent néanmoins en garde contre l'utilisation des graphites et suggérent l'utilisation de grains de carbone amorphe hydrogéné. L'utilisation de carbone amorphe diminue effectivement les masses de poussière estimées. Cela semble indiquer que les modèles de densité spectrale d'énergie incluant des données *Herschel* nécessitent l'utilisation des propriétés différentes de poussière.

Cette thèse porte donc sur l'étude des galaxies à faible métallicité observées dans des longueurs d'ondes encore peu explorées et cruciales pour contraindre avec certitude la densité spectrale d'énergie de nos galaxies et donc la distribution en température des grains ainsi que la quantification de la masse totale de poussière de ces galaxies. Les observations effectuées actuellement par le télescope Herschel vont, sans aucun doute, accroître et corriger nos connaissances actuelles sur la physique du milieu interstellaire.

Contents

List of Figures

List of Tables

Introduction

We still do not understand very well how galaxies are formed and how they evolve from the beginning of the Universe 13.7 billion years ago to present-day systems. We would especially want to improve our understanding of their star formation history, seed of their evolution. How stars are formed and with which efficiency? Are local galaxies forming more or less stars than galaxies of the Early Universe. What are the main components of these galaxies? How do these components interact and how are they distributed?

Galaxies are constituted of stars bathing in an interstellar medium of gas and dust. Gas is the major component of the medium, contrary to dust that only constitutes 1 % of the total mass of the interstellar medium. Nevertheless, it sparks off many physical processes such as the heating of the medium. Stars form in very dense cocoons of gas and dust and are thus invisible when they are very young. The dust grains of the medium absorb the radiation of stars to re-emit it at longer wavelengths, in the infrared. Dust is thus an indirect tracer of the nestled star formation.

Infrared spatial astrophysics has revolutionized our knowledge of the formation and evolution of galaxies at both local and global scales, thus from the resolved galaxies such as our Milky Way to the far young Universe. Images from the telescopes *IRAS* and *ISO*, respectively launched in 1983 and 1995, followed by those of the *Spitzer* telescope, launched in 2003, have permitted to probe the opaque interstellar clouds and thus to have access to the cradle of stars.

My PhD work is characterized by a multi-wavelength (optical, infrared, submillimeter) and thus a multi-instrumental (spatial and ground-based telescopes) approach of the spectral energy distributions of nearby galaxies. My analysis focused on the understanding of the spatial distribution and the interactions between gas and dust in order to probe the star formation history in the structures we are studying. I especially studied the evolution of the properties (mass of dust, dust-to-gas mass ratios, dust temperatures) of galaxies as a function of their enrichment with metals.

Most of my work is thus dedicated to dwarf galaxies, systems that are usually small and ir-regular and that show a low-metallicity compared to 'normal' spiral galaxies like our Milky Way. Most of the orbiting neighbours of our Galaxy are in fact low-metallicity galaxies. They are usually considered as structures that are less complex than bigger galaxies, especially due to their small size and the apparent homogeneity of their properties throughout the galaxy, even if we will see that they are more complex than expected. Dwarf galaxies are considered to be the building blocks of the large spirals that could be formed, in the current scenarios of formation of structures, by the fusion of smaller galaxies. They could also present analogies with galaxies of the Early Universe.

My PhD took place at a key time for infrared spatial astrophysics: the *Spitzer* telescope observing up to 160 μm ran out of helium last year and is starting its warm phase. We then attended to the arrival of the new space observatory *Herschel*, a telescope observing for the first time with this sensitivity and resolution a wide range of far-IR to submillimeter. We will come back later on the importance of that wavelength range in the understanding of the mecanisms of star formation and physical processes within the interstellar medium.

During this PhD, my home institute was the Laboratoire AIM, the astrophysical department of the Atomic Energy Commision in Paris/Saclay. This laboratory has been very involved in the construction process of the *Herschel* observatory, more specifically on the camera of the instrument PACS. I was observing in Chile when we all watched proudly its launch from the launch platform of Kourou, French Guyana, in May 2009. *Herschel* goes far beyond our hopes in the quality of the images it has been sending us since May 2009. I was very lucky to ave gain experience beforehand on the main tools (data reduction, spectral energy distribution modelling etc.) I used in the analysis I performed. *Herschel* data are the gifts of my last third year and offer us, combined with the huge amount of data from other instruments that still need to be explored, nice prospects for years to come.

Introduction (en français)

On comprend encore mal comment les galaxies sont nées et ont évolué depuis la naissance de notre Univers il y a quelques 13,7 milliards d'années jusqu'à aujourdhui. Les chercheurs aimeraient en savoir plus notamment sur leur histoire de formation d'étoiles, moteur de leur évolution. Comment les étoiles se sont ou sont-elles formées dans ces galaxies? Avec quelle efficacité? Les galaxies actuelles forment-elles plus ou moins d'étoiles que les premières galaxies de l'Univers? De quoi ces galaxies sont-elles constituées et comment sont distribuées et interagissent leurs différentes composantes?

Une galaxie est constituée d'étoiles baignant dans un milieu interstellaire constitué de gaz et de poussière. Le gaz en est l'ingrédient majoritaire. Si elle ne constitue qu'1% de la masse totale de ce milieu interstellaire, la poussière en est néanmoins également une composante importante tant au niveau des processus physiques dont elle est responsable que des régions de formation d'étoiles dont elle est le traceur indirect. Nous savons que les étoiles naissent dans des cocons très denses de gaz et de poussière et sont donc invisibles à leur naissance. Les grains de poussière présents dans le milieu ont la faculté d'absorber une partie du rayonnement des étoiles et de le réémettre dans l'infrarouge lointain, nous permettant ainsi de sonder les régions enfouies des galaxies.

L'arrivée de l'astrophysique infrarouge spatiale a donc révolutionné notre connaissance de la formation et de l'évolution des galaxies de l'échelle locale à l'échelle globale, des galaxies résolues comme celle à laquelle nous appartenons aux structures de l'Univers lointain et jeune. Les images des télescopes *IRAS* et *ISO*, respectivement lancés en 1983 et 1995, suivies de celles offertes par l'instrument *Spitzer* lancé en 2003 ont notamment permis de sonder les nuages interstellaires opaques et donc d'avoir enfin accès aux régions où naissent les étoiles.

Mon travail de thèse s'est caractérisé par une approche multi-longueur d'onde (optique, infrarouge, submillimétrique) et donc multi-instrumentale (télescopes spatiaux et terrestres) de la distribution spatiale d'énergie des galaxies proches. Je me suis attachée à la compréhension des différentes composantes du milieu interstellaire, gaz et poussière, par l'étude de leur distribution spatiale et de leur rapport afin de comprendre l'histoire de formation d'étoiles des objets étudiés. Plus particulièrement, mon travail s'est concentré sur l'étude de l'évolution des propriétés (masse de poussière, rapport gaz sur poussire, distribution en température etc.) de ces galaxies en fonction de leur métallicité, autrement dit en fonction de leur enrichissement en métaux.

Mes premières recherches se sont donc naturellement tournées vers les galaxies appelées "naines", galaxies de petite taille à morphologie parfois irrégulière et très pauvres en métaux. La plupart des systèmes orbitant autour de notre Voie Lactée sont des galaxies de ce type. Les galaxies naines sont généralement considérées comme des systèmes moins complexes à étudier que les grandes galaxies du fait de leur petite taille et donc de l'homogénéité apparente de leurs propriétés, même si nous verrons dans ce mémoire que ces systèmes sont beaucoup plus complexes qu'il n'y paraît. Les galaxies naines sont considérées comme les pierres de construction des galaxies spirales qui se formeraient par fusion de galaxies de plus petite taille selon les scénarios actuels de formation des structures. On pense également qu'elles pourraient présenter des caractéristiques similaires aux galaxies formées

lorsque l'Univers était encore très jeune.

Ma thèse s'est déroulée à un moment clef de l'astrophysique infrarouge spatiale. Alors que le télescope *Spitzer* observant en infrarouge jusqu'à 160 μm vient d'épuiser sa réserve d'hélium, entrant dans sa phase d'observation "chaude", nous venons d'assister à l'arrivée d'un nouveau observatoire spatial, *Herschel*, qui va observer pour la première fois à cette sensibilité et résolution un large domaine de l'infrarouge lointain au submillimétrique. Nous reviendrons dans ce mémoire sur l'importance de ce domaine de longueur d'onde dans la compréhension des mécanismes de la formation d'étoiles et des phénomènes physiques régissant les interactions entre les differentes phases du milieu interstellaire.

J'ai effectué ma thèse au sein du Laboratoire AIM, le service d'Astrophysique du Commisariat à l'Energie Atomique de Paris/Saclay, laboratoire très impliqué dans la construction du satellite *Herschel*, plus particulièrement de la caméra de son instrument PACS. J'étais en observation au Chili lorsque nous avons tous suivi en direct, fiers, son envol de la plate-forme de Kourou en Guyane française en Mai 2009. *Herschel* dépasse à l'heure actuelle, et de loin, tous les espoirs que les ingénieurs et chercheurs, du CEA ou d'ailleurs, ayant participé à sa construction avaient mis en lui. J'ai eu beaucoup de chance de pouvoir me former, en amont, aux outils d'analyse (réduction de données, modélisation de densité spectrale d'énergie etc.) nécessaires à la science que je souhaitais développer. Les données *Herschel* sont les cadeaux de ma troisième année de thèse et nous offrent, combinées aux nombreuses données des autres instruments encore à exploiter, de grandes perspectives pour les recherches à venir.

Part I

Physics of the interstellar medium of low-metallicity galaxies

Chapter 1

Structure of the interstellar medium

Contents

1.1 The Matter Life-Cycle

The interstellar medium of galaxies is a very dilute medium made of gas and dust that fills the space between stars. For our Milky Way, it represents 2.5 % of the baryonic mass (from Tielens 2005). The ISM plays a key role in galaxy evolution: stars are born from the ISM and reinject some of their matter into it when they evolve and die. Figure 1.1 synthesises the matter life cycle in the ISM. Low mass stars participate in the injection of dust within the ISM through stellar winds while high mass stars, through their winds or during supernova explosions, contribute to the turbulence and thermal pressure of the medium. The stellar evolution is thus responsible for the injection of gas and dust, and thus metals, in their environment. The ISM evolves through processes of chemical enrichment, dust processing (we will come back later to this point), grain seed formation etc. Table 1.1 gives, for the Galaxy, the gas and dust (silicate and carbon dust are separated) injection rates for different stellar objects. A complete cycle, from the ejection of a dust grain from a star to the formation of a new star can take 10^8 (Dwek 1998) to $\sim 10^9$ years (Tielens 2005).
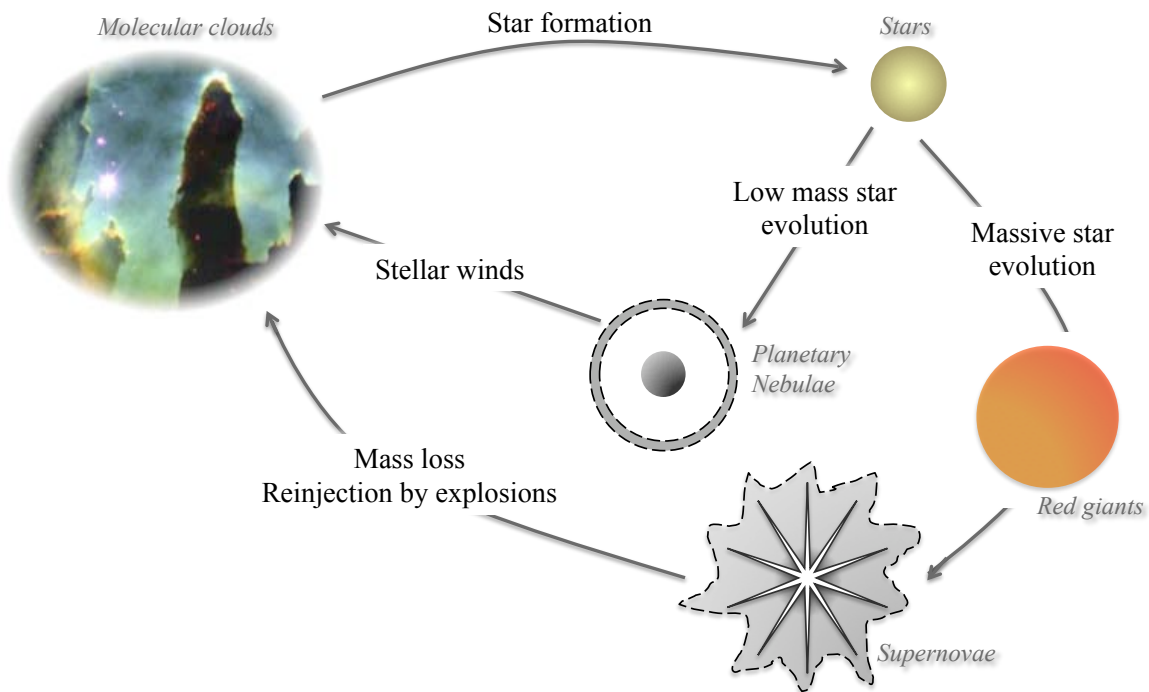
Figure 1.1. Recycling of matter in the interstellar medium

1.2 The gas

Interstellar gas constitutes $\sim$99% of the ISM mass. About 70% of this gas is in the form of hydrogen, while the remaining constituants are helium (28%) and heavier atoms. Gas in galaxies is characterised by three different phases which are described below.

1.2.1 The molecular gas

The molecular clouds are the densest components of the ISM and are considered to be stellar nurseries forming stars through fragmentation processes and gravitational collapses. They show a wide range of properties as far as size, density and temperature are concerned and are thought

Table 1.1. Interstellar gas and dust budgets in the Galaxy (from Tielens (2005))

Source	Injection rates ($M_\odot$ kpc^{-2} Myr^{-1})		
	Total gas mass	Carbon dust	Silicate and metal dust
C-rich giants	750	3.0	-
O-rich giants	750	-	5.0
OB stars	30	-	-
Novae	6	0.3	0.03
Wolf-Rayet stars	100 [a]	0.06	-
Red supergiants	20	-	0.2
Supernovae type I	-	<0.3	<2
Supernovae type II	100	<2	<10
Star formation	-3000	-	-
Halo circulation [b]	7000		
Infall [c]	150		

[a] Dust injection by carbon-rich Wolf-Rayet stars (WC 8-10) only.

[b] Mass exchange between the disk and halo estimated from HI in non-circular orbits and CIV studies.

[c] Infall of material from intergalactic medium and satellite galaxies.

Table 1.2. The phases of the interstellar medium in the Galaxy (based on Tielens (2005))

Phase	Density (cm^{-3})	Temperature (K)	Mass ($10^9 M_\odot$)	Σ [a] ($M_\odot$ pc^{-2})	Detection
Cold atomic medium	50.0	80	2.2	2.3	HI 21 cm line absorption
Warm atomic medium	0.5	8000	2.8	1.5	HI 21 cm line emission
Molecular clouds	>200.0	~10	~1.3	1.0	CO rotational lines
Hot ionised gas	0.003	10^6	-	0.3	X-ray emission ionised metal absorption lines
Warm ionised medium	0.1	8000	1.0	1.1	Hα emission
HII regions	1 - 10^5	10^4	0.05	0.05	Hα emission

[a] Surface density in the solar neighborhood.

to be gravitationally-bound rather than in pressure equilibrium with the other phases (Table 1.2 and Tielens 2005). The most abundant molecule is H_2 normally formed on dust grains at cold temperature but could also have been formed in primordial gas (Palla et al. 1983). It is also subjected to the destructive effects of UV photons but can be self-shielded from photodissociation or shielded by dust grains (see Franco & Cox 1986; Glassgold et al. 1985; Bergin et al. 2004 for more details). H_2 is efficiently heated by cosmic rays that are able to penetrate molecular clouds.

Several atomic and molecular species, on the contrary, participate in the cooling of the molecular phase, ^{12}CO being the dominant coolant (Goldsmith & Langer 1978).

The rotational transitions of H$_2$ are quite rare due to its lack of dipole moment, which makes it difficult to detect. It is thus indirectly observed, usually through CO rotational transitions, most often optically thick (e.g. CO(1-0) at 2.6 mm). Rotational transitions of CO are readily excited, even at modest interstellar densities, which leads to good detections of CO in the Galactic molecular clouds or in nearby galaxies (Morfill & Scholer 1987). The conversion factor from CO intensity to molecular hydrogen column density, X$_{CO}$, is still currently investigated due to its high dependence on parameters such as radiation field, metallicity etc. X$_{CO}$ was first determined, for the Galaxy, by studying the cold clouds of the Milky Way disk. Using γ-ray emission, Strong & Mattox (1996) determined X$_{CO}$ to be $1.9 \pm 0.2 \times 10^{20}$ cm^{-2}/ K km s^{-1}. Dame et al. (2001) refined the calibration of X$_{CO}$ as a function of latitude and determine a mean value of $1.8 \pm 0.3 \times 10^{20}$ cm^{-2}/(K km s^{-1}). Variations of the X$_{CO}$ factor with metallicity are discussed later in Chapter 2.

1.2.2 The neutral atomic gas

This phase is composed of warm ($\sim$8000K), intercloud, diffuse gas (Warm Neutral Medium or WNM) with a few atoms per ten cubic centimeters (Tielens 2005) and denser, cold (50-100 K) H$_I$ clouds (Cold Neutral Medium or CNM) with densities of 10-50 atoms.cm^{-3} (Table 1.2). This neutral gas is commonly mapped through the radio energy it emits, namely the transition between the two hyperfine levels of the hydrogen 1s ground state (λ21cm). Dust is associated with the gas and plays a very important role in the atomic gas heating cycle through photoelectric processes on dust grains (Spitzer 1978; Tielens & Hollenbach 1985; Hollenbach & Tielens 1999).
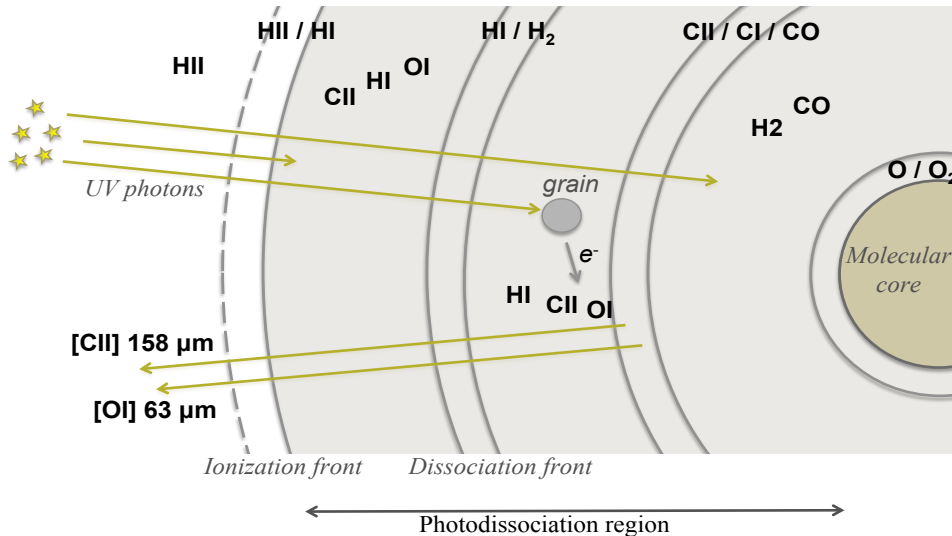
Figure 1.2. Photodissociation region operating scheme (inspired by Hollenbach & Tielens (1999))

Most of the neutral and molecular gas (but also dust) are in photodissociation regions (PDRs), sketched in Fig. 1.2. These regions are exposed to UV radiation of hot stars and are limited by an ionization front where interstellar gas changes from a mostly ionised state to a neutral state. Photons with energies inferior to 13.6 eV will dissociate H$_2$, leading to an HI / [CII] layer. When photons are significantly attenuated, the molecular hydrogen is dominant. Deeper in the clouds, C+ can recombine to form C$^\circ$ or CO, and transitions from atomic to molecular oxygen can take place.

The [CII] $\lambda 158$ μm and [OI] $\lambda 63, 146$ μm far-IR fine structure lines are the main cooling lines of the atomic gas (see Fig.1.2). Cooling through the [OI] fine-structure line is always significant in PDRs due to the general high densities of these regions. In fact, the [CII] line generally dominates the line cooling in galaxies while the [OI] line cooling becomes prominent in high luminosity, warm sources (Malhotra et al. 2001; Contursi et al. 2002). For high densities and radiation intensity, the temperature of the gas at the surface of PDRs can reach 5000K. Cooling processes through [S II], [OI] and [Fe II] lines can then take place. At high densities, cooling through collisions with cold grains could also be a significant mechanism (Burke & Hollenbach 1983).

Two processes dominate the heating of the interstellar gas: *1)* the photoelectric heating, where FUV photons absorbed by grains (e.g. PAHs, see section 1.3 on dust) create energetic electrons that can escape the grains and heat the medium. *2)* the photo-pumping of H_2, where line absorption of a FUV photon pumps H_2 molecules to a bound excited electronic state. The excited states cascade back (collisional de-excitations) to ground vibrational states (Hollenbach & Tielens 1999; Le Petit et al. 2006).

1.2.3 The ionised gas

Hot ionised gas

This phase is also called coronal gas or hot intercloud medium (HIM). The HIM shows very hot temperatures varying between 10^5 and 10^6 K and is very tenuous, with a density of $\sim 3 \times 10^{-3}$ cm^{-3} (Table 1.2). It fills most of the volume of the halo and is mainly heated and ionised by stellar winds of dying stars or by shock waves created by supernova explosions. Since coronal gas is thought to be made of supernova ejecta material, its study will give us information on the metal-enrichment history of galaxies. Several radiation processes are taking place in this hot plasma: bremsstrahlung continuum emission (transition of a free electron between two states), discrete line emission (transition between two levels of the ion), radiative recombination continuum (capture of an electron into a bound state), dielectronic recombination lines (capture of a free electron into a doubly excited ion state) or two-photon continuum mission (simultaneous emission of two photons) (see the review by Ehle 2005). The HIM, in cooling supernova remnants, is a significant source of X-ray thermal emission and UV absorption lines. Hurwitz & Bowyer (1996) studied OVI data and derived an exponential scale height of ~ 600 pc whereas Savage et al. (2000) explored OVI toward active galactic nuclei with FUSE (Far Ultraviolet Spectroscopic Explorer FUSE) and found a scale height of 2.7 ± 0.4 kpc. A following study on more than 100 early-type stars has been carried out by Bowen et al. (2008). Ferriere (1998) found that the hot gas seems to occupy a rather small fraction of the interstellar volume. This fraction is $< 20\%$ at low altitude and falls off gradually. The volume filling factor of this hot gas is, however, still highly debated.

Warm ionised medium

The warm ionized medium (or WIM) is a major ($> 90\%$ of the ionised hydrogen), wide-spread and diffuse (density of 10^{-1} cm^{-3}) component of our Galaxy's interstellar medium, consequence of the large-scale ionization of the medium by massive stars of the Galactic midplane, namely early O and B stars. Temperatures of the WIM range from about 6000 K to 10^4 K in the Galaxy. Properties of this medium can be studied through the intensity of the hydrogen Balmer (Hα) recombination lines or free-free emission. The distribution and kinematics of this gas have been mapped through deep Hα imaging by Dennison et al. (1998) and Gaustad et al. (2001) for the northern and southern sky respectively. The emission measure was estimated to be ~ 4.5 cm^{-6} pc by Reynolds (1984). The filling factor in the Galactic midplane was found to be ~ 0.26 and drops off with Galactic latitude (Hill et al. 2008). A recent study by Gaensler et al. (2008) also suggests that the filling factor could

increase from the Galactic plane to a height of $\sim$ 1-1.5 kpc, before declining again. We refer to Haffner et al. (2009) for a recent review of the warm ionised gas.

HII regions

Massive O and B stars or O-B associations emit strong UV radiation which is ionising their surroundings to create HII regions around those stars. The size of these regions is limited by the fact that ions and electrons within it recombine until the rate of recombination balances the rate of photoionization. Their expansion can also trigger star formation by processes of compression of pre-existing globules or density enhancement in a cloud, accumulation of gas into a dense shocked layer of neutral gas surrounding the expanding ionized zone or cloud collision (see Elmegreen 1998; Deharveng et al. 2005; Zavagno et al. 2010).

HII regions show wide ranges of properties (e.g. Hunter et al. 1993), with densities varying from 1cm^{-3} for diffuse nebulae to 10^3 - 10^4 cm^{-3} for compact HII regions like the Orion nebula, and can reach up to 10^5 cm^{-3} for the densest regions. Hodge & Lee (1990), studying HII regions in the low-metallicity galaxy IC 10, found that their size distribution has an exponential shape and discussed their variety. McKee & Williams (1997) compiled observations of HII regions in the Milky Way and in nearby galaxies and also found that the distribution of HII regions could be fitted by a truncated power law, with a scale length of 3.34 kpc over the range 3 kpc < R< 11 kpc.

The temperature of HII regions is strongly dependent on their density but also on the metallicity of the medium, which explains why they are extensively used to determine the metallicity of galaxies (Pilyugin et al. 2004; Pilyugin & Thuan 2005; Pilyugin et al. 2009). They are strong sources of thermal radio emission (bremsstrahlung or free-free emission) and are studied via Hα emission and many ionic lines (mostly due to the recombination of hydrogen and helium with free electrons). Inhomogeneities on the propagation of ionizing radiation and on in situ measurements of the electron density were observed in HII regions. They are commonly explained by the inhomogeneity of the ionized medium (see the models of Giammanco & Beckman 2005).

The bright IR continuum emission detected in these regions is linked with the presence of dust grains that absorb photons to reemit them at mid to far-IR wavelengths. Dust particles also scatter starlight (reflection nebuale). Dust grains are thus modifying the thermal properties of HII regions and have signficant consequences for the emergent optical spectrum with, in some cases, a complete obscuration of the HII region at visible wavelengths. Other effects of the presence of dust in HII regions are an observational absence of pure Balmer-line spectra or an enhancement of forbidden-line emission (Shields & Kennicutt 1995). Observations of HII regions in IR with the *Spitzer* telescope and now with *Herschel*, both in photometry and in spectroscopy, are significantly increasing our knowledge of the topology and physical processes in these environments. HII regions usually exhibit very warm temperature ranges. Relaño et al. (2007); Relaño & Kennicutt (2009) have studied HII regions in M33 and showed that the 24 μm emission seems to be closely related to the location of the ionized gas, while the 8 μm emission is more related to the boundaries of the molecular clouds, consistent with its association with PDRs. Furthermore, the star formation of HII regions seems to be well determined using a linear combination of their 24 μm and Hα emission (see the review by Calzetti et al. 2010). In the Magellanic Clouds, Lawton et al. (2010) found that the SEDs of HII are peaking around 70 μm at all radii, from $\sim$ 10 to $\sim$ 400 pc from the central ionizing sources. They also suggested that the 70 μm emission could be a more reliable indicator of the star formation rate than either 8 μm or 24 μm emission in these regions.

1.2.4 Molecular-to-atomic gas mass ratio

How molecular and atomic gas mass is distributed in galaxies is still a puzzlying issue. The majority of spiral galaxies show CO radial distributions and central CO peaks, in particular barred spirals.

On the contrary, central depressions have been observed in H I for Sc galaxies as well as relatively constant H I surface densities in the disk (see Scoville & Young 1983; Kenney & Young 1989 for studies of the molecular-to-atomic gas ratio in M51 or in large spirals of the Virgo cluster respectively). In spiral galaxies, Young & Knezek (1989) studied the ratio of molecular-to-atomic gas as a function of morphological type and found that this ratio is decreasing from Sa (diffuse arms, extended and bright nucleus) galaxies to Sd (fragmented bright arms, more diffuse nucleus) galaxies. Casoli et al. (1998) also studied a large number (~ 100) of isolated spirals and found that $M(H_2)/M(H I)$ was always inferior to 1, but they only found slight differences between the different morphologycal types of the spirals studied.

Further studies on interacting systems have shown that molecular gas should be the dominant gas phase in these systems. Mirabel & Sanders (1989) showed that the $CO(1 \rightarrow 0)$-to-integrated H I ratio was a function of the far-IR excess, defined as the far-IR-to-blue flux ratio f_{FIR}/f_b, in active galaxies (Fig. 1.3). They found that for luminous IR galaxies, the molecular-to-atomic gas mass ratio ($H_2/H I$) varies from 0.5 to 2 but could reach 5 to 20 for the highest far-IR excesss. Most of their luminous IR galaxies are interacting systems, which suggested that collisions between galaxies could enhance the IR activity. Horellou et al. (1999) found similar results but showed that the luminous interacting systems were not CO-bright, suggesting that the high $H_2/H I$ was not due to a better conversion of the H I gas into the molecular phase but could be linked with more efficient processes to transform the molecular gas into stars. Young & Scoville (1991) also showed that the $L_{IR}/M(H_2)$ shows a wide range of values, with up to 200 $L_{\odot} M_{\odot}^{-1}$ for interacting systems or starburst irregular galaxies.

Obreschkow & Rawlings (2009) recently developed a model to predict the evolution of H I, H_2 and the star formation rate across cosmic time. They suggest that galaxies contain similar amounts of H I but substantially more H_2 at redshift 1-5 than today. They found that the cosmic H_2 / H I ratio is evolving monotonically as $\Omega_{H_2}/\Omega_{Hi} \propto (1+z)^{1.6}$, and thus decreases with cosmic time. This decrease could be linked with the reduction of the cold gas pressure across time or the progressive growth of galactic disks.

The THINGS (The HI Nearby Galaxy Survey Walter et al. 2008 ; http://www.mpia-hd.mpg.de/ THINGS/Overview.html) program is now investigating the H I distribution (high spectral and spatial resolution) in 34 nearby galaxies. Leroy et al. (2009) have combined these data with CO observations from HERACLES (HERA CO - Line Extragalactic Survey) and estimated that the molecular gas masses of their sample is ranging from 7×10^6 to 6×10^9 $M_{\odot}$. They also derived H_2-to-stellar masses ratios of 0.01 to 0.25, with $H_2/H I$ ranging from 0.02 to 1.13 in their sample. Only upper limits for the H_2 masses have been determined for 4 low-metallicity galaxies of their sample, due to the non-detection of extended CO emission in these objects.

In the same team, Bigiel et al. (2008) also found that the star formation rate (Σ_{SFR}) is strongly dependent of the H_2 surface density (Schmidt-type power law) in subregions of spiral galaxies, meaning that H_2 seems to form stars with a constant efficiency in these objects (also see Kennicutt et al. 2007). They do not observe correlation between Σ_{SFR} and the H I surface density, which leads to strong variations in the star formation efficiency (SFE = Σ_{SFR} / Σ_{gas}) within these galaxies. Leroy et al. (2008) also note that where the ISM is mostly H I, the SFE decreases with increasing radius. More precisely, they found that $H_2/H I$ seems to follow a smooth function of radius, stellar surface density and pressure spanning from the H_2 to H I-dominated ISM.

Observations of molecular hydrogen through CO observations, and thus estimates of $H_2/H I$, in low-metallicity galaxies are rather difficult. Previous studies on the $H_2/H I$ in low-metallicity galaxies have nevertheless found a clear correlation between this ratio and metallicity (see Fig. 1.3 and Leroy et al. 2005). More details on the properties of molecular and atomic gas in low-metallicity environments and on the CO-to-H_2 conversion factor dependence with metallicity are discussed in the next chapter dedicated to dwarf galaxies.
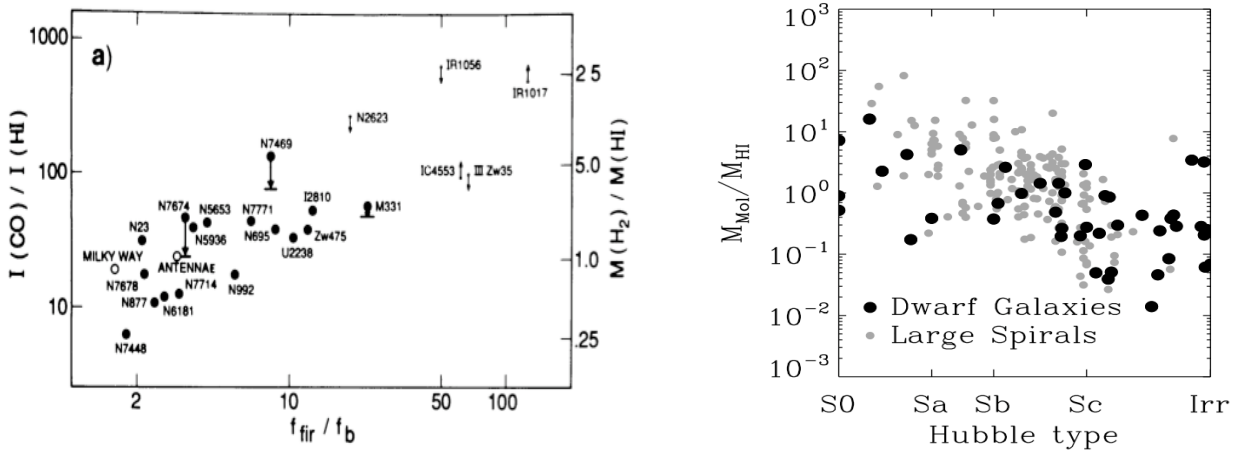
Figure 1.3. *Left:* CO$(1 \rightarrow 0)$/H$\textsc{i}$ flux ratios in Jy km s^{-1} as a function of the far-IR-to-blue flux ratios (f$_{FIR}$/f$_b$) for luminous IR galaxies. (Figure taken from Mirabel & Sanders (1989)). *Right:* Molecular-to-atomic gas mass ratio along the morphological sequence. (Figure taken from Leroy et al. (2005)).

1.3 The dust

1.3.1 Chemical Composition and size distribution

The dust mass only contributes up to 1% of the total mass of the ISM, far less than that of the gas, but is responsible for a significant part of the total luminosity of galaxies (30 to 99 %). Dust can be studied through its numerous effects on the ISM. Indeed, dust absorbs and scatters the starlight (extinction will be discussed later). Observations also reveal solid-state vibrational transitions in spectroscopy and polarisation effects on starlight.

The composition of dust is dependent on the amount of heavy elements (heavier than He) formed in the interior of stars. The observed depletions of some material usually participating in the dust formation are clues to their incorporation into dust. Figure 1.4 shows the elemental depletion as a function of the condensation temperature, thus as the function of their ease to be incorporated into dust (Jones 2009). We can indeed observe that C, N, O Si, Mg and Fe, which participate in dust formation, are partly locked into dust. They are thus not directly observable.
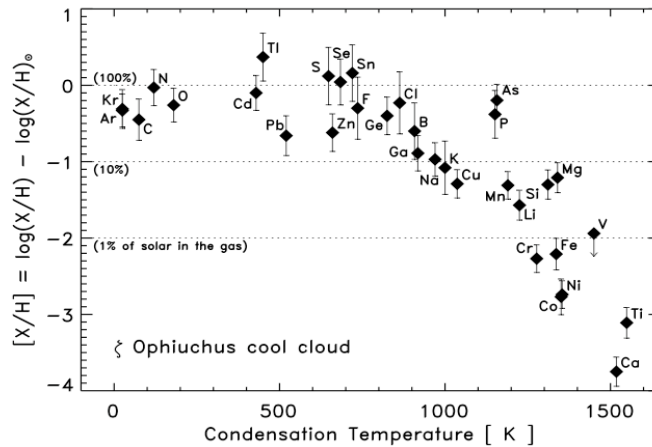
Figure 1.4. Elemental depletion along the ζ Ophiuchus cool cloud line of sight as a function of the condensation temperature of the element (from Palme & Jones (2005)).

Observations of the dust emission indicate that dust grains should be composed of amorphous
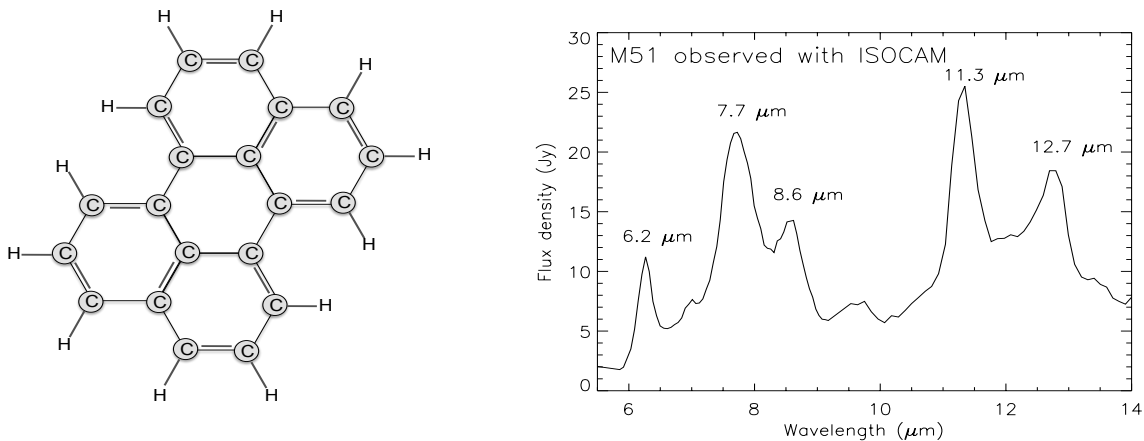
Figure 1.5. *Left:* Example of molecular structure of a PAH (Perylene: $C_{20}H_{12}$) *Right:* Mid-IR spectrum of the galaxy M51 observed with ISOCAM and showing the main PAH features.

and crystalline materials of silicate-based grains (e.g. $(Mg,Fe)SiO_3$, $CaMgSi_2O_6$ etc.) and carbon-rich solids (amorphous carbons, SiC etc.). Strong emission features are also observed in the near to mid-IR. The 3.3 and 11.3 μm features were first observed from ground-based telescopes and were identified as CH groups (Duley & Williams 1981). With the discovery of the 6.2, 7.7 and 8.6 μm features, further studies characterized these emission features as being associated with Polycyclic Aromatic Hydrocarbons (PAHs), large planar molecules made of aromatic cycles (Leger & Puget 1984). Figure 1.5 shows an example of such a molecule and the spectrum of the galaxy M51 obtained with the ISOCAM (and presented in Galliano et al. 2008) where PAH features can be observed. An average size of $\sim$50 C-atoms was derived from the emission temperature while broad emission plateaus underneath the 6.2 and 7.7 μm features revealed the presence of larger molecules ($\sim$ 300 C-atoms). These molecules contribute significantly to the photoelectric heating of the interstellar gas due to their small size (see Bakes & Tielens 1994 for details). In Fig. 1.5, we can observe typical vibrational modes of these molecules: the C-C stretching mode at 6.2 and 7.7 μm, the C-H in-plane bending mode at 8.6 μm and the C-H out-of-plane bending mode at 11.3 μm (if no adjacent H atom) and 12.7 μm (if 3 contiguous H atoms). The 12 μm (if 2 contiguous H atoms) and 13.55 μm (if 4 contiguous H atoms) are very weak in the M51 spectrum. *Spitzer* observations using the Infrared Spectrograph (IRS) have led to high resolution observations of the PAH emission bands as well as the broad plateaus underlying those bands and enable the study of the variations of the characteristics of PAHs with their environments (Peeters et al. 2010; Galliano et al. 2008). *Spitzer* has, in particular, discovered PAH features between 15 and 20 μm that are now considered to be new members of the PAH emission band family (Peeters et al. 2006). Properties of PAHs and very small grains (VSGs) in the low-metallicity galaxy LMC have been investigated by Paradis et al. (2009). The VSG abundance seems to trace star formation whereas the PAH abundance increases around molecular clouds and in the stellar bar of the galaxy, suggesting that they could have been injected in the ISM by the older stellar population. Roussel et al. (2007) investigated the warm molecular hydrogen in the SINGS (Spitzer Infrared Nearby Galaxies Survey; Kennicutt et al. 2003 ; http://sings.stsci.edu/) sample and note that the emission from PAHs and from excited H_2 were nearly cospatial, in agreement with the results of Tielens et al. (1993), among others, and predictions from theorethical models of PDRs that PAHs are found prominently in PDRs.

The dependance of the PAH bands with metallicity will be discussed in Chapter 2.

The particle-size distribution of the dust grains in the Galaxy is quite broad and was originally

15

modeled by a simple power-law (Mathis et al. 1977) for each dust species:

$$n(a) \propto a^{-3.5} \qquad\qquad a_- \ (5nm) \ \leq \ a \ \leq \ a_+ \ (250nm) \qquad\qquad (1.1)$$

where n(a) is the size distribution and n(a)da is the number of particles in the interval (a, a+da).

The smallest grains (less than $\sim$ 25 nm) seem to be dominated by carbonaceous and aromatic species while larger grains should mostly be amorphous silicates.

Kim et al. (1994), on the contrary, found that data at U, B and V indicate a deviation from the simple power-law and that the size distribution of larger grains could be compatible with an exponential tail between 200 nm to 1 μm. They also suggest a decrease in the number of smaller grains ($<$ 100 nm) in dense regions, probably due to accretion and coagulation processes (Martin & Whittet 1990; Chokshi et al. 1993) and thus can be responsible for a flattening of the UV extinction curve of these environments. (Massa & Savage 1989). We refer to Chapter 4 for more details on the dust composition and size distribution commonly used in dust models.

The dust size distribution in galaxies is strongly dependent on the destruction processes taking place on the dust grains of the ISM.

1.3.2 Formation, evolution, destruction

Dust is formed at high temperatures and densities in the envelopes of evolved stars and is reinjected in the ISM via dying stars through stellar winds and shock-waves generated by supernova explosions (see Fig. 1.1).

Dust grains formed via quiescent mass loss are expected to mostly survive the injection phase contrary to what happens during supernova explosions. Supernova shocks are first inducing grain-grain collisions, leading to the shattering of the dust grains, and thus a mass transfer from large grains into small grains, or the vaporization of those grains. The velocity thresholds for shattering and vaporization are of the order of 2 km s^{-1} and 20 km.s^{-1} respectively (Jones et al. (1996) and Tielens et al. (1994) respectively). They also generate collisions between the grains and the hot gas and provoke thermal and chemical sputtering or erosion of dust. The destruction of grains in supernova is the most dominant process recycling dust into gas (Dwek 1998; Jones et al. 1996).

No crystalline silicate bands have been observed in the Galactic ISM (the crystalline fraction of the interstellar silicates was estimated to be of $\sim$ 0.2 % by mass by Kemper et al. 2004), an absence that was associated with the efficient annealing of these grains by the energetic interactions with ions and cosmic rays generated in supernova shocks (Demyk et al. 2001).

The presence of large interstellar grains can be explained by constructive processes such as accretion, leading, for instance, to the formation of ice mantles of H_2O, CO, CO_2 etc (see the models of Nomura et al. 2009; Glassgold et al. 2009). Coagulation, that is to say grain growth due to sticking collisions, can also occur, especially in regions where the number of dust grains is significantly dense, such as in accretion disks of young stellar objects (see Stepnik et al. 2002; Blum 2004, for a detailed review on coagulation processes). Ormel et al. (2009) explored the collisonal evolution of dust in dense molecular clouds. His evolution model can be split in two phases: one dominated by grain growth and another dominated by fragmentation. The grain size is progressively increasing with time. The collision velocities then become sufficiently energetic to provoke the fragmentation of particules, leading to a possible equilibrium. This scenario is similar to that proposed by Dominik & Dullemond (2008) for protoplanetary disks. Collisional fragmentation or erosion mechanisms are indeed necessary to compensate for the turbulent coagulation taking place in those disks (T Tauri disks for instance) that usually exhibit signatures of small grains (e.g. Olofsson et al. 2009). Hirashita & Omukai (2009) also found that coagulation can occur in low-metallicity pre-stellar cores.

1.3.3 A few words on extinction by dust grains

Dust plays a big role in altering the propagating starlight in galaxies via its extinction properties. Extinction is expressed as A(ν), the optical depth $\tau(\nu)$ and the monochromatic intensity I_ν^o, thus the modified monochromatic intensity I_ν received by the observer will be:

$$I_\nu = I_\nu^o \times exp(-A(\nu)/1.086) = I_\nu^o \times exp(-\tau(\nu)) \tag{1.2}$$

To derive the λ-dependence of the extinction, the 'pair method' is generally used (see Fig. 1.6). The spectra of two stars of the same spectral type and luminosity class are compared, one of them being 'reddened' by interstellar dust, the other not affected by extinction. The dependence is thus calculated from the ratios of the two SEDs (with previous notations, $A(\nu) = -2.5 \, log(I_\nu/I_\nu^o)$). The two stars are never at the same distance. The fluxes are thus normalized to a common wavelength, usually A_V, before the calculation of the extinction (Fitzpatrick 2004).
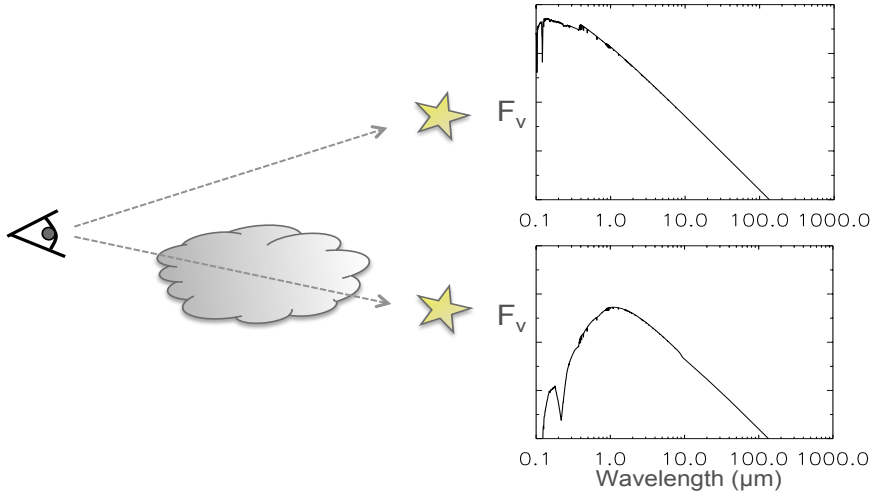
Figure 1.6. Schematic illustration of the 'pair method' (inspired by Fitzpatrick (2004)).

The extinction can also be expressed using $E(\lambda$-$V)/E(B$-$V)$. The studies of Cardelli et al. (1989) have first shown that the variation in Milky Way extinction curves could be described by an empirical relationship based on the single parameter, which is the ratio of the total-to-selective extinction $R_V = A_V/E(B$-$V)$. This parameter can be determined by extrapolating near-IR extinction to infinite wavelengths (Mathis 1990). Measurements of R_V typically lead to values of $R_V \sim 3$ in the diffuse ISM and $R_V \sim 5$ in dense regions within molecular clouds. The mean value of R_V in the Galactic diffuse ISM is $\sim$3.1. The Galactic extinction curve from far-UV to millimeter wavelengths is shown in Fig. 1.7 (Mathis 1990). IR wavelengths are less affected by extinction than UV wavelengths. Between ~ 0.9 μm and 5 μm, the continuous extinction curve can be approximated by a simple power-law $A_\lambda \propto \lambda^{-\beta}$, where β values of 1.61 in Rieke & Lebofsky (1985), 1.7 in Whittet (1988), 1.75 in Draine (1989) or 1.8 in Whittet et al. (1993). The 9.7 and 18 μm silicate features, probably due to the Si-O stretching mode and the O-Si-O bending mode respectively, dominate the 8 to 30 μm wavelength range. The silicate bands (from Dudley & Wynn-Williams 1997) are shown in Fig. 1.7. The absence of sub-features in the 9.7 μm feature, contrary to absorption profiles observed in the laboratory for crystalline silicates, could be proof of the amorphous and non crystalline nature of interstellar silicates (Draine 2003). This extinction curve can vary across the Galaxy and is very dependent on the environment, which means that it is also, in particular, dependent on the metallicity of the galaxy (see Chapter 2 and Fig. 2.4).
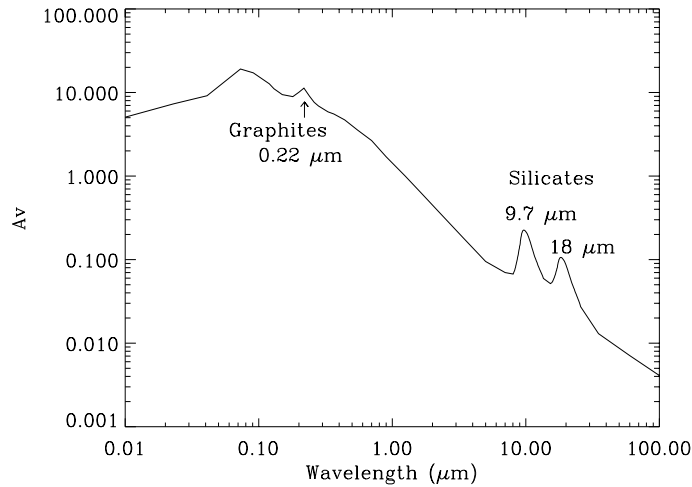
Figure 1.7. Galactic extinction curve. The curve is from Mathis (1990) and the silicate bands from Dudley & Wynn-Williams (1997). It shows a mean of the Galactic diffuse interstellar medium.

1.3.4 Physical processes of the interstellar dust grains

The Absorption and scattering by dust grains

If we consider a spherical particule with a radius a, the extinction cross section is given by:

$$C_{ext}(\lambda, a) = Q_{ext}(\lambda, a) \times \pi a^2 \tag{1.3}$$

The extinction by dust grains can be decomposed into scattering and absorption.

$$Q_{ext} = Q_{abs} + Q_{sca} \tag{1.4}$$

with Q_{ext} the efficiency of extinction and Q_{abs} and Q_{sca} the efficiencies of absorption and scattering. These values can be determined from laboratory measurements or by solving Maxwell's equations of propagation through the grains. Both methods suffer from the uncertainties of the composition of interstellar dust grains (Kwok 2007). The Mie theory (or Lorenz-Mie-Debye theory) is an analytical solution of the Maxwell's equations for absorption and scattering by spherical grains. The Mie efficiency factors are derived from the scattering amplitudes:

$$Q_{ext} = \frac{2}{x^2} \sum_{i=1}^{\infty} (2i + 1) Re(a_i + b_i) \tag{1.5}$$

and

$$Q_{sca} = \frac{2}{x^2} \sum_{i=1}^{\infty} (2i + 1)(|a_i|^2 + |b_i|^2) \tag{1.6}$$

with x the size parameter ($x = 2\pi a/\lambda$) and a_i, b_i the complex Mie coefficients obtained using appropriate boundary conditions at the surface of the sphere. a_i and b_i are directly dependent on the refraction index of the medium. An iteractive applet to calculate the efficiencies Q_{abs} and Q_{sca} can be found at http://www.lightscattering.de/MieCalc/eindex.html. The absorption efficiencies according to wavelength are plotted for different grain sizes in Fig. 1.8.
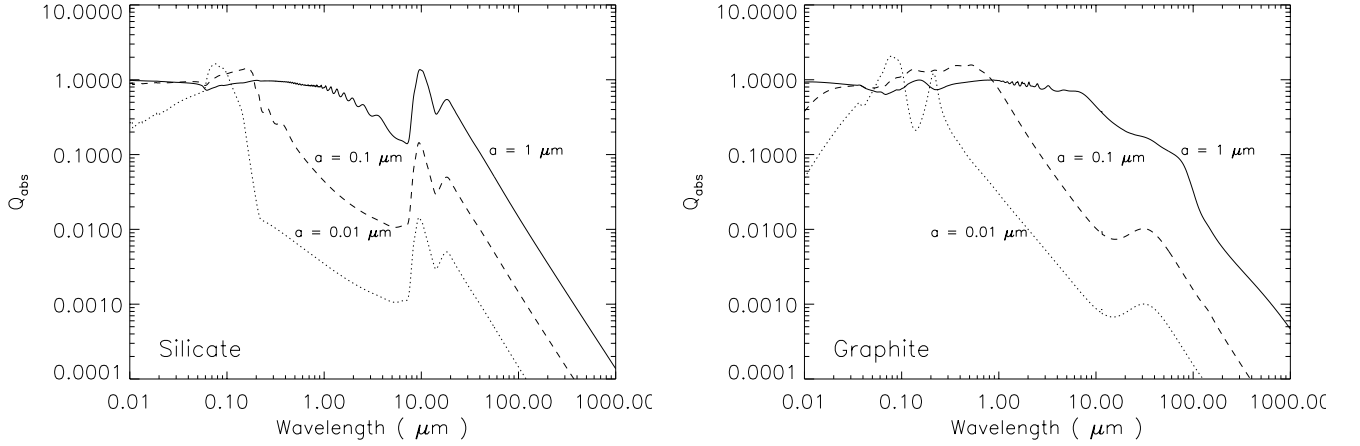
Figure 1.8. Absorption efficiencies for silicate and graphite for different grain radii, a.

From these efficiencies, we can calculate the total extinction A_λ of a dust cloud. The absorption coefficient is expressed as:

$$\alpha(\nu) = \rho \times \kappa(\nu) = \pi a^2 Q_\nu n_d \tag{1.7}$$

with Q_ν the extinction coefficient, κ the dust opacity, a the radius of the grain and n_d the number of dust grains per unit volume. We note that the quantity Q/a is independant of the radius a when $x = 2\pi a/\lambda \ll 1$.

The optical depth due to dust absorption along the line of sight is thus expressed by:

$$\tau(\nu) = \int_0^L \alpha(\nu) ds = \int_0^L \pi a^2 Q_\nu n_d ds \tag{1.8}$$

Each magnitude of visual extinction leads to a decrease of a factor of $10^{-0.4}$. We can thus easily link the total extinction, A_λ, with the optical depth τ_λ:

$$A_\lambda = 2.5 \times log(e) \times \tau_\lambda = 1.086 \tau_\lambda \tag{1.9}$$

Assuming realistic values: a dust-to-gas mass ratio Ψ of 10^{-2}, an extinction efficiency in the V-band Q_V of 2, a grain radius a of 0.1 μm and a dust grain density ρ_s of 1g.cm^{-3} , we find, for instance:

$$
\begin{aligned}
A_V &= 1.086 \pi a^2 Q_V \int n_d ds \\[2mm]
&= 1.086 \pi a^2 Q_V \frac{n_d}{n_H} N_H \\[2mm]
&= 1.086 \pi a^2 Q_V \Psi \frac{m_H}{m_d} N_H \\[2mm]
&= 1.086 \pi a^2 Q_V \Psi \frac{m_H}{\frac{4}{3}\pi a^3 \rho_s} N_H \\[2mm]
&\sim 10^{-21} N_H (cm^{-2})
\end{aligned}
\tag{1.10}
$$

19

Using optical extinction and column density measurements observationally determined in 7 supernovae remnants, Gorenstein (1975) found a similar value ($N_H/A_V = 2.2 \times 10^{21}$ cm^{-2}).

The heating and cooling of dust grains

Dust grains are mostly heated by absorption of the starlight and cooled by self-radiation (Kwok 2007). The dust densities are very low and gas collisions do not play a major role in the dust grain heating and cooling. Dust grains can be heated during collisions in dense regions where starlight is attenuated but this process of heating is not dominating. The temperature evolution of a dust grain will mainly depend on its size.

Let us now look at the balance of the energy of heating and cooling of a dust grain. The heating rate of a dust cloud is given by:

$$\Gamma = \int_0^\infty \alpha(\nu)(4\pi J_\nu)d\nu = \int_0^\infty \pi a^2 Q_\nu(a,\nu)n_d(4\pi J_\nu)d\nu \tag{1.11}$$

where J_ν is the mean intensity at the location of the grains.

The cooling rate (by self-radiation) of the dust grains is:

$$\Lambda = \int_0^\infty 4\pi j_\nu d\nu = \int_0^\infty 4\pi(\pi a^2 Q_\nu(a,\nu)n_d B_\nu(T_d))d\nu \tag{1.12}$$

with j_ν the emission coefficient (in erg s^{-1} cm^{-3} sr^{-1} Hz^{-1}).

At thermal equilibrium, $\Gamma = \Lambda$, so

$$\int_0^\infty \pi a^2 Q_\nu(a,\nu)n_d(4\pi J_\nu)d\nu = \int_0^\infty 4\pi(\pi a^2 Q_\nu(a,\nu)n_d B_\nu(T_d))d\nu$$

and

$$\int_0^\infty Q_\nu(a,\nu)J_\nu d\nu = \int_0^\infty Q_\nu(a,\nu)B_\nu(T_d)d\nu \tag{1.13}$$

The dust equilibrium temperature can then be deduced from this formula.

Thermal equilibrium is actually only observed for large dust grains. For smaller grains, the internal heat capacity is small compared to the energy of the absorption of one single photon. The temperature of the dust grain will thus significantly rise. In Fig. 1.9, we show the temperature history of dust grains of different sizes heated by the Galactic interstellar radiation field. Larger grains (a > 200 Å) maintain a steady temperature while the smaller grains (a < 50 Å) undergo large gradients of temperatures (Fig. 1.9). This stochastic heating of the grains induced by the absorption of starlight results in temperature spikes, most of the energy being re-emitted in the IR (We refer to Guhathakurta & Draine 1989; Draine & Li 2001 and to Chapter 4 for details on the study of temperature fluctuations of interstellar dust grains).

1.4   The Spectral Energy Distribution

1.4.1   A multiwavelength window on physical processes

The spectral energy distribution is the spectral footprint of a galaxy from which we can study the physical processes taking place within this galaxy. It synthesises the contribution of all its components to the total emission. Using this tool, we can peer into the integrated history of the galaxy
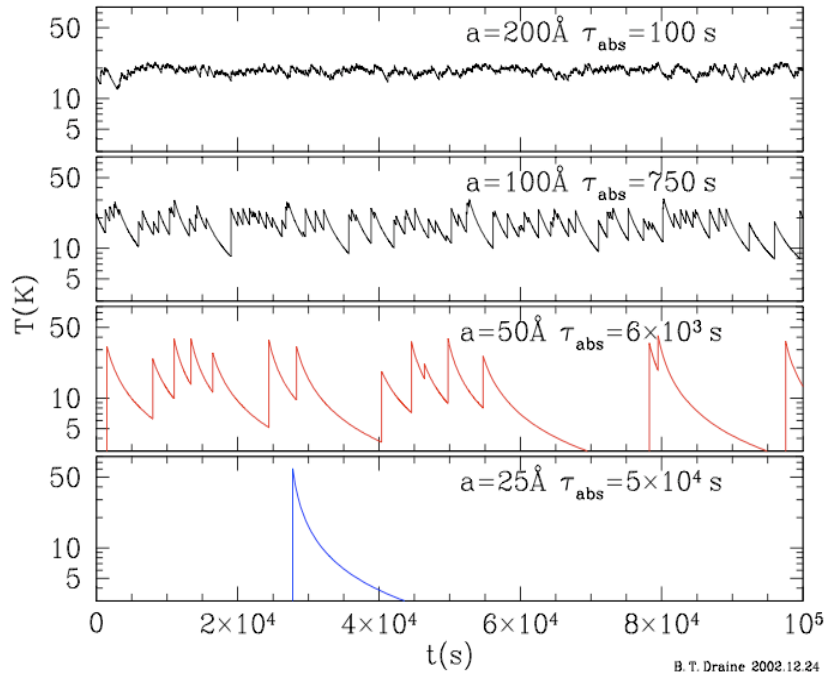
Figure 1.9. Carbonaceous grains heated by the Galactic radiation field. a is the radius of the grain, τ_{abs} the mean time between photon absorption. The figure is taken from Draine (2003).

and disentangle the various physical actors (stars, HII regions, molecular clouds) and processes (stellar radiation, dust emission) involved (Draine et al. 2007; Galliano et al. 2008). Many processes linked to star formation such as stellar winds (Hoefner 2009), supernova shocks, photodestruction by high-mass stars, etc, can also affect the spatial distribution and the local properties and abundance of the different dust components of a galaxy such as PAHs, amorphous carbon grains, silicates or composite grains, manifesting themselves in the mid-IR to submm wavelengths.

An example SED covering the wavelengths which are investigated in this thesis is shown in Fig. 1.10. The black points and lines indicate the observational constraints obtained by the observer (spectra in the mid-IR, broad-band fluxes with their error bars obtained from ground-based or space telescopes, emission lines such as CO(3-2), CO(2-1) etc.) and the dashed grey line indicates the total 'modeled' electromagnetic spectrum fitting these data. In this picture, we can separate the emission of the most massive stars (OB stars, in blue), that of the gas they ionize (in yellow) and the emission of the dust mixed within this gas (in magenta - Note the PAH band features in the mid-IR). We can also observe the emission of the other stellar populations (non-ionising stars, in red) and the emission of the dust heated by their radiation (in purple). The emission of the cold dust within dense molecular complexes is constrained by the submm part of the SED (in green). The radio emission is finally due to the radiation (free-free and synchrotron emisson) coming from charged particles in the magnetic field (in dark red). The striped regions indicate the energy absorbed to be re-emitted by the interstellar medium.

A few instruments and their wavelength coverage are overlaid on the figure:

GALEX (Galaxy Evolution Explorer) is an orbiting space telescope observing in UV at 1539 and 2316 Å.

2MASS (Two Micron All-Sky Survey) is a ground-based large survey performed with the Mt. Hopkins 1.3-m telescope, Arizona, USA, for the northern hemisphere and the Cerro Tololo In-

teramerican Observatory, Chili, for the southern hemisphere. The observations were perfomed in the J (1.25 μm), H (1.65 μm) and K (2.17 μm) bands.

ISOCAM and ISOLWS are two instruments onboard the ISO space telescope. ISOCAM is an IR camera observing between 2.5 to 17 μm. ISOLWS is a far-IR long-wavelength spectrometer observing between 45 and 196.9 μm.

IRAC, MIPS and IRS are three instruments onboard *Spitzer*. The telescope instruments cover 3.6 to 160 μm. A detailed description of the *Spitzer* instruments is given in Chapter 3.

Herschel possesses three instruments PACS, SPIRE and HIFI. The telescope instruments cover 70 to 500 μm. A detailed description of the *Herschel* instruments is given in Chapter 8.

SCUBA (Submillimetre Common-User Bolometer Array) is a submillimetre continuum array receiver (450 and 850 μm observations) mounted on the 15-m James Clerk Maxwell Telescope, Hawaii, USA (JCMT). SCUBA-2 was installed at the end of 2009 and possesses a much larger field-of-view and a sky-background limited sensitivity.

CSO (Caltech Submillimeter Observatory) consists of a 10.4-meter diameter Leighton radio dish located in Hawaii, USA. Heterodyne receivers are observing from 0.4 to 1.3 mm. A 24-element imaging bolometer array, SHARC (Submillimeter High Angular Resolution Camera, has been comissioned at the telescope for 350 and 450 μm continuum mapping.

SEST (Swedish-ESO Submillimeter Telescope) is a 15-m telescope located at the La Silla Observatory, Chili, observing at submm wavelengths. It was decommissioned in 2003, with the arrival of the APEX telescope in Chajnantor, Chili (see Chapter 3).

IRAM (Institute for Radio Astronomy at Millimeter wavelengths) possesses two observatories designed for radio astronomy: a 30-m telescope located on Pico Veleta, Granada, Spain, and the Plateau de Bure interferometer in the French Alps.

1.4.2   A wide range of SED shape

The shape of the SEDs is dependent on the type of galaxy we are looking at, more particularly on its stellar population (age distribution) and on its gas and dust reservoirs (star formation history) of the galaxy. Figure 1.11 shows the SEDs of galaxies showing a variety of morphological types and star formation activities. In the following paragraphs, we will describe briefly the main morphological types of galaxies, building blocks of the Hubble sequence. This classification does not, however, include a distinction between the different star formation activity within galaxies. We give examples of differents types of galaxies classified by star formation activity in section 1.4.2.2.

1.4.2.1 Classification by morphological types

Spiral galaxies possess a rotating disk formed of stars and ISM (gas + dust), with a central bulge where older stellar populations than the disk are usually observed. Observations of edge-on galaxies indicate that dust seems to be concentrated in a thick disk (high optical depth) but must not be optically thick (thus diffuse or patchy) in the vertical direction. Spiral galaxies can be quite rich in gas and dust (thus a significant dust continuum can be observed in their SEDs, as well as strong emission lines) and can possess very active star-forming regions in the spiral arms. Spiral galaxies also exhibit significant PAH features in the mid-IR that are associated with the numerous PDR regions of spiral disks (Fig. 1.11).
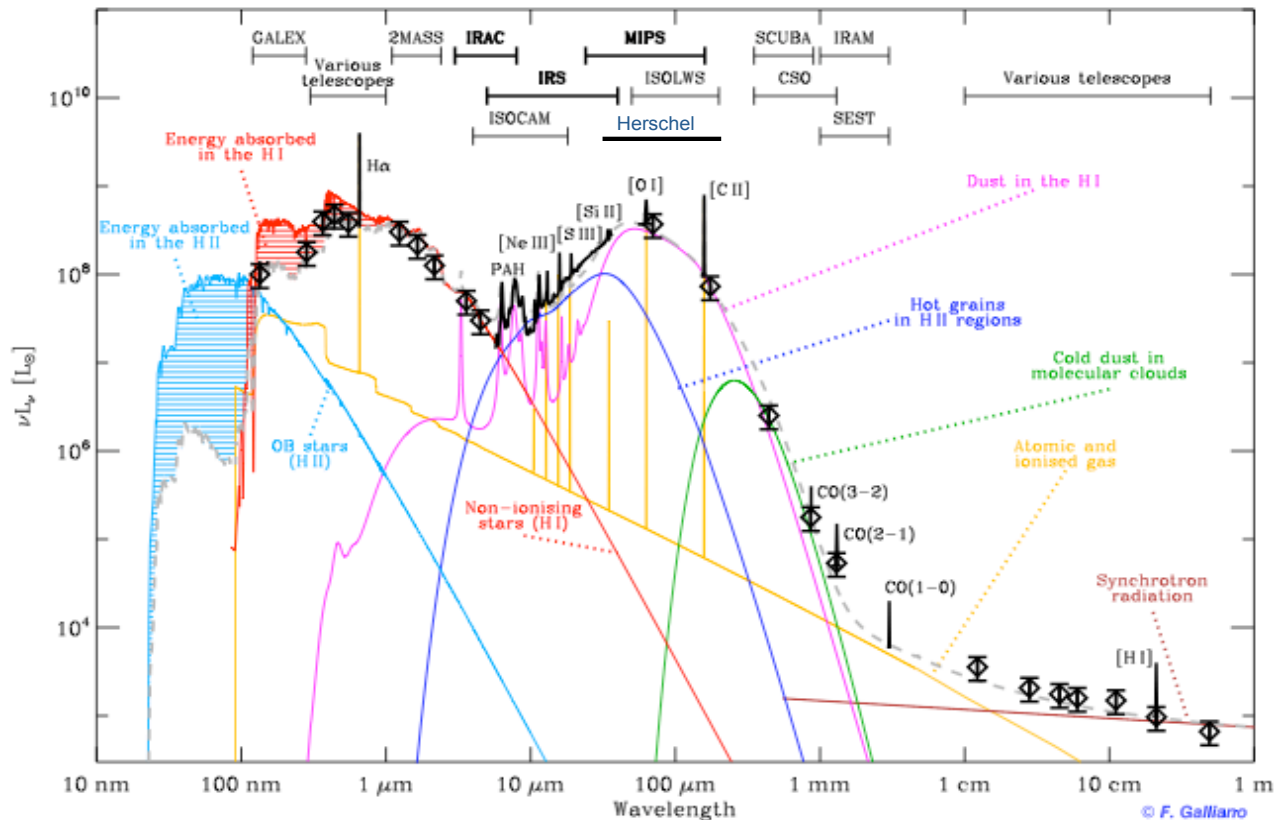
Figure 1.10. Detailed view of the spectral energy distribution of a galaxy. See section 1.4.1 for description.

Elliptical galaxies, as indicated by their name, show an elliptical morphology. They are classified in the Hubble sequence from E0 to E7, the number 0 to 7 corresponding to the quantity $10\times(1\text{-}b/a)$, where a and b are the semi major and semi-minor axis respectively. They typically show old low-mass stellar populations, mostly emitting in the near-IR (Fig. 1.11), with predominantly radial motions, sometimes with unusual kinematics observed in the inner regions (Kormendy 1989). The star formation rate of these galaxies can be quite low. They have a sparse interstellar medium and typically little HI accreted by ram-pressure (Sofue & Wakamatsu 1992) and little or not molecular gas (Sage et al. 2007), leading to a faint emission of the dust continuum at IR wavelengths (Fig. 1.11). They, however, are not completely devoid of dust and many elliptical galaxies actually show dust lanes produced by cold interstellar material at longer wavelengths (van Gorkom 1992).

Lenticular galaxies possess a disk and a bulge but do not show spiral arms. They are believed to be spiral galaxies from which gas has been removed by interactions with hot cluster gas, even if this scenario is still debated (More details in van den Bergh 2009). Observations of lenticular galaxies (Xilouris et al. 2004) have shown that those galaxies contain non negligible amounts of dust and PAH features.

Dwarf / Irregular galaxies possess a peculiar structure, which makes them difficult to classify in the Hubble sequence. Two very famous examples of irregular galaxies are the two nearby Magellanic Clouds. Most of irregular galaxies as well as most of Local Group galaxies are actually dwarf low-metallicity galaxies. Dwarf galaxies will be described in more detail in Chapter 2, since they are the main focus of this thesis.
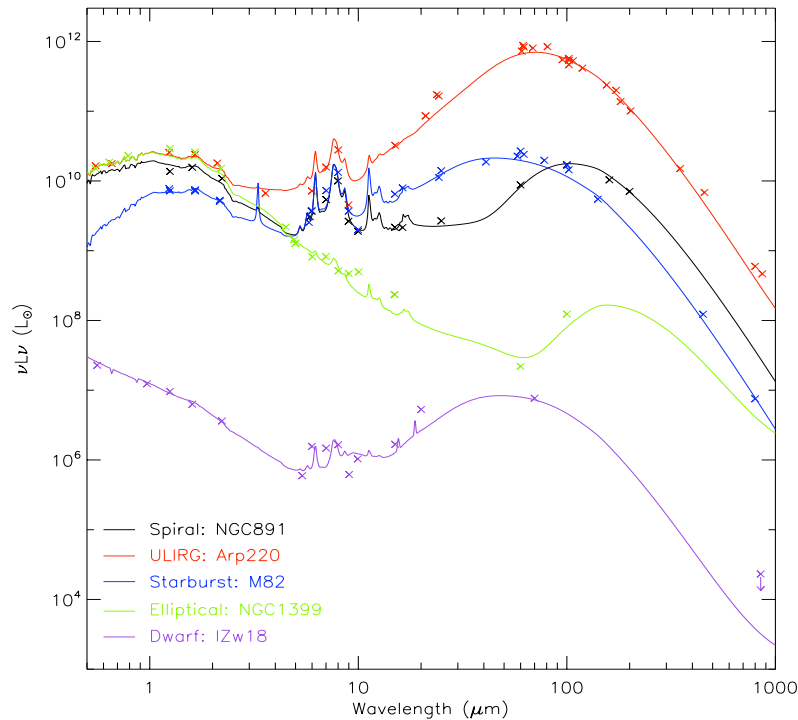
Figure 1.11. Variation of the Spectral Energy Distributions with star formation activity or morphological type

1.4.2.2 Classification by star formation activity

Starburst galaxies are characterized by significant star formation rate (up to 1000 $M_\odot$ yr^{-1}). Their gas reservoir being limited, the star formation activity of these galaxies only lasts a few 10^7 years. Their young stellar population ionizes the surrounding medium, leading to the formation of bright HII regions. The numerous PDRs lead to a strong emission of PAH bands in the mid-IR. The intense interstellar radiation field usually leads to a higher dust temperature range, with SEDs usually peaking at short wavelengths (around 40-50 μm for M82, see Fig. 1.11).

Active Galactic Nucleus, or AGNs, possess a compact and luminous nucleus. The nuclear luminosity can dominate the total emission of the galaxy and is due to accretion processes by a central supermassive black hole. AGNs are classified in sub-categories: Seyfert galaxies, radio-galaxies, blazars and quasars. All these types of AGNs are surrounded by an optically thick dust torus and are basically the same object but viewed from different lines of sight (Urry & Padovani 1995). The circumnuclear dust absorbs the AGN illumination and re-radiates the energy at IR wavelengths. They usually show a near-IR 'bump' (excess emission above the 2-10 μm continuum) corresponding to hot dust.

Luminous Infrared galaxies, or LIRGs, radiate more than 90 % of their light in the IR, emitting more than 10^{11} $L_\odot$. Galaxies emitting more than 10^{12} $L_\odot$ are called Ultra-luminous Infrared galaxies (ULIRGS). Many LIRGs are actually starburst galaxies and some of them contain an AGN. ULIRGs seem to be major mergers of gas-rich galaxies (90 % of them being in interacting or merging systems) and their spectra usually show strong emission lines ([OI], [OIII], [NII], etc). These galaxies are thought to be possible progenitors of elliptical galaxies (Kormendy & Sanders 1992; Genzel et al. 2001). Their SEDs are generally flatter in the

24

optical to mid-IR range (Fig. 1.11). They also often peak at short wavelengths, due to the warmer temperature range of their dust grains, compare to spiral galaxies for instance.

1.5 The difficulty of ground-based observations

Some observations are impossible to carry onut from Earth because of the atmospheric absorption. The atmospheric opacity is shown in Fig. 1.12. All gamma-rays, X-rays and UV observations have to be performed from space due to the absorption of these wavelengths in the upper atmosphere. Several absorption bands can also be observed between visible wavelengths to $\sim 15\ \mu$m. They are introducing distortion and absorption of the spectrum in this window. The atmospheric transmission is then significantly decreasing at IR wavelengths up to submm wavelengths. This large stretch of absorption obliges astronomers to observe these wavelengths from space, hence the construction of IRAS, ISO, *Spitzer* and now *Herschel*.
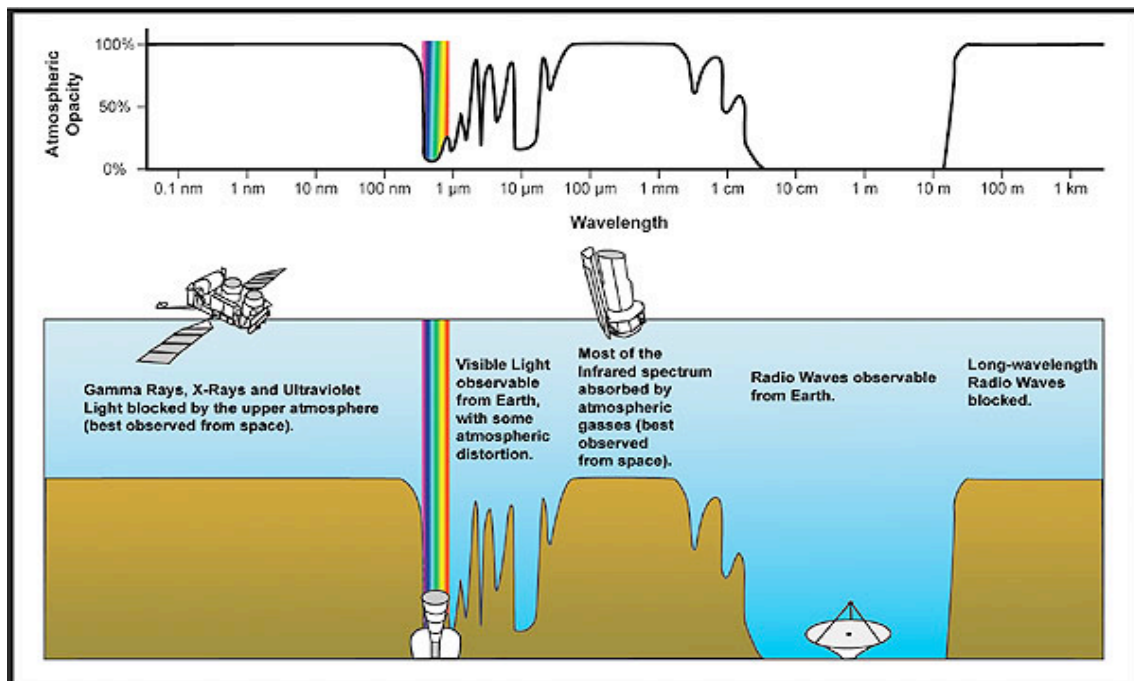
Figure 1.12. Atmospheric electromagnetic opacity

Several molecules are responsible for the absorption bands, among which are O_2 and H_2O. The H_2O molecule, for instance, is responsible for about 70% of all atmospheric absorption of radiation and possesses strong absorption bands (1.45, 1.95, 2.5 μm etc). In fact, each molecule will absorb differently and transitions will occur at slighly different wavelengths. This effect explains why broad absorption 'bands' are observed rather than narrow absorption lines.

A molecule possesses different discrete or quantified energy levels associated with different states: rotation, vibration, modification of the electronical configuration. The energy of the incident photons, and thus the wavelength, will determine how molecules will be affected. Interactions in the visible part of the spectrum usually lead to electronic transitions while in UV, the absorption of UV radiation by molecules can lead to a dissociation of the molecule. At IR wavelengths, the molecules will, on the contrary, experience vibrational and rotational transitions, but not for the same energy range. Rotational transitions are commonly taking place at micro-wave energies.

Chapter 2

Properties of low-metallicity environments

Contents

Studying the metallicity of galaxies is crucial in order to understand how systems evolve from early universe galaxies to those observed today. We especially want to understand the enrichment history and the physical processes involved (i.e. supernova feedback, stellar mass-loss through winds) and their efficiency and evolution over cosmic time. Several studies have tried to estimate the metal production of high-redshift galaxies (e.g. Steidel et al. 1996; Madau et al. 1996; Pettini et al. 1997; Mehlert et al. 2002; Lilly et al. 2003; Reddy et al. 2010, among others) but it is rather difficult to explore a broad range of metallicity for distant galaxies, especially due to the faint surface brightness of some distant galaxies (Salzer & MacAlpine 1988; Dalcanton 1995; Dalcanton et al. 1997), and especially low-metallicity objects. Nearby dwarf galaxies are thus ideal laboratories to study the properties of the ISM in conditions resembling those of the early universe, even if the link between these objects and early galaxies is still debated.

I will first briefly explain how metallicities are measured. I will then describe the interests of low-metallicity galaxies and what is already know about these systems.

2.1 The definition of metallicity

The 'metallicity' is the proportion of elements that were converted into heavy elements, namely elements heavier than hydrogen and helium. The letter Z is usually used to named the mass fraction of heavy elements, the mass fraction of hydrogen and helium are designated by the letter X and Y respectively. We can thus write:

$$X \; + \; Y \; + \; Z \; = \; 1 \tag{2.1}$$

The abundance of the lightest elements is given by standard cosmological models. These elements were produced shortly after the Big Bang (Big Bang nucleosynthesis). The production of heavier elements happened much later as a product of the nucleosynthesis in stars. At the scale of a galaxy, the metallicity is thus the testimony of its previous stellar activity.

The value of Z for the sun is ∼0.02. The metallicity is often expressed using the ratio of a heavy element abundance, for example oxygen or iron, to the hydrogen abundance (12+log(O/H) or 12+log(Fe/H)).

The metallicity is quite a complicated concept to define for a galaxy since many galaxies show significant gradients within them. Several techniques exist to derive abundances. We will describe the most commonly used methods. The two first methods allow the derivation of the metallicity from Hɪɪ regions or planetary nebulae. We refer to Kunth & Östlin (2000) for a review onf these methods.

2.1.1 The 'direct' method

This method consists of measuring the emission or absorption line intensities directly observed with spectroscopic instruments. After correction of the extinction and the reddening of the lines, one can deduce the parameters of the medium such as the electron temperature and density of the gas using line ratios. [S II] $\lambda6717$ / $\lambda6731$ or [O II] $\lambda3726$ / $\lambda3729$ are commonly used to estimate the electron density (N_e), knowing the energy level separation, their statistical weights and the radiative and collisional excitation rates.

The electron temperature (T_e) reflects the balance between heating and cooling processes and depends significantly on metallicity. At high metallicities, T_e is lower because more coolants are available. The [OIII] $\lambda(4959+5007)$ / $\lambda4363$ ratio is very sensitive to the temperature (see Fig. 2.1) and is usually used to estimate T_e. Figure 2.1 also highlights the difficulty in estimating line ratios at low temperatures.

These physical conditions are used to compute the emissivities (ϵ) of the respective lines using:
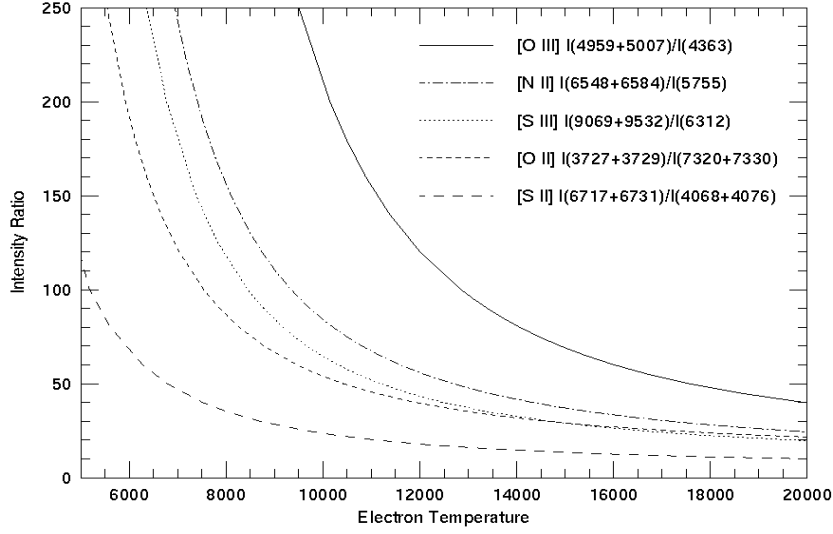
Figure 2.1. Emission line ratios for five species as a function of the electron temperature (in K) (from Skillman 1998).

$$\epsilon \propto N_i N_e h\nu \frac{\Omega_{12}(T_e)}{T_e^{1/2}} \frac{1}{g} e^{-\chi/kT_e} \tag{2.2}$$

with N_i the number density of the ion we are interested in, N_e the electron density, ν the frequency of the transition, g the statistical weight of the lower level, χ the energy difference between the two electronic levels ($= h\nu$), Ω the average electron collision strength from the lower level, k the Boltzman's constant and h the Planck's constant. The formula to derive the H_β emissivity given in Aller (1984).

The ionic abundance ratios are thus derived from:

$$\frac{N(X^i)}{N(H^+)} = \frac{I_\lambda}{I_{H\beta}} \frac{\epsilon_{H\beta}}{\epsilon_\lambda} \tag{2.3}$$

where $N(X^i)$ is the ionic abundance of the species of interest, I_λ the strength of the ionic emission line, $I_{H\beta}$ the strength of an H recombination line and ϵ the emissivities of the respective lines. We finally obtain the elemental abundance ratios by summing the ionic abundances and correcting for the unobserved ions.

We refer to Lee et al. (2006, 2007) for examples of how to deduce the metallicity with the 'direct' method from spectroscopic observations of nebulae for low-metallicity galaxies such as NGC 6822 or Centaurus A and other nearby galaxies.

A few words on photoionization models

Photoionization models are used to describe emission line regions such as HII regions, planetary nebulae, etc and permit us to investigate the different effects of dust : formation of emission lines in various environments (e.g. Le Bourlot 2000), heating processes affecting the shape of those lines (e.g. Balmer lines), size distribution of the dust grains that will influence the temperature distribution in the ISM, etc.

These models can be adapted to describe a specific region (fit of the line intensities derived from observations) or can be used directly as grids of models already generated and matching the

appropriate range of parameters. The parameters of the models can be the effective temperature of the ionizing stars, the gas temperature and density, elemental abundances etc. Building a model requires *a priori* assumptions such as the geometry (examples of simplified geometry: plane-parallel, spherical), the incident angle of observation (example of simplified case: perpendicular illumination and viewing), the dust grain optical properties etc. We will not enter into the details of these models here since there are different ways to grasp the modelling.

One popular photoionization model is CLOUDY (see http://www.nublado.org/ and Ferland et al. papers). It is designed to simulate a broad range of conditions in interstellar matter, from the intergalactic medium to the high-density medium. The code is able to predict the thermal, ionization and chemical structure of a cloud. Xue & Huang (2009), for instance, has recently used CLOUDY for PDR diagnostic calculations. Their models span gas densities ranging from $n=10^2$ to 10^6 cm^{-3} and radiation fields with $G_0=10^0$ to 10^6. They found slighlty different results than those using the models of Kaufman et al (e.g. Kaufman et al. 1999), another popular PDR model. Intensities and strength ratios of the observational lines are usually presented using contour diagrams as functions of the density and the incident radiation field (G_0) in those models.

2.1.2 The 'bright line' method

The oxygen abundance can also be derived from the brightest lines. It is known that the bulk of cooling in dusty environments is done by the IR fine structure lines while it is done by the high excitation optical lines in low-metallicity regions. We will thus observe an increase of the quantity [OII]λ3727+[OIII]λ4959,λ5007 / Hβ when the abundance decreases. This quantity was first introduced by Pagel et al. (1979) and is called the 'R$_{23}$' parameter. The relation between the oxygen abundance and the R$_{23}$ parameter is plotted in Fig. 2.2. [OIII]λ4959,λ5007 is no longer dominating the cooling at very low-metallicities and the relationship turns around at roughly 10% of the solar oxygen abundance. We can observe a possible degeneracy between high and low metallicity for a same R$_{23}$ value. This ambiguity can sometimes be solved using measurements of other lines (e.g. [SII] and [NII]).

An example of an application of this method for some nebulae of the low-metallicity galaxy NGC 6822 is presented in Lee et al. (2006).

A current debate exists on the correct way to estimate the metallicity of a galaxy. For instance, Pilyugin & Thuan (2005) discuss the problem of empirical calibration performed with strong oxygen line intensities / oxygen abundances and propose revised methods to estimate the metallicity.

2.1.3 Other methods for metallicity determination

Another method to derive metallicities is based on the photometry of stellar populations in color-magnitude diagrams (e.g. Lee & Geisler 1993). The color of the red giant branch (or sometimes the morphology of this giant branch) gives information on the stellar abundances. As calibration resides in the comparison with old Galactic globular clusters, the method is dependent on the similarities between the objects compared. Metallicity can also be derived from spectroscopy performed on individual stars (e.g. Haser et al. 1998; Shetrone et al. 1998, who respectively applied this technique to the Magellanic clouds and nearby dwarf spheroidals). Nevertheless, this technique will not lead to the determination of a global value due to statistical issues (only bright stars are observed) and variations between stars. One major limitation of these three methods is that they can only be applied to the very nearby Universe (Local Group and close neighbours).

Metallicity can also be determined from integrated spectroscopy when Hɪɪ regions are not present (e.g. observations of the absorption line of Mg$_2$ and comparisons with observed or models stars; Worthey 1994) or integrated photometry when spectroscopy is not available, even if this last method leads to very poor estimates of the metallicity (Favata et al. 1997).
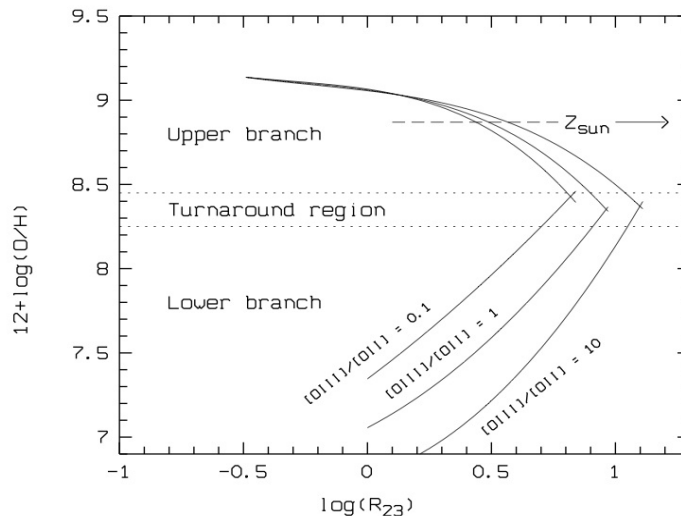
Figure 2.2. Oxygen abundance as a function of the line ratio R_{23}. The calibration between R_{23} and O/H was determined from the models from McGaugh (1991). The figure was taken from Maier et al. (2004).

Finally, one can use the cold neutral ISM and the observations of background sources. The study of the absorption lines from the neutral ISM allows the derivation of abundances (Kunth et al. 1994; Aloisi et al. 2003). Other techniques use X-rays from hot intracluster medium in galaxy clusters (e.g. Kapferer et al. 2007)

2.2 What do we know about low-metallicity galaxies

2.2.1 General characteristics

Dwarf galaxies are the dominant population of the Universe, even if a decline in the abundance of less massive star forming dwarf galaxies seems to be observed from the early to present-day Universe (Lilly et al. 1995; Ellis 1997). Dwarf galaxies of the Local Group are dominated by dark matter, which would mean, if this statement is universally correct, that dwarf galaxies could account for a large fraction of the total mass of the Universe (Mateo 1998). In the hierarchical scenario of structure formation in the Universe, they are thought to be the building blocks of more massive galaxies. They are thus studied as today's best analogs of galaxies of the Early Universe and are ideal laboratories to study the evolution of galaxies in primordial conditions. They are very small in size, and contain far less stars than usual spiral galaxies. They are characterized by low mass (the total mass can go down to 10^5 $M_\odot$), low luminosity (the total luminosity can go down to 10^5 $L_\odot$), low surface brightness and low metallicity (from 1/2 to $\sim 1/50$ or even less). One could think that their small size and low metallicity would imply that they are easier systems to study. In fact, the wide range of their star formation activity or chemical-enrichment history makes if difficult to build a general case for these galaxies.

The luminosity-metallicity (L-Z) relation was very often studied to link the star formation activity of a galaxy to its metal enrichment history. Tremonti et al. (2004), using SDSS observations of star-forming galaxies, established a correlation between gas-phase metallicity and stellar masses that extends over three decades in stellar mass. This correlation is linear from $10^{8.5}$ to $10^{10.5}$ $M_\odot$ and shows a flattening after $10^{10.5}$ $M_\odot$. Broadening their sample to lower metallicities, they found that the effective yield seems to decrease by a factor of ~ 10 from massive to dwarf galaxies and explained these results by a potential loss in metals due to galactic winds more efficient in objects

with a lower gravitational potential. Previous studies by Heckman et al. (2000) have already shown that starburst-driven flows seem to be independent of the host galaxy properties and concluded that outflows selectively escape the potential wells of the less massive galaxies. Recent work by Hong et al. (2010), and Zhao et al. (2010) have re-estimated the L-Z relation for star-forming dwarf galaxies and blue compact dwarfs respectively. They, in particular, found than the L-Z correlation in dwarf galaxies is shallower in the near-IR (K band or 8 μm luminosity) than the corresponding relation derived in the B band (Fig. 2.3).
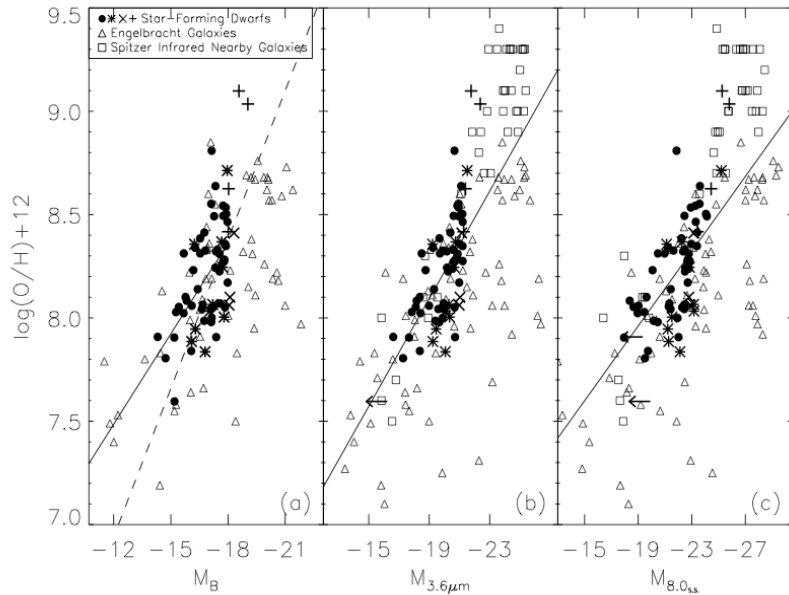
Figure 2.3. Metallicity as a function of absolute magnitude in the B, 3.6 and 8 μm bands. The figure was taken from Hong et al. (2010).

Dwarf galaxies also show evidence for older stellar populations than their metallicity suggests, posing enigmatic issues for galaxy evolution models (Aloisi et al. 1998). For instance, Östlin & Mouhcine (2005) observed I Zw 18, the most metal-poor galaxy known in the local universe ($12+\log(O/H) = 7.18$, Izotov et al. 1999), with NICMOS onboard HST (Hubble Space Telescope) and found that old stars (~ 1 Gyr) are required to explain the observed colour-magnitude diagrams. They suggest that the stellar population of I Zw 18 could be dominated by red supergiant stars, a puzzling population for such a low-metallicity galaxy.

The relatively short recent star formation episodes observed in some low-metallicity galaxies and their gradual enrichment seem to indicate that short bursts may dominate the evolution of these galaxies. For instance, the Local Group dwarf spheroidal galaxy Carina shows a long intermediate-age episode of star formation which seems to be the result of episodic bursts (that could have been triggered by accreted material or other environmental effects) and separated by quiescent periods of $\sim$ 1-2 Gyrs (Smecker-Hane et al. 1996).

Massive starbursts and interacting systems are able to reach the conditions of gas column densities and high pressures required to form massive star clusters. Dwarf galaxies, on the contrary, can only produce relatively few massive star clusters and studies on globular clusters in the Local Group have shown that there is a large scatter in the number of globular clusters per galaxy. Billett et al. (2002) used HST observations to probe compact star clusters in nearby dwarf irregular galaxies and found that 8 of their 22 galaxies were hosting compact clusters (three of them even host super star clusters (SSC)). Their study suggest that only a few dwarf galaxies can form SSC, even the more

active ones, and that dwarf galaxies with a low SFR (e.g. less that 3×10^{-3} $M_\odot$ yr^{-1} kpc^{-2}) can not form SSCs. Dwarf galaxies which, nevertheless, form clusters often have specfic globular cluster frequencies (S_N, number per unit luminosity) similar to those of elliptical galaxies and a trend of increasing S_N with decreasing galaxy luminosity was confirmed in Miller & Lotz (2007). Billett et al. (2002) suggest that the low density of dwarf galaxies could prevent the destructive mechanisms of globular clusters in disks and that large-scale flows or gravitational instabilities could lead to the formation of the massive clouds in which SSCs are formed. Recent observations of the blue compact dwarf galaxy SBS 0335-052 by Johnson et al. (2009) have shown that the galaxy hosts SSCs that could reach SFRs up to 1.3 $M_\odot$ yr^{-1} (so close to the maximum starburst intensity limit). This implies that dwarf galaxies of the Local Group are also ideal objects to probe the conditions of massive star formation in galaxies.

Lee et al. (2009) also addressed the very interesting question of the rate of starburst-dominated systems in the star formation history of low-mass systems of the Local Volume (d < 11 pc). They found that only 6 % of those galaxies were hosting massive starbursts and that those bursts were only producing 1/4 of the star formation in dwarf galaxies.

2.2.2 The morphology classification

Dwarf galaxies are usually classified in the categories described below. How they may or may not be related is a debated subject today. These descriptions are based on Grebel (2001):

Dwarf spiral galaxies are the high-mass population of the dwarf galaxies, with low central surface brightness ($\mu_V \geq 23$ mag arcsec^{-2}), low HI mass ($M_{H_I} \leq 10^9$ $M_\odot$) (Schombert et al. 1995). They exhibit slow continuous star formation and are found both inside (e.g. IC3328 in the Virgo Cluster, Jerjen et al. 2000) and outside clusters, even though in clusters, disks of dwarf galaxies tend to be destroyed by gravitational interactions with companions.

Dwarf irregular galaxies (dIrrs) are irregular galaxies characterized by $\mu_V \leq 23$ mag arcsec^{-2} and $M_{H_I} \leq 10^9$ $M_\odot$. They are gas-rich compared to the other types of dwarfs. Their HI distribution usually shows fractal (clumps, shells, rings) structures. While massive irregulars seem to be dominated by solid-body rotation, low mass irregulars do not systematically show rotation. A gradation in the properties from dIrrs to dwarf ellipticals seems to support the hypothesis that dIrrs could eventually evolve into dwarf ellipticals (e.g. Aparicio et al. 1997) but this is still a big debate.

Dwarf elliptical galaxies (dEs) are spherical, compact galaxies with high central surface brightness ($\mu_V \leq 21$ mag arcsec^{-2}) and low HI mass ($M_{H_I} \leq 10^8$ $M_\odot$). They are quite common in clusters or galaxy groups. Like dIrrs, they do not seem to be supported by rotation.

Dwarf spheroidal galaxies (dSphs) are diffuse, low-surface brightness dwarf galaxies ($\mu_V \geq 22$ mag arcsec^{-2}) devoid of gas ($M_{H_I} \leq 10^5$ $M_\odot$). They are the faintest galaxies known.

Blue compact dwarf galaxies are very compact galaxies dominated by a recent burst of star formation and thus show a strong and bright central surface brightness ($\mu_V \leq 19$ mag arcsec^{-2}). They contain a large population of very hot and young massive stars responsible for their extreme blue colors. They can show HI asymmetric distributions, sometimes kinematically distinct (e.g. NGC 1705 - see Cannon et al. 2006b).

Tidal dwarf galaxies are the remnants of the interactions (material-stripping or mergers) with more massive galaxies. They can be gas-rich (massive HI clouds) and show active star formation activity, but these characteristics strongly depend on the conditions of the interaction

that gives birth to this galaxy. This peculiar mode of formation also implies that tidal dwarfs have higher metallicities, for their mass, than other dwarf galaxies (Duc et al. 1997).

2.2.3 The atomic and molecular gas in low-metallicity galaxies

Some of the dwarf galaxies are devoid of neutral hydrogen while others are gas-rich with usually clumpy HI distribution ($\sim$ 200 pc scales, Young & Lo 1997), sometimes showing large holes around dying massive stars (e.g. Oey et al. 2001) or gravitational instabilities (e.g. Wada et al. 2000). HI envelopes can, in some cases, extend far from the optical disk of the galaxy. HI observations in dwarf galaxies suggest that a minimum HI column density of 10^{21} cm^{-2} would be required to initiate star formation (Skillman et al. 1988). Nevertheless, some dwarf galaxies which fulfill this criterion do not show any current star formation. This suggests that yet-unknown processes much exist to trigger or sustain the star formation activity in these galaxies (Mateo 1998). Indeed, de Blok & Walter (2006) showed that the cool gas could be more important in determining the local star formation than the total HI mass.

The LITTLE (Local Irregulars That Trace Luminosity Extremes) THINGS Survey (Hunter et al. 2007 ; http://www.lowell.edu/users/dah/littlethings/) is a current programme observing the HI-line with the VLA (Very Large Array, New Mexico, USA) for a sample of 42 dwarf irregular galaxies which aims to better understand the mechanisms of star formation in small low-metallicity systems. Brinks et al. (2008) recently analysed the rotation curves of two dIrrs of the THINGS sample and found that the dark matter distribution could be fitted by an isothermal halo model. Bigiel et al. (2008) also suggest that the star formation efficiency of dIrrs seems to be similar to those found in the outer optical disks of the spirals.

CO detections, commonly used as a tracer of the molecular hydrogen, have been very challenging in dwarf galaxies (e.g. Leroy et al. 2009). Sage et al. (1992) note that CO is more easily detected in dwarf elliptical galaxies than in dwarf irregulars. The fragmented structure and clumpiness of the ISM of low-metallicity galaxies allows UV light to penetrate deeper in metal-poor molecular clouds. The beam filling factor of the atomic and molecular phases can thus vary significantly in these environments and a large amount of H_2 could reside in PDRs where CO is photodissociated.

Numerous studies have used Local Group dwarf galaxies to study the variations of the conversion factor from CO intensity to molecular hydrogen column density (I(CO)/M(H_2) = X_{CO}) with metallicity (Wilson 1995; Taylor et al. 1998; Israel 2000; Leroy et al. 2005; Wolfire et al. 2010). For instance, Israel (2000) determined a linear relation between X_{CO} and metallicity:

$$log(X) = -2.5log([O]/[H]) + 12.2 \tag{2.4}$$

where X is N(H_2)/I_{CO} (in cm^{-2}/ K km s^{-1}).

Boselli et al. (2002b) also studied X_{CO} in 266 normal late-type galaxies. They derived X_{CO} factors ranging from $\sim 10^{20}$ cm^{-2}/K km s^{-1} in giant spirals to 10^{21} cm^{-2}/K km s^{-1} in dwarf irregulars and conclude that using a constant X_{CO} factor to derive the molecular gas mass from CO observations could lead to an underestimation of a factor $\sim$ 10. They also analysed the relation of X_{CO} with the UV radiation field or with the H and B band luminosity.

The uncertainties linked with the X_{CO} factor implies that CO should thus not be a reliable tracer of molecular gas in low-metallicity environments. Observations of the far-IR fine structure cooling line [CII] revealed a strong enhancement of the I[CII]/I(CO) in low-metallicity environments compared to metal-rich counterparts (e.g. Poglitsch et al. 1995; Madden et al. 1997; Bolatto et al. 2000; Rubin et al. 2009). These studies suggest that the [CII] line could provide a good tracer of

the total molecular gas mass in dwarfs while CO observations may not reliably probe this quantity on C+ emitting regions. Theoretical work on PDR models (Röllig et al. 2006; Wolfire et al. 2010) seem to confirm this assumption. Boselli et al. (2002a) also suggest that the [CII] luminosity could be a reliable tracer of the massive SFR in distant galaxies and try to calibrate this relation using ISO/LWS data. They also note the difficulty in determining such a relation due to the variety of [CII] line sources, which could create confusion, and the saturation of the upper fine-structure level of [CII] at high temperature and densities.

2.2.4   Dust in low-metallicity galaxies

The extinction law of low-metallicity galaxies is rather different than in galaxies such as our Milky Way. Figure 2.4 shows the extinction curve determined for the Large and Small Magellanic Clouds (LMC and SMC). Like in our Galaxy, local variations are observed within these two galaxies. Weingartner & Draine (2001) manage to reproduce these extinction laws using approximate mixtures of carbonaceous and silicate grains. In particular, the missing 2175 $\mathring{A}$ extinction feature observed in the SMC bar is reproduced by models which lack carbonaceous grains with radii inferior to 0.02 μm. More recent work by Gordon et al. (2003) have shown that the majority of the Magellanic Cloud extinction curves are significantly different from the Milky Way curves. Nevertheless, they suggest that LMC, SMC and Milky Way dust properties should not be considered separately and that a continuum of dust properties could exist between quiescent and more active regions.
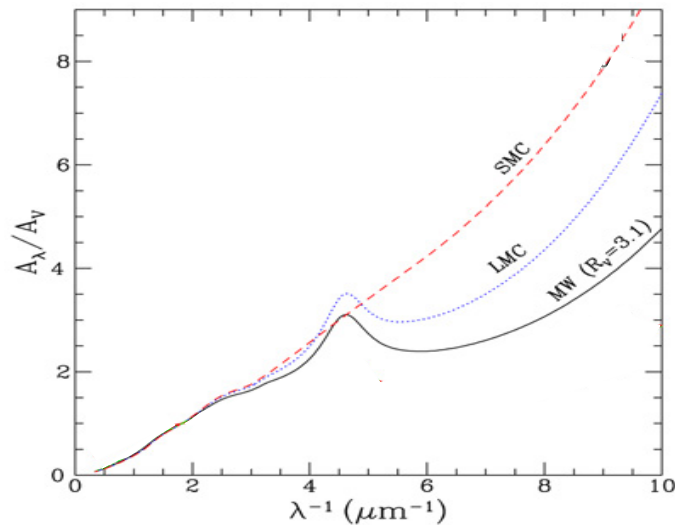
Figure 2.4. Interstellar extinction curves of the Milky Way (R_V=3.1), the Small Magellanic Cloud (SMC) and Large Magellanic Cloud (LMC)

Observations of low-metallicity galaxies with ISO, IRAS and *Spitzer* have highlighted that those galaxies exhibit very different SEDs compared to normal galaxies. They usually show the weakest aromatic features in the mid-IR (Sauvage et al. 1990; Engelbracht et al. 2005; Madden 2005; Wu et al. 2007; Engelbracht et al. 2008). PAHs mostly reside in PDRs and are stochastically heated by the escaping radiation from OB clusters. The lack of PAHs in low-metallicity environment was thus first associated with the hardness of the radiation field of low-metallicity environments (young stellar population, higher effective temperature of stars) and to the paucity of the ISM (more efficient penetration of hard photons in the ISM) that could lead to an efficient destruction of PAHs (Galliano et al. 2003, 2005; Madden et al. 2006). This dependence of PAHs with metallicity was also explained by the delayed injection of carbon dust by AGB stars (Dwek 2005; Galliano et al.

2008). Sauvage et al. (1990) also note that they must be a continuous grain size distribution from PAHs to normal grains responsible to the thermal emission they detect at 25 μm in the LMC.

Finally, the dust temperature distribution for the different dust components is still not completely known, not only in dwarf galaxies. Most galaxies have not yet been observed at submm wavelengths where the coldest phases of dust can be probed. Since dust mass is proportional to the temperature as $T^{4+\beta}$ (Wien's law), the coldest phases of dust will account for a significant, if not a majority of the total dust mass of a galaxy. In some galaxies, usually dwarf galaxies, an excess at submm wavelengths is detected compared to what could be extrapolated from far-IR observations and commonly used dust properties (Lisenfeld et al. 2001; Galliano et al. 2003; Dumke et al. 2004; Galliano et al. 2005; Bendo et al. 2006; Marleau et al. 2006; Galametz et al. 2009; Zhu et al. 2009). Several scenarios have been suggested to explain this excess, among which enhancement of very small grains, very cold (<10K) dust component or change in the dust emissivity properties at submm wavelengths. We will come back to this point in Chapter 5 which is dedicated to observations of dwarf galaxies in which a submm excess was detected. Nevertheless, we can already feel that a complete coverage of the near-IR to submm wavelength range is crucial to properly sample the dust SEDs of galaxies, understand its main characteristics (dust temperature distribution, aromatic features strenght, total dust mass, dust-to-gas mass ratio, star formation activity) and thus have a more complete overview of the physical processes and the dust and gas quantification in the ISM.

In the following chapters, I first describe the telescope and instruments I used to explore the dust properties of galaxies (Chapter 3), and the SED modelling technique we develop to model our galaxies (Chapter 4). I will then describe the analyses we performed on LABOCA submm observations of dwarf galaxies (Chapter 5, 7 and the study we carried out to quantify the influence of submm observations on the total dust mass estimates (Chapter 6). The last part of this thesis (Part III) is dedicated to new *Herschel* results on low-metallicity galaxies.

Part II

Low-metallicity ISM: an IR to submm view

Chapter 3

Obtaining observational constraints to sample SEDs

Contents

The main ingredients to feed into our SED models are the observational constraints. To deduce the maximum amount of information from the dust SED of a given source (dust distribution, temperatures, etc), it must be fully observed from near-IR to far-IR and submm wavelengths. In this thesis, I perform a multiwavelength analysis of global galaxies or structures within galaxies using several instruments and telescopes: 2MASS, IRAS, *Spitzer*, APEX/LABOCA, SCUBA, *Herschel* etc. I will not enter into the details of all instruments and data but will only describe the newest facilities observing the IR and submm I mainly used. In this Chapter, I will present the *Spitzer* telescope I used to probe the near to far-IR range and the LABOCA instrument observing in the submm regime (870 μm).

Spitzer was the first telescope to observe in the IR (from 3.6 to 160 μm) with good spatial resolution (FWHM of the PSF: from 1.7 to 40") and already enables us to broaden our knowledge on dust properties and to study the embedded star formation in local and distant galaxies. Prior to *Spitzer*, ISO spanned the same wavelength range at lower resolution (2' at 100 μm).

Only a few studies have been carried out to probe the very cold dust component (<20K) in galaxies traced by submm observations, mainly due to the difficulty of such observations from Earth. I will also present maps observed with the newly available submm instrument LABOCA mounted on APEX in Chile and observing at 870 μm. In this PhD thesis, I also used data from the *Herschel* Space Observatory. The telescope was launched during my PhD. It is described in the third part of this report (Chapter 8) dedicated to *Herschel* observations and results.

3.1 Spitzer

3.1.1 General Description

The Spitzer Space Telescope was launched from Florida's Cape canaveral Station on August, the 25th, 2003, aboard a Delta II launch rocket. It is the third IR space telescope after IRAS (launched in 1983) and ISO (launched in 1995). A description of the different components of the telescope is given in Fig. 3.1. The telescope possesses three instruments whose data were used in the thesis: IRAC (Infrared Array Camera), MIPS (Multiband Imaging Photometer) and IRS (Infrared Spectrograph).

The sensitivity of the *Spitzer* instruments enabled significant breakthroughs in IR astronomy and enabled reseachers to better understand and quantify the star formation activity or the dust distribution and properties of galaxies. Due to the large database that still has to be interpreted, we can expect *Spitzer* to still bring new discoveries on IR physical processes. The telescope ran out of helium in May, 2009 after more than five-and-a-half years of observations. It then started its 'warm mission'. The temperature of the telescope is about $\sim$ 30K and two channels of IRAC (at 3.6 and 4.5 μm) are still working at full capacity.

3.1.2 The Infrared Array Camera (IRAC)

IRAC (Fazio et al. 2004) has been developed by the Smithsonian Astrophysical Observatory, the Ames Research Center, the Goddard Space Flight Center, the University of Arizona, and the University of Rochester (USA). The instrument was designed and built at the Goddard Space Flight Center. IRAC is a four-channel camera that obtains simultaneous broadband images at 3.6, 4.5, 5.8, and 8 μm with a full-width-half maximum (FWHM) of the Point-spread functions (PSFs) of 1.7", 1.7", 1.9" and 2" respectively. The two first channels InSb detectors operate at $\sim$ 15 K while channels 3 and 4 (Si:As detectors) operate at $\sim$ 6 K (Fig. 3.2). The size of the array is 256 $\times$ 256 pixels (physical pixel size of 30 μm). Bands are imaged in pairs (3.6 and 5.8 microns; 4.5 and 8.0 microns). The main characteristics of IRAC channels are summarized in Table 3.1.
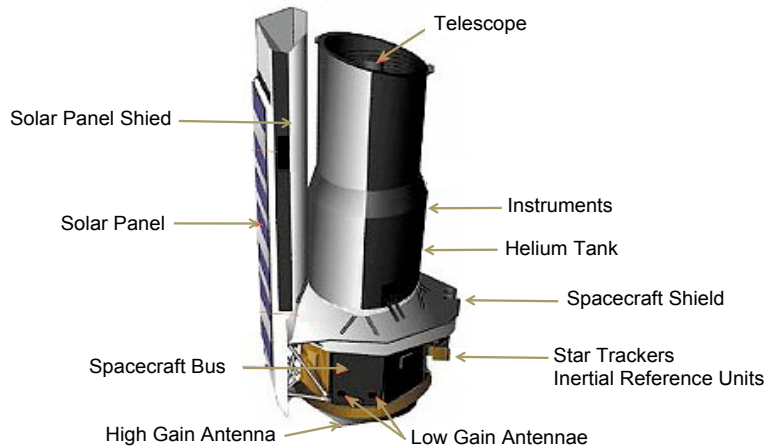
Figure 3.1. Description of the Spitzer telescope
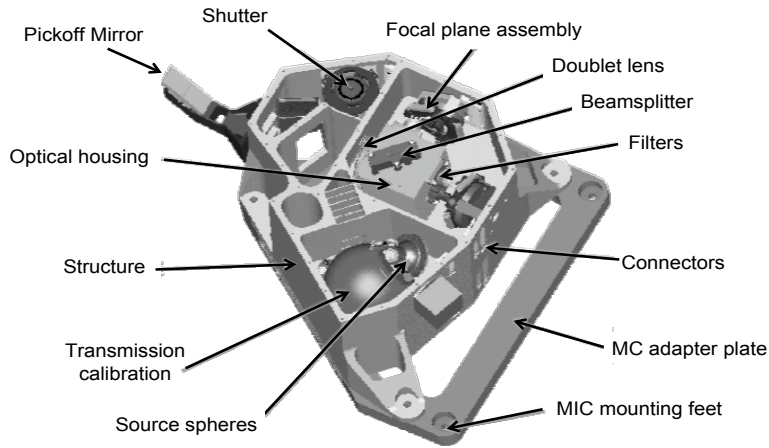
Figure 3.2. IRAC Cryogenic Assembly model

Most of the IRAC maps used in this thesis come directly from the *Spitzer* data archive hosted by the *Spitzer* Science Center (SSC), from the post-basic calibrated data (post-BCDs). The post-BCD maps are obtained after calibration of the individual BCD exposures. The main steps of the reduction pipeline for BCDs includes sky subtraction, flatfielding, cosmic ray detection, flux calibration. Those BCDs are then mosaicked and coadded to produce post-BCD data. This treatment is described in the IRAC data handbook available on the *Spitzer* website (http://ssc.spitzer.caltech.edu /irac/iracinstrumenthandbook/).

3.1.3   The Multiband Imaging Photometer (MIPS)

MIPS (Rieke et al. 2004) has been developed by the University of Arizona and the Ball Aerospace Corporation (USA). The development of the instrument was funded by NASA through the Jet Propulsion Laboratory, Pasadena, CA, USA. MIPS provides observations in the imaging bands 24, 70 and 160 μm with a FWHM of the PSFs of 6", 18" and 40" respectively. The MIPS has three detector arrays: a 128×128 Si:As array at 24 μm, a 32×32 Stressed Ge:Ga array at 70 μm and a 2x20 Ge:Ga array at 160 μm (Fig. 3.3). The components of MIPS are cooled by superfluid liquid hemium to a temperature of $\sim$1.5K. The main characteristics of MIPS channels are summarized in Table 3.1. The nominal fields of view in each band are also indicated in this table.
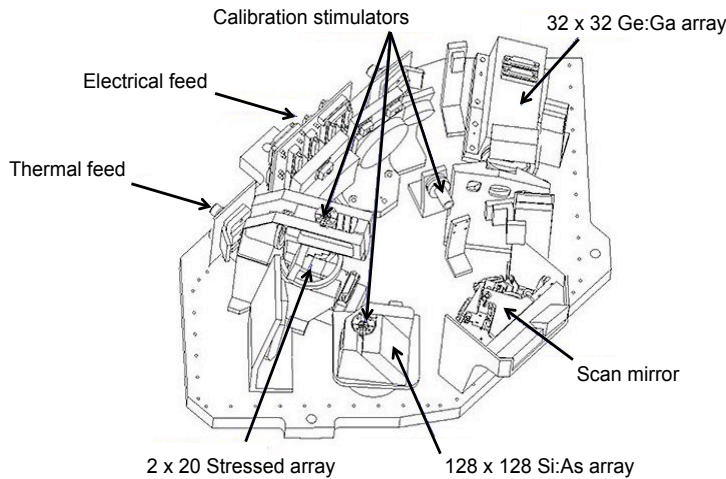
Figure 3.3. Drawing of the MIPS design

The MIPS images used in this thesis were taken in Photometry/Super-Resolution mode or in the scan map mode. The Photometry/Super-Resolution is a dithered observational mode that covers small regions, typically 8' × 8' at 24 μm and 7' × 2.5' at 70 and 160 μm. The data were obtained through the *Spitzer* archive (raw data) and processed using the MIPS Data Analysis Tools (Gordon et al. 2005) version 3.10 along with additional processing steps. The following notes detail the main steps of the MIPS reduction performed by George Bendo, from Imperial College, London, UK.

Notes :

Steps of the MIPS 24 μm data reduction - *The individual 24 μm frames are processed through a droop correction (removing an excess signal in each pixel that is proportional to the signal in the entire array) and are corrected for non-linearity in the ramps. The dark current is subtracted. Next, scan-mirror-position dependent flats are created and applied to the data in each Astronomical Observation Request (AOR). Detector pixels that measure significant signals (2500 DN s^{-1}) in any frame are masked out in the following three frames to avoid latent images in the data. A scan-mirror-position independent flat is created and applied to the data in each AOR. Following this, the zodiacal light is subtracted from the data. In the photometry mode data, planes were fit to the zodiacal light emission in the background regions in each frame. These planes are then subtracted from the data. In the scan map data, third order polynomials are fit to the background in each leg of each scan map, and this background is subtracted from the data. We also measure and subtract any scan-mirror-position dependent residual offset in the background.*

For observations performed in scan-map mode, preliminary mosaics of the data from each AOR are built at that stage. They are then used to identify transient objects (e.g. asteroids), which are then masked out in the individual data frames. A robust statistical analysis is then applied: the values of cospatial pixels from different frames are compared to each other and statistical outliers (e.g. probable cosmic rays) are masked out. The final mosaic is created and data are calibrated into astronomical units. The calibration factor for the 24 μm data is given by Engelbracht et al. (2007) as 4.54 ± 0.18 × 10^{-2} MJy sr^{-1} [MIPS instrumental unit]$^{-1}$.

Steps of the MIPS 70 and 160 μm data reduction - *In the 70 and 160 μm data processing,*

the first step is to fit ramps to the reads to derive slopes. In this step, readout jumps and cosmic ray hits are also removed, and an electronic nonlinearity correction is applied. The stim flash frames taken by the instrument are then used as responsivity corrections. The dark current is subtracted from the data, and an illumination correction is applied. Short term variations in the the signal (often referred to as drift) are removed from the 70 and 160 μm scan map data; this also subtracts the background from the data.

For observations performed in scan-map mode, the background from the photometry map data is subtracted at this stage. A robust statistical analysis is applied to cospatial pixels from different frames in which statistical outliers (e.g. pixels affected by cosmic rays) are masked out. Final mosaics are then built. The residual backgrounds in the 70 and 160 μm data are measured in regions outside the optical disks of the galaxies and subtracted. Flux calibration factors are finally applied to the data. The 70 μm calibration factors are given by Engelbracht et al. (2007) as 702 $\pm$ 35 MJy sr^{-1} [MIPS instrumental unit]$^{-1}$ for coarse-scale imaging and 2894 $\pm$ 294 MJy sr^{-1} [MIPS instrumental unit]$^{-1}$ for fine-scale imaging. The 160 μm calibration factor is given by Stansberry et al. (2007) as 41.7 $\pm$ 5 MJy sr^{-1} [MIPS instrumental unit]$^{-1}$. An additional 70 μm non-linearity correction given as $f_{70\mu m}(true)=0.581(f_{70\mu m}(measured))^{1.13}$ by Dale et al. (2007) was applied to coarse-scale imaging data where the surface brightness exceeded 66 MJy sr^{-1}.

Table 3.1. IRAC and MIPS channels characteristics

	IRAC				MIPS		
	ch1	ch2	ch3	ch4	ch1	ch2	ch3
Wavelength (μm)	3.6	4.5	5.8	8.0	24.0	70.0	160.0
FWHM (arsec)	1.7	1.7	1.9	2.0	6	18	40
Nominal Fields	5.2' $\times$ 5.2'				5' $\times$ 5'	5' $\times$ 5'	0.75' $\times$ 5'
Size of the detector array(pixels)	256 $\times$ 256				128 $\times$ 128	32 $\times$ 32	2 $\times$ 20

3.1.4 IRS spectra

IRS (Houck et al. 2004) has been developed by the Cornell University and the Ball Aerospace Corporation funded by NASA through the Jet Propulsion Laboratory and the Ames Research Center, USA. IRS provides both high- and low-resolution spectroscopy at mid-infrared wavelengths. It possesses four separate modules: a low resolution short-λ mode (covering wavelengths from 5.3 to 14 μm), a high-resolution short-λ mode (from 10 to 19.5 μm), a low-resolution long-λ mode (from 14 to 40 μm) and a high-resolution long-λ mode (from 19 to 37 μm) (Fig. 3.4). The silicon detectors are 128 $\times$ 128 arrays and are treated with arsenic for the short-λ (Si:As) and antimony for the long-λ (Si:Sb). The main characteristics of the IRS modules are summarized in Table 3.2.

In this paragraph, we briefly describe the different steps of point-source data reduction. IRS Basic Calibrated Data products, when available, can be downloaded directly from the *Spitzer* data archive. We then use IRSClean, an interactive IDL tool, in order to create bad pixel masks and 'clean' the masked pixels in a set of data (Fig. 3.5). The frames are coadded. We then used the *Spitzer* IRS Custom Extraction software (Spice - version 2.0.1) to extract the spectrum of Haro 11, using the default pipeline for point source observations. We subtracted the background contribution estimated from zodiacal models using the software SPOT (version 18.0.1). SPOT is also a software
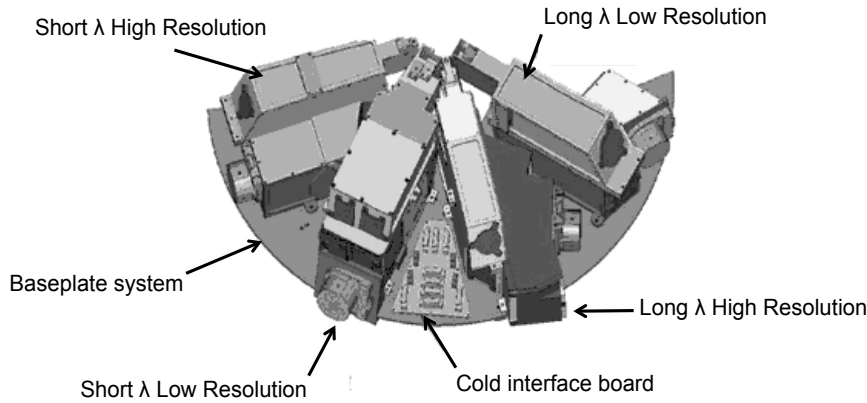
Figure 3.4. Interior of the IRS spectrometer

Table 3.2. IRS properties

Module	Array	Pixel Size	Order	Slit Size	λ	$\lambda/\Delta\lambda$
		(arcsec)		(arcsec)	(μm)	
Short-Low	Si:As	1.8	SL2	3.6×57	5.2 - 7.7 [a]	80 - 128
—	—	—	SL1	3.7×57	7.4 - 14.5	64 - 128
—	—	—	'Blue' peak-up	56×80	13.3 - 18.7 [b]	~ 3
—	—	—	'Red' peak-up	54×82	18.5 - 26.0 [b]	~ 3
Long-Low	Si:Sb	5.1	LL2	10.5×168	14.0 - 21.3 [a]	80 - 128
—	—	—	LL1	10.7×168	19.5 - 38.0	64 - 128
Short-High	Si:As	2.3	11-20	4.7×11.3	9.9 - 19.6	~ 600
Long-High	Si:Sb	4.5	11-20	11.1×22.3	18.7 - 37.2	~ 600

Notes.- [a] Bonus orders cover the 7.3 - 8.7 μm range ('SL3') and the 19.4 - 21.7 μm range ('LL3').

[b] FWHM of the filter.

package for *Spitzer* users to plan observations or submit proposals. The final error on the photometry derived from peak-up acquisition windows is about 15%, the value recommended by the IRS data handbook.

3.1.5 Probing the ISM properties and the dust distribution with *Spitzer*

Spitzer observations probe the distribution of dust grains. The four bands of IRAC trace the stars, PAH and hot dust emission while MIPS 24 μm is often used as a tracer of the star formation activity in galaxies (e.g. Calzetti 2007), since it is probing the warm dust primarily associated with HII regions. It also enables us to quantify the abundance of small dust grains and their size distribution. Properties of the smallest grains (and how they evolve from one galaxy to another) are of crucial importance to understand the thermodynamics of the ISM. Small grains are, indeed, very efficient in the processes of heating of the gas through photoelectric effects. Finally, most of the dust mass of a galaxy resides in its population of largest grains traced by far-IR dust emission, and thus by MIPS 70 and 160 μm observations or longer wavelengths. The IR observations mainly probe the embedded star formation in galaxies and thus unveil the invisible.
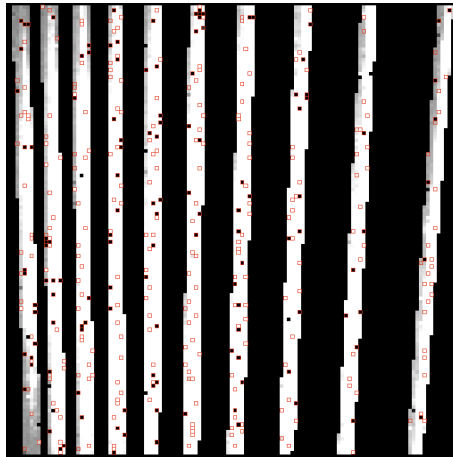
Figure 3.5. IRSClean interactive interface. A first automatic search of bad pixels (red squares) is performed by the software. The user is then invited to choose with his/her mouse, if necessary, the bad pixels that are still remaining after the automatic detection.

3.2 The APEX / LABOCA instrument

3.2.1 Description

APEX (Atacama Pathfinder Experiment, Fig. 3.6) is a collaboration between the Max Planck Institut für Radioastronomie (MPIfR), Germany, at 50%, the Onsala Space Observatory, Sweden, at 23%, and the European Southern Observatory at 27%. It was designed as a 12-m single dish prototype antenna for the ALMA Observatory and is located on the high altitude site of Chajnantor in the Atacama desert in Chile. I was very lucky to go and observe at the APEX telescope during my PhD in May 2009 where we installed and observed with our visitor instrument p-ArTéMiS (450 μm), the prototype of the ArTéMiS mission. ArTéMiS is a collaboration between CEA/Sap (Service d'Astrophysique), IAS (Institut d'Astrophysique Spatiale), CRTBT (Centre de recherche sur les très basses températures, now Institut NEEL) and IAP (Institut d'Astrophysique de Paris), France.
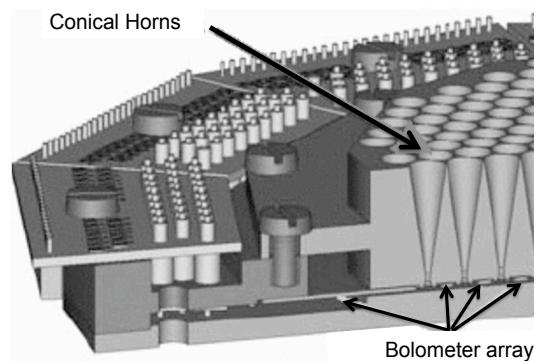
Figure 3.6. The APEX teslescope on which LABOCA is installed and the assembly at the focal plane of LABOCA

I also received time to observe with LABOCA (Large Apex BOlometer CAmera), a multi-channel bolometer array for continuum observations, built by the MPIfR and located on the Cassegrain cabin of APEX. It was installed in September 2006 but the commissioning and science verification only took place in May and June 2007. The bolometer array is mounted on to a copper ring, under

a monolitic array of conical horn antennas (see Fig. 3.6) and above a plane subreflector. The instrument needs to be cooled down to below 0.3 K. It is thus mounted on a cryostat which uses liquid nitrogen and liquid helium combined with a closed cycle double-stage sorption cooler.

The LABOCA array consists of 295 composite bolometers (260 are actually functional) arranged in an hexagonal layout. It undersamples the sky. The separation between channels in one row is twice the beam size (36"). It is thus necessary to use scanning or jiggling to produce fully sampled maps. The bolometers have a broad spectral sensitivity, defining an operating central frequency of 870 μm. The LABOCA instrument has an angular resolution of 18.6" for a total field of view of 11.4'. Pointings are usually combined with a raster spiral (see Fig. 3.7).
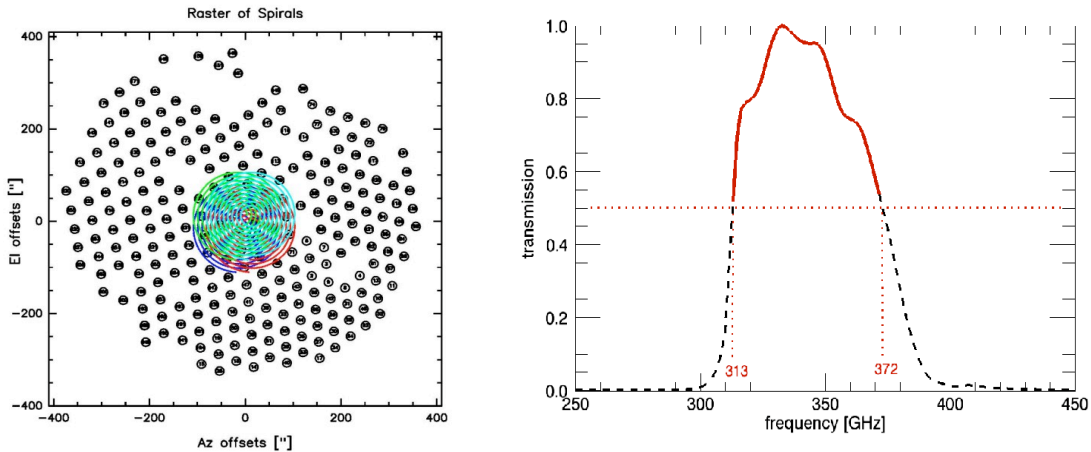
Figure 3.7. Telescope path for a four point raster of spirals and Spectral Response of LABOCA.

3.2.2 Data reduction of LABOCA data with BoA

Several software packages are commonly used to reduce LABOCA data among which Minicrush, shorter version of the software CRUSH adapted for the APEX bolometers, and the software BoA (BOlometer Array Analysis Software). We chose to use the latter for our reduction.

BoA was developed through a collaboration of scientists from the MPIfR, AIfA (Argelander-Institut für Astronomie, Bonn, Germany), AIRUB (Astronomisches Institut der Ruhr-Universität, Bochum, Germany), and IAS (Institut d'Astrophysique Spatiale, Orsay, France). The software is based on a Python programming language and provides a range of classes, functions and methods (Object Language philosophy) for the reading, handling and analysis of bolometer data. It allows online visualization and offline processing and naturally interfaces with the MBfits format in which the raw data we received from ESO were stored.

The following lines will explain the main steps of the data reduction of point sources with BoA. The reduction is performed on each observation scan. The reduced observation scans are then combined at the end of the procedure. The data reduction with BoA can be very long for large observations like those of the LMC/N159 region (35' × 28') also presented in this thesis (Chapter 7). We used a multi-core machine to reduce LABOCA data. The reduction of large maps for extended sources required a loop procedure that is described in Chapter 7.

Reduction pipeline:

Read the data. s is a string containing the scan name. Data are saved in a variable called 'data' by default.

```
read(s)
```

A file called 'Laboca-taus-All.dat' is generated independantly using the script *reduce-skydip.boa* available by default in the BoA package. The input of this functions are respectively the reference number of the skydips taken every hour during the observations. The nearest opacity value at the Modified Julian Day 'mjdref' is retrieved from the './Laboca-taus-All.dat' file directly or with a linear interpolation of the zenith opacity from bordering skydips.

```
mjdref=fStat.f_mean(data.ScanParam.MJD)
tau = getTau(mjdref,'linear', './Laboca-taus-All.dat')
data.correctOpacity(tau)
```

A file called 'Laboca-Calibration-All.dat' is generated independantly using the Boa script *reduce-calib.boa*. The inputs of this function are the reference numbers of the observations of calibration sources. Calibration is performed through observations of stars and planets such as Uranus, Mars, HLTAU, J0423-013, J0050-095, J0006-064,V883-ORI, PMNJ0403-3605, PMNJ0106-4034, PKS0537-441 or N2071IR. A linear interpolation of the calibration correction is directly read in the './Laboca-Calibration-All.dat' file or derived with an interpolation from boardering flux calibrator observations. Calibrators are observed routinely every 2H between the scientific observations to improve the absolute ux determination.

```
calcorr = getCalCorr(mjdref,'linear','./Laboca-Calibration-All.dat')
data.Data /=array(calcorr,'f')
```

Remove the 33 LABOCA pixels shadowed by a plate in the beam from October 18th to November 15th.

```
shadowed=[18,28,171,172,174,177, ...  ,283,294,299,305,309,314,316,320]
data.flagChannels(shadowed)
```

Convert the signal in Jy/beam - Correct the calibration factors (BoA uses the old 6.3 version by default)

```
data.BolometerArray.JyPerCount = VtoJy
data.Data *= array((61.0/63.0*VtoJy),'f')
```

Remove bad channels and remove initial offsets

```
data.flagChannels(resistor,flag=1)
data.flagChannels(cross,flag=1)
data.flagChannels(blind,flag=1)
data.zeroStart()
```

The signals are then divided by the bolometer gains to normalize them. By default, the method applied is an estimate of the point source relative gains.

```
data.flatfield()
```

We then remove data taken outside reasonable telescope scanning velocity, thus data taken when the telescope was too slow to produce a signal inside the useful part of the post-detection frequency band of LABOCA (stationary points) or data obtained when the telescope acceleration was very high, leading to some excess noise (high acceleration data).

```
data.flagSpeed(below=30.)
data.flagSpeed(above=500.)
data.flagAccel(above=800.)
```

During the commissioning period, correlated noise was observed across the array but also between groups of channels sharing some parts of the electronics. We remove the correlated noise per amplifier box ($\sim$ 80 channels can be connected to the same box) and per cable.

```
correlbox(data,factor=0.8,nbloop=2)
correlgroup(data,factor=0.8,nbloop=1)
```

Remove spikes, thus flag iteratively data below and above a given rms value.

```
data.iterativeDespike(below=-10,above=10)
```

Remove median baselines per channel and per subscan or polynomial baseline per scan. We used a polynomial of order 1. The polynomial baseline removal is performed per scan, but not per subscan (subscan=0).

```
data.medianBaseline()
data.polynomialBaseline(order=1,subscan=0)
```

Channels are then flagged according to their rms, with limits determined according to the median rms of all channels. The keyword *ratio* indicates the fraction of the median rms value above and below which data will be flagged.

```
data.flagFractionRms(ratio=5)
```

Flatten the 1/f noise caused by thermal variations. It flattens the 1/f part of the FFT. The keyword *below* is used to define the value below which to filter the data and *href* the value with which amplitudes at f<*below* has to be replaced. These parameters have to be chosen with caution in the case of our sources due to the significant influence it will have on the final map, especially on faint extended emission.

```
data.flattenFreq(below=0.1,href=0.2)
```

Construct the weighted map and save the data. The default method is $1/\mathrm{rms}^2$.

```
data.slidingWeight()
ms=data.Map
dumpData('dump'+s+'.sav')
```

Plot the map in (RA, Dec) coordinates in the BoA environment. The parameters *sizeX* and *sizeY* define the limits of the map. The keyword *limitsZ* defines the limit in the pixel values to define the color scale.

```
doMap(system='EQ',sizeX=[84.4,85.8],sizeY=[-70,-69.4],limitsZ=[-1,1])
```

The different scans individually reduced are summed using the Boa *mapsum* procedure and the final map is saved.

```
a47026=newRestoreData('./dump47026.sav')
a47027=newRestoreData('./dump47027.sav') ...

mapList=[]
mapList.append(a47026.Map)
mapList.append(a47027.Map) ...

ms=mapsum(mapList)
ms.writefits('mygalaxy.fits')
```

3.2.3 Probing the cold dust with LABOCA

Submm observations are crucial to constrain the coldest grain populations and thus quantify the total dust mass of galaxies. In this thesis, we present the first observations of dwarf galaxies with LABOCA. LABOCA is the first instrument of the southern hemisphere to probe the submm with such resolution (18.6"). Prior to LABOCA, there was SIMBA (resolution of 22") on the SEST (Swedish-ESO Submillimetre Telescope) telescope, observing at 1.2 mm. This enabled us to quantify the submm emission and thus the coldest dust phases of southern sources for the first time but also to resolve the cold dust emission within nearby sources such as our neighboring Large Magellanic Cloud.

3.3 Convolution kernels

To compare the fluxes at different wavelengths and perform SED modelling, we convolve every observation to the same resolution. Indeed, the physical regions we are studying will show changes with wavelength. Every image of a single galaxy or object is thus convolved to the lowest common resolution. Most of the time, *Spitzer* data are available for our sources and the lowest resolution is that of MIPS 160 with a FWHM of 40". When MIPS 160 μm is not available, we convolve images to the resolution of LABOCA (18.2").

3.3.1 Convolve *Spitzer* maps to lower resolution *Spitzer* maps

Convolution kernels to convert a higher resolution IRAC/MIPS point-spread function (PSF) to lower resolution IRAC/MIPS PSF are available on the web. The convolution kernels built by Karl D. Gordon are, for instance, available here : http://dirty.as.arizona.edu/ kgordon/mips/conv_psfs/conv_psfs.html (Gordon et al. 2008). Their kernels are built using Fourier transforms, a technique we also used to generate Herschel convolution kernel (see Chapter 8).

We use IDL to convolve the images using a relevant convolution kernel (for example the kernel 'irac_c1_to_mips_160_75K.fits' to convolve an IRAC channel 1 (3.6 μm) image to the resolution of MIPS 160 μm) and use the IDL procedure *Hastrom* to align images according to a reference image.

3.3.2 Convolve maps to the LABOCA resolution

No kernels are available to convolve images to the LABOCA resolution. We thus convolve the observations using a gaussian kernel (using the IDL procedure *convolve*) and regridded the images to match the MIPS 160 μm observation (using the IDL procedure *Hastrom*).

The following lines show an example of convolution steps to lower the resolution of IRAC1 to the resolution of LABOCA.

IDL script :

```
; Define the input resolutions and image

initial_resolution = 1.7                    ; Resolution of IRAC Channel 1 in arcsec
desired_resolution = 18.2                   ; Resolution of LABOCA in arcsec
image_to_convolve = readfits ( 'image_irac1.fits' , initial_header)     ; IRAC 1 image to convolve
old_platescale = 1.2                        ; Platescale of the IRAC 1 image in arcsec
rebin_step = 1                              ; If you want to rebin your image

; Define the parameters of the Gaussian convolution kernel

fwhm = SQRT(desired_resolution^(2.) - initial_resolution^(2.))
platescale = rebin_step * old_platescale
r_half = fwhm / platescale
w = r_half / 2.35482      ; FWHM(Gaussian) = 2*sqrt(ln(4)) times the standard deviation
min_thresh = 1d-8
r_max = w * sqrt(-1d0 * alog(min_thresh) * 2)

; Define the PSF centered on the middle of the image

Npix = 2L * ceil(r_max)+1L           ; ceil (A) = closest integer ≥ A
image = make_array(Npix, Npix, value=0d0)
x = dindgen(Npix)#make_array(Npix,value=1) - Npix/2
y = dindgen(Npix)##make_array(Npix,value=1) - Npix/2
r = sqrt(x^2+y^2)
PSF = exp(-1d0 * r^2 / (2d0 * w^2))
PSF = PSF/total(PSF)                  ; Normalize the final PSF

; Once obtained, we use the convolution kernel to lower the resolution of our IRAC1 image

convolved_image = convolve ( image_to_convolve , PSF )

; We then use the Hastrom procedure to regrid the image to our reference image.
```

3.4   Photometry on the sources

We use the IDL function *aper* to compute concentric aperture photometry in several circles with aperture radii defined by the user. *aper* was adapted from DAOPHOT and is available in the astronomical library of the NASA Goddard Space Flight Center. I give a detailed description on how this IDL function works:

```
APER,image,x,y,flux,errflux,sky,skyerr,radius,annulus,/NAN,/EXACT,/FLUX
```

- **image -** Input image array
- **x and y -** Coordinates of the photometric aperture (in image coordinates)
- **flux -** Flux within the aperture (in image units)
- **errflux -** Error on the flux estimate
- **sky -** Background value estimated in an annulus around the photometric aperture (in image units)
- **skyerr -** Error on the background estimate
- **radius -** Photometric aperture radius (in number of pixels)
- **annulus -** Two element vector giving the inner and outer radii of the annulus used for the background estimate.
- **/NAN -** NAN pixels are ignored during the computation
- **/EXACT -** The intersection of the circular aperture with a square pixel is computed exactly.
- **/FLUX -** Results will be kept in flux units

Aperture corrections have to be applied to the IRAC fluxes to correct the photometry of our extended sources. These correction factors take into account the extended emission from the IRAC PSF itself but also contains the correction of the scattering of incident light within the detector material, in the focal plane arrays (see Reach et al. 2005 for further details on how these factors were obtained). The scaling factors are respectively 91, 94, 71 and 74% applied to the extended flux densities estimated at 3.6, 4.5, 5.8 and 8 μm.

Now that our data are reduced, calibrated and convolveed to a common resolution, we are ready to model the SEDs of the galaxies and analyse the properties of the various dust phases in our galaxies.

Chapter 4

The SED modelling technique

Contents

4.1 Introduction

The SED of a galaxy is very complex to interprete. The integrated SED of a galaxy indeed synthesises the different components that constitute its global emission, including HII regions, molecular clouds, nebulae, diffuse ISM etc., which can not all be studied independently in galaxies due to the lack of resolution. For a macroscopic region of the ISM (HII region, cirrus), on the contrary, the SED summarises a wide range of physical conditions linked with the non-uniformity of its illumination and the variations of the dust composition.

An SED model should then strike a balance between the complexity of the physical processes it aims to describe and quantify and the necessity to find a simple model which will avoid *1-* an overinterpretation of the observational constraints *2-* degeneracies in the model due to too many free parameters. Our main objective in modelling the SEDs of our galaxies is to deduce general properties of the various dust phases such as the PAH abundances, the range of possible heating intensities etc. and to quantify their total dust masses, a parameter that will allow us to study global dust-to-gas mass ratios and to characterise the current chemical state of these galaxies as well as the evolution of the dust and gas budget with metallicity.

In the following paragraph, I describe the main building blocks of our SED model and the assumptions and choices we made *a priori* to simplify the model.

4.2 The interstellar radiation field

We assume that the source of excitation of the dust is the interstellar radiation field (ISRF). Many studies show that the form of the global ISRF of the galaxies could be rather different from galaxy to galaxy and could especially evolve with the metallicity or the star formation activity of the galaxy. Dwarf galaxies often show harder global ISRFs than that of the Galaxy, an effect attributed to the lower dust attenuation in the low-metallicity ISM and, as a consequence, the larger mean free path length of the ionising photons, and to the predominance of massive stars.

Madden et al. (2006) synthesized the ISRF of the four low-metallicity galaxies He 2-10, II Zw 40, NGC 1140 and NGC 1569 (see Fig. 4.1a) using a dust SED model, the stellar evolution synthesis code PEGASE (Fioc & Rocca-Volmerange 1997) and the photoionisation model CLOUDY (Ferland 1996). We refer to Galliano et al. (2003, 2005) for further explanation of the process. They observe an evolutionary sequence among the ISRF, with quiescent galaxies showing a softer ISRF while starburst galaxies showed harder radiation fields. The lack of PAH molecules observed in some dwarf galaxies also seems to be correlated with the hardness of the ISRF (Madden et al. 2006; Lebouteiller et al. 2007), leading some authors to invoke a process of destruction of PAHs by hard radiation fields. Nevertheless, some authors also explained that the lack of PAHs could simply reflect a delayed injection of carbon dust into the ISM by the main source of PAHs in galaxies, namely AGB stars, or via shocks (O'Halloran et al. 2008; Micelotta et al. 2010).

Due to the lack of constraints to determine the individual ISRF of our galaxies, we choose to use the spectral shape of the ISRF found in the Galactic diffuse ISM (Mathis et al. 1983). The ISRF intensity will be scaled using a factor U defined in Draine & Li (2007):

$$u_\nu = U u_\nu^{Galaxy} \tag{4.1}$$

with u_ν the specific energy density of starlight and u_ν^{Galaxy} corresponding to the value estimated in the local solar neighbourhood ($\sim 2.2 \times 10^{-5}$ W m^{-2}).

We chose to use the Mathis et al. (1983) ISRF shape but other spectral shapes of the ISRF can be tested, for instance the ISRFs synthesized by Madden et al. (2006). We test their influence

on the total dust mass estimates of galaxies in Chapter 5. We also produce a grid of dust models for the ISRF of a young and non-ionising cluster, created just after an instantaneous burst, with a Salpeter IMF (Fig. 4.1b). We note that the dust mass is dominated by equilibrium grains which are insensitive to the hardness of the radiation field.
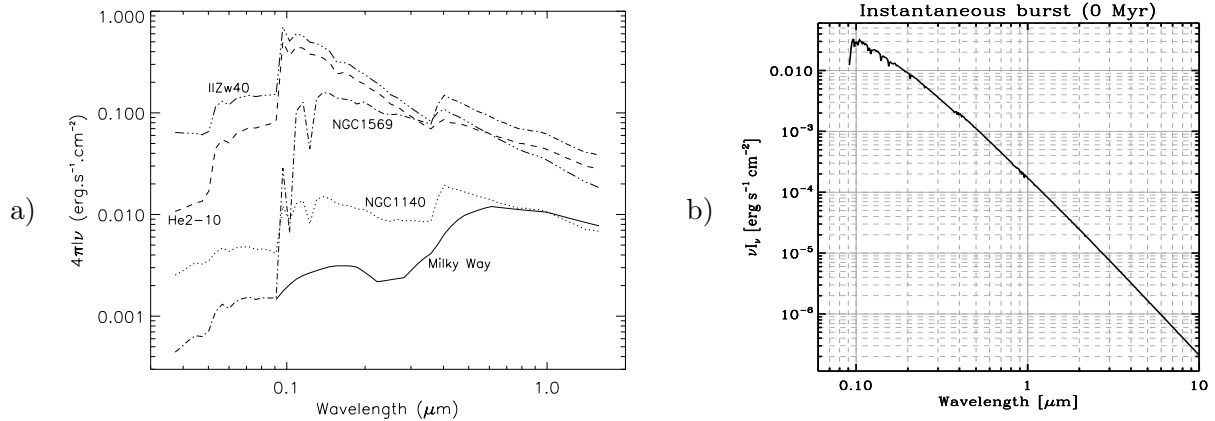
Figure 4.1. *a)* ISRFs of the Galaxy, NGC 1140, NGC 1569, II Zw 40 and He 2-10 synthesized by Madden et al. (2006). *b)* ISRF of a young non-ionising cluster created just after an instantaneous burst .

4.3 The Dale prescription for the radiation field

Because we do not have sufficient observational constraints to model the ISRF, we adopt the simple prescription of Dale et al. (2001) to link the dust mass exposed to a given intensity ($dM_{dust}(U)$) to the different heating environment intensities (§4.2) to which dust is exposed.

$$dM_{dust}(U) \propto U^{-\alpha}dU, \qquad U_{min} \leq U \leq U_{max} \qquad (4.2)$$

This prescription is flexible enough to describe dense and diffuse media. The index α thus represents the contribution of the different local SEDs exposed to a certain intensity U. We introduce the three quantities α, the minimum heating intensity U_{min} and the maximum heating intensity U_{max} as free parameters in our modelling. Fig. 4.4 shows the evolution of the emission of dust grains as a function of the factor U (defined in 4.2).

4.4 Dust properties

We assume that the sources of IR emission are dust and old stars. One of the main assumptions of our model is that the dust composition is homogeneous throughout the galaxy. For silicates, graphites and PAHs, we adopt the composition and size distribution of Zubko et al. (2004) (Fig. 4.2). We summarize the ranges of size and the density of each grain in Table 4.1. The Bare-GR-S dust model of Zubko et al. (2004) assumes that the dust particles are PAHs, graphites and silicate grains and that the ISM has a solar abundance.

The dust size distribution of the different components of this model is plotted in Fig. 4.2. $f_{dist}(a)$ represents the size distribution function. $f_{dist}(a)=Ag(a)$, with A a normalization coefficient in H^{-1}. The function g follows the property:

$$\int_{a_-}^{a_+} g(a)da = 1 \tag{4.3}$$

g(a) is a function of 14 parameters (b_0, c_0, a_1, b_1, m_1, a_2, b_2, m_2, a_3, b_3, m_3, a_4, b_4, c_4) where:

$$log\bar{g}(a) = c_0+b_0 log(a)-b_1|log(a/a_1)|^{m_1}-b_2|log(a/a_2)|^{m_2}-b_3|log(a-a_3)|^{m_3}-b_4|log(a-a_4)|^{m_4} \tag{4.4}$$

All of these coefficients can be found in Zubko et al. (2004).
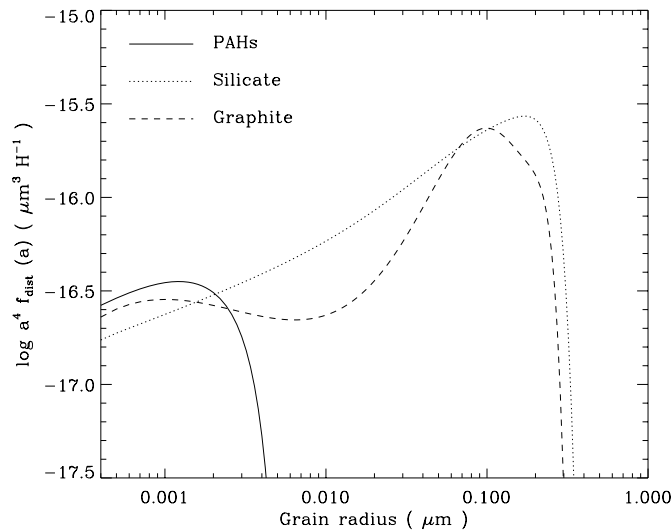
Figure 4.2. Size distribution of PAHs, silicate and graphite grains in the Bare-GR-S dust model of Zubko et al. (2004). For explanations on $f_{dist}(a)$, see section 4.4.

Table 4.1. Size range and mass densities of the three dust grain components from Zubko et al. (2004).

	PAHs	Graphites	Silicates
Minimum Size (μm)	3.5×10^{-4}	3.5×10^{-4}	3.5×10^{-4}
Maximum Size (μm)	5×10^{-3}	0.33	0.37
Mass density (g cm^{-3})	2.24	2.24	3.5

The total dust mass, M_{dust}, is a free parameter of our modelling. To model the PAH component, we introduce two parameters, the ionised PAHs-to-neutral PAH ratio (f_{PAH+}) and the PAH-to-total dust mass ratio (f_{PAH}) normalised to the Galactic value of 0.046.

The assumed optical properties of dust grains are taken from Draine & Li (2007; PAHs), Laor & Draine (1993; graphites) and Weingartner & Draine (2001; silicates). The dust optical properties used in this modelling can partly be found at http://www.astro.princeton.edu/~draine/dust/dust.html (except those of Draine et al. 2007). Fig. 4.3 shows the absorption efficiencies of the neutral and ionized PAHs (Draine & Li 2007).
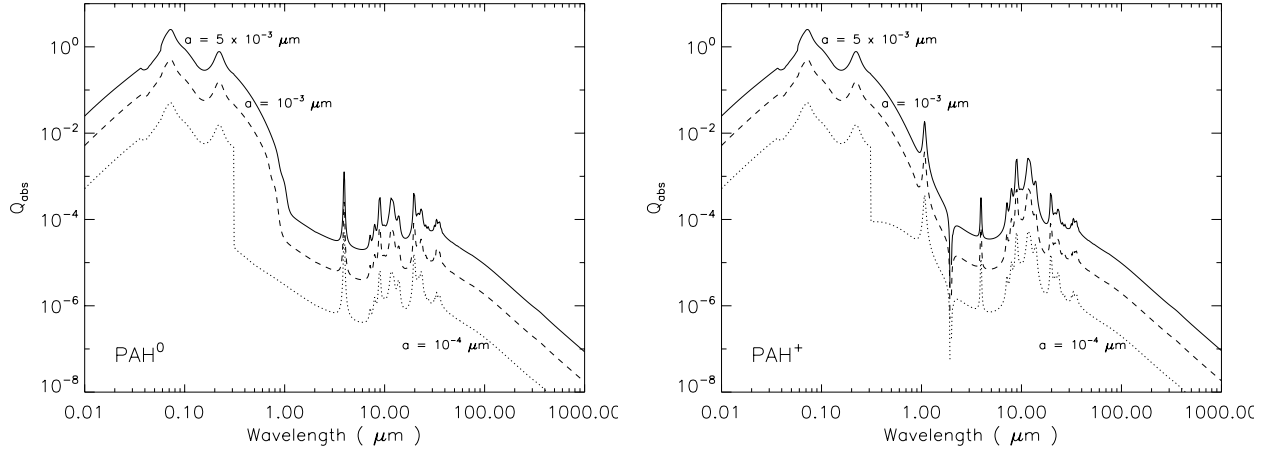
Figure 4.3. Absorption efficiencies for neutral and ionized PAHs. Values are derived from Draine & Li (2007).

We compute the temperature fluctuation in dust grains heated by the absorption of the stellar radiation using the method of Guhathakurta & Draine (1989). Synthesized spectra are finally computed for each of the silicates, graphites, neutral and ionized PAHs also allowing grains to be stochastically heated.

Note : A few words on the temperature distribution calculation technique

We use the Guhathakurta & Draine (1989) method to calculate the steady state temperature distribution of a spherical dust grain. The different elements $A_{i,f}$ of the transition matrix A are the probabilities per unit time that a grain in a state i is making a transition to state f.

The cooling rate in the kth enthalpy bin is given by:

$$-\left(\frac{dH}{dt}\right) = 4\pi a^2 \int Q_{abs}(\nu)\pi B_\nu(T_k)d\nu - \pi a^2 c \int_0^{\nu_{cut}} Q_{abs}(\nu)u_\nu d\nu \tag{4.5}$$

$$= 4\pi a^2 <Q_{abs}>_{T_k} \sigma T_k^4 - \pi a^2 c \int_0^{\nu_{cut}} Q_{abs}(\nu)u_\nu d\nu \tag{4.6}$$

where the left term is the cooling through radiation and the right term is the continuous heating rate. $<Q_{em}>_{T_k}$ is the Planck average emissivity of the dust grain. The cooling into the final state from the state above it is thus given by:

$$A_{f,f+1} = -\frac{1}{\Delta H_{f,f+1}}\left(\frac{dH}{dt}\right)_{f,f+1} \tag{4.7}$$

On the contrary, the discrete heating to go from state i to state f is expressed as:

$$A_{f,i} = Q_{\nu,abs}\pi a^2 c u_{\nu\|h\nu=Hdisc} \tag{4.8}$$

$$= Q_{\lambda,abs}\pi a^2 u_\lambda \Delta H_f \frac{\lambda^3}{h^2 c} \tag{4.9}$$

with $\lambda_{i,f} = hc/(H_f - H_i)$, *the wavelength of the photon leading to the transition.*

Now that the transition matrix is defined, and the steady state solution P^{SS} is calculated. It is defined as:

$$\sum_1^N A_{f,i} P_i^{SS} = 0, \qquad f = 1, 2, ..., N \tag{4.10}$$

and

$$\sum_1^N P_i^{SS} = 1 \tag{4.11}$$

We thus have access to the temperature probability distributions. We refer to Guhathakurta & Draine (1989) for more details on the process.
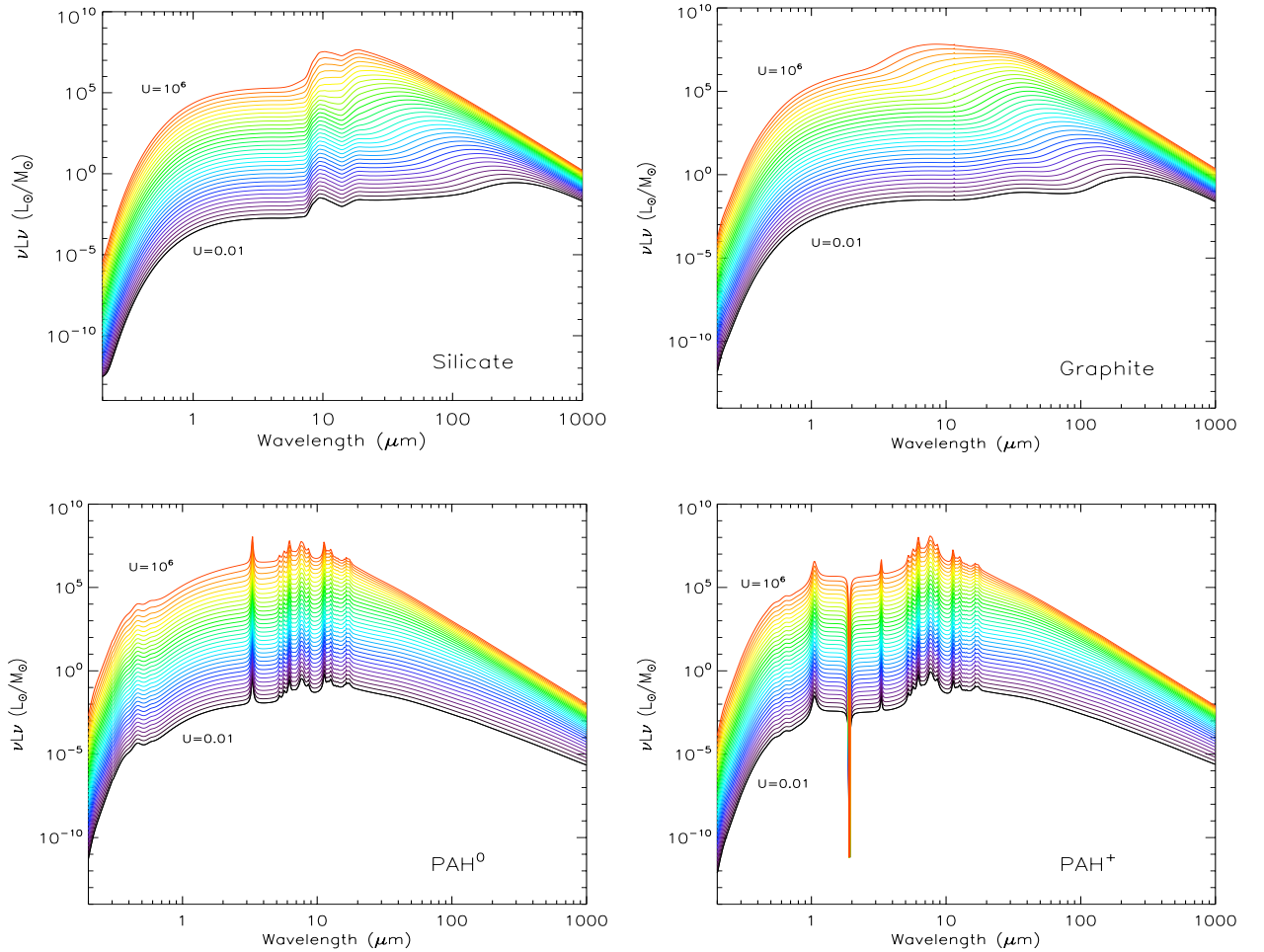
Figure 4.4. Emission of silicate, graphite, neutral and ionized PAHs for different values of *U*. *U* is defined in § 4.2.

4.5 Modelling the stellar contribution

The stellar emission contributes to the near-IR part of the SED. The stellar spectrum is synthesised using the stellar evolution code PEGASE (Fioc & Rocca-Volmerange 1997). Our IDL routine is actually calling pre-saved stellar spectra generated with PEGASE. We assume a Salpeter Initial Mass Function (IMF). The stellar population is considered to have undergone an instantaneous burst 5 gigayears ago and the initial metallicity is assumed to be solar ($Z=Z_\odot$). The emission is scaled by the mass of stars ($M_{oldstar}$), introduced as a parameter of our modelling.

4.6 Color correction

We perform a color correction for the *Spitzer* and *IRAS* bands. The corresponding filters are plotted in Fig. 4.5. The correction is performed by integrating the modeled SED in the instruments filters.
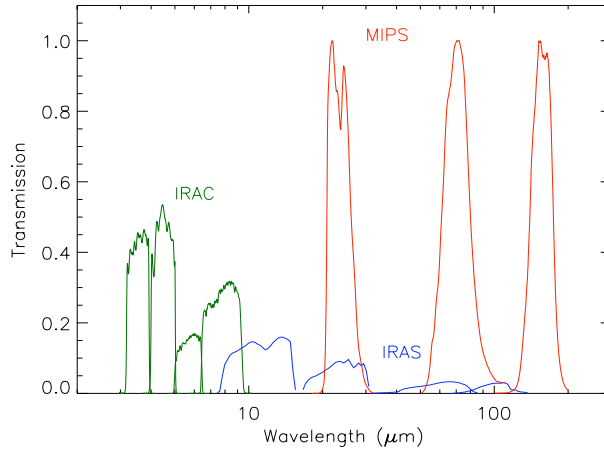
Figure 4.5. Spectral Response of the IRAS (12, 25, 60, 100μm), IRAC (3.6, 4.5, 5.8, 8 μm) and MIPS (24, 70, 160 μm) instruments.

For IRAS fluxes, we used the convention $\nu \times F_\nu = $ constant. For IRAC fluxes, the factor applied to correct the flux is given by the following formula, as indicated in the IRAC handbook.

$$K_{Irac} = \frac{\int (F_\nu/F_{\nu_0})(\nu/\nu_0)^{-1}R_\nu d\nu}{\int (\nu/\nu_0)^{-2}R_\nu d\nu} \tag{4.12}$$

with :

- $\mathbf{F_\nu}$ - the modeled spectrum

- $\mathbf{F_{\nu_0}}$ - the flux density at the nominal wavelength

- $\mathbf{R_\nu}$ - the response function

Finally, MIPS fluxes are corrected using the following formula (here again, refer to the MIPS handbook for details):

$$K_{Mips} = \frac{\int (F_\lambda/F_{\lambda_0})\lambda R_\lambda d\lambda}{\int B_\lambda(\lambda, 10000K)/B_\lambda(\lambda_0, 10000K)\lambda R_\lambda d\lambda} \tag{4.13}$$

with :

59

- **F_λ** - the modeled spectrum

- **R_λ** - the response function

- **$B_\lambda(\lambda, \text{10000K})$** - a 10000K blackbody

While color correction of the flux densities is necessary for observations using instruments with photomultipliers, this is not necessary for instruments built with bolometers (directly integrated power flux). Thus the bolometers for LABOCA are not color-corrected.

4.7   An iterative process

The modelling is an iterative process in which we assume, *a priori*, an initial dust grain distribution (size and composition). The stellar contribution to the SED is constrained by the 2MASS bands and IRAC 3.6 μm. The near-IR to submm wavelengths of the SEDs, signatures of the dust and physical conditions of the galaxies, are constrained by *IRAS*, *Spitzer*, *Herschel*, SCUBA or LABOCA data (when available).

No radio component is taken into account as a model constraint. The non-dust contribution to the submm fluxes (radio contribution, molecular contamination by CO) can be estimated for the studied source and removed from the submm fluxes.

We summarize here the free parameters of our modelling:

- **M_{dust}** - total mass of dust

- **f_{PAH}** - PAHs-to-dust mass ratio (normalised to the Galactic value)

- **f_{PAH+}** - ionised PAHs-to-total PAHs mass ratio

- **α** - index describing the fraction of dust exposed to a given intensity

- **U_{min}** - minimum heating intensity

- **U_{max}** - maximum heating intensity

- **$M_{oldstar}$** - mass of old stars

The discrete contributions of each dust grain (different sizes, different properties), at each intensity are summed, which leads to a global SED model of the galaxy:

$$
\begin{aligned}
L_\nu^{tot}(\lambda) &= L_\nu^{PAH+dust}(\lambda) + L_\nu^{star}(\lambda) \\
&= \frac{1-\alpha}{U_{max}^{1-\alpha} - U_{min}^{1-\alpha}} \int_{U_{min}}^{U_{max}} l_\nu^{PAH+dust}(U,\lambda) U^{-\alpha} M_{dust} dU + L_\nu^{star}(\lambda)
\end{aligned}
\tag{4.14}
$$

with

$$
\begin{aligned}
l_\nu^{PAH+dust}(U,\lambda) &= f_{PAH}[L_\nu^{PAH^0}(U,\lambda)(1 - f_{PAH+}) + L_\nu^{PAH+}(U,\lambda)f_{PAH+}] \\
&+ L_\nu^{graphites}(U,\lambda) + L_\nu^{silicates}(U,\lambda)
\end{aligned}
\tag{4.15}
$$

The interactive fitting stops when deviations from the observational constraints are minimized. The χ^2 minimisation algorithm is based on the Levenberg-Marquardt methods (function *MPCURVE-FIT* of IDL). To prevent χ^2 from being influenced by the density of points, we weigh each data point

depending on the density of points surrounding its wavelength. $\Delta\, \mathrm{L}_\nu^{obs}(\lambda_i)$ represents the error on the luminosity at a given wavelength.

$$\chi^2 = \sum_i \left(\frac{\lambda_{i+1} - \lambda_{i-1}}{2\lambda_i} \right) \left[\frac{L_\nu^{obs}(\lambda_i) - L_\nu(\lambda_i)}{\Delta L_\nu^{obs}(\lambda_i)} \right]^2 \tag{4.16}$$

We call this basic model the 'fiducial' model.

4.8   Limitations

This model presents some limitations, mainly linked to the *a priori* assumptions we made to simplify the model. Indeed, we choose the radiation field shape of the Galaxy (Mathis et al. 1983), a profile which is known to be different from galaxy to galaxy and also due to the low-metallicity environment (less dust attenuation, clumpiness of the ISM etc). The choice of a radiation field profile will usually affect the PAH mass and small grains mass derived from the modelling.

Another strong assumption was in the use of the Dale et al. (2001) prescription to describe the distribution of the general ISRF (Eq. 4.2). This formula directly relates the cold and the hot phases of the galaxy, an assumption which is not valid if cold dust is physically residing in regions different from star forming regions. Our simple model nevertheless has sufficient levels of complexity (e.g. detailed dust properties) to accurately derive the global properties we want to study, even with the small number of observational constraints available for some galaxies.

4.9   The other SED models

For a few decades now, people have been trying to model SEDs accounting for the entire optical/far-IR/submm constraints. Many authors have tried to fit the far-IR constraints with an isothermal temperature dust population (simple modified blackbody) or a two-component model (Dunne & Eales 2001). These simple models, based on blackbodies, are still very much in use today, as shown in Popescu et al. (2002) or in the recent papers of Eales et al. (2010); Grossi et al. (2010); Smith et al. (2010) using *Herschel* data. These models constitute the default solution when there is not enough data to constrain the SED. They depend on two main parameters: the emissivity (expressed by the emissivity index β), which indicates the efficiency with which dust grains of a particular temperature emit far-IR thermal radiation, and the temperature of the dust grains. The β parameter is still poorly constrained and many authors base models for different galaxies on Galactic assumptions estimated years ago, before we had submm observations. Moreover, defining a single temperature means assuming that the flux densities arise from a purely thermal continuum emission. Emission from PAH features or from mid-IR emitting grains show that this simple assumption will not be sufficient to account for the total emission of the objects studied.

More complex models define a range of dust grains and use their thermal and continuous cooling to derive the dust emission spectrum, as we did. The principle of the first graphite-silicate grain model was developed for the first time in Mathis et al. (1977), based on the properties of the Galactic extinction. The Draine & Anderson (1985) model tried to refine this model, favoring an enhancement of small grains ($a \sim 3 \mathring{A}$) to account for the high mid-IR dust continuum. Several models were then developed using a silicate-graphite-PAH composition (e.g. Desert et al. 1990; Li & Draine 2001) model. Finally, other 'composite' models assume that dust can be modeled by low-density aggregates of small silicate-carbon grains (e.g. Zubko et al. 2004 , used here).

We also note that Draine et al. (2007) have supposed that a large fraction of the dust is located in the diffuse ISM. They idealized this component by exposing it to a single radiation field, with $U=U_{min}$ (U_{min} is defined previously in this chapter). This model is used for comparision of our results and is discussed further in Chapter 6.

More recently, Serra Díaz-Cano & Jones (2008) cautioned the use of graphite in dust models and proposed that hydrogenated amorphous carbon could be the most probable form of carbonaceous grain material, as previously studied by Dartois et al. (2004) or Jones (2009). This assumption is analysed in Chapter 7.

Other parameters that can vary between the different SED models tested concern:

the geometry : a slab or 'sandwich' configuration, which are the simplest ones (Disney et al. 1989; Xu & Buat 1995), a cylindrical geometry for the modelling of spiral galaxies or torus (e.g. Pier & Krolik 1992), a spherical geometry, more adapted for starbursts (Witt et al. 1992; Dopita et al. 2005) and dwarf galaxies (Galliano et al. 2003).

the clumpiness of the medium: presence of active clumps (clumps with embedded young stars), passive clumps (clumps with no embedded stars, e.g. Witt & Gordon 1996) in the model etc. We refer to Misselt et al. (2001) for examples of an SED modeled with a different density ratio between diffuse and clumpy media. Sauty et al. (1998), in the same way, have built a radiative transfer to model spiral galaxies. This model is based on a two-phase ISM composed of molecular clouds (masses ranging between 10^3 and 10^6 $M_\odot$, mean density of 50 H_2 cm^{-3}) and a smooth diffuse phase (mean HI density ranging from 0.8 H cm^{-3} in the inner disk to 2 H cm^{-3} in the outer disk). The major effects of clumps on SEDs are that, depending on the filling factor of the clumps, 'active clumps' can lead to warmer far-IR/submm colors and to an increase of the attenuation of the UV/optical emission and that 'passive clumps' can lead to cooler far-IR/submm and to a decrease of the attenuation of the UV/optical emission (Popescu & Tuffs 2005).

We will now use our SED model as a key tool in the following analyses.

Chapter 5

Low-metallicity galaxies observed in the submm with LABOCA

Contents

5.1 Introduction

Studying the interplay between galaxy properties and metal enrichment is crucial to understand galaxy evolution. The metallicity of a galaxy is deeply linked with the dust properties of the ISM and its substructures such as HII regions and molecular clouds. How it affects the ISM is nevertheless poorly known. Metal poor galaxies in the Local Universe are ideal laboratories to study the effects of metallicity on the gas and dust. As mentionned in Chapter 2, they are considered to be the building blocks of much larger and more metal-rich galaxies (see the review by Tosi (2003)). Starburst dwarfs also show analogies with Gamma Ray Burst (GRB) hosts. Indeed, Chen et al. (2009) have shown that the galaxy population hosting GRBs exhibits a broad range of UV absolute magnitude and ISRF that could reach 35 to 350 times the Galactic value. Their ISM also spans a broad range of metallicy, from 1/100 solar to 1/2 solar.

A broad wavelength coverage in the mid-IR to submm regime is imperative to constrain the modelling of the observed SEDs, leading to a better understanding of the dust properties of galaxies. Since *Spitzer* only observed dust emission at wavelengths less than 160 μm, submm data are necessary not only to extend the wavelength coverage to longer wavelengths but also because the potential reservoir of cold dust, which contributes to this submm flux, could contain a signficant fraction of the dust mass. Only a handful of galaxies of the Local Universe have been studied using submm ground-based instruments (e.g. JCMT/SCUBA). When submm observations of dwarf or late-type galaxies are studied, an excess in the dust SEDs is often found in the mm/submm domain (Lisenfeld et al. 2001; Böttner et al. 2003; Dumke et al. 2004; Galliano et al. 2003, 2005; Marleau et al. 2006; Bendo et al. 2006). This excess can be interpreted as very cold dust (< 10K), in which case more than 50 % of the total dust mass of these galaxies should reside in a very cold component. Cold dust is also needed to explain the break in the D/G as a function of metallicity for low-metallicity galaxies (Galliano et al. 2008; Muñoz-Mateos et al. 2009a).

The presence of this cold dust component is still a contentious issue in the ISM community and will have important consequences on our understanding of ISM properties of low metallicity environments. Lisenfeld et al. (2001), Reach et al. (1995), Dumke et al. (2004), Bendo et al. (2006) or Meny et al. (2007) suggested that changes in dust emission properties (changes in dust emissivity or resonances related to dust impurities) should be responsible for boosting submm emission above the 15-20K thermal emission expected at these wavelengths. However, not all low metallicity galaxies show a submm excess, as shown recently by the observations of the nearby Local Group Galaxy IC10 (Parkin et al. 2010 in prep) using SCUBA data at 850 μm. Draine et al. (2007), using SINGS galaxies observed with SCUBA, showed that their submm observations can largely be reproduced by dust models which do not contain a very cold dust component. Nevertheless, their sample, observed at submm wavelengths, does not contain low-metallicity galaxies. Studies using submm observations for a wider range of metallicity values are thus necessary to check the relevance of these conclusions for low metallicity environments.

Herschel observations will extend the *Spitzer* 160 μm to 500 μm and will be able to provide enough constraints to reach a conclusion on this outstanding issue.

5.2 The initial sample

Our first sample gathers 4 low-metallicity galaxies spanning a wide range of metallicities (from $\sim$1/9 $Z_\odot$ for Haro 11 to $\sim$1/3 $Z_\odot$ for NGC 1705), distance (Table 5.1), morphologies, size scales and characteristics, and includes resolved galaxies (NGC 1705), compact galaxies (Haro 11, UM 311), merging environments (Mrk 1089). These galaxies have already been detected by many instruments at a range of wavelengths including the *Spitzer* telescope. We extend the wavelength coverage to 870 μm to shed light on the submm excess question.

NGC 1705 - NGC 1705 is a Local Group galaxy situated at a distance of 4.7 Mpc. The galaxy was observed at IR wavelengths with the *Spitzer* telescope as part of the *Spitzer* Infrared Nearby Galaxies Survey (SINGS; Kennicutt et al. 2003). The galaxy is one of the only objects where the luminosity in the UV is dominated by one single central bright $10^5 M_\odot$ Super Star Cluster (SSC), at the origin of a galactic outflow (Heckman & Leitherer 1997). The Hα emission of NGC1705 extends over the entire optical emission of the galaxy (Gil de Paz et al. 2003) while the H I emission is exceptionally extended beyond the optical emission (Meurer et al. 1998) and lies on either side of the SSC (Fig. 5.1). On each side of the SSC, two off-nuclear H II regions, called D1 and D2 were resolved, for the first time, with *Spitzer* and dominate the mid-IR and far-IR dust emission (Cannon et al. 2006b). Finally, *Spitzer* IRS spectroscopy reveals PAH emission originating from D1 but does not seem to come from the SSC or the region D2 (Cannon et al. 2006b). PAH emission was expected in D2 due to its high surface brightnes Hα emission. The decrease of PAH emission in D2 and in the SSC could be linked to a higher radiation field in those regions as suggested in Madden (2005).
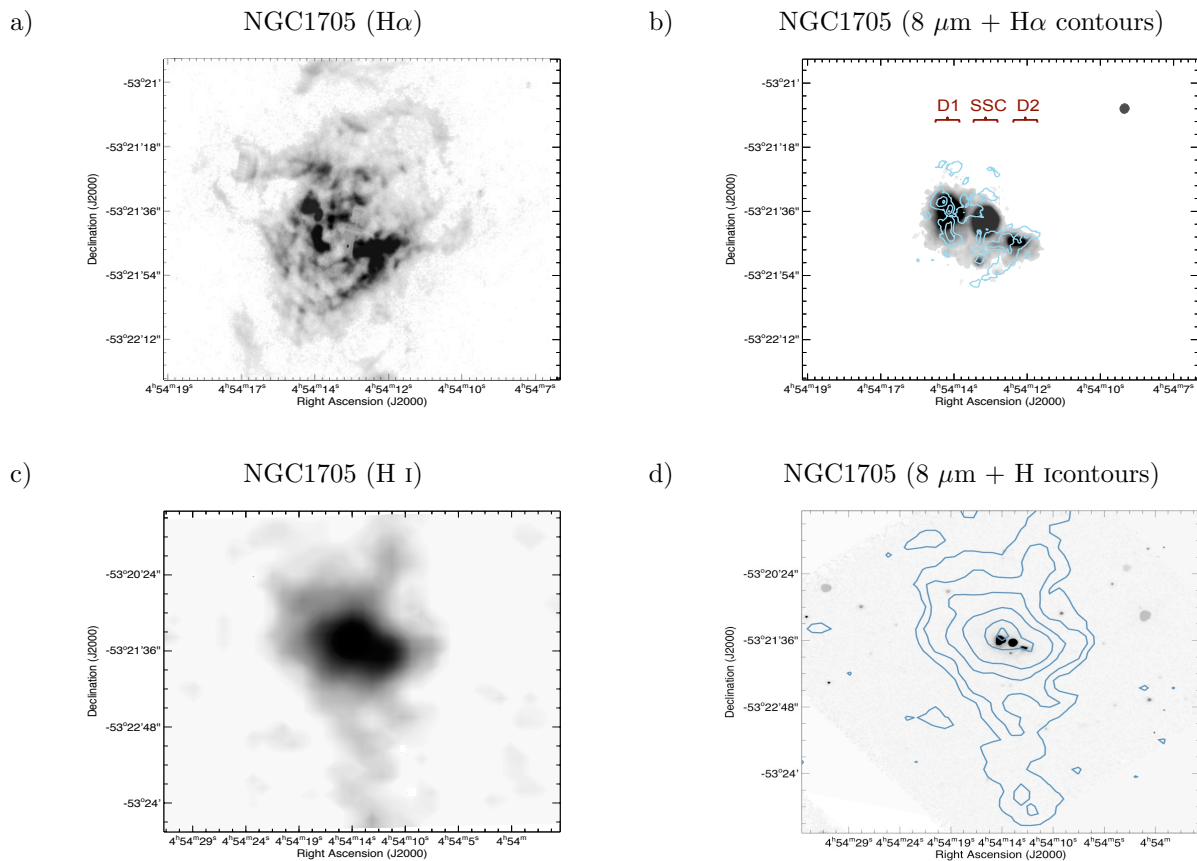
Figure 5.1. *a)* Hα image of NGC 1705. The SSC is masked in the image (Gil de Paz et al. 2003). *b)* NGC 1705 observed at 8 μm with *Spitzer*. Hα contours are overlaid. We indicate the SSC and the two bright off-nuclear H II regions labeled D1 and D2 in Cannon et al. (2006b). *c)* H I image of NGC 1705 (Meurer et al. 1998). *d)* NGC 1705 observed at 8 μm with *Spitzer* with H I contours overlaid.

Haro 11 - Also known as ESO 350-IG038, Haro 11 is the most distant galaxy of the sample (92 Mpc; Bergvall et al. 2000) with a very low metallicity (Z~1/9 Z$_\odot$). Haro 11 possesses characteristics of an extreme starburst with L$_{FIR} \sim 10^{11}$ L$_\odot$ (Sanders et al. 2003), making it a luminous infrared galaxy (LIRG), with a high star formation rate of $\sim$ 25 M$_\odot$ yr^{-1}

a) Haro 11 (Hα)   b)   Mrk1089 (Hα)
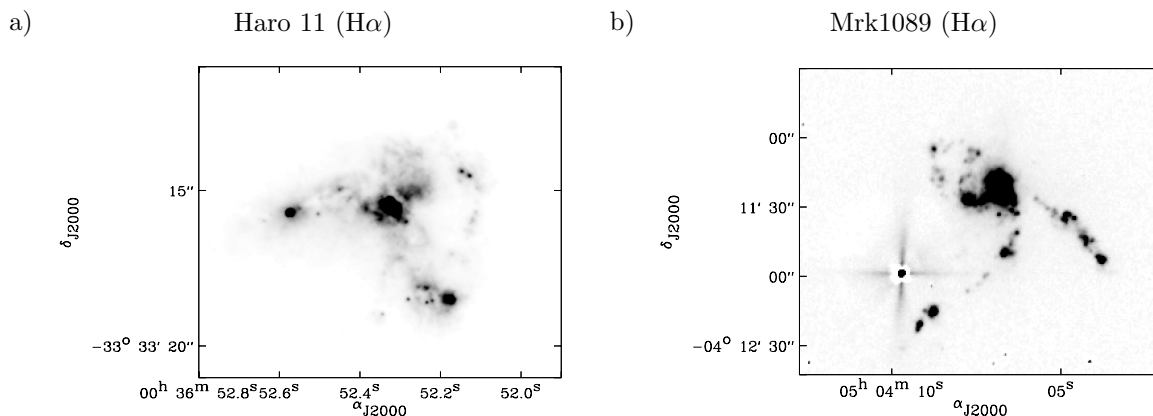
Figure 5.2. Hα images of *a)* Haro 11 and *b)* Mrk 1089

as determined from Hα, radio continuum, FIR and hard X-ray observations (Grimes et al. 2007). Broadband images of Hα show three bright star-forming condensations (Fig. 5.2) with unrelaxed kinematic structure and faint extended shell structures in the outer regions of the galaxy, all suggesting an ongoing merger (Bergvall & Östlin 2002; Östlin et al. 1999). Haro 11 is a moderately strong radio source (essentially free-free continuum) with spatially extended continuum emission at 6 and 20 cm (Heisler & Vader 1995). Very little H I was detected in Haro 11, leading to a very low M_{HI}-to-L_B ratio, with L_B the blue luminosity. The upper limit on the molecular gas mass, derived from the CO (1-0) observations, is estimated to be 10^8-10^9 $M_{\odot}$ (Bergvall et al. 2000). Thus this is a remarkable galaxy with little evidence for molecular gas and little atomic gas (the central column density N_{HI} was estimated to be $\sim$ 2×10^{21} atoms cm^{-2} by Bergvall et al. 2000) but very evident star formation activity. We come back to these points later during the SED interpretation section.

Mrk 1089 - Mrk 1089 is a Wolf-Rayet (WR) galaxy (Kunth & Schild 1986) and the most luminous of the eight members of the Hickson Group 31 (Hickson 1982). The morphology of the group is very disturbed (see Fig. 5.2) with tidal interactions between Mrk 1089 (HCG 31 C) and the galaxy NGC 1741 (HCG31 A). The two galaxies have similar kinematics suggesting a single entity (Richer et al. 2003). At the location of their interaction is a very strong 24 μm source and high levels of infrared emission can be found throughout the whole group (Johnson et al. 2007). Mrk 1089 and NGC 1741 are referred to collectively as NGC 1741 in the catalog of WR galaxies of Conti (1991). Nevertheless, many surveys (Rubin et al. 1990; Conti et al. 1996; Iglesias-Páramo & Vílchez 1997; Johnson & Conti 2000) showed that the interacting system was undergoing a starburst which was attributed to HCG 31 C. In this thesis, we designate the interacting system compounded of HCG 31 A and HCG 31 C together as Mrk 1089.

UM311 - UM 311 is a compact H II galaxy (Terlevich et al. 1991) located between the pair of spiral galaxies NGC 450 and UGC 807, 2 galaxies which were once thought to be interacting but have now been demonstrated to be physically separated (Rubin & Ford 1983). There are three very bright sources of compact H II emission between the two galaxies, UM 311 being the brightest (Fig. 5.3). The galaxy has been misidentified as a projected galactic star due to its quasi-stellar and compact morphology. Its Hα luminosity and equivalent width are remarkably high for an H II galaxy (Guseva et al. 1998).
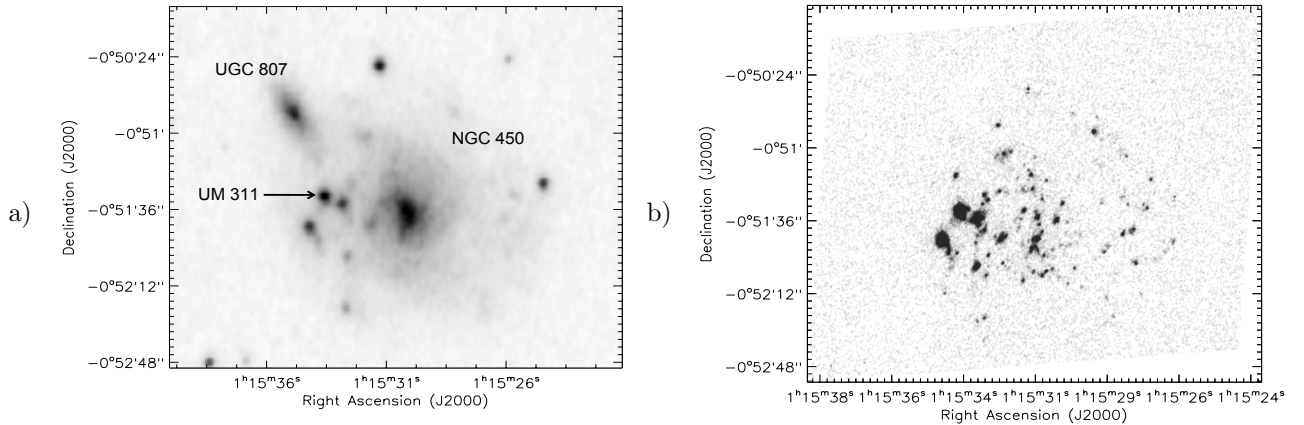
Figure 5.3. UM 311 observed *a)* at 0.65 μm (Palomar Observatory Sky Survey) and *b)* in H$_{alpha}$.

Table 5.1. General properties of the sample

Name	Ra (2000)	Dec (2000)	12+log(O/H)	Ref.	Distance (Mpc)	Ref.	M(HI)$^{(a)}$ ($M_\odot$)	Ref.	Apparent size
NGC 1705	04h 54' 13.5"	-53° 21' 40"	8.46	1	4.7	1	5.1×10^7	5	1.9'×1.4'
Haro 11	00h 36' 52.5"	-33° 33' 19"	7.9	2	92	4	$\sim10^8$	2	0.5'×0.5'
Mrk 1089	05h 01' 37.8"	-04° 15' 28"	8.0	3	59.8	3	2.7×10^{10}	6	0.61'×0.23'
UM 311	01h 15' 34"	-00° 51' 32"	8.3	3	21.3	3	2.3×10^9	7	0.11'×0.11'

Notes.- $^{(a)}$ The H I masses are rescaled to the distances we used.

References.- [1] Meurer et al. (1992) - [2] Bergvall & Östlin (2002) - [3] Hopkins et al. (2002) - [4] Bergvall et al. (2000) - [5] (Meurer et al. 1998) - [6] (Williams et al. 1991) - [7] (Smoker et al. 2000)

5.3 A multiwavength coverage of the SEDs

5.3.1 The *Spitzer* photometric IRAC and MIPS data

Our four sources were observed with IRAC using the dithering imaging mode. The maps of Mrk 1089, UM 311 and Haro 11 were obtained through the *Spitzer* data archive. We worked directly with the post-basic calibrated data for these three galaxies. For NGC 1705 the IRAC maps were obtained from the SINGS data delivery page. Details on the data reduction of the SINGS Fifth Enhanced Data Release can be found on the official SINGS website (http://sings.stsci.edu/).

The four galaxies were also observed with MIPS using the scan mapping mode for NGC 1705 and Photometry/Super-Res mode for Haro 11, Mrk 1089 and UM 311. The MIPS observations were obtained from the *Spitzer* data archive (raw data) and reduced using the MIPS Data Analysis Tools (Gordon et al. 2005), version 3.10 along with additional processing steps described in Chapter 3.

Spitzer maps of Mrk 1089 and NGC1705 were previously discussed in Johnson et al. (2007) and Cannon et al. (2006b) respectively.

5.3.2 *Spitzer*/IRS spectrum

For Haro 11, we supplemented our dataset with the mid-IR IRS spectrum to better constrain the 5 μm to 40 μm range of the SED. NGC 1705 and UM 311 were also observed by IRS but we did not use these observations due to calibration problems; the spectra did not match the broad-band photometry. This is probably due to the limiting IRS coverage of the extended galaxies which were fully mapped in the IRAC and MIPS bands. We used public released data (*Spitzer* AOR key:

9007104) performed in staring mode. The position of the slits of the IRS high resolution observations is shown in Fig. 5.4a. We refer to Chapter 3 for details on the reduction.

The obtained IRS spectrum is shifted, from a redshift of z=0.021 (Bergvall et al. 2000), to rest wavelengths. The spectrum, with labels identifying the main emission features, is shown in the panel on the right in Fig. 5.4b. The 6.3, 7.6, 8.2 and 11.3 μm family of PAH features are clearly detected in the IRS spectrum. We also observe a steeply rising continuum from 10 to 30 μ, with strong fine structure line emission ([S IV], [Ne II], [Ne III] or [S III]), characteristic of very active star forming regions. This continuum could be attributed to an enhanced very small grain population in Haro 11, as suggested by the model of Desert et al. (1990) and observed in other low-metallicity starbursting galaxies (Lisenfeld et al. 2001; Galliano et al. 2003, 2005). The mid-infrared [NeIII] 15.6 μm / [NeII] 12.8 μm ratio is a powerful diagnostic of the ionization state of emission line objects. Indeed, these strong neon lines are only weakly affected by extinction. We calculated [NeIII] / [NeII] to be ~ 3.2 for Haro 11, an indicator of a hard radiation field possibly dominated by a young stellar population (Madden et al. 2006).
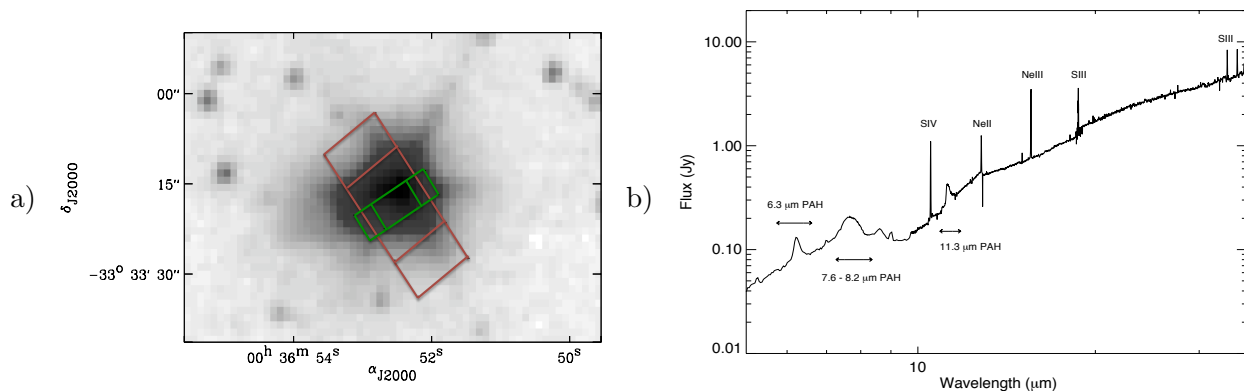
Figure 5.4. a) Positions of the short-high (green) and low-high (red) slits of the IRS observations superimposed on the *Spitzer*/3.6 μm image of Haro 11. b)The short-low and short-high spectrum of Haro 11

5.3.3 LABOCA submm observations

These galaxies were observed with LABOCA between November 9th and 20th 2007 during a campaign of ~ 30 hours (Program ID: 080.B-3003(A)). Basic spiral patterns with 4 pointings were combined with a raster mapping mode (raster-spiral) to completely fill the array (homogenous sampling of each map), to obtain enough off-source position for background subtraction and to effectively execute long integration times (8.7h, 8.3h, 4h and 7.6h for Haro 11, UM 311, Mrk 1089 and NGC 1705 respectively). As mentioned in Chapter 3, we used the software BoA to reduce the data. The atmospheric attenuation was determined via skydips every hour. Opacities ranged from 0.103 to 0.353 throughout the observing run. We refer to Chapter 3 for details on the reduction steps.

5.3.4 Multiwavelength description of the images

Figure 5.5 shows the IRAC 3.6 μm (4.5 μm for UM 311), IRAC 8 μm, MIPS 24 μm and LABOCA 870 μm maps of our 4 galaxies. The contours of the IRAC 8 μm observations (4.6 μm for Haro 11) are overlaid on the LABOCA images.

NGC 1705 - There is a significant change in the morphology from near-IR to far-IR wavelengths. The bright 3.6 μm source is observed toward the location of the SSC while two strong mid-IR and far-IR emission peaks appear at 5.8 μm and longer wavelengths, offset from the SSC and coincident with the Hα maximum (Fig. 5.1 and Fig. 5.5a). These two off-SSC emitting regions do not have bright stellar counterparts. The *Spitzer* 8 μm image shows the SSC in the middle of these two off-nuclear HII regions. The eastern region is the brightest source at 24 μm, with a flux density two times higher than the SSC flux density at this wavelength (Cannon et al. 2006b). The three regions are also barely resolved in the 870 μm images. An offset peak is detected toward the west of the centre of the galaxy. Two faint 24 μm sources are possible counterparts of the emission.

Haro 11 - This galaxy is not resolved by *Spitzer* at wavelengths greater than 4.5 μm. It is clearly detected but barely resolved with LABOCA (Fig. 5.5b). The final images present extended structures but this extension is not observed in the mid-IR images and was removed while calculating the submm flux in order to be conservative.

Mrk 1089 - The 8 μm image (Fig. 5.5c) clearly shows the interaction between the galaxies NGC 1741 (East) and Mrk 1089 (West). A *Spitzer* color composition image of the complete Hickson group observed with *Spitzer* is described in Johnson et al. (2007). The merging center of Mrk 1089 dominates the emission at mid-IR, far-IR and 870 μm. Diffuse emission probably linked with intergalactic dust, presumably from galaxy interactions, is detected throughout the whole region and was removed while performing the photometric measurements.

UM 311 - The 4.5 μm image of the interacting field (Fig. 5.5d) shows the spiral structure and arms of NGC 450 as well as the spiral companion UGC 807 and the three bright HII regions between these two spirals, one of which is UM 311. We adopt the same numbering as Moles et al. (1994) to describe these 3 HII sources and will call them 'the UM 311 system'. UM 311 is the region called 3 on the 4.5 μm image. This compact HII galaxy is the brightest source of emission at 24 μm. In the LABOCA image, the emission peaks toward the location of UM 311. The galaxy is expected to dominate the SED of the UM 311 system.

5.3.5 IRAC, MIPS and LABOCA fluxes

We want to determine and compare the global flux densities of our sources at each observed wavelength. As explained in Chapter 3, the observations are first convolved and regridded to a common resolution. We use the aper function (see Chapter 3 for a detailed description of the function) to perform photometry on our sources. For the *Spitzer* photometric data, the background is estimated locally using an annulus around our galaxies. IRAC fluxes are corrected by the calibration factors of Reach et al. (2005) (see Chapter 3). For the LABOCA images, the background significantly varies in intensity throughout the entire map. We calculated the flux densities in small circles in the immediate surroundings of the galaxy and averaged them to determine a local background for each source, which was removed during the photometric calculation.

I will detail now the choice of the photometric apertures we used:

NGC 1705 and Haro 11 - The lowest spatial resolution is the resolution of MIPS 160 μm (FWHM: 40") so the maps were convolved to the MIPS 160 μm resolution. The photometric aperture chosen has a diameter of 144" for these two galaxies to encompass the entire emission of the galaxy.
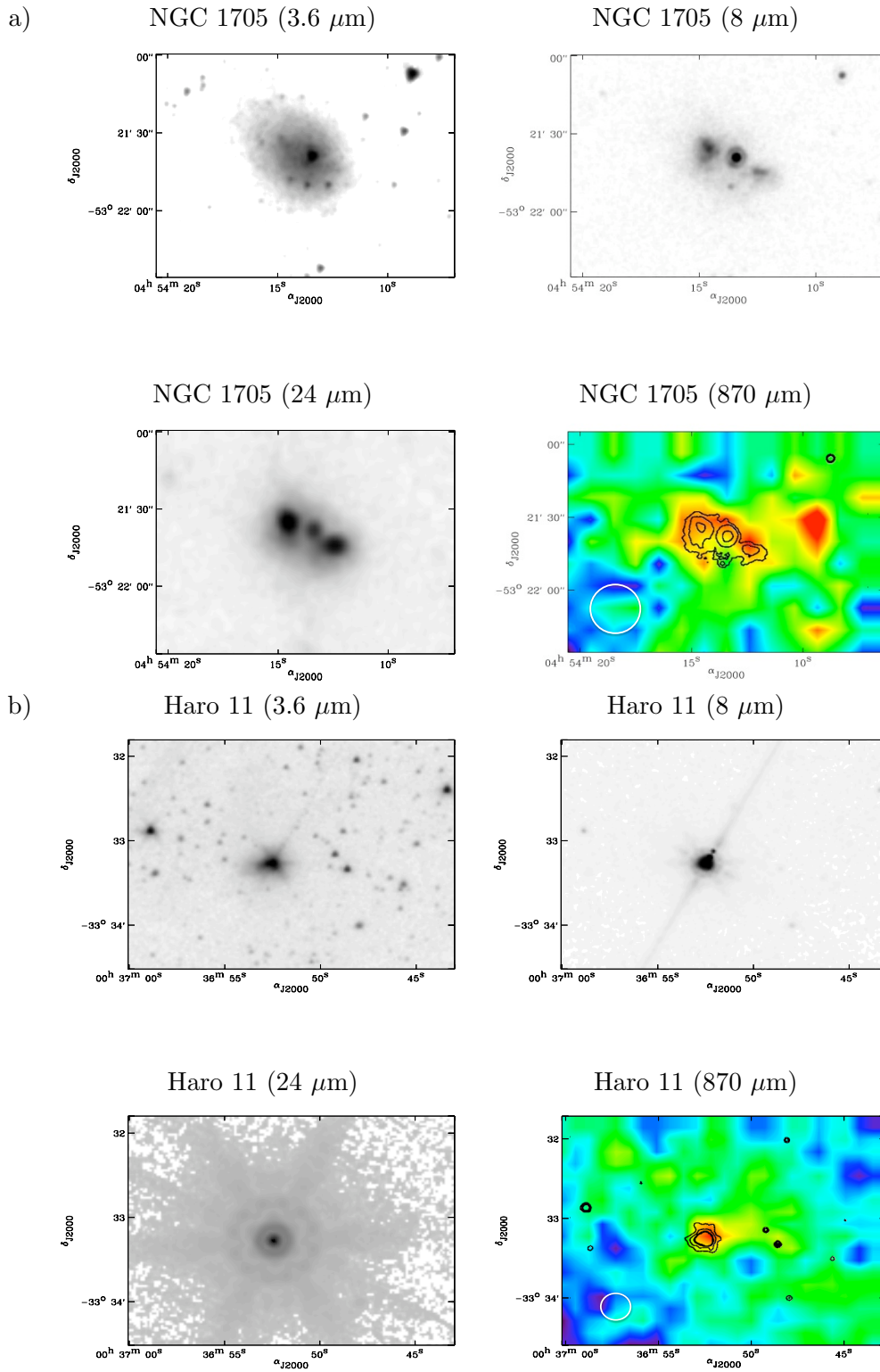
Figure 5.5. 3.6 μm (4.5 for UM 311), 8 μm , 24 μm and 870 μm images of our four galaxies: a) NGC 1705, b) Haro 11, c) Mrk 1089, d) UM 311 (source number 3). North is upwards and East is to the left. The FWHM of the PSF of LABOCA is shown by a white circle. 8 μm (4.5 μm for Haro11) contours are overlaid on the LABOCA images: a) 0.5, 1, 2.5 MJy/sr - (b) 0.34, 0.77, 8.58 and 9 MJy/sr - c) 2, 2.5, 4.5, 8 MJy/sr - d) 4.6, 5.61, 7.8 MJy/sr. For UM 311, the photometric aperture chosen (54") encompasses the flux of the 3 sources at the edges of the two spiral galaxies and is marked by the dashed circle. These sources are numbered according to Moles et al. (1994).

70

c)

Mrk 1089 (3.6 μm)

Mrk 1089 (8 μm)

Mrk 1089 (24 μm)

Mrk 1089 (870 μm)

d)

UM 311 (4.5 μm)

UM 311 (8 μm)

UM 311 (24 μm)

UM 311 (870 μm)

71
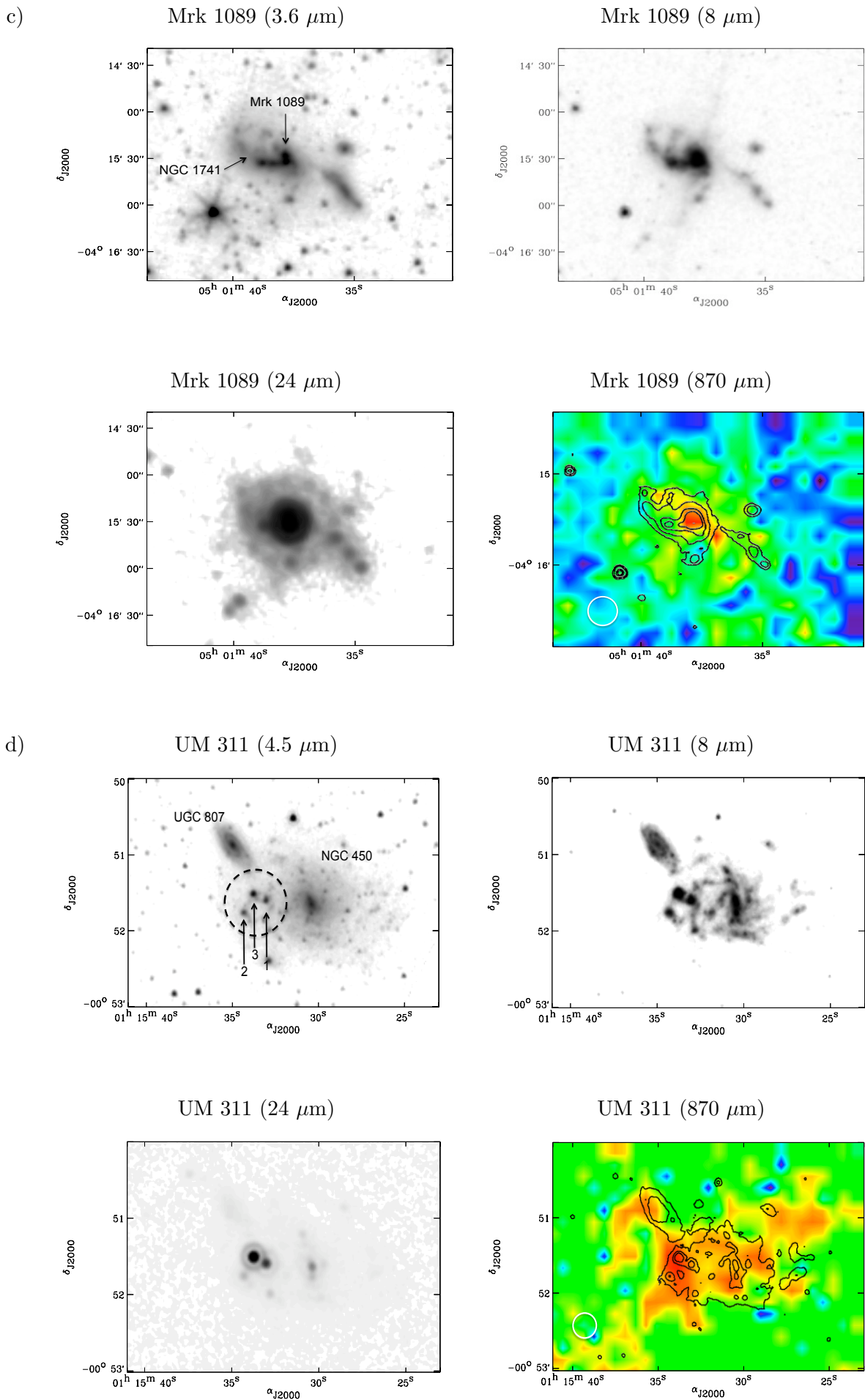
Figure 5.5. continued

Mrk 1089 - Mrk 1089 was not observed at 160 μm. Images were thus convolved to the resolution of LABOCA (18.2"). We chose an aperture of 72" avoiding the flux arising from the other nearby companions. However, Mrk 1089 clearly dominates the whole system at mid to far-IR wavelengths.

UM 311 - The resolution of the MIPS bands and the proximity of the 2 nearby Hɪɪ regions make it difficult to study UM 311 alone. We decided to perform the photometry of the UM311 system (encompassing sources 1, 2, 3 in Fig. 5.5d). The 2MASS, IRAC and MIPS 24 and 70 μm images were regridded to the LABOCA resolution of 18.2" for the UM 311 system. In the 160 μm image, the broad PSF may cause emission from other sources outside the region around UM 311 to bleed into that region (Fig. 5.5d). To be conservative, we chose a 54" aperture which encompasses the UM311 system and use the 160 μm observation as an upper limit when modelling the SED of this system. The procedure we use to model this system gives us solutions for the limits on the parameter space for UM 311 as if this interacting system were more distant causing these 3 sources to blend together.

Non-dust contamination of the 870 μm flux

We now correct the LABOCA flux for possible non-dust contamination before modelling the dust SEDs. The CO(3-2) line can, in principle, fall within the 870 μm band. While CO(1-0) has been a great challenge to detect in low-metallicity galaxies (c.f. Leroy et al. 2005), we can not be sure, with the smaller beam, that higher excitation CO(3-2) is not present. CO observations were attempted in NGC 1705 without positive detections (Greve et al. 1996). In the same way, CO seems to be very faint in the Hickson Group to which Mrk 1089 belongs (Yun et al. 1997). Finally, for Haro 11, Bergvall et al. (2000) found an upper limit for $L_{CO(1-0)}$ of 10^{29} W. We can derive an upper limit to $L_{CO(3-2)}$ from the $L_{CO(1-0)}$ estimate using the Meier et al. (2001) relations for dwarf starburst galaxies: $L_{CO(3-2)}/L_{CO(1-0)}$ is usually lower than 1. For the four galaxies, we conservatively estimate the CO (3-2) contribution to the 870 μm band to be $\sim 5\%$.

Additionally, we can expect contributions to the 870 μm fluxes from radio continuum emission (synchrotron emission and/or bremsstrahlung). Three radio fluxes were estimated for Haro 11 with the NRAO VLA Sky Survey (8.46 and 1.4 GHz - Condon et al. 1998) and the Sydney University Molonglo Sky Survey (843 MHz - Mauch et al. 2003). We derive the 870 μm radio continuum contribution by extrapolation of the radio data tendancy (ν^{-1}). We find a radio contribution of 3% of the LABOCA flux for Haro 11. The radio observations in the literature are not sufficient to constrain the expected 870 μm radio contamination for NCG 1705, UM 311 and Mrk 1089. We thus consider that the radio continuum contamination is of the same order for these other galaxies. In summary, we conservatively estimate the global non-dust contamination from potential CO(3-2) emission and radio continuum emission (synchrotron/bremsstrahlung) in the 870 μm band to be 10% for our four galaxies, similar to the submm contributions determined in Galliano et al. (2005) for their submm observations of dwarf galaxies.

Underestimating the non-dust contributions to the 870 μm flux values could have important consequences for the submm flux densities estimated and thus on the dust mass. Direct measurements of the CO(3-2) line and more millimeter radio observations would place greater confidence in the submm flux densities and thus on the dust mass determinations.

5.3.6 Ancillary data

We supplement the *Spitzer* and LABOCA observations with *2MASS* J, H, K flux density estimates available on the NASA/IPAC Infrared Science Archive. These data enable us to constrain the stellar contribution of the SEDs of the galaxies Mrk 1089, Haro 11 and NGC 1705. The *2MASS* flux

densities are global measurements for the galaxies. For the UM 311 system, we directly perform the photometry on images also obtained from the NASA/IPAC Infrared Science Archive. To complete the IR coverage, IRAS broadband flux densities at 12, 25, 60 and 100 μm are also added. These fluxes are obtained through the NASA/IPAC Infrared Science Archive, the IRAS Faint Source catalogue, |b| > 10, Version 2.0 (Moshir & et al. 1990), the IRAS catalogue of Point Sources, Version 2.0 (IPAC 1986) and Dultzin-Hacyan et al. (1990). For Haro 11, the IRAS fluxes are consistent with the values of the IRS spectrum. For UM 311, IRAS data would encompass emission from both of the nearby galaxies and are thus not used in the analysis.

The flux densities of our sample are summarized in Table 5.2.

Table 5.2. Integrated flux densities measured with *2MASS*, *IRAS*, *Spitzer* and LABOCA (in mJy).

		NGC 1705	Haro 11	Mrk 1089	UM 311 system
2MASS	1.25 μm	52 $\pm$ 1.6	13 $\pm$ 0.3	12.2 $\pm$ 0.6	12.8 $\pm$ 1
2MASS	1.65 μm	50.9 $\pm$ 2	13 $\pm$ 0.5	13.9 $\pm$ 0.9	12.6 $\pm$ 1
2MASS	2.17 μm	41.1 $\pm$ 2.4	13.8 $\pm$ 0.7	12.2 $\pm$ 1.2	11.5 $\pm$ 1
IRAC	3.6 μm	26.3 $\pm$ 3	22.5 $\pm$ 2	14.9 $\pm$ 2	...
IRAC	4.5 μm	17.9 $\pm$ 2	28.9 $\pm$ 3	11.2 $\pm$ 1	5.5 $\pm$ 0.5
IRAC	5.8 μm	16 $\pm$ 2	72.7 $\pm$ 7	33.3 $\pm$ 3	...
IRAC	8 μm	17.9 $\pm$ 2	177 $\pm$ 18	92.5 $\pm$ 9	35.6 $\pm$ 4
IRAS	12 μm	...	417 $\pm$ 46	106 $\pm$ 21	...
MIPS	24 μm	52.7 $\pm$ 5	1930 $\pm$ 193	460 $\pm$ 46	151 $\pm$ 15
IRAS	25 μm	...	2500 $\pm$ 25	579 $\pm$ 29	...
IRAS	60 μm	868 $\pm$ 61	6880 $\pm$ 41	4010 $\pm$ 40	...
MIPS	70 μm	1113 $\pm$ 222	4190 $\pm$ 838	3993 $\pm$ 798	1476 $\pm$ 148
IRAS	100 μm	1610 $\pm$ 100	4730 $\pm$ 640	5430 $\pm$ 181	...
MIPS	160 μm	1115 $\pm$ 222	1663 $\pm$ 332	...	...
LABOCA[a]	870 μm	114 $\pm$ 17	40 $\pm$ 6	67.4 $\pm$ 10.1	32.2 $\pm$ 7

[a] The 10% non-dust contamination was subtracted from the LABOCA flux densities.

5.4   Results derived from the fiducial model

For our 4 galaxies, we run the SED modelling described in Chapter 4 using our multi-wavelength data. The SED models obtained with our fiducial model are shown in Fig. 5.6, along with the observational data (black dots). The Haro 11 broad-band data and IRS spectrum are corrected to take into account the redshift of the galaxy. The Haro 11 IRS spectrum (in orange in Fig. 5.6), from 5.1 μm to 37.2 μm, provides additional constraints to better describe the PAH properties as well as the slope of the rising mid-IR continuum.

Submm constraints are, for now, rarely used in the study of dust properties in dwarf galaxies, due to the difficulty of observing in this wavelength range. Most of the cold dust mass in the SED is actually constrained by submm observations, and the strong dependence of the mass of dust grains with the temperature (M $\propto$ T$^{-(4+\beta)}$, where β is the emissivity of the grain) implies that submm emission could actually help us to constrain the major component of dust in galaxies, namely the coldest dust. Our SED models use the 870 μm observational constraint, and we compare the resulting parameters with those obtained without the 870 μm data, in order to study the influence of the submm data on the derived dust mass (Table 5.3).

We note that the PAH-to-dust mass ratios (f_{PAH}), which is normalized to the Galactic value, is always inferior to 1 (Table 5.3). This was expected since low-metallicity galaxies usually show a PAH deficit compared to dustier galaxies (Madden 2005; Engelbracht et al. 2005; O'Halloran et al.

2006; Engelbracht et al. 2008; Wu et al. 2007). Cannon et al. (2006b) note that the 11.3 μm PAH emission is detected in NGC1705 with IRS in the most luminous of the two dust emission peaks (D1, Fig. 5.1) but not in the second off-nuclear region nor in the SSC. The parameter α, which describes the fraction of dust exposed to a given intensity of ISRF, is quite similar for the three galaxies ($1.7 < \alpha < 2.2$, Fig. 5.3), with Haro 11 having the smallest α. We note that the galaxies with smaller α usually contain more intensely heated regions and therefore are more likely to be associated with global prominent star formation activity.
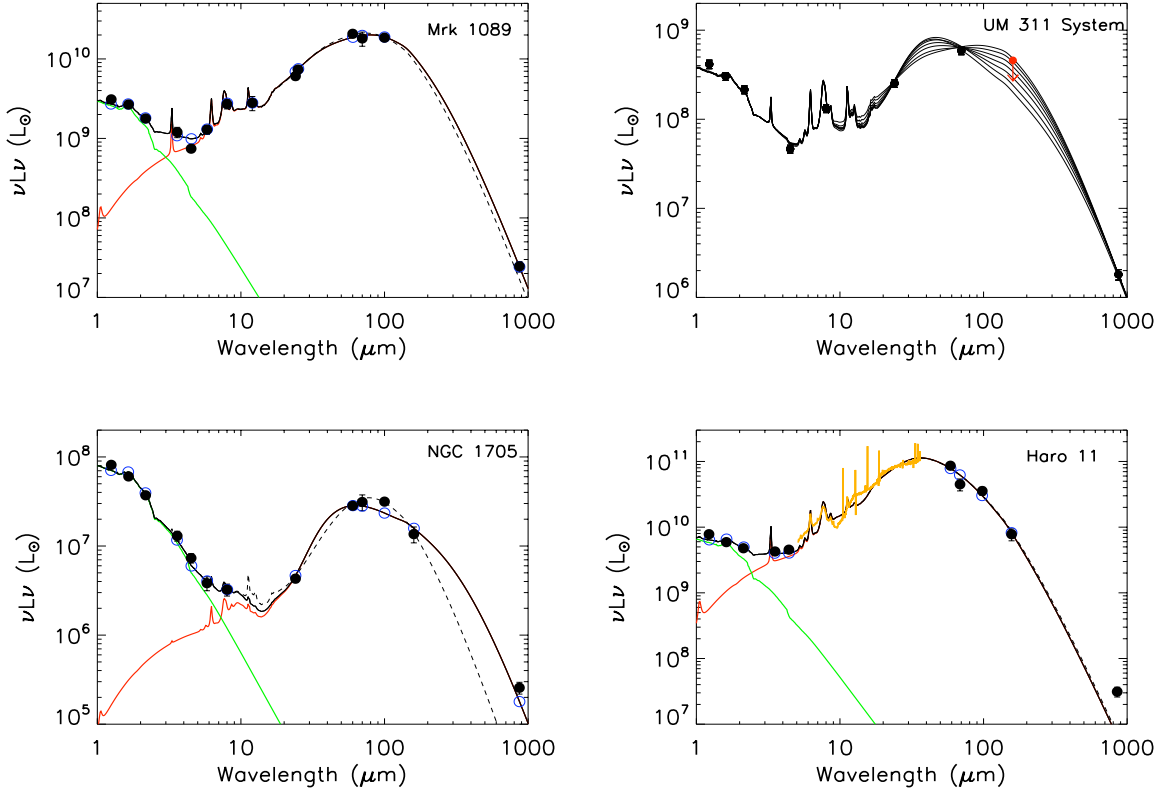
Figure 5.6. SED models of Mrk 1089, the UM 311 system, NGC 1705 and Haro 11 using the fiducial model. SEDs are plotted in black. Observational data are superimposed (filled circles). The green and red lines respectively distinguish the stellar and the dust contributions. The dashed black lines present the SED models for our galaxies obtained when the LABOCA data is not used to constrain the modelling. The open circles represent the expected modeled fluxes integrated over the instrumental bands. When the error bars are not shown, the errors are smaller than symbols. The IRS mid-IR spectrum of Haro 11 is overlaid in orange. For the UM 311 system of 3 compact sources, the 160 μm flux is an upper limit since it was calculated with a 40" aperture. The different SEDs represent the possible SED models that fit the observational constraints with good accuracy.

To quantify the errors on our dust mass determinations, we produced, using IDL, a grid of 500 randomly modified observational constraints. We allow the observational fluxes to vary within their error bars, following a Gaussian distribution around their reference value:

$$\mathrm{L}_\nu{}^{rand}(\lambda_i) = (1 + \delta(\lambda_i)) \mathrm{L}_\nu{}^{obs}$$

with $\delta(\lambda_i)$ randomly generated between -1 and 1 (gaussian distribution), in IDL using the routine 'randomn':

Table 5.3. Parameters for our SED models with and without the submm data constraints and the Dust-to-Gas mass ratios for our galaxies.

	Haro 11		Mrk 1089		NGC 1705	
	no submm	submm	no submm	submm	no submm	submm
M_{dust} ($M_\odot$)	6.2×10^6	1.7×10^7 ($\pm40\%$)	3×10^7	$\mathbf{5.12\times10^7}$ ($\pm20\%$) [a]	2.9×10^4	1.3×10^6 ($\pm50\%$)
f_{PAH}	0.22	0.1	0.18	0.18	0.11	4.4×10^{-2}
α	1.88	1.73	2.21	2.18	2.5	1.84
U_{min}	12.2	1.44	1.5	0.82	3.68	9×10^{-3}
U_{max}	1.3×10^5	5.77×10^4	3.84×10^5	3.5×10^5	1.47×10^4	8.67×10^2
M_{HI} ($M_\odot$)	$\sim 10^8$		2.7×10^{10}		4.1×10^7 [b]	
M_{dust}/M_{HI}	6×10^{-2}	0.17	10^{-3}	$\mathbf{1.9\times10^{-3}}$	7×10^{-4}	3.2×10^{-2}

Notes.- [a] Boldface numbers are the dust mass and the dust-to-gas mass ratio values for our prefered SED for the galaxy Mrk 1089.

[b] H I mass associated with the aperture chosen for the dust mass determination, namely 80% of the the total H I mass.

```
Lnu_rand=Lnu+randomn(seed,Nwave)*Lnu_error
```

This command generates a new set of observational constraints, with Nwave the number of constraints and Lnu_error an array containing the error bars.

We focus now on the interpretation of each galaxy, separately:

Mrk 1089 - In spite of the lack of 160 μm observations, we are able to fit the observations accurately both with and without the LABOCA observations. The peak of the SED is rather flat in the far-IR (Fig. 5.6). This flat shape of the SED is very different from that of the Galaxy or more metal-rich galaxies, but is often seen for active low-metallicity galaxies, such as II Zw 40 and He 2-10 (Galliano et al. 2003, 2005), in the Large Magellanic Cloud (Bernard et al. 2008) and the Small Magellanic Cloud (Bot et al. 2004). This could be linked with the low metal abundance and the decrease in dust attenuation, resulting in a higher ISRF. The increased abundance of very small stochastically-heated grains could also inflate the continuum on the Wien side of the SED. We find a total dust mass of 5.12×10^7 $M_\odot$ ($\pm$ 20%). This mass is a factor of 1.7 larger than that without submm constraints. This galaxy is the least affected by the addition of the submm constraint.

The UM311 system - The 160 μm beam is too large to isolate the UM 311 system alone. We thus lack sufficient observational constraints at far-IR wavelengths to accurately determine the position of the SED peak of the system. We thus measure the 160 μm flux in a bigger aperture (80") than that used in the other bands (54") and use this value as an upper limit. To explore the range of parameter space constrained by the 160 μm upper limit, we decrease the 160 μm flux in steps of 10% down to 50% and find the range of shapes with associated parameters that could fit our observational constraints (see Fig. 5.6 and Table 5.4). We also produced a grid of 200 randomly modified observational constraints to study the spread of the SED models induced by these uncertainties and establish a range of possible dust masses for this galaxy system. We conclude that the dust mass of the system should reside between 5.2×10^6 and 1.1×10^7 $M_\odot$, and that the parameter α should reside between 1.79 and 2.13 (Table 5.4). The various SED models obtained include both solutions that maximise the

contribution from the hot dust with a far-IR peak at about 50 μm and solutions that, on the contrary, favor a large dust mass peaking at longer wavelengths (see Fig. 5.6).

We also convolve the 8 μm images of the UM 311 system to the resolution of MIPS 24 μm and calculate the luminosities of the 3 different substructures at these wavelengths. The luminosities in ν L$_\nu$ of region 1 and 2 are respectively 1.5 and 2.9 times lower than that of UM 311 (region 3) at 8 μm and respectively 2.6 and 8.4 times lower at 24 μm. This results in different 8/24 luminosity ratios for the 3 regions, respectively 0.36, 0.61 and 0.21 for region 1, 2 and UM 311 respectively. We note that the global ratio for the whole system is 0.24. The 24 μm flux is considered to be a good indicator of the star formation activity of the region (Helou et al. 2004; Relaño et al. 2007; Calzetti 2007). Region 2, which has the lowest 24 μm flux, may thus be relatively less active than the others. We also note that, even if the system is not clearly resolved at 70 μm, the 70 μm emission seems to peak at the location of UM 311. In conclusion, the compact galaxy UM 311 should dominate the system at mid-IR and FIR wavelengths and the global dust SED of the UM 311 system.

Table 5.4. Parameters for our SED models for the UM 311 system using different values for the 160 μm constraint.

	f$_{160}$ [a]	0.9 f$_{160}$	0.8 f$_{160}$	0.7 f$_{160}$	0.6 f$_{160}$	0.5 f$_{160}$
M$_{dust}$ ($M_\odot$)	5.2×10^6	5.5×10^6	6.1×10^6	7.0×10^6	8.4×10^6	1.1×10^7
f$_{PAH}$	0.34	0.38	0.39	0.4	0.41	0.42
α	2.13	2.08	2.00	1.93	1.86	1.79
U$_{min}$	0.25	0.19	0.12	0.07	0.04	0.02
U$_{max}$	1.6×10^5	5.0×10^4	1.8×10^4	10^4	6.7×10^3	4.9×10^3

Notes.- [a] f$_{160}$ is the upper limit at 160 μm.

NGC 1705 - The fiducial model fails to fit the *IRAS* 100 μm data when we introduce the LABOCA constraint but does fit this constraint when the SED is modeled without submm constraints. Fig. 5.6 presents the fit which gives the lowest χ^2 for this galaxy. We test the influence of the *IRAS* 100 μm flux on the fit performing SED models with and without this data point but with the submm constraint. The global shape of the SED does not change and the dust masses derived in these 2 cases vary by less than 5%. Cannon et al. (2006b) estimated the dust mass of NGC 1705 using the models of Dale & Helou (2002) and Li & Draine (2001), obtaining respectively $(3.8 \pm 1.9) \times 10^5$ $M_\odot$ and 7×10^4 $M_\odot$ ($\pm$ 50%). The model of Li & Draine (2001) combines laboratory studies and astronomical observations and fits the MIPS fluxes very well. The dust mass deduced from the Li & Draine (2001) model, accounting for its 50% uncertainty and the different distance they used (5.1 Mpc), compares well with our results obtained without the submm constraint: 3×10^4 $M_\odot$ (Table 5.3). Including the submm LABOCA constraint, we obtain a dust mass of 1.3×10^6 $M_\odot$, which is 50 times higher than our results without the submm data. In any event, our fiducial model, even using the 870 μm observations, is not satisfactory and gives a high $\bar{\chi}^2$ value. For this galaxy, the uncertainty in the mass estimate obtained using the submm constraint is mostly due to the flattening FIR peak and to the elevated 870 μm emission, for which the model has difficulty to find a self consistent solution. Considering that the error in the dust mass reaches more than 50%, we consider this first dust mass estimate obtained with our fiducial model uncertain and not satisfactory for this galaxy. We will explore a solution in the following

section.

Haro 11 - The SED of Haro 11 is very striking in that it peaks at very short wavelengths - 36 μm, highlighting the extreme nature of the young starburst. This is also evidenced by the high global value of the Ne[III]/[NeII] ratio (ratio > 1), already seen in other low-metallicity dwarf galaxies (Madden et al. 2006), which is normally an indication of the hard interstellar radiation field dominated by a young (< 5 Myr) stellar population. The peak of the IR SED compares to that of the $1/40\ Z_\odot$ galaxy SBS0335-052 (Houck et al. 2004) or IC10 NW (Parkin et al. 2010 in prep). The IRS spectroscopy provides a tight constraint on the slope of the hot mid-IR dust continuum emission as well as for the f_{PAH}. The model does not clearly fit all the details of the IRS spectrum due to the lack of sophistication and flexibility in the dust properties. More complex modelling would be required to perfectly model the different features of the spectrum but this does not affect the following conclusions on the dust mass parameter. Engelbracht et al. (2008) previously estimated the total dust mass of the galaxy to be $6.2 \times 10^6\ M_\odot$ using *Spitzer* observations and a distance of 87 Mpc. This value is consistent with the dust mass we obtain without submm constraints for a distance of 92 Mpc: $7.2 \times 10^6\ M_\odot$. Note that when the IRS spectrum is not used for the modelling but only IRAC broadbands, the dust mass is estimated to be $2 \times 10^8\ M_\odot$ with a poor-fit ($\bar{\chi}^2 = 24$). Thus the IRS spectrum greatly influences and constrains the global shape around the peak of the SED. The large uncertainty in the dust mass estimated from the modeled SED (the error reaches 40 % for this galaxy) is due to the excess emission at submm wavelengths that the model does not fit (Fig. 5.6). We model this excess in the following section.

5.5   Modelling the submm excess

5.5.1   Previous studies

Galliano et al. (2003, 2005) detected a submm excess in their metal-poor galaxies and suggested that it could originate from a very cold dust grain population accounting for 40-80% of the total dust mass of these galaxies. Bendo et al. (2006) studied NGC 4631 at 450 and 850 μm with SCUBA and also found that the 850-1230 μm emission exceeds what would be expected from thermal emission. They tried to model this submm excess by a very cold dust component but rejected this scenario due to the high D/G they deduced. In fact, a submm excess is not always detected in low-metallicity galaxies. Parkin et al. (in prep) investigated the very well sampled SED of the low-metallicity galaxy IC10, using SCUBA observations. Their modelling of the two main star forming regions do not lead to the detection of any submm excess, even if further studies should be done to perform an SED modelling of the galaxy on global scales.

Draine et al. (2007) also performed an SED modelling of a large sample of 65 galaxies as part of the SINGS program. For 17 galaxies observed with SCUBA, they fit SED models with and without this submm constraint. Five of their 17 galaxies show an increase in the dust mass when calculated using SCUBA constraints whereas 5 other galaxies show a decrease of this dust mass. Their dust masses obtained with and without SCUBA data agree to within a factor of 1.5 for 11/17 cases and to within a factor of 2.2 for all cases. They concluded that their dust models do not require cold ($\leq$10K) dust to account for their submm fluxes. In fact, the SINGS sample mainly contains metal-rich galaxies, especially the 17 galaxies observed with SCUBA. These galaxies may show different dust properties and dust temperature distributions than the low-metallicity galaxies we present in this study. Moreover, Draine et al. (2007) warn that some of their galaxies observed with SCUBA are not completely mapped or are not taken in scan map mode. A detailed description of SINGS submm fluxes uncertainties is given in the following chapter. The data processing is difficult and could have oversubtracted diffuse, extended emission for these galaxies, leading to an

underestimation of the submm fluxes. *Herschel* will observe these galaxies thoroughly in the submm as a part of the Kingfish program (PI: R. Kennicutt, http://www.ast.cam.ac.uk/research/kingfish/).

Several explanations have been given in the literature to explain the submm excess:

1) Lisenfeld et al. (2001) suggested that the submm excess could originate from hot (∼100 K) dust with a dust emissivity index $\beta=1$ and the temperature fluctuations of very small grains.

2) Models of Meny et al. (2007) have also modified the dust optical properties to find an effective decrease in the submm emissivity index as the dust temperature increases as suggested by the observations of Dupac et al. (2003). However, Shetty et al. (2009) express caution in the inverse temperature - β interpretation, showing that flux uncertainties, especially in the Rayleigh-Jeans regime, can affect the results for the SED fits as far as temperature and emissivity are concerned. Moreover, it it still not clear what would be the nature of this new grain population or which processes could lead to their dominance in dwarf galaxies.

3) Recently, Paradis et al. (2009) focused on the dust emissivity variations within the Milky Way and interpret the increase of the far-IR emissivity in molecular clouds containing cold dust by fractal aggregates consisting of amorphous individual grains. They note that an increase of a factor of 3-4 in the dust emissivity is required to explain the unusually low dust temperatures observed by dust aggregation. This explanation of a submm excess by grain coagulation was already suggested by Bazell & Dwek (1990) (theorethical approach) and Stepnik et al. (2001) (using data of the baloon-borne experiment ProNaos).

4) Ferrara & Dettmar (1994) showed that the rotating charged dust grains (also known as 'spinning dust') located in the ionised gas of many galaxies were producing radio emission. Anderson & Watson (1993) and then Draine & Lazarian (1998) have then tried to characterise and quantify the main contributors to the rotational excitations of these grains by studying collisions of the grains with neutrals or ions, plasma-grain interactions etc. Recent improvements to the Draine & Lazarian (1998) model have been studied recently by Hoang et al. (2010), Silsbee et al. (2010) and Ysard & Verstraete (2010). This emission could be responsible for submm emission.

5) Finally, Serra Díaz-Cano & Jones (2008) cautionned about using graphite in dust models and proposed that hydrogenated amorphous carbon could be the most probable form of carbonaceous grain material. Amorphous carbons having a flatter emissivity, their use in SED models will require less mass to account for the same emissivity. This hypothesis is tested in Chapters 7 and 9.

We do not reject any of these hypothesis in this study, but decide here to explore the cold dust hypothesis, since it enables us to investigate its consequences on the global properties of the galaxies.

5.5.2 Adding a cold dust component

In an attempt to improve the model results, we refine our fiducial SED model for the two galaxies Haro 11 and NGC 1705 using an additional thermal cold dust component with a flux, S_ν, characterised by a modified blackbody:

$$S_\nu \propto \nu^\beta B_\nu(T_d) \tag{5.1}$$

where B_ν is the Planck function, T_d is the dust temperature and β the emissivity index . We adopted the values $\rho=2.5 \times 10^3$ kg m^{-3}, $\lambda_0=100$ μm and $Q_0/a_0=150$ cm^{-1} for the mass density,

the reference wavelength and the absorption coeffcient at λ_0 of the grains respectively. The lack of observational constraints in the submm wavelength range forces us to fix the temperature and the dust emissivity index of this blackbody, choices that can influence the dust masses we deduce.

Emissivity - The Draine & Li (2007) model we are using, describes the carbon dust in terms of graphite which possesses an emissivity index of 2. Some studies, on the contrary, suggest that amorphous carbon could be the probable form of carbonaceous grains (Serra Díaz-Cano & Jones 2008). Amorphous carbon, for instance, is known to present a lower emissivity index (Rouleau & Martin 1991). We look into amorphous carbon / graphite differences in Chapter 7. As we do not have information on the properties of the cold grains we want to model, we propose to describe them by extrapolating the properties of graphite and assume an emissivity β of 2 or 1. Galliano et al. (2005) found indeed that $\beta{=}1$ was the most likely value to describe the extra component. Moreover, when two submm constraints are available, a bend is usually observed in the SED near 450 μm. Due to the physical parameters of the grains behaving like a modified black body in the submm, having a natural bend on the submm slope could be explained by a sudden change in the emissivity of the grains at 450 μm. Last but not least: we fix the absorption of the cold dust component to the model of Li & Draine (2001), which might deviate when a dust emissivity index of 1 (and not the standard emissivity of 2) is used. We assume that this value is still applicable here.

Temperature - Galliano et al. (2003, 2005); Marleau et al. (2006) suggest that their submm excess observed in low-metallicity galaxies could be explained by the presence of cold dust distributed in small and dense clumps and modelled it by an independant cold dust component with temperatures between 5 and 10 K. Since this temperature directly influences the dust mass derived from our modelling, we consistently used 10K (and not <10K) dust, to prevent overestimating of the cold dust, and thus the total dust mass derived from the modelling.

The new SED produced is obtained by adding the fiducial SED model and the cold blackbody. Chi-square values are estimated from the deviations of the new SED model to the observational constraints. In this revised model, the warm dust component is described by the observational constraints covering the far-IR wavelengths to 160 μm while the cold component is mainly constrained by the 870 μm observations.

5.5.3 Results with the submm excess modelled by cold dust

The SED models of Haro 11 and NGC 1705 which include an independant cold dust component are presented in Fig 5.7. The dust masses obtained from the different models are summarized in Table 5.5.

We find that including a 10 K dust component, the dust masses derived with a $\beta = 2$ for the cold dust grains are 6 and 8 times higher than those with a $\beta {=}1$ (Table 5.5) for Haro 11 and NGC 1705 respectively. This can easily be explained by the fact that a 10K modified blackbody using a λ^{-1} emissivity is flatter on the millimetre tail. The model thus requires less mass than when a steeper emissivity coefficient of 2 is used to account for the same emission. For Haro 11, the best-fit model implies $\beta{=}1$, leading to a total mass of dust (warm and cold) of 2×10^7 $M_{\odot}$, although the success in using $\beta{=}1$ or 2 is not very different in terms of the reduced chi-square ($\bar{\chi}^2$). Moreover, the $\bar{\chi}^2$ values of the models including a cold component indicate better fits than the fiducial models for both galaxies. For NGC 1705, when we try to increase the temperature of the cold dust component, the 160 μm observations become difficult to fit and χ^2 values increase. For Haro 11, increasing the temperature of the cold dust with $\beta{=}1$ does not significantly influence the χ^2 value until the temperature lof the cold dust reaches $\sim$20K. More observational constraints would be necessary to pin down the precise temperature of the cold dust component.
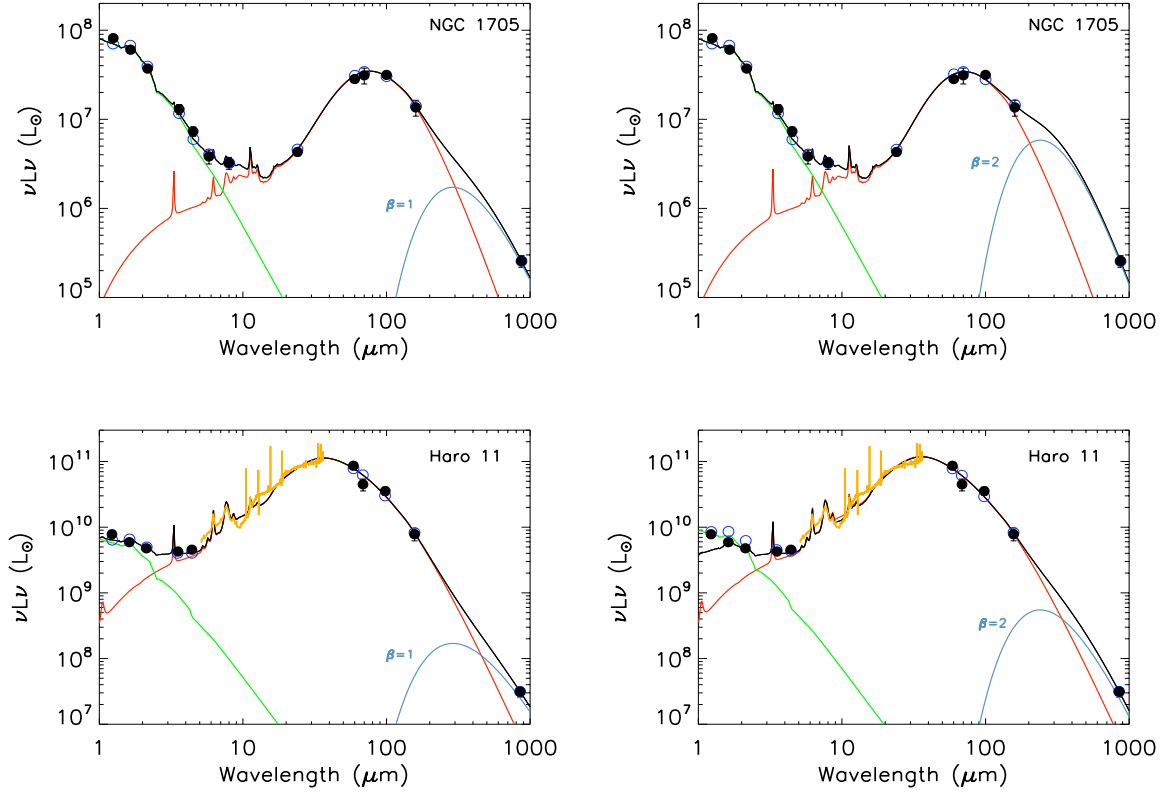
Figure 5.7. SED models of NGC 1705 and Haro 11, adding a cold dust component at 10K with an emissivity coefficient β of 1 and 2 to our fiducial model. Observational constraints are superimposed with filled circles. The IRS mid-IR spectrum is overlaid in orange for Haro 11. The green, red and blue lines represent the contributions of stars, warm and cold dust respectively. The red lines is close to the model generated when submm is omitted in the SED fit. The new models fit well the far-IR peak and the 870 μm flux.

Table 5.5. Parameters for the SED models introducing a cold dust component at 10K.

| | NGC 1705 | | | Haro 11 | | |
| | Fiducial modelling | Cold dust component | | Fiducial modelling | Cold dust component | |
		$\beta=1$	$\beta=2$		$\beta=1$	$\beta=2$
$\bar{\chi}^2$	15.7	2.4	3.3	17.2	11.3	11.5
M_{dust} $(M_\odot)$ [a]	$1.3\times10^6(\pm50\%)$	$\mathbf{1.7\times10^5}(\pm28\%)$[b]	$1.3\times10^6(\pm21\%)$	$1.7\times10^7(\pm40\%)$	$\mathbf{2\times10^7}(\pm17\%)$	$1.3\times10^8(\pm17\%)$
M_{dust}/M_{HI}	3.2×10^{-2}	$\mathbf{4.1\times10^{-3}}$	2.8×10^{-2}	0.17	$\mathbf{0.2}$	1.3
M_{PAH}/M_{dust}	2×10^{-3}	8.1×10^{-4}	8×10^{-5}	1.04×10^{-2}	3.1×10^{-3}	6.2×10^{-4}

Notes.- [a] This mass includes the cold (10K) dust mass for NGC 1705 and Haro 11.

[b] Bold numbers represent the dust mass and D/G values of our prefered SED models.

PAH abundances were estimated from the broadband constraints and mid-IR dust continuum, except for Haro 11 for which the IRS spectrum is available. For this galaxy, we find that the abundance of PAHs relative to the total dust mass is a factor of 15 lower than the Galactic value of 4.6×10^{-2}. This decrease of PAH features in low-metallicity starbursting galaxies was already observed in several studies and could be explain by the hardness of the radiation field of that type of galaxies (Galliano et al. 2005; Lebouteiller et al. 2007).

Instead of a cold dust component fitting the submm excess, we also test the formalism presented

in Draine et al. (2007) and try to fit the excess with an extra diffuse ISM component heated at $U=U_{min}$ for our two galaxies. This addition, in both cases, leads to a very cold component with $U_{min} < 10^{-2}$ due to the fact that the extra component tends to fit the submm excess contrary to the SINGS galaxies where this 'diffuse ISM component' represented most of the far-IR emission(Draine et al. 2007). Fixing a lower limit for the U_{min} parameter as done in Draine et al. (2007) does not resolve this issue since the model does not, in that case, fit the excess at all for our dwarf galaxies. The dust masses derived from the SED models using this method are 3.3×10^6 $M_{\odot}$ for NGC 1705 and 1.2×10^8 $M_{\odot}$ for Haro 11, thus 19 and 6 times higher, respectively, than the mass of dust derived from a SED model using a cold blackbody of 10K with $\beta=1$, unrealistic values due to the D/G mass ratios they imply. (The Draine et al. (2007) model is discussed in Chapter 6)

As Chapter 6 is dealing with the study of dust-to-gas mass ratios for a larger sample of galaxies, we will discuss the derived D/G values of NGC 1705, Haro 11 and Mrk 1089 in the following chapter. Nevertheless, we note that the D/G of Haro 11 seems very high compared to what should be expected from chemical evolution models (10^{-3} following the Dwek (1998) model). If our estimate of the dust mass is correct, that could indicate a lack of gas mass of $\sim 10^{10}$ $M_{\odot}$ for this galaxy (see Chapter 6 for discussion).

The SED results we will discuss in the following sections are those obtained with our fiducial model for Mrk 1089 and the SED models, which include a cold dust component at 10K with $\beta=1$ for NGC 1705 and Haro 11.

5.6 Robustness of the results with the assumed radiation field

We remind the reader that the ISRF used in our fiducial modelling has the shape of that of the Galaxy (Mathis et al. 1983). As mentionned in Chapter 3, our results could be dependent on the shape of the average radiation field to which the dust grains are exposed.

To quantify this dependence, we run our SED model with several ISRFs determined by (Madden et al. 2006) but also with the ISRF produced by a young non-ionizing cluster (see Chapter 3). The evolution of the dust masses derived from the SED models with the ISRF shape and hardness is summarized in Table 5.6. We find that the radiation field shape does not have a significant influence on the total dust mass parameter. Indeed, the dust masses derived with these different ISRFs differ by less than 10% than those determined using the Galactic ISRF for SEDs with reasonable χ^2 values.

The shape of the radiation field essentially controls the emission of out-of-equilibrium grains. In galaxies showing a 'harder' radiation field, we thus observe an increase in the maximum temperature that small grains reach when they fluctutate. This produces a short wavelength excess of the grain spectrum, as reflected in the resulting modified SEDs (Fig. 4.1). However, this excess is compensated in the global model by lowering the weight of the high intensity regions. Since these hot regions do not contribute significantly to the total dust mass of the galaxy, the latter does not strongly depend on the shape of the ISRF.

5.7 Distribution of the dust temperature

To get an idea of how the dust mass is distributed as a function of the temperature, we calculate the fraction of the dust mass in several ranges of temperatures: above 50K (hot), between 25 and 50K, between 15 and 25K and a cold 10K component for the two galaxies NGC 1705 and Haro 11. We estimate the fraction of dust between two temperatures as the mass of dust exposed to a radiation field such that the large silicates, which are at thermal equilibrium, have temperatures between

Table 5.6. Dust masses derived from SED models using different shapes of ISRFs

| Synthesized ISRF | NGC 1705 [a] | | | Haro 11 [a] | | | Mrk 1089 | |
	$M_{warm\ dust}$ [b]	M_{dust} [c]	$\bar{\chi}^2$	$M_{warm\ dust}$ [b]	M_{dust} [c]	$\bar{\chi}^2$	M_{dust}	$\bar{\chi}^2$
Milky Way	2.6×10^4	1.7×10^5	2	5.9×10^6	2×10^7	13	5.2×10^7	5.7
Non-ionising cluster	2.5×10^4	1.7×10^5	5	6.5×10^6	2.1×10^7	25	5.0×10^7	21
He 2-10	3.3×10^4	1.75×10^5	20	8.7×10^6	2.19×10^7	45	7.0×10^7	52
IIZw40	2.8×10^4	1.71×10^5	12	8.7×10^6	2.24×10^7	36	4.9×10^7	41
NGC1140	2.8×10^4	1.72×10^5	12	8.1×10^6	2.2×10^7	38	4.7×10^7	46
NGC1569	2.6×10^4	1.69×10^5	2	6.6×10^6	2.02×10^7	14	5.0×10^7	16

Notes.- [a] The models include a very cold dust component (10K - β=1).

[b] $M_{warm\ dust}$ is the dust mass without including the 10K dust mass (but with cold dust included in the fit)

[c] M_{dust} is the total dust mass of the galaxy including the mass of the 10K dust.

these two temperatures.

The energy absorbed by a dust grain is given by :

$$\Gamma_{abs} \propto \int_0^\infty Q_{abs}(\lambda) U_\lambda(\lambda) d\lambda \tag{5.2}$$

where Q_{abs} is the absorption efficiency and U the mean intensity of the radiation field.

The energy emitted by a dust grain is given by :

$$\Gamma_{em} \propto \int_0^\infty \nu^\beta B_\nu(T_{eq}) d\nu \propto T_{eq}^{4+\beta} \tag{5.3}$$

where B_ν is the Planck function and T_{eq} the equilibrium temperature.

As $\Gamma_{abs}=\Gamma_{em}$, we can equate these two expressions. We thus obtain a relation of proportionnality between the radiation intensity U and the equilibrium temperature T_{eq}. Grains are assumed to possess an emissivity β=2:

$$U(T_{eq}) \propto \left(\frac{T_{eq}}{17.5}\right)^{4+\beta} \propto \left(\frac{T_{eq}}{17.5}\right)^6 \tag{5.4}$$

Note that in this equation, the equilibrium temperature is normalised to the equilibrium dust temperature of the Galaxy of 17.5K (Boulanger et al. 1996).

From the prescription of Dale et al. (2001) (Eq. 4.2), we can derive the heated dust mass associated with each radiation intensity U and thus to each equilibrium temperature. The fraction of the total mass exposed to radiation between temperatures T_1 and T_2 is given by:

$$f_{mass}([T_1, T_2]) = \frac{U_2^{1-\alpha} - U_1^{1-\alpha}}{U_{max}^{1-\alpha} - U_{min}^{1-\alpha}} = \frac{T_2^{6(1-\alpha)} - T_1^{6(1-\alpha)}}{T_{max}^{6(1-\alpha)} - T_{min}^{6(1-\alpha)}} \tag{5.5}$$

where U_{min} and U_{max} are the boundaries of the intensity range obtained from the SED modelling.

For Haro 11 and NGC 1705, the fraction of dust at 10K is given by the ratio between the dust mass of the cold dust component and the total dust mass of the galaxy . The results are summarized in Table 5.7. The cool phase ($\leq$ 25K) constitutes the major part of the dust in our galaxies, at least 70% for Haro 11 and up to 90% for Mrk 1089 and NGC 1705. The SED of Haro 11 peaks at unusually short wavelengths (36 μm), with a significant fraction ($\sim$ 30%) of the dust mass at a temperature > 25K while this same dust mass fraction does not exceed 10% for NGC 1705 and Mrk 1089. Thus, their global SEDs reflect the different levels of star formation activity (and/or morphologies) and the consequences on the dust heating.

Table 5.7. Minimum and maximum equilibrium temperature and distribution of the dust mass with dust temperature ranges

	NGC 1705 [a]	Haro 11 [a]	Mrk 1089
$T_{eq\ (max)}$ (K)	88.2	125	146
$T_{eq\ (min)}$ (K)	10	10	16.9
f_{mass} ([50 K ; 150 K])	0.1 %	0.4 %	0.15 %
f_{mass} ([25 K ; 50 K])	7.2 %	28.9 %	9.5 %
f_{mass} ([15 K ; 25 K])	8.3 %	0 %	90.4 %
f_{mass} (10 K)	84.4 %	70.4 %	0 %

Notes.- [a] The models include a very cold dust component (10K - β=1).

5.8 Total Infrared Luminosities

We calculate the total IR luminosity (L_{TIR}) for our galaxies by integrating our modeled SEDs from 3 μm to 1100 μm and compare our L_{TIR} values with prescriptions in the literature using IR broadbands. For example, Dale & Helou (2002) have made phenomenological SED models to derive L_{TIR} based on *IRAS*, *ISO* and some 850 μm data and provide a recipe to estimate the 3 μm to 1100 μm luminosity using the *Spitzer* MIPS bands:

$$L_{TIR} = 1.6\ L_{24} + 0.77\ L_{70} + 1.35\ L_{160} \tag{5.6}$$

In the same fashion, Draine & Li (2007) expand this L_{TIR} relation to include the IRAC 8 μm flux.

$$L_{TIR} = 0.95\ L_8 + 1.15\ L_{24} + L_{70} + L_{160} \tag{5.7}$$

We compare the L_{TIR} obtained using these two formulae with that obtained from our SED model. For the galaxy Mrk 1089, the 160 μm observation is not available but the flux density at 160 μm can be extrapolated from our SED models. We estimate this flux density to be 5334 ($\pm$ 266) mJy from the model which uses the submm constraint. For Haro 11 and NGC 1705, the L_{TIR} was calculated from the revised models which include a cold dust component with an emissivity β=1. Results are summarized in Table 5.8.

The L_{TIR} values derived with the Dale & Helou (2002) formula seem to be lower than those derived directly from our SED models. The L_{TIR} derived with the Draine & Li (2007) formula lead to a better agreement. We also extend this study to a larger sample of galaxies. We derive the L_{TIR} of the galaxies of Galliano et al. (2008) by integrating their SEDs from 3 μm to 1100 μm and compare the results to the L_{TIR} obtained by both the Dale & Helou (2002) and Draine & Li

(2007) relations. Engelbracht et al. (2008) also calculate the L_{TIR} of their galaxies from their SED modelling. We calculated the L_{TIR} derived from the Dale & Helou (2002) and the Draine & Li (2007) relations for their galaxies (from the fluxes available in the paper) and add these galaxies to the sample. The ratio between these different estimates are plotted in Fig. 5.8 as a function of metallicity. We clearly observe a systematic underestimation of the L_{TIR} when using the Dale & Helou (2002) relation, with a shift of about 20% and a large scatter. The Draine & Li (2007) formula seems to better estimate the L_{TIR} of the galaxies (scatter less than $\sim$ 20%). For the lowest metallicity galaxies used in this comparison (12+log(O/H)<7.7), we note a potentially systematic underestimation but larger samples would be required to investigate this point.

Table 5.8 also summarizes the distribution of the IR luminosity according to wavelength windows: from 3 to 50 μm, from 50 to 100 μm and from 100 to 1100 μm. For Mrk 1089 and NGC 1705, the luminosity is roughly evenly distributed over the wavelength windows while for Haro 11, 70% of the L_{TIR} comes out at wavelengths shorter than 50 μm. While the longer wavelengths account for the major fraction of the dust mass, no more than 6% of the L_{TIR} comes out at wavelengths greater than 100 μm, consistent with the 'hot' SED peaking at $\sim$40 μm for Haro 11.

Table 5.8. Luminosities, sizes and SFRs of our galaxies

		NGC 1705 [a]	Haro 11 [a]	Mrk 1089
$L_{TIR} = L_{[3\mu m, 1100\mu m]}$ $(L_\odot)$ [b]	(1)	5.8×10^7	1.7×10^{11}	3.9×10^{10}
	(2)	4.9×10^7	1.4×10^{11}	3.8×10^{10}
	(3)	5.9×10^7	1.6×10^{11}	4.3×10^{10}
$L_{[3\mu m, 50\mu m]}$ $(L_\odot)$		1.9×10^7	1.2×10^{11}	1.4×10^{10}
$L_{[50\mu m, 100\mu m]}$ $(L_\odot)$		2.2×10^7	4.1×10^{10}	1.3×10^{10}
$L_{[100\mu m, 1100\mu m]}$ $(L_\odot)$		1.6×10^7	9.6×10^9	1.1×10^{10}
$L_{FIR} = L_{[8\mu m, 1100\mu m]}$ $(L_\odot)$		5.1×10^7	1.6×10^{11}	3.7×10^{10}
$L_{H\alpha}$ (erg s^{-1})		6.34×10^{38} [1]	3.2×10^{42} [2]	4.57×10^{41} [3]
Size		0.5' × 0.5'	0.25' × 0.25'	0.31' × 0.12'
SFR $(M_\odot$ yr^{-1} kpc$^{-2})$ [c]	(4)	1.6×10^{-3}	5.1×10^{-2}	5×10^{-2}
	(5)	9.4×10^{-4}	-	5.8×10^{-2}
	(6)	5.2×10^{-4}	2.4×10^{-2}	1.4×10^{-2}
	(7)	5.7×10^{-4}	3×10^{-2}	1.8×10^{-2}

Notes.- [a] The models include a very cold dust component (10K, β=1).

[b] Total infrared luminosities (L_{TIR}) are estimated (1) by integrating our SED models with a submm constraint from 3 to 1100 μm - (2) from the Dale & Helou (2002) formula - (3) from the Draine & Li (2007) formula.

[c] Star formation rates (SFR) are estimated using (4) the relation of Kennicutt (1998) based on L_{FIR} - (5) the relation of Zhu et al. (2008) based on ν L_ν[24 μm]. (This last relation is only valid for galaxies with a $L_{TIR} < 10^{11}$ $L_\odot$ and can not be used for Haro 11) - (6) the relation of Calzetti (2007) based on the 24 μm luminosity (L_{24}) alone - (7) the relation of Calzetti (2007) based on L_{24} and $L_{H\alpha}$.

References.- [1] Cannon et al. (2006b) - [2] Bergvall et al. (2000) - [3] Iglesias-Páramo & Vílchez (1997).
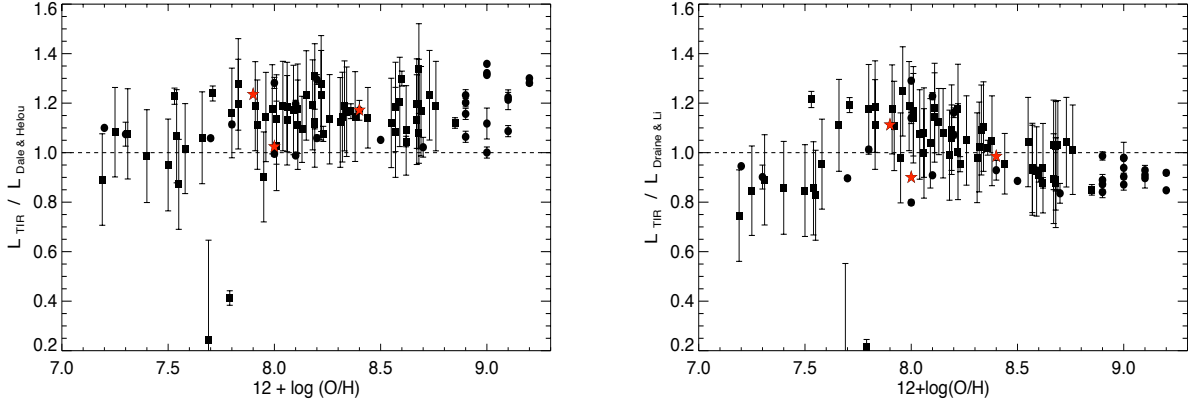
Figure 5.8. *Left:* Ratio between the total infrared luminosty (L_{TIR}) derived by directly integrating the SED models from 3 to 1100 μm and L_{TIR} given by the Dale & Helou (2002) formula. The squares indicate the Engelbracht et al. (2008) galaxies whereas the circles indicate the Galliano et al. (2008) sample. Stars represent our three galaxies Haro 11, Mrk 1089 and NGC 1705 in metallicity increasing order . *Right:* Ratio performed with L_{TIR} given by the Draine & Li (2007) formula.

5.9 Star Formation Rates

We want to investigate how these galaxies behave with respect to the Schmidt law. This law describes the tight relationship between global star formation rate (SFR) and gas density and was originally formulated for normal spirals. We estimate the star formation rates (SFRs) of our galaxies using the Kennicutt (1998) relation:

$$SFR\ (M_\odot\ yr^{-1}) = 4.5 \times 10^{-44}\ L_{FIR}\ (erg\ s^{-1}) \tag{5.8}$$

where L_{FIR} is the IR luminosity obtained integrating our SED models between 8 and 1000 μm.

We compare these values with the SFRs obtained by the Zhu et al. (2008) formula for star forming galaxies, which is only valid when $L_{TIR} < 10^{11}\ L_\odot$ and thus can not be used for the LIRG Haro 11:

$$SFR\ _{24\mu m}\ (M_\odot\ yr^{-1}) = \frac{\nu L_\nu [24\mu m]}{7.79 \times 10^8 L_\odot} \tag{5.9}$$

We finally use the relations of Calzetti (2007) to derive SFR estimates from the 24 μm luminosity L_{24} and the Hα luminosity ($L_{H\alpha}$).

$$SFR\ (M_\odot\ yr^{-1}) = 1.24 \times 10^{-38}\ [L_{24}\ (erg\ s^{-1})]^{0.88} \tag{5.10}$$

$$SFR\ (M_\odot\ yr^{-1}) = 5.3 \times 10^{-42}\ [L_{H\alpha} + 0.031\ L_{24}] \tag{5.11}$$

The different SFR estimates are presented in Table 5.8. The values obtained with the Kennicutt (1998) relation are higher than those derived with the Calzetti (2007) formula but compare well with those of Zhu et al. (2008). We plot the SFR estimated with the relation of Kennicutt (1998) as a function of the gas density for our three galaxies (Fig. 5.9). We overplot a large sample of spirals and starburst galaxies presented in Kennicutt (1998) for comparison.

The two galaxies Mrk 1089 and NGC 1705 seem to follow the Schmidt law. For Haro 11, we

take the large upper limit of the H I + H$_2$ mass ($\sim 10^9$ $M_\odot$ - Bergvall et al. 2000) to account for the total gas mass of the galaxy. Haro 11 does not fall close to the Schmidt law. Its location in Fig. 5.9 might be due to the fact that it is a dwarf galaxy, which can explain why the gas seems to be consumed at a much higher rate than in normal spiral galaxies. Undergoing a merger, Haro 11 should also have a high star-formation rate with a lower gas consumption time than less luminous galaxies (see Kennicutt et al. 1994; Tacconi et al. 2006 for studies on normal nearby and submm galaxies respectively). Nevertheless, Kennicutt (1998) suggests that the SFR in LIRGs do follow the Schmidt Law dependence on gas surface density, which means that the relation linking the SFR and L$_{FIR}$ of starburst systems should not differ significantly from normal disk galaxies.

To follow the Schmidt law, Haro 11 would require 10^{10} $M_\odot$ of gas, which would imply an order of magnitude more than that suggested by CO and H I measurements. The location of Haro 11 as an outlier of the Schmidt law seems to suggest that there is a large amount of gas mass missing in the current gas inventory based on current H I and CO observations (see Chapter 6 and the discussion on D/G for Haro 11).
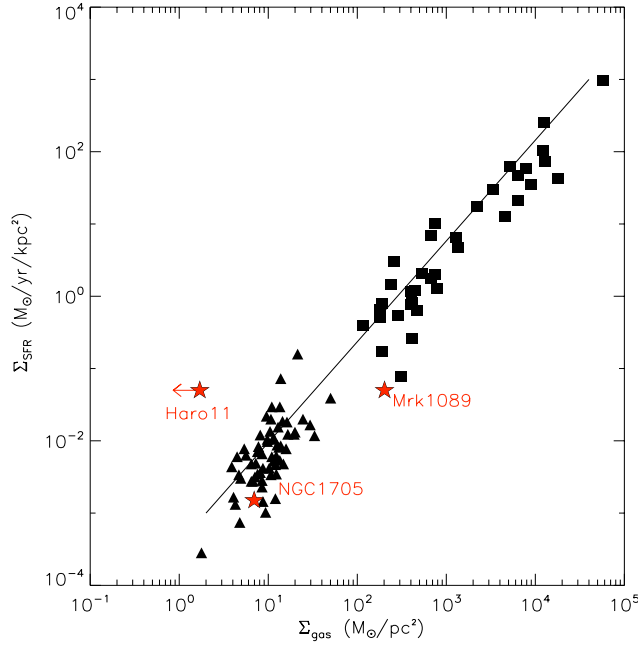
Figure 5.9. Positions of Haro 11, NGC 1705 and Mrk 1089 in the Schmidt-Kennicutt diagram. The triangles represent normal spirals and squares represent starburst galaxies (see Kennicutt 1998 for details on the galaxies represented by triangles). Red stars indicate our sources. The position of Haro 11 in this diagram accounts for the HI+H$_2$ upper limit of total gas mass ($\sim 10^9 M_\odot$) of the galaxy.

5.10   Conclusions

The quantification of the dust mass of a galaxy is crucial to understand its evolution and star formation history. Larger dust masses are found in our 4 low metallicity galaxies when using submm constraints in the SED modelling. In this context, submm observations are clearly necessary for a more complete description of the distribution and properties of dust. Our study focuses on the dust modelling of four low-metallicity galaxies observed with LABOCA.

We tested the effect on the SED model results when submm 870 μm observations are taken into account and compare with SED models not taking into account the 870 μm flux, but with

observational constraints at wavelengths up to 160 μm. We find that the use of submm observational constraints always leads to an increase of the total dust mass derived for our low metallicity galaxies. For two galaxies (NGC 1705 and Haro 11), we chose to include an additional component to account for the excess submm emission. A cold dust component ($\sim$10K) with a β emissivity index of 1 substantially improves the fit. We find that at least 70 % of the total dust mass resides in a cold ($\sim$ 10K) dust component for these two galaxies. We note that describing a cold component of β = 2 leads to similar χ^2 values, but would give unrealistically larger D/G. This study however does not rule out the hypothesis of a change in dust emissivity as a function of wavelength proposed in recent studies (e.g. Dupac et al. 2003; Meny et al. 2007).

Haro 11 has a substantial ($\sim$ 70 %) cold dust component and harbours a signicant fraction of dust mass (30 %) in a warmer dust component ($>$ 25K). The SED peaks at unusually short wavelengts (36 μm), highlighting the significance of the warm dust in the total dust mass of the galaxy. From our SED models, we determine the total infrared luminosity of our galaxies. The L_{TIR} are systematically higher than those obtained using the Dale & Helou (2002) formula but compare better to the Draine & Li (2007) formula. While $\sim$ 90 % of the dust mass is residing in the far-IR to submm regime, not more than 6 % of the total IR luminosity in Haro 11 emerges from the far-IR to submm (100 to 1100 μm), while most of the luminosity (70 %) emerges in the near-IR to mid-IR (3 to 50 μm) window. This is in contrast to Mrk 1089 and NGC 1705 which distribute their luminosities more equally in these two wavelength windows. Better observational coverage of the submm regime of the SEDs with *Herschel* should help us to disentangle possible scenarios to explain the excess detected in some galaxies in the submm: dominant diffuse ISM dust, modications of the dust optical properties at submm wavelengths, very cold dust component.

We would now like to study the consequences of this increase of the dust mass due to the addition of submm constraints on dust-to-gas mass ratio estimates. By broadening our sample of galaxies, we will also study the influence of submm constraints on the dust masses derived for low-metallicity to metal-rich galaxies and the D/G relation with metallicity.

Chapter 6

Dust-to-gas mass ratio vs metallicity relation: constraints from the submm contribution

Contents

6.1 Genesis of the study

Our knowledge of the dust properties in the ISM has greatly improved since the early days of infrared instruments. As presented in the previous chapter, the basic question of the accurate quantification of the dust mass of a galaxy and how the D/G is affected by metallicity are issues that still require to be studied. The D/G of a galaxy is the main output of dust evolution models and a clue to access to the history of the cycle of matter within galaxies. Previous studies have investigated the evolution of D/G as a function of the metal enrichment of galaxies. The first studies of Franco & Cox (1986) suggested that the D/G should be proportional to the metallicity of the galaxy. Investigations in the Milky Way (MW) led to a D/G of $\sim 10^{-2}$ for our galaxy (Sodroski et al. 1997). Further analysis into depletion of metals from the ISM or into comparisons of dust extinction versus hydrogen column densities have both shown that the D/G of the MW falls within the range of 1-5 $\times 10^{-2}$ (Whittet 2003; Krügel 2003, 2008). In the Magellanic Clouds, the D/G was found to be lower than that estimated for more metal-rich environments (e.g. Gordon et al. 2009 found a D/G of $\sim$ 3-5 $\times 10^{-3}$ in the SMC, consistent with the low metallicity of the galaxy).

To investigate the relation between the metallicity and the D/G, Lisenfeld & Ferrara (1998) studied a broad sample of dwarf irregular (dIrrs) and blue compact dwarfs (BCDs) from IRAS observations at 60 and 100 μm. A logarithmic correlation between D/G and the oxygen abundance was found for the dIrrs: 12 + log (O/H) $\propto$ (0.52$\pm$0.25) $\times$ log (M_{dust}/M_{HI}), but no relation was found for the BCDs which are more actively forming stars. Therefore, they observed that metals are less effectively incorporated into dust in dwarf galaxies than in more metal-rich galaxies. Relations between D/G and other parameters, such as the Star Formation Rate, should be expected. However, James et al. (2002), using SCUBA 850 μm observations concluded that the fraction of metals incorporated into dust was a universal constant, that is to say similar for dwarf and giant galaxies, which was in contradiction to the Lisenfeld & Ferrara (1998) conclusions. They also noted that their D/G mass ratios estimated with submm observations are usually higher than that previously estimated by Lisenfeld & Ferrara (1998) for the same galaxies. Galliano et al. (2003, 2005) also showed that taking the very cold dust traced in some galaxies by SCUBA or MAMBO, the dust-to-metals ratios is getting closer to the Galactic value. The previous chapter presented the SED models of 4 low-metallicity galaxies observed with the APEX/LABOCA instrument at 870 μm and note that the dust masses estimated from their models increase when using the submm observation. On the contrary, Draine et al. (2007) found that the dust masses of their SINGS-SCUBA sample is rather unaffected when using or not submm data and that the D/G omitting the submm data only modestly rises. Finally, Muñoz-Mateos et al. (2009b) also observed that the D/G was correlated with metallicity and therefore decreases with galactocentric radius.

This leaves open the question of the impact of submm observations in the assessment of the total dust mass of a galaxy and the information directly linked with this quantity: relation between metallicity, D/G and star formation, distribution of the equilibrium temperature of the largest grains, intensity of starlight heating the dust etc. In this chapter, we gather a large number of galaxies with different metallicities to study the effect of submm constraints on the dust mass estimation and its implications for the D/G relation with metallicity.

We have gathered published dust and gas masses of a broad sample of galaxies, some of them observed with submm telescopes, to study the relation of D/G with metallicity. The dust and gas masses used in this preliminary study are published in Lisenfeld & Ferrara (1998), James et al. (2002), Draine et al. (2007), Hirashita et al. (2008), Engelbracht et al. (2008), and Galliano et al. (2008). We add the three galaxies NGC 1705, Haro 11 and Mrk 1089 studied in the previous chapter to this large sample.

In detail:

The Lisenfeld & Ferrara (1998) sample groups together dwarf irregular galaxies (dIrrs) and BCDs. Their SEDs were constrained using only *IRAS* data. Their dust mass estimates are thus considered as lower limits to the total dust masses of the galaxies.

The James et al. (2002) sample gathers galaxies observed at submm wavelengths with SCUBA at 850 μm. They fitted their data with the Dunne & Eales (2001) two-component model (temperature of the cold component fixed to 20K and emissivity of the two components fixed to 2) to derive the total dust mass of their galaxies.

The Hirashita et al. (2008) sample is a small sample of eight low-metallicity galaxies observed with *AKARI* at 65, 90, 140 and 160 μm. They derived a total mass of dust for their galaxies from the FIR emission using a single temperature modified blackbody model, using the mass absorption coefficient of dust grains taken from Hildebrand (1983).

The Draine et al. (2007) sample includes spirals, ellipticals, starburst galaxies and both metal-rich and metal-poor galaxies from the *Spitzer*/SINGS survey. Their realistic dust SED modelling is performed with *Spitzer* IRAC and MIPS data, some of their galaxies being observed with SCUBA at 450 or/and 850 μm.

The Engelbracht et al. (2008) sample observed with *Spitzer*, covers a wide range of metallicity values (from 12+log(O/H)=7.1 for SBS 0335-052 to 8.85 for IC342). Their dust masses are estimated using the standard formula and the absorption coefficients from Li & Draine (2001).

The Galliano et al. (2008) sample has been partly observed with SCUBA 450 μm and/or 850 μm. All of their SED models included either the *Spitzer*/IRS spectra or the ISOCAM spectra for optimum contraints in the mid-IR.

Our small sample of Chapter 5 gathers low-metallicity sources observed with the *Spitzer* telescope and LABOCA at 870 μm. We did not use the galaxy UM 311 in this study since we can not isolate the galaxy from the rest of the group below 24 μm.

The gas masses of this sample were estimated using H I 21cm line measurements and the H_2 mass determined from CO observations when available.

Figure 6.1 shows the D/G of this sample of galaxies as a function of metallicity. Several different chemical evolution models are overlaid on this figure. We overlay the one-zone single-phase chemical evolution model of Dwek (1998) presented in Galliano et al. (2008). We also overlay the Edmunds (2001) dust formation models. They note that they adopt a less detailed quasi-analytic model compared to Dwek (1998). These models include mantle growth in the interstellar medium and take into account the grain core production in both supernovae and giant stars. These two modes of dust formation correspond to the two relations overlaid in Figure 6.1: solid line: dust produced in low and intermediate mass stars; dashed line: dust production strongly affected by the role of supernovae.

The filled symbols localise the galaxies for which dust mass is estimated using submm data. These galaxies tend to follow the Edmunds (2001) and Dwek (1998) models and clearly differ from the linear regression performed with the whole sample (dot dashed line), i.e. which also include galaxies that were not observed at submm wavelengths. Low-metallicity galaxies whose dust masses were estimated with submm data have higher D/G than galaxies modeled without submm data.
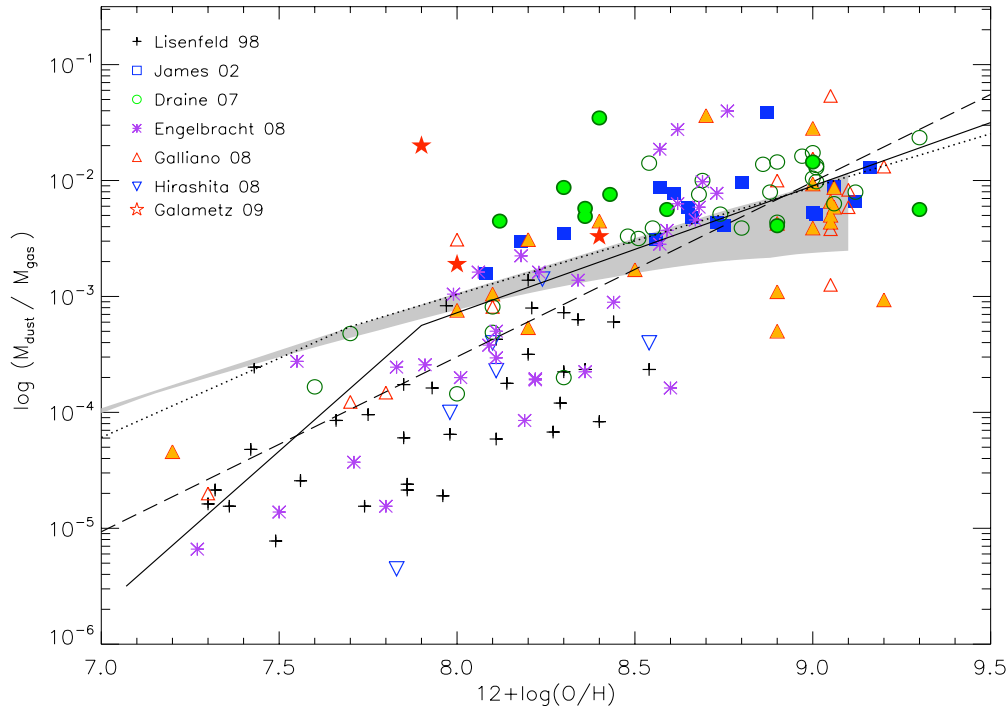
Figure 6.1. Dust-to-gas mass ratio as a function of oxygen abundance. Black crosses represent the Lisen-feld & Ferrara (1998) sample of Blue Compact Galaxies and dwarf Irregulars. Purple asterisks show the Engelbracht et al. (2008) sample using *Spitzer* data. Blue squares indicate the James et al. (2002) galaxies. Green circles represent the galaxies of the SINGS survey (Draine et al. 2007) for which metallicity is already published. Orange upward triangles are the Galliano et al. (2008) sample, blue downward triangles are the Hirashita et al. (2008) sample. Stars indicate the location of the three low-metallicity galaxies Haro 11, NGC 1705 and Mrk 1089 discussed in Chapter 2. Filled triangles, squares, circles or stars indicate when submm data were used in the SED modelling to estimate the total dust mass of the SED. The solid line and the dotted line are the predictions of the dust formation models from Edmunds (2001): the solid line represents a model in which dust is produced in low and intermediate mass stars while the dotted line represents the model in which supernovae play an important role in the production of dust. The gray stripe is the expectation of the one-zone, single-phase chemical evolution model presented in Dwek (1998). The dashed line represents the linear regression of the whole sample. The D/G errors can be significant for many galaxies but should not exceed ± 50%.

This could imply that for dwarf galaxies, the use of submm data leads to higher dust mass predictions, and thus higher D/G.

Of course, these various samples do not necessarily have any selection criteria in common. Some of the surveys were deliberately targeting dwarf galaxies yet others are meant to cover a wider variety. For instance, the SINGS sample represents a broad range of galaxies meant to evenly fill a three-parameter space defined by morphology - infrared luminosity and $L_{FIR}/L_{optical}$. Moreover, the dust models and SED fitting used to derive D/G are different from one sample to another, which could lead to biases in the analysis and interpretation. In conclusion, analysing the dust and gas masses of these galaxies directly given by the literature as one broad collection should be limited. We decided to reprocess this analysis using a unique SED model to avoid biases in comparing galaxies modeled with different SED models. We chose to restrict ourselves to galaxies observed at submm wavelengths to actually study the influence of this submm flux on the estimate

of the total dust mass of the galaxies. Thus we use a subsample of the galaxies from Fig. 6.1 in the following study.

6.2 Observational constraints and modelling

As said above, we only keep galaxies for which submm data are available, namely observations above 200 μm. The restricted sample is presented in Table 6.1. Metallicities, distances and submm 450 and/or 850 (or 870) μm data are also summarized. We refer to the respective papers for reference on distances. Other references are quoted in the table. The galaxies Haro 11, NGC 1705 and Mrk 1089 of chapter 1 are added to this analysis.

6.2.1 Submm observations

Flux densities at 450 and/or 850 μm SCUBA or 870 μm LABOCA are given in James et al. (2002), Dale et al. (2007). SCUBA flux densities of the Galliano et al. (2008) sample come from a private communication. A few galaxies of this sample were not observed with SCUBA or LABOCA but with other submm instruments. M83 was observed at 540 μm with the 4-m telescope at Cerro Tololo Inter American Observatory (Hildebrand et al. 1977). NGC 1068 was observed at 350 μm and 390 μm, respectively with the Submm High Angular Resolution Camera (SHARC on the CSO) (Benford 1999) and with the University of Hawaii 2.2m telescope at the Mauna Kea Observatory (Hildebrand et al. 1977). NGC 891 was observed at 350 and 1300 μm, with the 3m Infrared Telescope Facility (IRTF) and the 88" telescope of the University of Hawaii on Mauna Kea (Chini et al. 1986). Finally, IC342 was observed at 1mm with the Palomar 5m telescope (Elias et al. 1978). Only an upper limit was derived for this galaxy.

We also include the SINGS galaxies that were observed with SCUBA. The quality of some of the submm fluxes used in this analysis have been discussed. The Draine et al. (2007) paper warned that their submm fluxes could have been underestimated in some of their galaxies for various reasons. The galaxy NGC 6946, for instance, has been scan mapped with SCUBA. The data processing could have removed some extended emission for this galaxy, leading to an underestimate of the SCUBA 850 μm flux. For NGC 1097, SCUBA observations only cover the galaxy center and the total submm flux was estimated by inferring how much flux resides in the outer regions not observed, assuming a constant MIPS-to-submm ratio (see Dale et al. 2005 for further details on the process and multiplication factors). This assumption could be incorrect if radial color variations are present. SCUBA maps of NGC 3521, NGC 3627, NGC 4536 and NGC 7331 also have small field of views. The submm fluxes taken from Dale et al. (2007) should therefore be used with caution in a global analysis of these galaxies.

6.2.2 Optical and infrared data

2MASS data are added as measures to account for the stellar contribution of the SEDs. *2MASS* flux densities are taken from the 2MASS Large Galaxy Atlas (Jarrett et al. 2003) and Dale et al. (2007). *Spitzer*/IRAC and MIPS flux densities are used to sample the infrared part of the SED, when available. The *Spitzer* flux densities of the SINGS galaxies used in this study are given in Dale et al. (2007). For the Galliano et al. (2008) sample, *Spitzer*/IRS spectral information is, in most cases, available and used in our modelling. These spectra are presented in Galliano et al. (2008).

We complete our wavelength coverage using available *IRAS* flux densities. For the Draine et al. (2007) galaxies, the *IRAS* flux densities were obtained from SCANPI and the *IRAS* High Resolution Image Restoration Atlas (HIRES; Surace et al. 2004). Those of the James et al. (2002) sample come from the *IRAS* Revised Bright Galaxy Sample (Sanders et al. 2003), HIRES for the galaxies NGC 3994 and NGC 3995 and from the *IRAS* Faint Source Catalog (Moshir & et al. 1990)

for NGC 4670. The *IRAS* flux densities of the Galliano et al. (2008) sample were obtained from the *IRAS* Faint Source catalogue and the *IRAS* catalog of Point Sources (IPAC 1986).

6.2.3 The SED modelling of the sample

We model the SEDs using the technique described in Chapter 4. For 9 galaxies (NGC 1569, NGC 1140, He 2-10, II Zw 40, NGC 4303, NGC 2903, NGC 7674, and two galaxies of Chapter 5, NGC 1705 and Haro 11), an excess at submm wavelengths is detected when our fiducial SED model is applied. The basic model can not fit the FIR data and the high submm fluxes together. As described in Chapter 5, this submm excess has already been reported in the literature. We chose to use the same technique as in Chapter 5 and model this excess using a cold dust modified blackbody and an emissivity of 1, since $\beta=2$ usually leads to significant dust masses incompatible with chemical evolution models (see Chapter 5). The SEDs of the 9 galaxies modeled with an extra cold dust component are presented in Fig. 6.2.

6.3 Effects of submm observations on the total dust mass

From the SED models we derive the total dust masses of our galaxies. The errors on dust masses are linked to the uncertainties on our observational measures and are estimated using the technique described in Chapter 4. Dust masses and errors are summarized in the last columns of Table 6.1.

We also test the presence of the mid-IR spectrum as a constraint on the submm slope but no systematic increase or decrease of the total dust mass was observed.

The two plots of Fig.6.3 show the dust mass estimated using submm data versus the dust mass estimated without using submm data and the ratio of these two quantities as a function of metallicity. Both plots demonstrate that, for metal-rich galaxies, the dust mass is overestimated when submm measures are not used. The submm fluxes clearly constrain the submm slope of the SED and thus more particularly the minimum intensity U_{min}, leading to an increase of this parameter when submm data are used in metal-rich galaxies (Fig. 6.4). In the case of a lack of constraints on the submm slope, there is a risk that the SED procedure invokes a large mass of cool dust. Fig. 6.5 illustrates this effect on the galaxy NGC 337 modeled with (solid line) and without (dashed line) the 850 μm SCUBA flux. The submm slope of the SED is reasonably sampled when the submm flux is available. The total dust mass decreases by a factor of 8 when using a submm measure for this galaxy. This systematic overestimation of the dust mass without submm mostly affects metal-rich galaxies. This can be linked to the fact that their SEDs peak at longer wavelengths than low-metallicity galaxies. The 160 μm flux alone is thus not sufficient to fully sample the dust SED peak and constrain the submm slope.

The influence of submm data on the dust mass estimates was also investigated in previous studies. Draine et al. (2007), for instance, found that the dust masses of their SINGS-SCUBA sample is rather unaffected by the use of submm data and that the D/G values obtained when omitting the submm data, only modestly rises. For the SINGS (mostly metal-rich) galaxies observed in submm, we, on the contrary, find that the dust masses we derive without submm can be significantly higher than those obtained using submm data. This can be explained by the fact that we are assuming that the illuminating radiation fields follow a simple power-law distribution of radiation fields whereas the model used in Draine et al. (2007) includes both this power-law and a 'diffuse' dust component heated by a radiation field with a low U that, in fact, describes most of the far-IR emission. They furthermore restricted the radiation fields to $U_{min} \geq 0.7$ to precisely avoid their model invoking a large mass of cold dust. Figure 6.4 shows in dashed lines the boundaries they fixed for the U_{min} range. They acknowledge that this assumption could lead to an underestimate of the dust mass
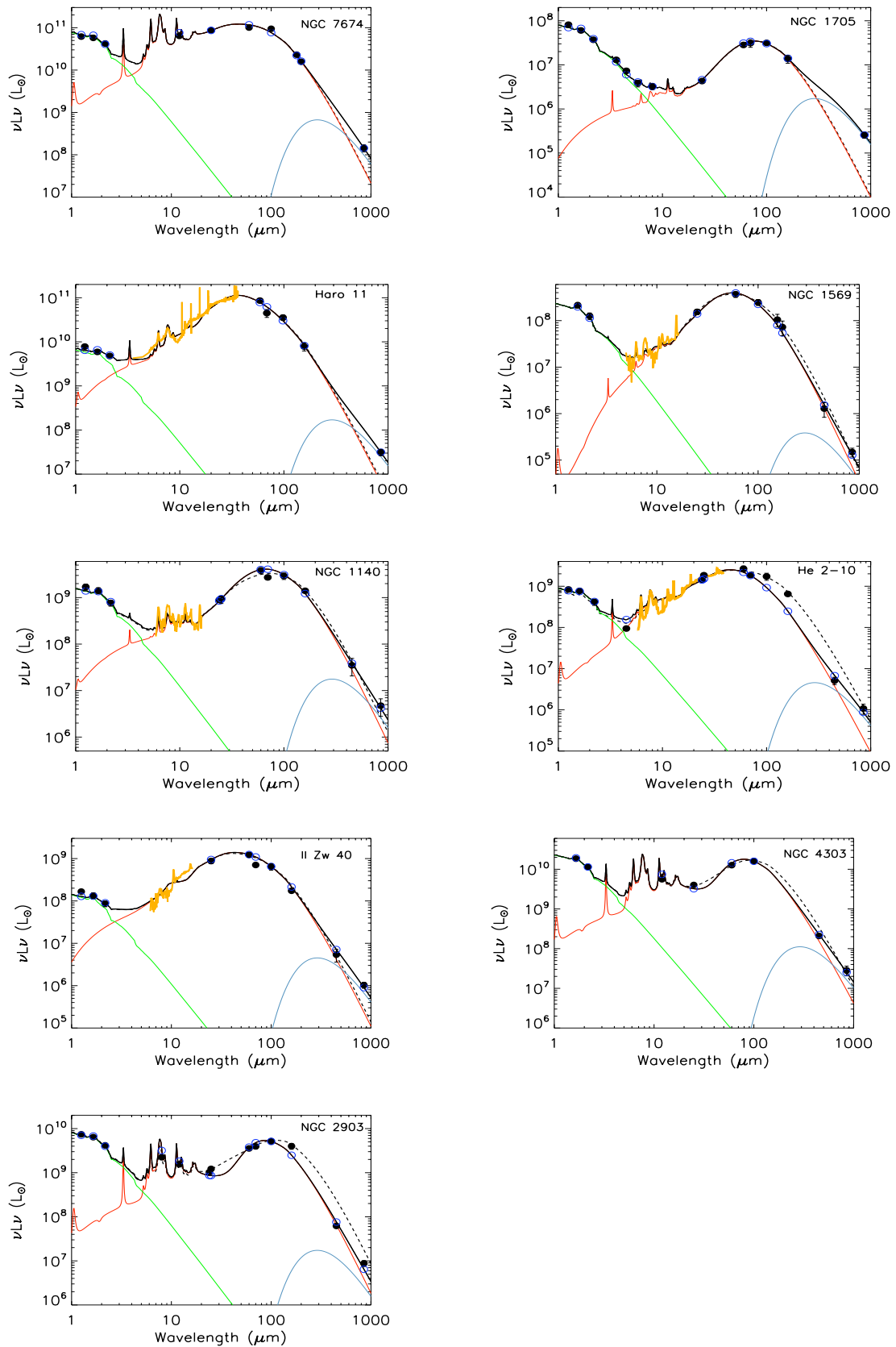
Figure 6.2. SED models of galaxies showing an excess in submm. SEDs were modeled with submm data (black line) and without submm data (dashed line). Observational fluxes are superimposed (filled circles). When not shown, errors are smaller than symbols. IRS spectrum is used in the modelling in some cases when available. Open circles represent the expected fluxes integrated over the instrumental bands. Green, red and blue lines respectively show the stellar, the warm dust and the cold dust contributions.
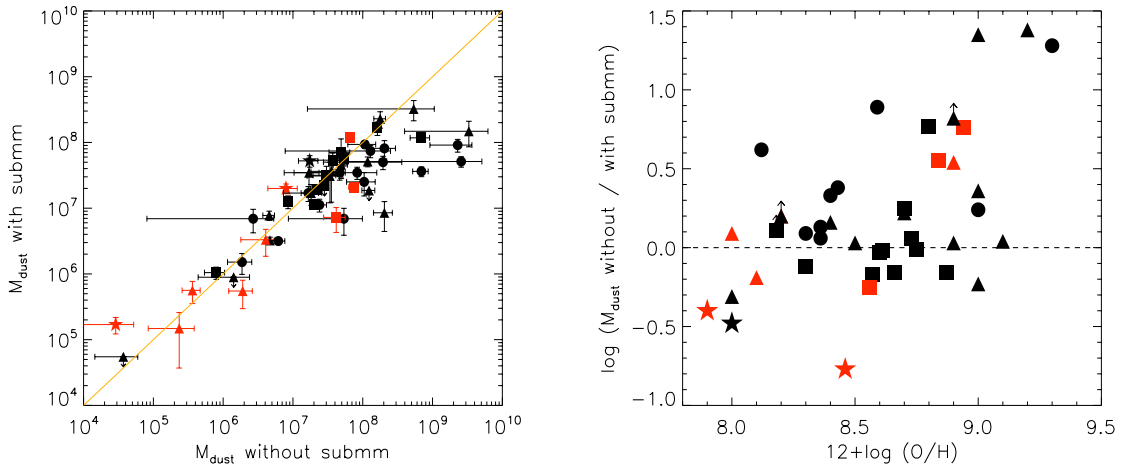
Figure 6.3. *Left:* Total dust mass estimated with submm observations versus total mass of dust estimated without submm observations. The line shows the 1:1 relation. Squares indicate the James et al. (2002) galaxies. Circles represent the galaxies of the SINGS survey (Draine et al. 2007) for which metallicity is already published. Triangles are the Galliano et al. (2008) sample and stars indicate the location of the three galaxies Haro 11, NGC 1705 and Mrk 1089 of Chapter 2. Red symbols represent the galaxies that present a submm excess and for which a cold dust (10K) component with an emissivity $\beta=1$ is added. *Right:* Evolution of the ratio of the total mass of dust estimated with and without submm data as a function of the oxygen abundance of the galaxy.
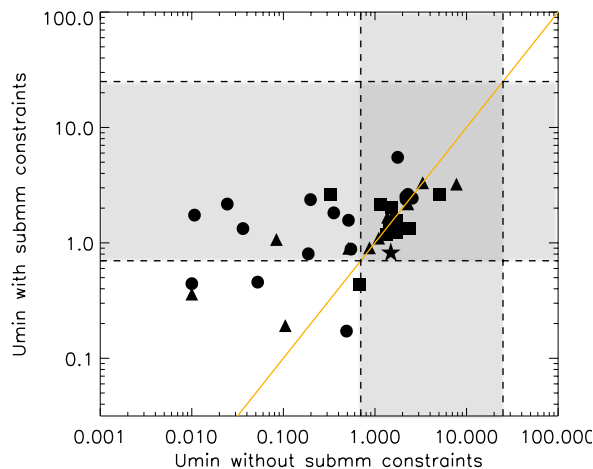
Figure 6.4. Minimum heating intensity derived from the SED model using submm data compared to minimum heating intensity determined without submm data. The orange line indicates the 1:1 relation. The dashed lines define the limits Draine et al. (2007) used as boundaries for their minimum heating intensity U_{min}. For convention on symbols, see Fig. 6.3.

when submm data are unavailable and that the SINGS-SCUBA sample could be biased in favor of increased dust mass and associated star formation. The restriction of the U_{min} interval is consistent with the type of galaxies they are observing but should be used with caution for other galaxies like dwarfs. We conclude that errors on the dust mass of galaxies (as given in Table 6.1) can be significant when submm data are not available for the SED modelling, especially for dustier galaxies.
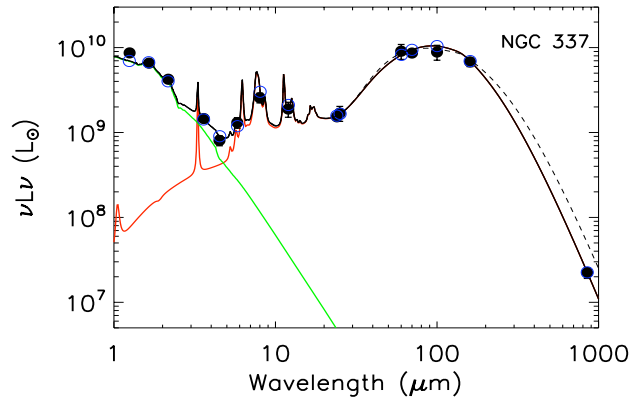
Figure 6.5. SED of the galaxy NGC 337 using the 850 μm SCUBA flux (solid line) and without the submm flux (dashed line). Observational constraints are superimposed (filled circles). Open circles are the expected modeled fluxes integrated over the instrumental bands. Green and red lines respectively distinguish the stellar and the dust contributions of the SED. This is a metal-rich galaxy which gives a lower total dust mass when the SED is constrained by submm.

For some galaxies, the dust masses estimated with submm observations are, on the contrary, higher than those determined without submm measures. Larger dust masses due to the addition of the submm data are usually observed in low-metallicity galaxies (Fig. 6.3). This increase of the total dust mass while using submm data was already mentionned in James et al. (2002). They observed some of the galaxies presented in Lisenfeld et al. (2001) with SCUBA and noticed an increase of the total dust mass of their galaxies when submm measures are used. As explained in their paper, the Lisenfeld et al. (2001) study was performed based on *IRAS* 60/100 μm fluxes only and could have underestimated the dust mass by missing dust at longer wavelengths.

Figure 6.3 also shows that an increase of the dust mass when submm measures are used can be observed in galaxies showing a submm excess (red symbols). Nevertheless, we can also observe that our modelling of the submm excess (addition of a modified blackbody with T=10K) does not systematically lead to an increase of the dust mass estimate. We note that a linear regression of the sample with and without galaxies modeled with an extra cold dust component leads to similar coefficients.

Table 6.1. Description of the sample and dust mass estimates with and without submm data

(1)	(2)	(3)		(4)		(5)		(6)		(7)		(8)			(9)		
		12+log(O/H)		S_{450}		S_{850}		log HI		log H_2		log $M_{dust\ no\ submm}$			log $M_{dust\ with\ submm}$		
Name	Distance	Value	Ref.	Value	Ref.	Value	Ref.	Value	Ref.	Value	Ref.	Value	unc		Value	unc	
	(Mpc)			(Jy)		(mJy)		$(M_\odot)$		$(M_\odot)$		$(M_\odot)$	$\%M_{dust}$		$(M_\odot)$	$\%M_{dust}$	
NGC 337	24.7	-	-	-	-	350	11	-	-	-	-	8.29	86%		7.7	23%	
NGC 2798	24.7	-	-	-	-	190	11	9.29	13	9.77	13	7.22	56%		7.23	26%	
NGC 4631	9	-	-	30.7	11	5730	11	10.09	13	9.49	13	9.36	60%		7.96	22%	
NGC 5195	8.2	-	-	-	-	260	11	-	-	8.55	13	6.43	97%		6.84	39%	
NGC 5713	26.6	-	-	-	-	570	11	9.93	13	10.02	13	8.31	44%		7.91	31%	
NGC 5866	12.5	-	-	0.8	11	140	11	<8.28	13	8.93	13	6.79	24%		6.50	10%	
NGC 520	27	-	-	-	-	325	2	9.54	20	9.54	21	7.55	49%		7.56	66%	
NGC 6240	98	-	-	1.0	4	150	4	9.95	22	10.5	22	8.25	19%		8.36	28%	
NGC 4569	20	9.3	64	-	-	470	11	8.80	13	9.97	13	8.84	25%		7.56	17%	
M83	4.5	9.2	47	-	-	-	-	9.71	15	9.69	16	8.31	30%		6.93	48%	
NGC 1808	11	9.1	48	8.13	9	1300	9	9.25	18	9.30	19	7.53	53%		7.49	61%	
NGC 7552	22.3	9.0	64	-	-	800	11	9.68	14	-	-	8.11	94%		7.87	21%	
NGC 1097	12	9.0	49	-	-	1440	11	9.71	23	9.01	24	8.07	47%		7.71	17%	
M82	3.6	9.0	50	49	1	-	-	8.95	25	9.11	26	6.66	19%		6.89	16%	
NGC 1068	15	9.0	51	-	-	-	-	9.35	27	9.69	28	9.52	88%		8.17	42%	
NGC 2903	6.3	8.94	46	7.94	9	2120	5	8.98	5	8.03	5	7.62	34%		6.86 [b]	41%	
NGC 4536	25	8.9	64	-	-	420	11	9.71	13	10.0	13	9.41	98%		7.71	18%	
NGC 891	9.6	8.9	45	-	-	-	-	9.88	22	9.69	22	7.69	23%		7.66	25%	
He 2-10	8.7	8.9	52	0.34	8	130	8	8.49	29	8.20	29	6.28	37%		5.74 [b]	46%	
IC 342	3.8	8.9	46	-	-	-	-	10.1	22	9.70	22	8.09	21%		<7.27	-	
MCG+02-04-025	122	8.87	5	-	-	390	5	9.24	5	-	-	7.69	33%		7.85	60%	
NGC 4303	15.2	8.84	46	4.6	9	1180	5	9.42	5	8.99	5	7.87	15%		7.32 [b]	4%	
NGC 7469	64	8.8	53	-	-	2640	5	9.18	5	9.80	5	8.84	31%		8.07	3%	
NGC 5256	109	8.75	5	-	-	820	5	0.00	5	10.24	5	8.21	10%		8.22	23%	
NGC 5953	26	8.73	5	18.5	11	1820	5	8.76	5	9.29	5	7.34	19%		7.28	14%	
NGC 6946	5.5	8.7	46	-	-	1200	11	9.49	5	8.72	5	7.30	6%		7.05	1%	
M51	8.4	8.7	54	-	-	15000	10	9.70	30	9.75	28	8.73	97%		8.51	34%	
NGC 3995	43	8.66	5	-	-	1260	5	9.79	5	-	-	7.57	57%		7.73	28%	
NGC 3994	41	8.61	5	-	-	1060	5	9.45	5	-	-	7.48	36%		7.50	37%	
NGC 6052	62	8.6	5	0.72	3	950	5	9.58	5	10.1	5	7.73	15%		7.76	24%	

Table 6.1. continued

(1)	(2)	(3)	(4)	(5)	(6)	(7)	(8)	(9)	(10)	(11)	(12)	(13)	(14)	(15)	(16)
NGC 4826	5.6	8.59	44	-	-	1230	11	8.49	14	9.03	14	7.73	84%	6.84	44%
NGC 1222	32	8.57	55	-	-	840	5	9.08	5	-	5	6.93	13%	7.10	22%
NGC 7674	113	8.56	5	-	-	1080	5	10.03	5	10.73	5	7.82	6%	8.07 [b]	13%
NGC 7714	37	8.5	56	-	-	72	2	9.91	32	9.34	32	7.26	28%	7.23	35%
NGC 1705	4.7	8.46	63	-	-	114 [a]	12	7.61	31	-	-	4.46	81%	5.23 [b]	28%
NGC 1705	4.7	8.46	63	-	-	114 [a]	12	7.61	31	-	-	4.46	81%	5.23 [b]	28%
NGC 3627	8.9	8.43	44	-	-	1860	11	8.88	13	9.76	13	7.92	91%	7.41	21%
Mrk33	20	8.4	57	-	-	40	11	8.47	33	8.64	34	6.67	15%	6.51	12%
NGC 3190	17.4	8.4	14	-	-	190	11	8.65	13	-	-	7.38	26%	7.05	22%
NGC 7331	14.7	8.36	44	20.6	11	2110	11	9.96	14	10.1	14	8.03	43%	7.97	13%
NGC 3521	9.0	8.36	44	-	-	2110	11	9.75	13	9.79	13	7.67	20%	7.54	23%
NGC 4670	11	8.3	17	-	-	49	5	8.22	5	8.10	5	5.90	32%	6.02	21%
NGC 2976	3.6	8.3	14	-	-	610	11	8.12	14	8.08	14	6.27	38%	6.18	35%
NGC 5253	3.2	8.2	58	-	-	180	7	7.96	35	7.00	36	6.15	69%	< 5.95	-
NGC 1569	2.2	8.2	52	1.33	6	280	6	8.11	37	7.70	38	5.24	64%	5.02 [b]	75 %
NGC 5929	33	8.18	5	-	-	1190	5	8.63	5	9.46	5	7.45	11%	< 7.34	-
NGC 1482	22	8.12	14	-	-	330	11	8.88	13	9.77	13	8.03	44%	7.40	39%
II Zw 40	10	8.1	59	0.24	8	87	8	8.62	22	7.36	22	5.56	56%	5.75 [b]	44%
UM 448	70	8.0	60	-	-	39	5	9.67	39	9.38	39	7.23	39%	7.54	51%
Mrk 1089	59.8	8.0	62	-	-	67.4 [a]	12	10.43	40	-	-	7.24	31%	7.72	20%
NGC 1140	25	8.0	58	0.27	8	69	8	9.71	41	-	-	6.61	29%	6.52 [b]	37%
Haro 11	92	7.9	42	-	-	40 [a]	12	8.0	42	9.0	42	6.90	45%	7.3 [b]	17%
I ZW 18	13	7.2	61	-	-	< 1.25	7	8.08	43	-	-	4.57	61%	< 4.74	-

Notes.- (1) Galaxy Name. (2) Distance to object. (3) Metallicity of the galaxy. (4) 450 μm flux. (5) 850 μm flux [^{a} 870 μm fluxes estimated through LABOCA observations]. (6) H I mass of the galaxy. (7) H_2 mass of the galaxy. (8) Total dust mass estimated from our SED modelling performed with measures below 300 μm. (9) Total dust mass estimated from our SED modelling performed with submm data [^{b} A cold dust component of 10K with an emissivity $\beta=1$ is added to the model to account for the submm excess].

References.- [1] Smith et al. (1990) - [2] Dunne et al. (2000) - [3] Dunne & Eales (2001) - [4] Klaas et al. (2001) - [5] James et al. (2002) - [6] Galliano et al. (2003) - [7] Hunt et al. (2005) - [8] Galliano et al. (2005) - [9] Stevens et al. (2005) - [10] Meijerink et al. (2005) - [11] Dale et al. (2007) - [12] Previous chapter - [13] Kennicutt et al. (2003) - [14] Draine et al. (2007) - [15] Tilanus & Allen (1993) - [16] Lundgren et al. (2004) - [17] Lisenfeld & Ferrara (1998) - [18] Dahlem et al. (2001) - [19] Dahlem et al. (1990) - [20] Bernloehr (1993) - [21] Yun & Hibbard (2001) - [22] Bettoni et al. (2003) - [23] Ondrechen et al. (1989) - [24] Gerin et al. (1988) - [25] Appleton et al. (1981) - [26] Walter et al. (2002) - [27] Staveley-Smith & Davies (1987) - [28] Helfer et al. (2003) - [29] Sauvage et al. (1997) - [30] Dean & Davies (1975) - [31] Meurer et al. (1998) - [32] Struck & Smith (2003) - [33] Thuan et al. (2004) - [34] Israel (2005) - [35] Reif et al. (1982) - [36] Meier et al. (2002) - [37] Stil & Israel (2002) - [38] Israel (1997) - [39] Sage et al. (1992) - [40] Williams et al. (1991) - [41] Hunter et al. (1994) - [42] Bergvall et al. (2000) - [43] van Zee et al. (1998) - [44] Walter et al. (2008) - [45] Otte et al. (2001) - [46] Pilyugin et al. (2004) - [47] Webster & Smith (1983) - [48] Ravindranath & Prabhu (2001) - [49] Storchi-Bergmann et al. (1995) - [50] Boselli et al. (2002b) - [51] Dutil & Roy (1999) - [52] Kobulnicky & Skillman (1997) - [53] Bonatto & Pastoriza (1990) - [54] Bresolin et al. (2004) - [55] Petrosian & Burenkov (1993) - [56] Gonzalez-Delgado et al. (1995) - [57] Mas-Hesse & Kunth (1999) - [58] Heckman et al. (1998) - [59] Pérez-Montero & Díaz (2003) - [60] Izotov & Thuan (1998) - [61] Izotov et al. (1999) - [62] Hopkins et al. (2002) - [63] Meurer et al. (1992) - [64] http://sings.stsci.edu/Sample/

6.4 Dust-to-gas mass ratio as a function of metallicity

6.4.1 Gas masses and metallicities from the literature

Values and references of the gas masses of our galaxies are given in Table 6.1. Both atomic and molecular gas masses are given when available in the literature and gas masses were evaluated using the same distances as those used to derive the dust masses. Note that some studies show that the X_{CO-H2} factor could be dependent on the metallicity (Wilson 1995; Israel 1997, 2000; Barone et al. 2000; Strong et al. 2004). In this study, the H_2 masses were derived from CO observations, using a standard X_{CO-H2} factor of 2×10^{20} cm^{-2}. Molecular gas masses obtained in the literature were rescaled to use to Galactic X_{CO} factor. The gas masses of the Draine et al. (2007) sample are, moreover, strongly dominated by the H I mass and the D/G derived should not normally depend critically on the H_2 mass estimate.

The metallicities of the galaxies are also given in Table 6.1 and were estimated in the different papers using standard R23 methods, except in some cases discussed in section 6.4.3. As mentioned previously in Chapter 2, Pilyugin & Thuan (2005) discuss the problem of empirical calibrations performed with strong oxygen line intensities / oxygen abundances relations. The choice of other methods should not affect the general trend of our sample but could, nevertheless, introduce a systematic offset in our metallicity values.

6.4.2 A revised relation

Figure 6.6 shows the D/G as a function of oxygen abundance. The D/G is estimated using the dust masses calculated without submm data in Fig. 6.6a and with submm data in Fig. 6.6b. The error bars indicate the errors on the dust mass estimated with our Monte-Carlo simulations. We separate the two plots for clarity. Figure 6.6c gathers the two previous plots. The dot-dash vertical lines indicate how galaxies 'move' on the D/G axis when submm measures are used in the dust mass estimation and clearly show that for dustier galaxies, submm data significantly affect the total dust mass estimates. The predictions of Edmunds (2001) and Dwek (1998) presented in section 6.1 are indicated on the plots. We also overlay the linear regression (dashed line) determined with the complete sample of galaxies observed with and without submm data (Figure 6.1).

Our sample restricted to the galaxies observed at submm wavelengths does not follow the general regression of the whole sample presented in Figure 6.1 as a dashed line. The D/G versus metallicity relation, in fact, tends to flatten when submm data are used in the SED modelling, with D/G of low-metallicity galaxies systematically higher that those determined without submm data. Furthermore, the use of submm measures significantly tightens the D/G vs metallicity relation and clearly decreases the error bars. Unfortunately, the current observations are still not sufficient to discriminate between the two models of Edmunds (2001), mainly due to the lack of low-metallicity galaxies observed at submm wavelengths linked with the difficulty in performing such observations. Newly available ground based submm instruments (e.g. SCUBA-2, LABOCA) would be necessary to observe more low-metallicity environments at better sensitivity. Furthermore, the *Herschel* Guarantee Time Key Program SAG2/Dwarf Galaxy Survey (PI: S.Madden), is dedicated to the observation of a wide range of low-metallicity environments with both PACS and SPIRE. These observations will enable us to extend our knowledge on the D/G vs metallicity relation to lower metallicities, using 70 to 500 μm data to constrain the submm slope of the SEDs.

6.4.3 Detailed discussion on the outlying galaxies

In this section, we discuss in detail the galaxies that deviate from the D/G relation with oxygen abundance (named in Fig. 6.6b).
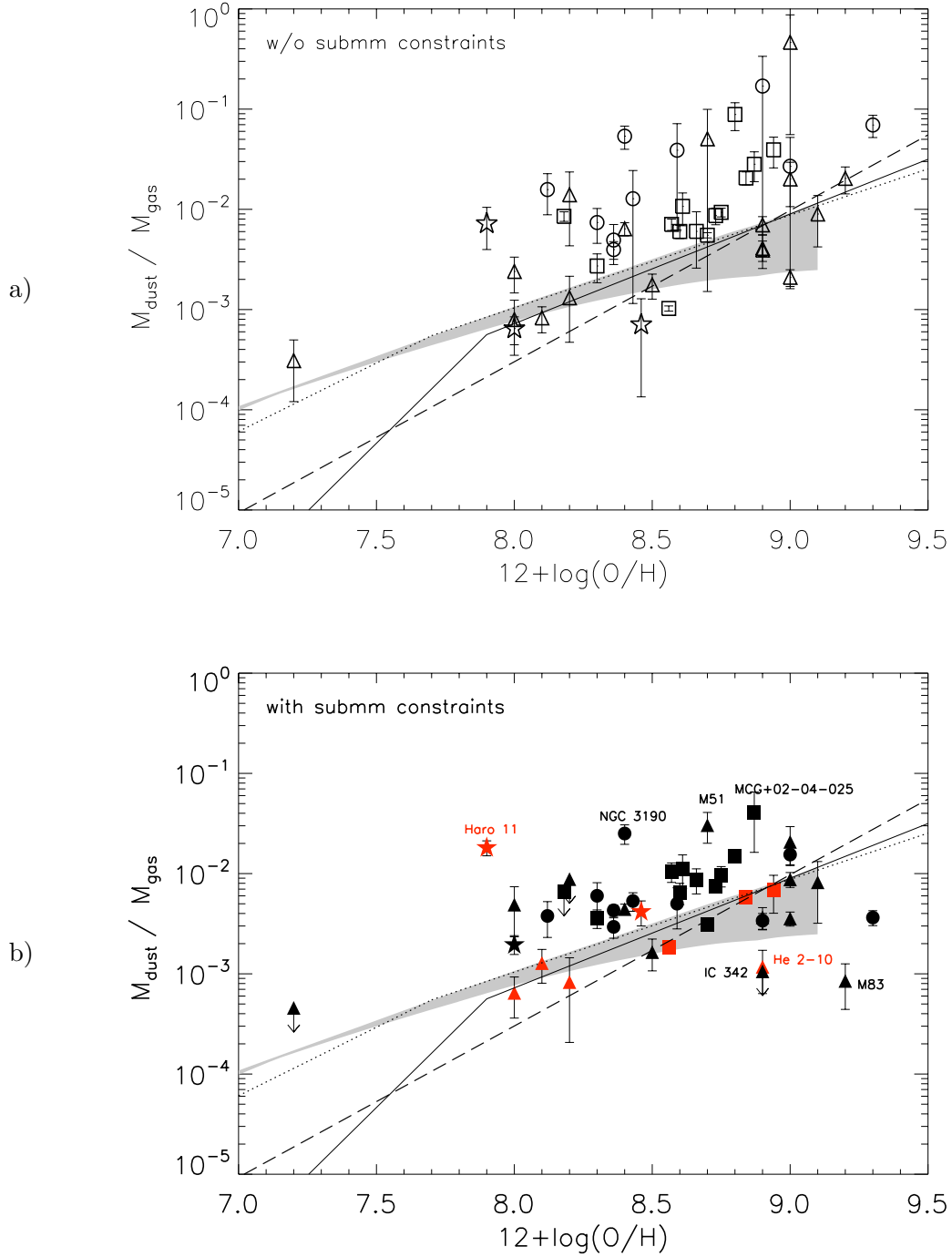
Figure 6.6. *a)* Dust-to-gas mass ratio as a function of oxygen abundance for our restricted sample of galaxies that were observed at submm wavelengths. For the convention on colors and symbols, refer to Fig. 6.3. In this plot, the dust masses of the galaxies are derived from our SED models without introducing submm measures. The solid line and the dotted line are the predictions of the dust formation models from Edmunds (2001). The gray stripe is the expectation of the one-zone, single-phase chemical evolution model of Dwek (1998). Both models are presented in section 6.1. The dashed line represents the linear regression of the broad sample of §6.1 where all galaxies, including those without submm data, are used. *b)* Same but the dust masses of the galaxies are derived from our SED models using submm measures. Labeled galaxies are discussed in section 6.4.3. Error bars do not take the gas mass errors into account. *c)* We gather the two previous plots to emphasize how the D/G 'moves' (dot-dash vertical lines) in the diagram when submm data are used to estimate the dust mass in the SED modelling.

c)
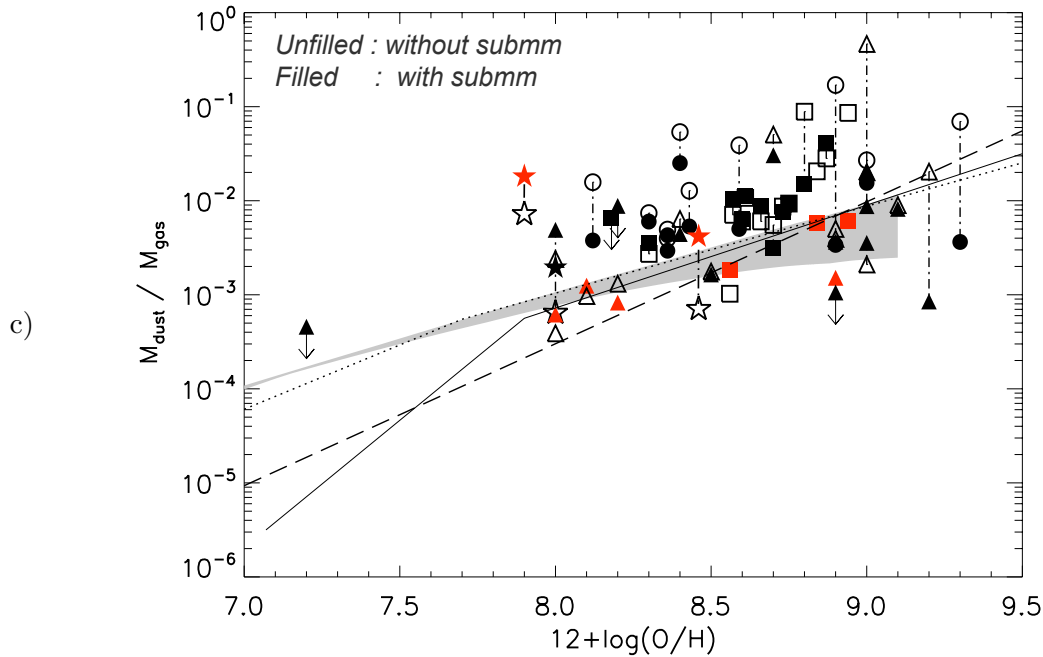
Figure 6.6. continued

MCG+02-04-025 - The H_2 mass was not estimated for the galaxy which implies that the presented D/G is an upper limit.

M51 - This galaxy has a unusually 'cold' global SED. Applying only *IRAS* constraints, the SED modelling gives much lower total mass of dust but the use of *Spitzer* data, especially the 160 μm of MIPS already significantly increases the dust mass, thus increases the D/G. There are still difficulties in estimating a global metallicity due to the extension of the galaxy and the fact that metallicity usually varies as a function of radius for spiral galaxies (e.g. Phillipps & Edmunds 1991; Issa et al. 1990). For M51, Moustakas & Kennicutt (2006) also estimated the metallicity to be 12+log(O/H)=8.7 using Pilyugin & Thuan (2005) but their estimate reaches 9.2 using the McGaugh (1991) strong-line calibration of the R_{23}. A higher average metallicity would, in fact, make the galaxy move rightward, close to the James et al. (2002) relationship but we prefer to keep the value 8.7 estimated by Bresolin et al. (2004), which is based on high-quality HII-region observations and calculated in the arms of the galaxy, where star-forming regions are concentrated. Nevertheless, M51 could have a strong gradient of metallicity, thus complicating the global values we use here.

M83 - This galaxy is surrounded by a very large H I envelope, with a radius superior to 125 kpc - 6.5 times the optical radius (Huchtmeier & Bohnenstengel 1981). The H I mass estimated by Tilanus & Allen (1993) covers a more extended region than that used to calculate the integrated flux in IRAC and MIPS bands and derived the total mass of dust, which can explain the low D/G found by Galliano et al. (2008). Lundgren et al. (2004) studied the kinematics of molecular gas of this galaxy with CO observations performed at SEST and estimate

the total gas mass, including H_2 and H I to be $\sim 7.8 \times 10^9 M_\odot$, close to that used by Galliano et al. (2008) for the D/G estimate plotted in Fig. 6.6. The metallicity we used here (12+log(O/H)=9.2) was determined by Webster & Smith (1983). More recently, Engelbracht et al. (2008) estimated the oxygen abundance of M83 to be 12+log(O/H)=8.62, using the direct electron-temperature (Te) method applied to individual H II regions by Skillman et al. (1998). This newly estimated metallicity would bring the galaxy closer to the model predictions.

IC342 - Its location at low Galactic latitudes makes it difficult to study because of its large extent. It is also affected by foreground extinction due to our Galaxy and the background subtraction issues it generates. This galaxy possesses a very peculiar optical/near-IR shape (see Galliano et al. 2008).

He 2-10 - This Blue Compact Dwarf (BCD) differs from other BCDs because of its near solar metallicity (Kobulnicky & Johnson 1999) and contains a relatively large amount of molecular gas (Meier et al. 2001), which is unusual for low-metallicity dwarf galaxies. Nevertheless, the metallicity of the galaxy is rather uncertain due to the lack of measured [O III] $\lambda4363$.

NGC 3190 - No H_2 mass estimates have been obtained in NGC 3190. The value presented on the plot is thus an upper limit. An amount of molecular gas equivalent to that of the H I mass would lead to a higher D/G.

6.4.4 Discussion of the D/G of our sample observed with LABOCA

Here we study the D/G of the dwarf galaxies presented in Chapter 5.

NGC 1705 - This galaxy is surrounded by a very large H I envelope up to 10 times larger than the optical extension (see Fig. 5.1), which is commonly observed in dwarf irregular galaxies (e.g. Wilcots 2001). From the H I integrated map of NGC 1705, we estimate that only 80% of the total H I flux is contained in the aperture we chose to derive our dust mass. We then consider that only 80% of the H I mass, i.e $4.1 \times 10^7 M_\odot$, should be used for the D/G estimate. The D/G of NGC 1705 estimated using the dust mass derived with an extra cold dust component (β=1) is $\sim 4.1 \times 10^{-3}$ (Table 5.5). This value compares to that expected by the chemical evolution model of Dwek (1998) used in Galliano et al. (2008) for a galaxy with the metallicity of NGC 1705 ($2 \times 10^{-3} < D/G < 5 \times 10^{-3}$). The solution for β=2, obtained with a slightly higher $\bar{\chi}^2$, leads to a D/G of 2.8×10^{-2}, which is a factor of 8 higher than that of β=1. This high D/G value would be difficult to reconcile with chemical models. The use of β=1 seems to be the more likely emissivity value to explain the submm excess and remain consistent with what can be expected from chemical evolution models.

Haro 11 - The D/G is very extreme (~ 0.2) when a very cold dust component of β=1 is used (Table 5.5). If we were to use an emissivity index of 2 for the very cold grains, the D/G derived is even higher and not physical considering the lack of metals in the galaxy. Here again, β=1 seems to lead to results more consistent with the chemical evolution models, even if the D/G derived with this emisivity index is still too high compared to realistic values. Indeed, for such a low-metallicity (12+log(O/H) = 7.9), a D/G of $\sim 10^{-3}$ should be more likely considering chemical evolution models. Our high values for the D/G, constrained by the new submm data, are not easily explained with current models.

Haro 11 is a peculiar case. The H I mass used for our calculation is an upper limit of 10^8 $M_\odot$ given in Bergvall et al. (2000). Bergvall & Östlin (2002) already note from their VLA observations that Haro 11 is dramatically deficient in neutral hydrogen. The mean H I mass for BCGs of the size of Haro 11 should be $\sim 8.1 \times 10^8$ $M_\odot$, following Gordon & Gottesman (1981) results. If we consider that the existing H I observations provide a reliable upper limit on the mass of atomic hydrogen (Bergvall et al. 2000), the large estimated dust mass may suggest that the H I mass is not sufficient to account for the total gas mass of the galaxy and that a significant fraction of the total gas mass should reside in molecular and ionized forms. Bergvall & Östlin (2002) derived an upper limit of 10^9 for the H_2 mass from their CO(1-0) observations (Galactic conversion factor between H_2 and CO) carried out with the Swedish-ESO Submillimetre Telescope (SEST) telescope, increasing the total gas mass by a factor of 10. An upper limit of 10^9 $M_\odot$ is also determined for the H_2 mass traced by the [CII] 158 μm line (Bergvall et al. 2000). Finally, Östlin et al. (1999) estimate the ionized gas to be $10^9 M_\odot$ from the kinematics (rotation curves) of the galaxy, a similar order of magnitude as that suggested for the molecular gas. Nevertheless, these accumulated gas masses (and we remind the reader that they are already upper limits) are still not sufficient to reach reasonable D/G.

CO is known to be a poor tracer of molecular gas in low-metallicity environments due to the high excitation and density of these environments and the small filling factor of the molecular clouds. Self-shielding can be extremely efficient for H_2 in regions where CO is photodissociated. Furthermore, the CO to H_2 conversion factor is usually calibrated with cold ($\approx$ 12K) Galactic clouds (solar metallicity) and may not necessarily resemble the physical conditions of our low-metallicity galaxies. Some studies show that this conversion factor can be far higher in low-metallicity environments than in metal-rich ones (Wilson 1995; Madden et al. 1997; Leroy et al. 2005, 2007). In the event much of the ISM is in dense gas, CO is finally a poor tracer of dense gas. Molecules like HCN can be appropriate to trace an additional amount of dense gas within the galaxy. We conclude that current observations are probably 'missing' a non negligeable amount of molecular gas not traced by CO (e.g Poglitsch et al. 1995; Madden et al. 1997). In order to reach the D/G value expected by chemical models, a large mass of molecular gas would be required, namely $\sim 10^{10}$ $M_\odot$, that is to say an order of magnitude more molecular gas than that deduced from current CO upper limits. One scenario could be that the cold dust is residing in small molecular/cold dust cores embedded in [CII] emitting envelopes, where the H_2 can be self-shielded from UV radiation which photodissociates the CO. *Herschel* observations of the far-IR fine structure cooling lines such as [CII] and [OI] will help ellucidate the molecular gas reservoir. High values of L([CII])/L(CO) have been found in low-metallicity galaxies, sometimes up to 10 times higher than normal dusty starbursts or spirals (Madden et al. 1997; Madden 2000). The high [CII] emission compared to the CO upper limit of Haro 11 ($\geq 10^5$; Bergvall et al. 2000) is consistent with this theory and suggests that the galaxy may possess a clumpy ISM.

The high dust mass derived from our modelling compared to the gas mass estimate of Haro 11 could also suggest that the scenario of cold dust may be physically inappropriate for this galaxy, as suggested in previous studies (Lisenfeld et al. 2001; Dumke et al. 2004; Bendo et al. 2006; Zhu et al. 2009). Nevertheless, in the particular case of Haro 11, we have shown, in Chapter 5, that, even taking all the contributions of gas into account in the total gas mass estimate, the galaxy is an outlier of the Schmidt law (Kennicutt 1998), thus suggesting by an other independent method that a large amount of gas is indeed not 'detected' by current observations in Haro 11.

Mrk 1089 - Our SED model estimate of the D/G leads to a value of 1.9×10^{-3}. For a galaxy

with the metallicity of Mrk 1089 ($\sim$ 12+log(O/H)= 8.0), the chemical evolution model of Dwek (1998) used in Galliano et al. (2008) which links the D/G with metallicity, leads to an estimated D/G of $\sim 10^{-3}$, consistent with the value we obtain to within a factor of 2.
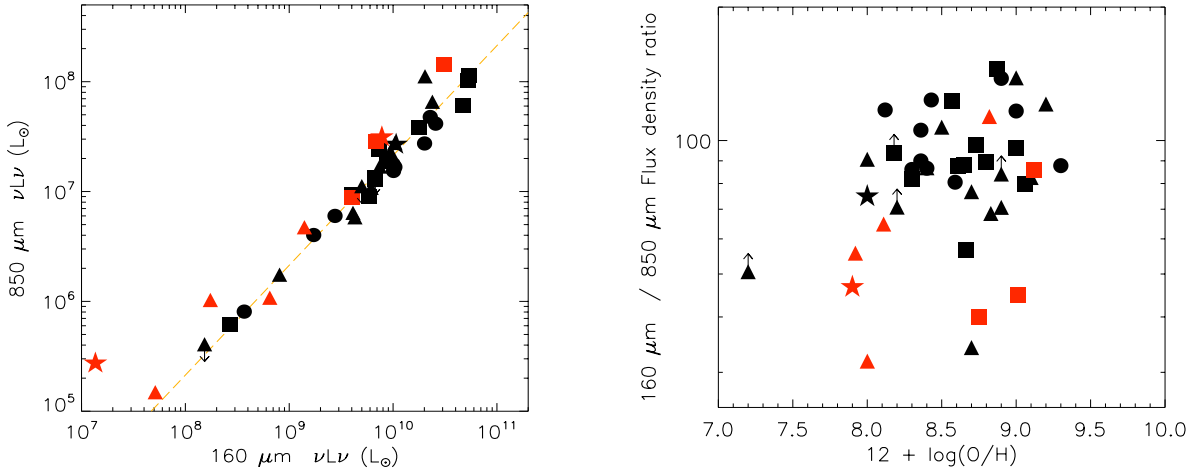
Figure 6.7. *Left:* Correlation between the 160 μm and the 850 μm fluxes of the galaxies. A linear regression is overlaid (dashed line). When the galaxies do not possess an observational flux at 850 μm, the flux value was deduced from the SED model. *Right:* 160 μm / 850 μm flux density ratios as a function of metallicity. For convention on colors and symbols, see Fig. 6.3.

6.5 Very Cold Dust

To study the physical conditions leading to an excess emission in submm, we plot the 850 μm flux as a function of the 160 μm flux (Fig. 6.7). When the fluxes are not directly observed, values are derived from the SED models we generated. Red symbols identify galaxies showing a submm excess and whose SED was modeled with an additional very cold dust (10K) component. While other galaxies follow a tight correlation, galaxies with submm excess present a 160-850 correlation that seems to be shifted. Figure 6.7 shows the 160 μm / 850 μm flux density ratios as a function of metallicity. The 160 μm to 850 μm flux ratio is lower for galaxies in which a submm excess is detected but no clear correlation is found at this point with metallicity. Nevertheless, the sample is clearly lacking very low-metallicity galaxies (12+log(O/H)<7.9), which prevents us from studying submm excess with an unbiased metallicity coverage. We also note that a submm excess is detected in some dustier galaxies and usually appears when the 160 μm to 850 μm flux density ratio is below $\sim$ 65.

Why is the submm excess, in most cases, detected in low-metallicity galaxies? If we assume that this excess is due to very cold dust, could it be possible that very cold dust is more apparent in dwarf galaxies compared to more metal rich galaxies? Indeed, on average, global SEDs of BCGs generally peak at relatively short wavelengths (30-60 μm), compared to quiescent higher metallicity sources. For a metal-rich galaxy, peaking around 100 μm for example, the submm emission at 870 μm should be very difficult to distinguish from the emission of warm grains while in the case of a low-metallicity galaxy peaking shortward, the separation between two types of grain population temperatures, one warm and one very cold, may be easier to detect. We test this idea by modelling four galaxies with different metallicities (M51, M82, SBS 0335-052, Haro 11), supposing that the mass and the

properties (β, T) of the very cold dust (VCD) is everywhere the same (M_{VCD}/M_{dust}=constant). These tests lead to the inverse conclusion. The difference in the temperature of dust grains and very cold grains is smaller in galaxies having a solar metallicity in our hypothesis. With a constant mass ratio, the emissivity ratio between the two components is thus higher in these galaxies than in low-metallicity galaxies. If a very cold dust component exists with the same characteristics, it should be more evident, i.e. more easily shown by submm observations as excess in the SEDs, in dustier galaxies rather than in low-metallicity galaxies.
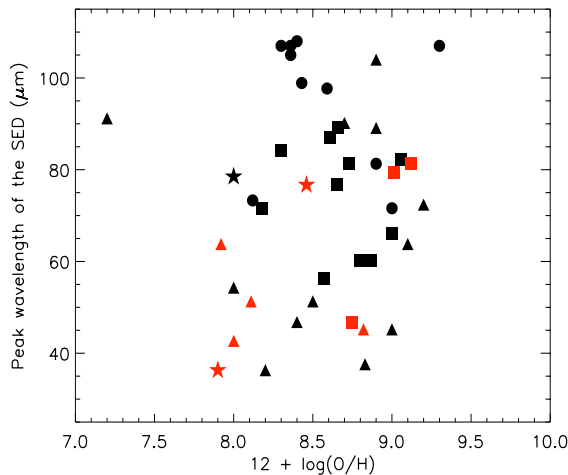
Figure 6.8. Wavelength of the peak of the dust emission as a function of metallicity. For convention on colors and symbols, see Fig. 6.3.

The SEDs of low-metallicity galaxies usually show relatively 'warm' ($f_{70}/f_{160} > 1$) dust temperatures. For these 'warm' galaxies, the temperature of the SED is then well constrained but the flux at 870 μm will significantly influence the total amount of dust while in 'colder' galaxies ($f_{70}/f_{160} < 1$), the SED model without submm already leads to a large amount of dust. We plotted the ratio of the dust mass obtained with submm data over the dust mass without submm observations as a function of f_{70}/f_{160} but did not find any correlation for our galaxies. We also plot the wavelength of the IR peak as a function of metallicity in Fig. 6.8. We do not clearly detect a correlation between the position of the dust emission peak and the metallicity of the galaxy. However, we note that submm excess is not detected when the SED peaks above 85 μm.

In some galaxies, the fact that submm excess is not detected could also be due to an underestimation of the submm fluxes due to background subtraction issues (e.g. NGC 6946) or a lack of coverage of the complete emission in the submm observations (e.g. NGC 1097). Having several observational constraints in the submm slope of the SED would also help us to be more confident about the presence of a submm excess: as shown in Fig. 6.2, most of the galaxies where submm excess was detected were actually observed at different submm wavelengths (at 450 and 850 μm). The addition of submm limits will be the solution to avoid biases and sample 1- a possible knee in the submm emission 2- a smoothness of the far-IR/submm slope, that could favor one of the two possible theories to explain the excess: a cold dust population or a change in the dust emissivity. The *Herschel* telescope, and more specifically the SPIRE instrument observing from 250 to 500 μm, will better constrain the submm slope and the peak of the very cold dust emission if present. Combined with submm fluxes, a few galaxies may reveal a cold dust component not detected due to the lack of sufficient current measures.

Additionally, having the spatial resolution *Herschel* provides in mapping the nearest sources (e.g. the Magellanic Clouds) will allow us to zoom in on the cold dust component. These galaxies are well studied at all wavelengths and also have complete atomic and molecular gas observations to study the spatial variations in the D/G within galaxies.

6.6 Conclusions

In this study, we have gathered observational constraints of a large sample of galaxies from low-metallicity to metal-rich environments to focus on the influence of submm data on the total dust mass estimates. Indeed, submm observations probe the coldest dust grain emission of galaxies, a component that could account for a signicant mass of the total dust mass of galaxies. We derive the total dust mass of our sample with and without submm limits in our SED models. For 8 galaxies, our fiducial model can not fit the FIR data and the submm fluxes together and a submm excess is apparent. We model this excess with an independent cold dust modified blackbody with a temperature of 10K and a dust grain emissivity of 1. The error bars on the total dust mass estimates signicantly decrease when using submm fluxes. Submm data clearly affect the dust mass derived for our galaxies for different reasons:

1) for dustier galaxies for which the SED usually peaks at longer wavelengths, submm fluxes are crucial to position the peak and constrain the submm slope of their SED, thus the dust temperatures.

2) for low-metallicity galaxies, the submm wavelength domain often harbours an excess that may imply a large amount of very cold dust. Nevertheless, we show that submm excess is not only detected in low-metallicity galaxies.

We have also estimated the D/G of our sample. We find a tightened relation between the D/G and the metallicity of the galaxies while using submm data. More submm observations of low-metallicity galaxies would be necessary to extend the coverage to a broader range of metallicity, and especially study how the relation evolves in metal-poor environements.

Chapter 7

Resolving the cold dust in the LMC / N159 star forming region

Contents

7.1 Aim of the study

The Large Magellanic Cloud (LMC) and the Small Magellanic Cloud (SMC) are perfect laboratories to study the lifecycle and recycling of the interstellar matter in detail. They are our closest neighbours after the Sagittarius and Canis Major dwarf galaxies (50kpc in Schaefer (2008) for the LMC; 61kpc in Szewczyk et al. (2009) for the SMC). Current IR instruments enable us to resolve, across a wide range of wavelengths, the different substructures of the ISM (HII regions, molecular clouds, diffuse emission) and to link them with the stellar population and the sites of star formation activity.

The LMC lies in a nearly face-on plane and has an irregular structure, with an off-center bar and a lack of stellar spiral morphology. It is a low-metallicity galaxy, with Z $\sim$ 0.3-0.5 $Z_\odot$ (e.g. Dufour et al. 1982). This metallicity is similar to the mean metallicity of the ISM during the epoch of peak star formation in the Universe (z$\sim$1.5 Madau et al. 1996).

The LMC was observed with the *Spitzer* telescope as part of the SAGE (Surveying the Agents of Galaxy Evolution) project (Meixner et al. 2006). The observing strategy and the data analysis of the *Spitzer* data are also explained in detail in Meixner et al. (2006). Figure 7.1 shows a *Spitzer* 3-color image of the LMC, revealing 3 different galactic components: the stellar bar appears in blue, observed with IRAC at 3.6 μm; MIPS 24 μm traces the star forming regions of the galaxy (in yellow); the cooler phases of dust are traced by the MIPS 160 μm observations (in red). The morphology of the galaxy clearly evolves as a function of wavelength. The main contributors to the IR emission are the HII regions, especially the 30 Doradus (30 Dor) complex, which is the brightest HII region of the Local Group ($\sim$ 20 % of the L_{FIR}, Aguirre et al. 2003). It is part of a large region in the northeast edge of the LMC bar in which star formation has been active for 10^8 yr.

A SED model of the integrated emission of the LMC was already analysed by Bernard et al. (2008) using IRAS, DIRBE, IRAC and MIPS data. This global SED was compared to those of the SMC and the Milky Way. Bernard et al. (2008) detect an excess at 60 and 70 μm. Similar results were previously found in the LMC by Sauvage et al. (1990) with *IRAS* observations but also in the SMC (Bot et al. 2004). This excess seems to increase from the Galaxy to the SMC, suggesting a possible dependence with metallicty. Moreover, the mid-IR slope of the SED is steeper in the SMC and the LMC than in the Milky Way, implying that the two low-metallicity galaxies could show different small grain distributions, which are partly responsible for the mid-IR emission. They also studied the distribution of the temperature of big grains using the ratio of the MIPS 160 μm and the IRAS image at 100 μm. They note that detecting the presence of cold dust at very low temperature (T < 10K) in the LMC would require submm observations, eventually with *Herschel* via the HERITAGE key program (Meixner et al. 2010).

The aim of this study is to locally probe the dust grain properties, the temperature (warm, cold and very cold dust) within the galaxy and compare the results with the global properties we derived from our previous studies on global galaxies. We chose to focus on a very bright star forming region, the N158 / N159 / N160 complex, that was already observed in all *Spitzer* bands as part of the SAGE project. We complete the data coverage of the SED adding submm observations with 870 μm LABOCA data, observations that will enable us to constrain, for the first time at this resolution, the coldest phase of the dust. As these regions are well studied in atomic and molecular gas, we should be able to estimate directly D/G. We aim also to explore the possibility of hidden molecular gas not detected by CO, but possibly revealed through the dust measurements.

The N158 / N159 / N160 complex is situated at $\sim$ 600 pc in projection south of the 30 Doradus region. It extends over $\sim$ 22' ($\sim$ 330 pc) with, from north to south, N158, N160 and finally
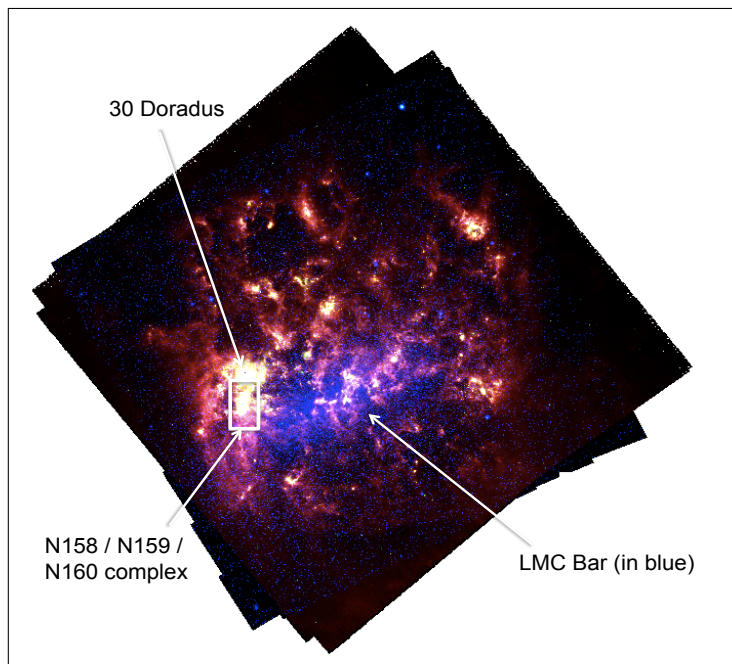
Figure 7.1. 3-color image of the Large Magellanic Cloud observed with *Spitzer*/IRAC at 3.6 μm (in blue), *Spitzer*/MIPS 24 μm (in yellow) and MIPS 160 μm (in red). The star forming region N158/N159/N160 that we are studying in this chapter is indicated by the white box.

N159 (see Fig. 7.3). The H$_{II}$ regions N159 and N160 were first catalogued in Henize (1956). The entire complex also contains a large reservoir of CO (Cohen et al. 1988; Bolatto et al. 2000; Pineda et al. 2008). An evolution of the star formation activity is observed with extremes from north to south. In the North, the evolved starburst of 30 Dor dominates and the molecular cloud seems to have dissipated. In N160, massive star formation is also well evolved and molecular clouds have mostly been photodissociated or have dissipated. Further south, in N159, we observe strong star formation still surrounded by molecular gas. The first extragalactic protostar was found in N159 (Gatley et al. 1981). From IRAC observations, Jones et al. (2005) found that the morphology of N159 is consistent with a wind-blown bubble of 1 or 2 Myr that has initiated star formation. This star formation occurs now on the rim of the region. The complex finishes with a quiescent region usually called N159S where little star formation is observed (Cohen et al. 1988). This region is located at the border of the 30 Dor CO ridge, a large front of molecular gas situated at 1° from 30 Dor.

This study is still a work in progress but here, I present some initial results.

7.2 Optimisation of the LABOCA data reduction for extended sources

The LABOCA observations of the N158 / N159 / N160 complex were taken in a spiral mapping mode between the 7th and the 18th of August, 2008 in a large ESO program of which 35.5 hours covered 35' × 28' of this star forming complex (PI: S. Hony).

To reduce the data of N159, we first applied the same steps as those applied for the observations of point sources (see Chapter 3). For extended sources such as N159, the presence of very bright structures in the map often leads to negative artefacts in their surroundings (Fig. 7.2a). These structures are 'created' numerically during the correction of correlated noise or the subtraction of the median baselines (artefacts that are also observed in *Herschel*/PACS maps - see Chapter 8).

A solution to reduce these artefacts is to mask the bright structures and to iterate to improve on the reduction. First, we generate the initial map using the steps described in Chapter 3. This basic map will be used to define a source model. Pixels whose values are superior to a given Signal-to-Noise in this map are isolated in a mask. We then subtract this model from the data and perform a new skynoise reduction. We finally re-add the model to obtain a new reduced map. This new map can then be used as a model for another iteration. The process is repeated until the model and the flux of the peaks converge. We will describe the main steps of this iteration process.
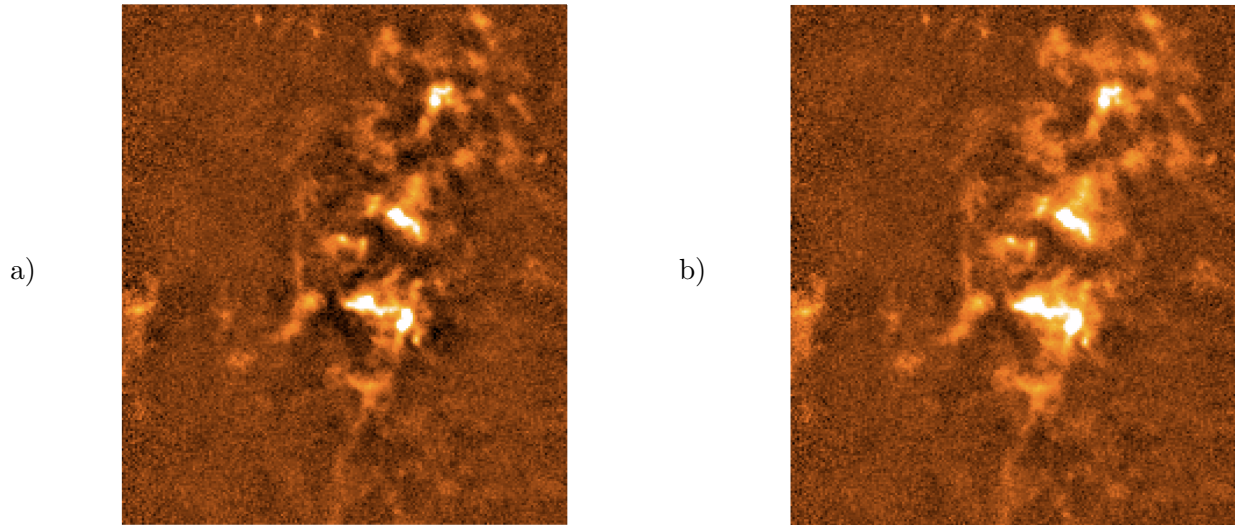
Figure 7.2. The star forming complex N158-N159-N160 located in the Large Magellanic Cloud observed with LABOCA. *a)* The data reduction is performed without masking the bright structures during the reduction. *b)* Bright structures are masked during the reduction. The image is the result of 10 iterations of the masking procedure. This procedure improves the signal-to-noise ratio of the extended emission.

Steps of the iterative pipeline:

Restore the basic reduction (or of a previous iteration).

```
model=newRestoreData('./N159_map.sav')
```

Define the mask. Pixels superior to a given threshold are put to 1, others to 0. 'snr' is the signal-to-noise ratio, 'nbX' and 'nbY' are the dimensions of the map.

```
snr = copy.deepcopy(model)
mask=copy.deepcopy(model)
snr.Data = model.Data * sqrt(model.Weight)
nbX,nbY= shape(model.Data)
threshold=3.
for i in range(nbX):
    for j in range(nbY):
        mask.Data[i,j]=0
for i in add(range(nbX-2),1):
```

```
    for j in add(range(nbY-2),1):
        if (snr.Data[m+i,n+j] > threshold):
            mask.Data[m+i,n+j]=1

    # Define the model

for i in range(nbX):
    for j in range(nbY):
        model.Data[i,j] = model.Data[i,j]*mask.Data[i,j]
```

The first steps of this new reduction are identical to the initial reduction but the model is subtracted from the data after the calibration steps.

Define the parameters necessary to access the data within the cube

```
chanList = data.BolometerArray.checkChanList('all')
chanListIndexes = data.BolometerArray.getChanIndex(chanList)
XYOffsets = array([data.ScanParam.get('RA',flag='None'),
                   data.ScanParam.get ('Dec',flag='None')])
rotAngles = array(data.ScanParam.ParAngle)
chanListAzEl = array(data.BolometerArray.UsedChannels)-1
OffsetsAzEl=array((take(data.BolometerArray.Offsets[0,:],chanListAzEl),
                   take(data.BolometerArray.Offsets[1,:],chanListAzEl)))
refChOffsets=data.BolometerArray.Offsets[:,data.BolometerArray.RefChannel-1]
AXIS1 = array([model.WCS['NAXIS1'],model.WCS['CRPIX1'], model.WCS['CDELT1'],
              model.WCS['CRVAL1'],1.])
AXIS2 = array([model.WCS['NAXIS2'],model.WCS['CRPIX2'], model.WCS['CDELT2'],
              model.WCS['CRVAL2'],1.])
```

Subtract the model with the function *addsource* and the parameter '-1'

```
tmp = fMap.addsource(chanListIndexes, data.Data, model.Data,XYOffsets,
                OffsetsAzEl, rotAngles, refChOffsets,AXIS1, AXIS2, -1)
data.Data = tmp
```

We repeat the treatment of the correlated noise, spikes and baselines as described in Chapter 3. We finally re-add the source and save the new map.

```
...
tmp = fMap.addsource(chanListIndexes, data.Data, model.Data,XYOffsets,
                OffsetsAzEl, rotAngles, refChOffsets,AXIS1, AXIS2, 1)
data.Data=tmp
```

We then repeat the process using this second reduced map as a model etc. 10 iterations were applied for the N159 map. Iterations lead to a significant retrieval of extended emission around the bright structures (Fig.7.2).
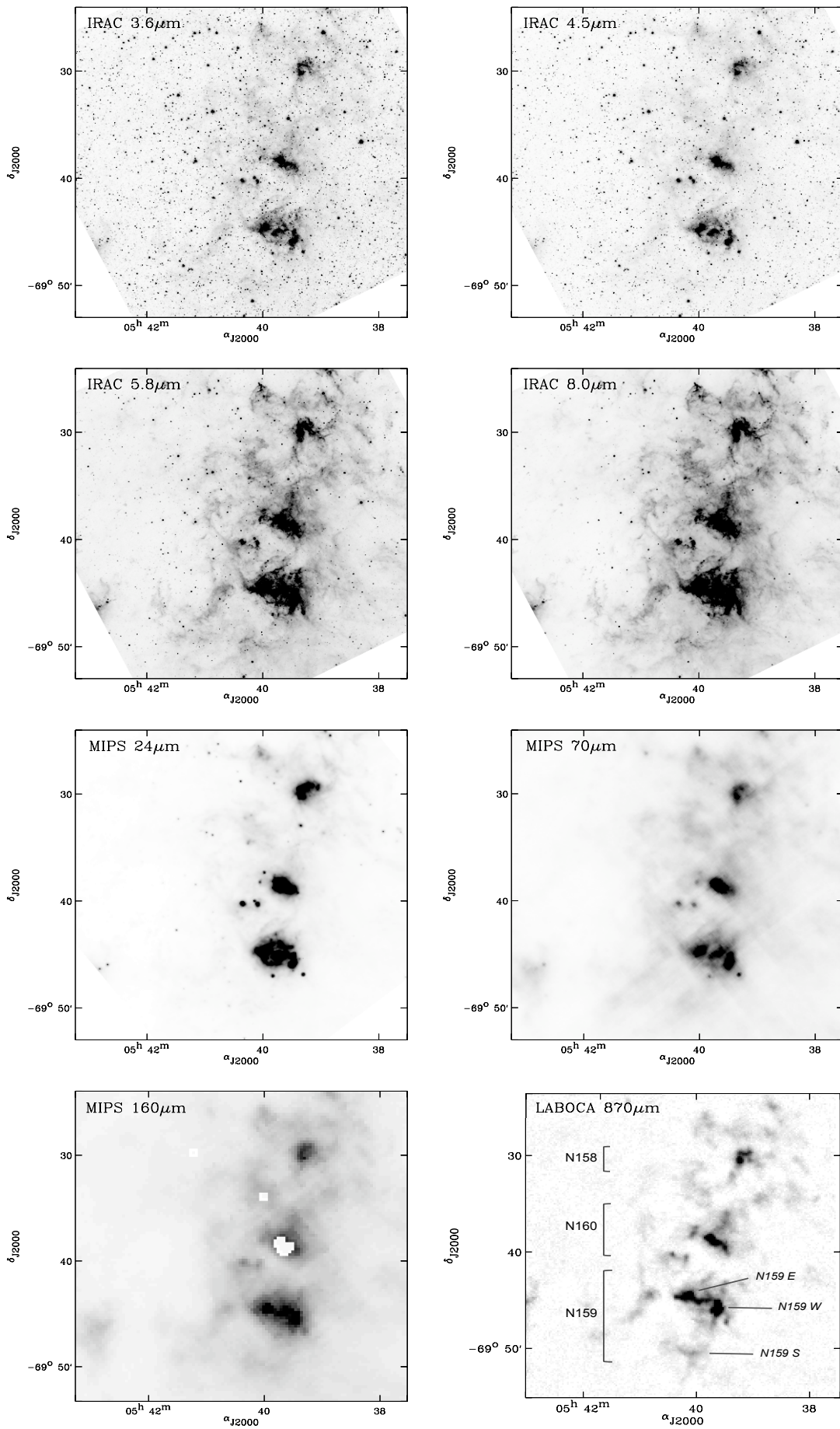
114

Figure 7.3. The N158 / N159 / N160 complex observed with Spitzer and LABOCA from 3.6 to 870 μm.

7.3 Dust properties across the region

7.3.1 The maps

The *Spitzer* (3.6, 4.5, 5.8, 8, 24, 70 and 160 μm) and LABOCA (870 μm) maps of the whole complex plotted together clearly show the difference in emission from the near to far-IR (Fig. 7.3). The main HII regions of the complex are named on the LABOCA map. The first two bands of *Spitzer* reveal the stars while the 8 μm map traces the diffuse dust emission and PAHs and its large extension. The MIPS 24 μm observation seems to be more compact and mainly located toward the center on the bright star forming HII regions. Note that the N160 region is saturated at 160 μm.

Figure 7.4 shows in particular the LABOCA contours overlaid on the IRAC 8 μm image. Features of the two maps coincide very well. We clearly resolved the emission of the bright star forming regions of the complex with LABOCA but also amazingly detect and resolve the diffuse emission at faint levels. Several authors, like Haas et al. (2002), already observed a spatial correlation between the PAH features traced by the 8 μm observations and the peaks of 850 μm surface brightness for a wide range of galaxy types, suggesting that PAH excitation could be caused by a distributed population of stellar FUV-emitters and not just due to star forming regions alone (Whaley et al. 2009) or that the local 850 μm flux essentially comes from the inside of the molecular clouds whose surfaces produce the PAH features (Sauvage et al. 2005).

These data will allow us to determine the precise correlation and conditions between the PAHs, presumably originating from the PDRs around molecular clouds and the coldest dust emission. Additionally, it will allow us to get a better total handle on the gas reservoir since the CO-to-H$_2$ is unknown in low-metallicty regions or rather ambiguous.

7.3.2 Selected regions and flux densities

We want to study local SEDs to first deduce information on dust properties across this complex. We selected individual apertures across the region. These selected apertures are shown in Fig. 7.5 (left). Circles indicate the size of the photometric apertures we used. The selected regions gather the bright star forming regions of the complex as well as diffuse emission between and around these regions. Table 7.1 describes in more detail the centers and sizes of the photometric apertures selected.

We convolved all the images to the lowest resolution, that of MIPS 160 μm (40"). As the bright star forming region N160 (Region 2) is saturated at 160 μm, we convolve all images to the resolution of LABOCA to extract the flux densities linked with N160 at each wavelength. Flux densities for 2MASS, IRAC, MIPS and LABOCA bands can be found in Table 7.2.

We also want to estimate the non-dust contribution to the LABOCA fluxes. 4.8 and 8.6 GHz images of the entire LMC have been obtained by Dickel et al. (2005) using the Australia Telescope Compact Array (ATCA). These observations reveal a strong radio emission in 30 Dor (peak of the radio emission of the entire LMC) but also in the 3 bright star forming regions N158, N159 and N160 we are studying, more specifically the regions we numbered 1, 2, 3 and 6. Figure 7.5 (right) shows the radio map of the complex observed by ATCA at 4.8 GHz. We estimated the radio (4.8 and 8.6 GHz thus respectively 6.25 and 3.5 cm) fluxes within our apertures for the 4 regions showing radio emission. With these two constraints, we perform a regression ($L_{radio} \propto \nu^{-1}$) and estimate the radio contamination in the LABOCA band at 870 μm. We estimated the contamination to be 14 %, 22 %, 40 % and 30 % in the regions 1, 2, 3 and 6 respectively and 11 %, 18 % and 30 % in
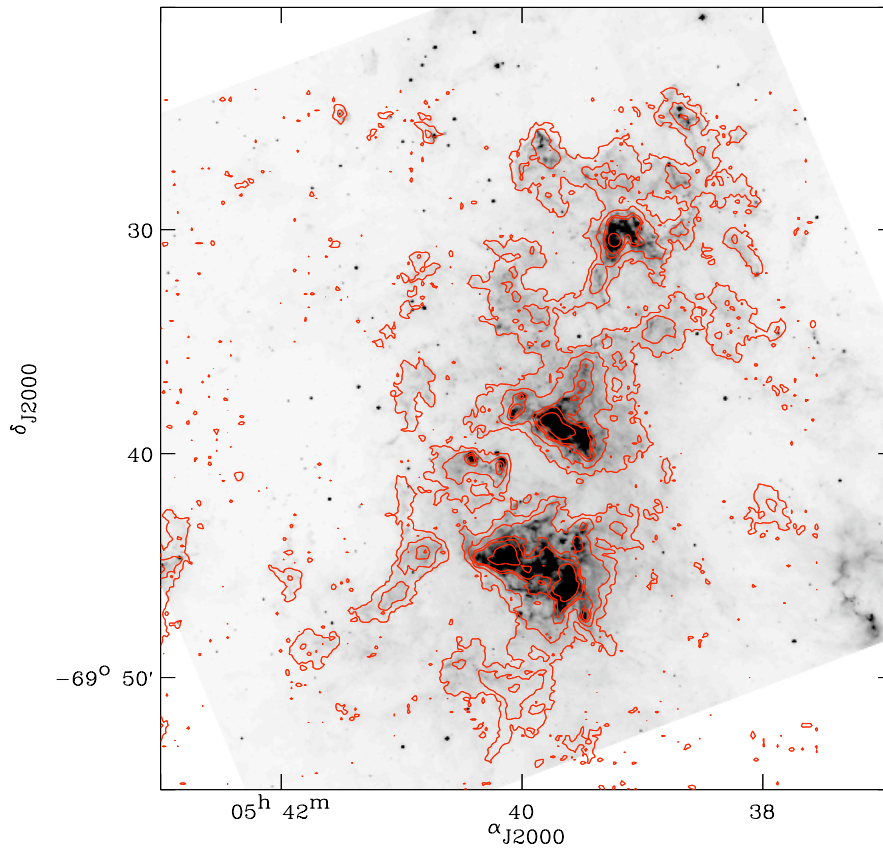
Figure 7.4. LABOCA 870 μm contours overlaid on the IRAC 8 μm observation. The contours are at 15, 55, 125, 165 and 300 mJy/beam.
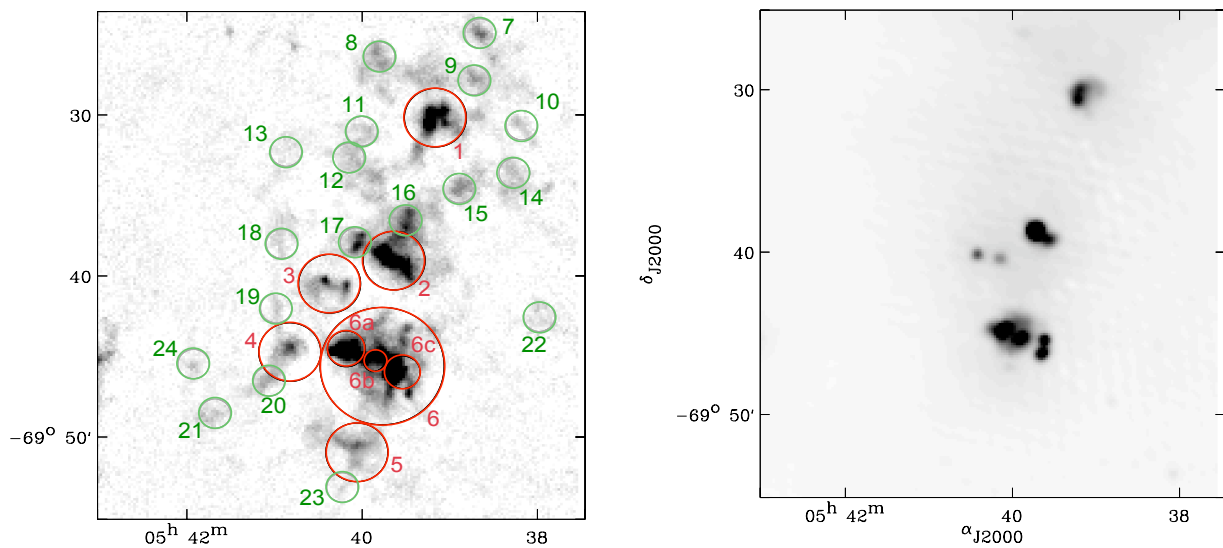
Figure 7.5. *Left:* Regions we selected to create local SEDs. Circles also indicate the size of the photometric apertures. *Right:* ATCA radio map at 4.8 GHZ (see Dickel et al. 2005 for the complete map of the LMC).

the individual regions 6a, 6b and 6c respectively.

7.3.3 Variation of the SED shape across the complex

We apply our SED modelling procedure to the individual regions of the complex. As shown in Fig. 7.6, the SED shape is changing significantly as a function of the regions modelled. We note the obvious evolution from the dust temperature range between bright star forming regions like Region 6, intermediate star forming regions like Region 3, 17, 16 to very quiescent regions like Region 10 or 21. The SEDs of the brightest HII regions show 'flat' profiles with an increased warm dust population as we will also see in Chapter 9 in NGC 6822 resolved wih *Herschel*.

The submm slope is also varying significantly from one region to another. We note that in the 6 brightest selected regions, region 5 (corresponding to N159S) possesses the lowest 160/870 flux density ratio, due to its very high emisson at 870 μm. Most of the SEDs of the individual regions peak at wavelengths between 70 and 160 μm. Two fluxes (160 and 870 μm) are thus crucial to constrain both the SED peak and the submm slope.

Table 7.1. Regions selected within the N158/N159/N160 complex with coordinates and size of the photometric aperture

Id	Name	Ra (J2000)	Dec (J2000)	Aperture (arcmin)
Reg 1	N158	5h 39' 11.2"	-69° 30' 13.7"	1.8
Reg 2	N160	5h 39' 38.6"	-69° 39' 06.8"	1.8
Reg 3	-	5h 40' 22.2"	-69° 40' 33.5"	1.8
Reg 4	-	5h 40' 49.4"	-69° 44' 48.2"	1.8
Reg 5	N159 S	5h 40' 03.7"	-69° 51' 01.6"	1.8
Reg 6	N159	5h 39' 46.6"	-69° 45' 39.9"	3.6
Reg 6a	N159 E	5h 40' 11.0"	-69° 44' 35.8"	1.1
Reg 6b	-	5h 39' 52.1"	-69° 45' 23.2"	0.6
Reg 6c	N159 W	5h 39' 32.5"	-69° 46' 02.7"	1.1
Reg 7	-	5h 38' 41.5"	-69° 24' 58.8"	0.9
Reg 8	-	5h 39' 49.0"	-69° 26' 26.4"	0.9
Reg 9	-	5h 38' 45.7"	-69° 27' 53.1"	0.9
Reg 10	-	5h 38' 13.3"	-69° 30' 39.5"	0.9
Reg 11	-	5h 40' 00.7"	-69° 31' 04.8"	0.9
Reg 12	-	5h 40' 09.4"	-69° 32' 44.6"	0.9
Reg 13	-	5h 40' 51.6"	-69° 32' 21.0"	0.9
Reg 14	-	5h 38' 17.9"	-69° 33' 37.5"	0.9
Reg 15	-	5h 38' 55.0"	-69° 34' 36.0"	0.9
Reg 16	-	5h 39' 30.6"	-69° 36' 37.4"	0.9
Reg 17	-	5h 40' 04.6"	-69° 37' 59.9"	0.9
Reg 18	-	5h 40' 54.6"	-69° 38' 04.2"	0.9
Reg 19	-	5h 40' 58.5"	-69° 42' 04.2"	0.9
Reg 20	-	5h 41' 03.5"	-69° 46' 36.9"	0.9
Reg 21	-	5h 41' 40.4"	-69° 48' 36.2"	0.9
Reg 22	-	5h 38' 00.2"	-69° 42' 33.0"	0.9
Reg 23	-	5h 40' 13.6"	-69° 53' 12.6"	0.9
Reg 24	-	5h 41' 54.7"	-69° 45' 30.8"	0.9
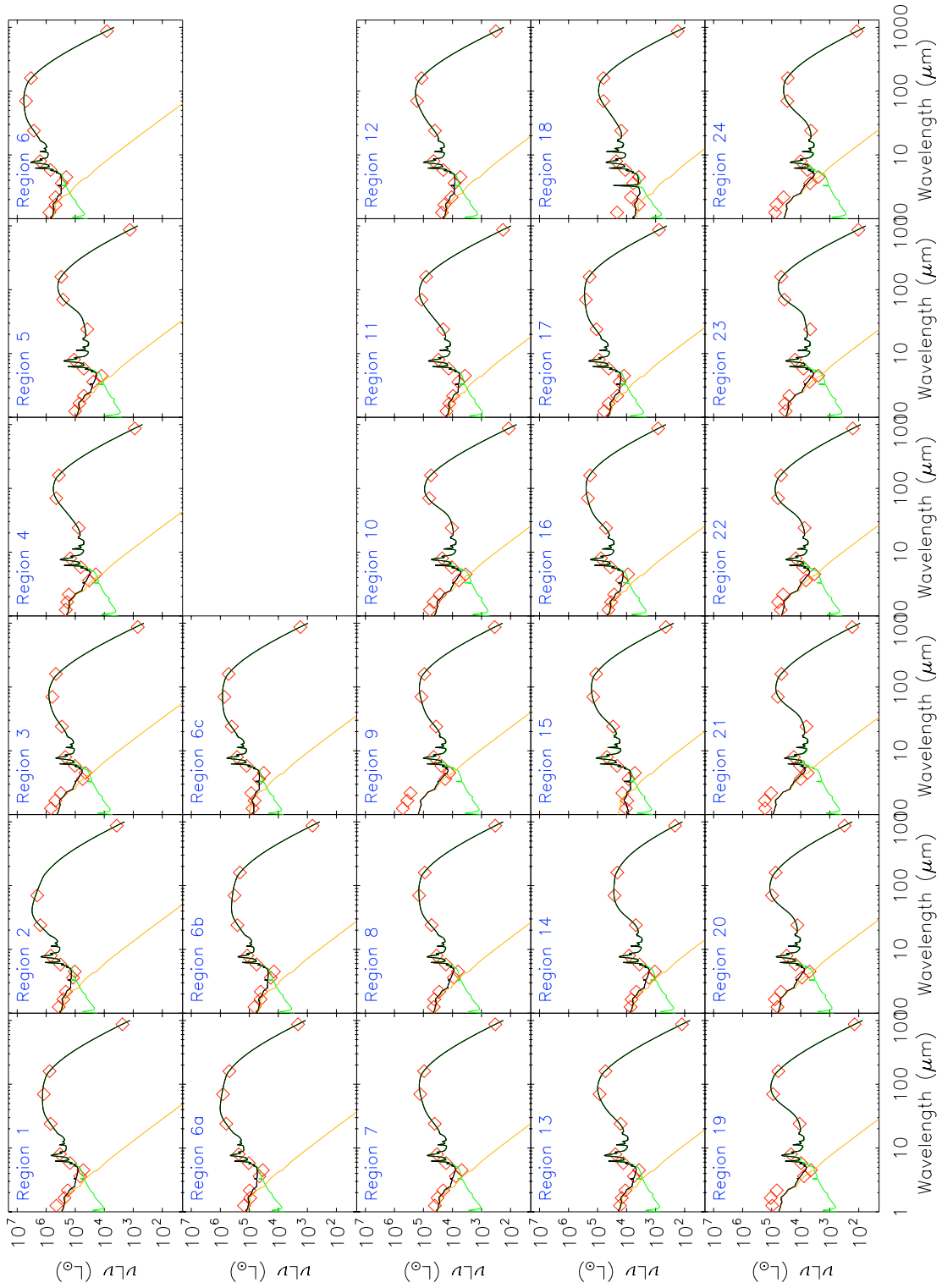
Figure 7.6. SEDs of individual regions of the N158 / N159 / N160 complex. Regions refer to Fig. 7.5 - left. The SED models are in black. In red are overlaid the observational constraints. The stellar and dust contribution appear in orange and green respectively.

Table 7.2. Flux densities of our selected regions

Id	2MASS 1.23 μm (mJy)	2MASS 1.65 μm (mJy)	2MASS 2.17 μm (mJy)	IRAC 3.6 μm (mJy)	IRAC 4.5 μm (mJy)	IRAC 5.8 μm (mJy)	IRAC 8.0 μm (Jy)	MIPS 24 μm (Jy)	MIPS 70 μm (Jy)	MIPS 160 μm (Jy)	LABOCA[a] 870 μm (mJy)
Reg 1	2080	1446	1475	1002	941	4624	13.6	63.4	317	458	8886
Reg 2[b]	1726	1580	1698	1763	1856	9877	28.0	143.5	534.2	-	15493
Reg 3	3219	2999	2508	818	793	3130	8.9	25.8	161.0	276.7	3805
Reg 4	984	1169	1346	490	351	1959	6.0	6.8	117.5	219.3	2895
Reg 5	470	443	410	352	223	153	0.4	0.3	68.8	180.0	4272
Reg 6	3607	2941	3893	4314	3652	21626	65.4	237.5	1296.3	2006.1	37803
Reg 6a	711	573	789	665	610	3183	9.34	55.9	210.7	290.5	7674
Reg 6b	312	253	328	271	255	1332	3.9	23.2	84.7	126.9	2637
Reg 6c	362	406	698	684	569	3780	10.8	36.1	190.1	309.6	8080
Reg 7	189	201	170	113	87	504	1.4	3.7	33.7	56.6	1093
Reg 8	207	262	232	132	116	516	1.4	4.7	36.8	53.9	1098
Reg 9	2391	2220	2276	263	229	732	1.8	3.3	30.7	55.8	1141
Reg 10	280	277	220	88.5	62.9	322	0.9	0.9	16.5	32.7	378
Reg 11	74.8	79.4	77.3	92.5	66.3	410.0	1.2	1.9	30.4	48.4	590
Reg 12	107	118	87.2	125.2	96.0	631.5	1.8	3.6	43.5	70.0	1043
Reg 13	78.5	90.6	89.5	82.8	6.6	306	0.8	1.4	22.3	31.9	404
Reg 14	34	41	37	26	19	109	0.3	0.4	6.8	12.5	699
Reg 15	49	59	112	126	92	644	1.9	2.6	36.9	66.8	1448
Reg 16	198	210	217	211	159	1089	3.1	4.6	56.3	108.3	2680
Reg 17	274	258	171	256	220	1258	3.6	9.8	66.1	112.8	2498
Reg 18	99.5	23.8	57.5	87.2	67.2	334.6	0.9	1.4	16.5	37.5	567
Reg 19	449	662	541	113	79	294	0.9	1.0	23.4	35.3	451.8
Reg 20	296	479	389	134	89	460	1.2	1.2	25.4	43.8	1011
Reg 21	78.7	1063	853	149	103	319	0.7	0.6	16.0	27.6	543
Reg 22	228	371	328	97.3	60	247	0.6	0.7	15.8	28.6	519
Reg 23	154	214	201	73	44	245	0.6	0.4	9.6	28.2	336
Reg 24	357	422	315	70	44	175	0.4	0.4	7.6	16.7	378

Notes.- [a] The radio contamination is not subtracted from these flux densities.

[b] Because of the saturation of this region at MIPS 160 μm, the images were convolved to the LABOCA resolution before extracting the flux densities.
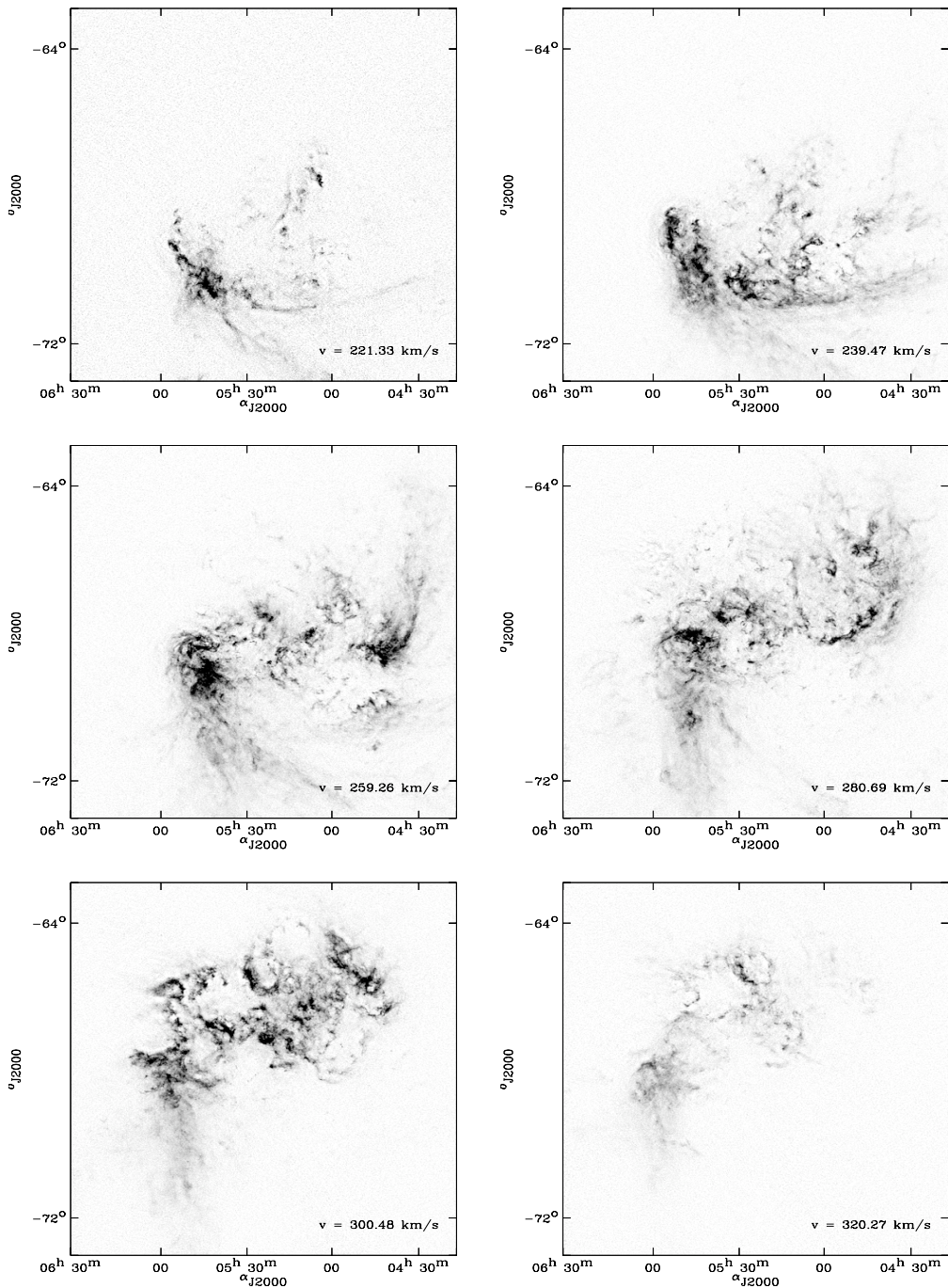
Figure 7.7. Individual channel maps for the HI data cube in the LMC. The heliocentric velocities are indicated in the bottom right corner.

7.4 The HI distribution and mass in our selected regions

We want to estimate the gas budget in our individual regions to investigate the D/G across the complex. High-resolution maps have been built for the complete LMC. The HI data cube we used combines data from the Australian Telescope Compact Array (Kim et al. 2003) and the Parkes single-disk telescope (Staveley-Smith et al. 2003). We refer to Kim et al. (2003) for further details

on the cube. The individual channel maps have a velocity resolution of 1.649 km s^{-1}. Some of these individual channels are shown in Fig. 7.7. The 30 Dor complex lies in the $05^h49^m<$ R.A. $<05^h36^m$, -73°00' $<$Dec.$<$ -68°30' range.
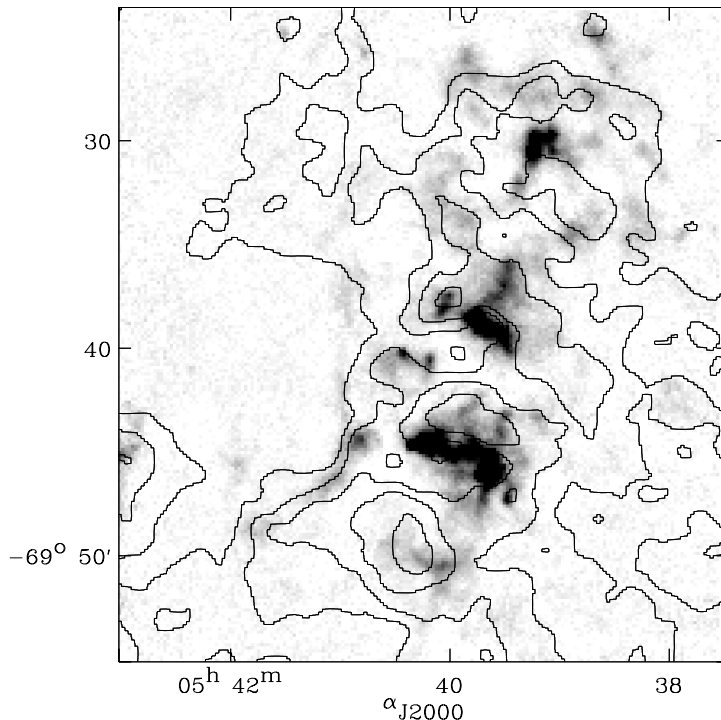
Figure 7.8. The N158 / N159 / N160 complex observed with LABOCA with HI contours overlaid. The HI contours are 5×10^{21}, 6×10^{21} and 7×10^{21} atom cm^{-2}.

The HI integrated map was obtained integrating the cube over the range $190 <$ v$_{hel} < 386$ km s^{-1}. The LMC integrated map is presented and discussed in details in Kim et al. (2003) and Bernard et al. (2008). We clearly note an offset between N159 (third brightest region) and the HI peak. This offset of 1.5' can be due to the astrometry and is also observed between every *Spitzer* map and the HI map. We refer to section 7.6 for more detail about this HI offset in N159.

We estimate the gas mass in each aperture (summarized in Table 7.3). The initial unit of the map is H cm^{-2} which was converted in solar masses.

7.5 How to model carbon dust

From our SED models, we derived the dust masses of our selected regions. We thus deduced the HI-to-dust mass ratio (D/HI) in each aperture. Dust masses and D/HI are given in Table 7.3 (column 3 and 4). The D/HI are very high compared to what would be expected for a galaxy with the metallicity of the LMC. These results could be linked with the high dust masses we deduced.

It is well known that carbon constitutes a major fraction of the dust in galaxies, especially in the circumstellar dust of carbon stars. Nevertheless, the exact form of carbon dust is rather unclear. Many SED models use graphite to describe the interstellar carbon dust as first suggested by Mathis et al. (1977). Graphite, indeed, has well-known physical properties, which makes it easy to model, and explains well the observed (Galactic) extinction and polarization (Draine & Lee 1984).

However, several lines of observational evidence oblige us to reassess the graphite theory (at least the pure monocrystalline graphite theory), among which:

- variations in the 2175 $\mathring{A}$ profile not explained by changes in graphite grain size (Draine & Malhotra 1993)

- a non detection of the graphite broadband emission feature near 33 μm (e.g. Draine et al. 2007)

- erosion of the carbon dust in shocks not reproduced with graphite (Welty et al. 2002; Serra Díaz-Cano & Jones 2008)

Graphite is thus not expected to survive as such in the ISM due to erosion and irradiation in shock waves. Serra Díaz-Cano & Jones (2008) suggested that interstellar hydrogenated amorphous carbons could be the most probable form of carbon material, their erosion being more efficient than graphite in shocks. Amorphous carbon (AC) shows a flatter submm slope compared to graphite (see Fig. 7.9). The use of AC to represent carbon dust in SED models will automatically lead to a decrease in the number of large grains required to fit the SED constraints at submm wavelengths and thus to less mass to account for the same emission.

To study how this choice affects our dust masses, we replace our graphite grains by amorphous carbon (Rouleau & Martin 1991). Table 7.3 summarised the dust masses obtained with our SED modelling using graphite and amorphous carbon. The dust masses, as expected, are systematically inferior (from 3 to 6 times) when using amorphous carbon. In that case, the D/HI deduced are more realistic given the metallicity of the LMC. We plan to estimate the molecular gas mass within our apertures to study how the D/G evolves taking molecular gas into account. If we consider that the D/G is constant across the complex, we will be able to estimate the gas mass from the dust mass estimates and compare this mass with that traced by current HI and CO observations.
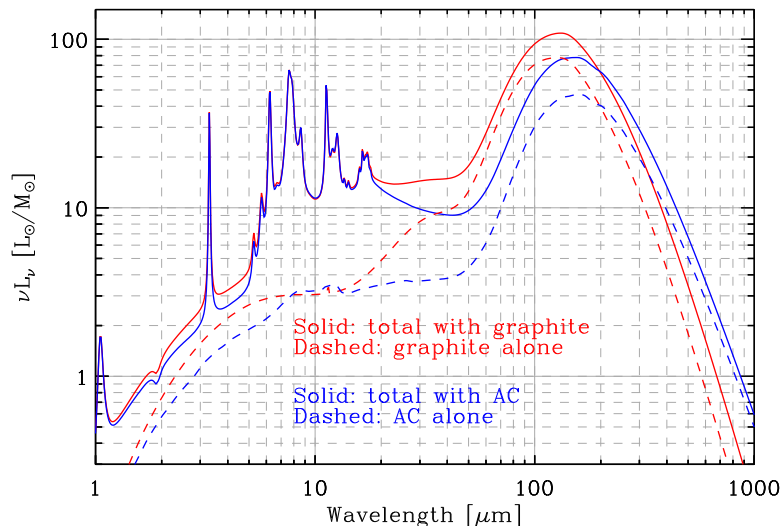
Figure 7.9. Effect of graphites or amorphous carbons on the SED shape

Table 7.3. Dust and Gas mass estimates in our selected regions within the complex

Id	M_{HI} ($\times 10^3\ M_\odot$)	$M_{dust\ Gr}$ [a] ($M_\odot$)	$M_{dust\ Gr}/M_{HI}$	$M_{dust\ AC}$ [b] ($M_\odot$)	$M_{dust\ AC}/M_{HI}$
Reg 1	93.8	6396.4	6.8×10^{-2}	1201.7	1.3×10^{-2}
Reg 2	117.7	11838.4	0.1	1772.3	1.5×10^{-2}
Reg 3	100.2	1597.9	1.6×10^{-2}	312.4	3.1×10^{-3}
Reg 4	105.45	1869.1	1.8×10^{-2}	529.4	5.0×10^{-3}
Reg 5	137.0	4813.1	3.5×10^{-2}	811.7	5.9×10^{-3}
Reg 6	509.5	20367.6	4×10^{-2}	3978.6	7.8×10^{-3}
Reg 6a	44.1	6958.4	1.6×10^{-1}	1190.6	2.7×10^{-2}
Reg 6b	13.6	1944.3	1.4×10^{-1}	357.9	2.6×10^{-2}
Reg 6c	50.1	4930.4	9.8×10^{-2}	932.3	1.9×10^{-2}
Reg 7	18.5	882.1	4.8×10^{-2}	175.3	9.5×10^{-3}
Reg 8	16.8	933.4	5.5×10^{-2}	168.3	1.0×10^{-2}
Reg 9	21.5	951.6	4.4×10^{-2}	185.2	8.6×10^{-3}
Reg 10	17.8	237.3	1.3×10^{-2}	71.8	4.0×10^{-3}
Reg 11	26.5	348.2	1.3×10^{-2}	101.8	3.8×10^{-3}
Reg 12	28.4	705.3	2.5×10^{-2}	153.4	5.4×10^{-3}
Reg 13	27.4	249.7	9.1×10^{-3}	66.5	2.4×10^{-3}
Reg 14	18.5	1160.8	6.3×10^{-2}	207.9	1.1×10^{-2}
Reg 15	26.6	1264.7	4.7×10^{-2}	229.9	8.6×10^{-3}
Reg 16	29.9	2453.7	8.2×10^{-2}	434.9	1.4×10^{-2}
Reg 17	34.8	2235.8	6.5×10^{-2}	420.1	1.2×10^{-2}
Reg 18	20.1	395.6	2.0×10^{-2}	111.3	5.5×10^{-3}
Reg 19	22.0	318.2	1.4×10^{-2}	81.8	3.7×10^{-3}
Reg 20	28.8	1122.9	3.9×10^{-2}	171.9	6.0×10^{-3}
Reg 21	28.7	592.8	2.1×10^{-2}	99.6	3.5×10^{-3}
Reg 22	27.4	487.5	1.8×10^{-2}	95.6	3.4×10^{-3}
Reg 23	31.0	234.8	7.5×10^{-3}	71.4	2.3×10^{-3}
Reg 24	14.1	341.7	2.4×10^{-2}	69.7	5.0×10^{-3}

[a] Dust mass derived using graphite (Gr) or amorphous carbon (AC).

[b] HI mass corresponding to the region mapped with *Herschel*.

7.6 The N159 region and CO

What do we know about the molecular gas in N159. Several CO observations of the N159 nebula have been carried out so far.

Israel et al. (1993) observed CO(1-0) in numerous positions in the LMC as part of the SEST (Swedish-ESO Submillimeter Telescope) Key Programme on CO in the Magellanic Clouds. They obtained maps with a resolution of 45", corresponding to a resolution of ~ 15 pc for the LMC. Bolatto et al. (2000) more specifically mapped the N158 / N159 / N160 complex in four transtions: $^{13}CO(1\text{-}0)$, $^{12}CO(2\text{-}1)$, $^{12}CO(4\text{-}3)$, [CI]($^3P_1 \rightarrow {}^3P_0$) also with SEST and the 1.7m AST/RO (Antartic Submillimeter Telescope and Remote Observatory) (Resolutions for the CO(1-0) and CO(4-3) : $\sim$ 15 pc and 50 pc respectively). These observations were nevertheless limited by the spatial coverage.

The first spatially resolved complete survey of the LMC was performed with the NANTEN 4-m telescope in the 2.6 mm carbon monoxide emission with a 40 pc resolution by Fukui et al. (1999), permitting a study of the giant molecular clouds at global scales.

Several observations of the CO(4-3) transition and of the CO(3-2) transition have been carried out in selected regions of the LMC. These two transitions have been observed in the N158 / N159 / N160 complex by Mizuno et al. (2010), respectively with NANTEN2 (beam size at 490 GHz: 18") and ASTE (Atacama Submillimeter Telescope Experiment, beam size at 350 GHz: 22").

Finally, the Magellanic Mopra Assessment (MAGMA) survey is currently performing a high angular resolution 12CO(1-0) mapping survey of giant molecular clouds across the LMC with the Mopra telescope in Australia Hughes et al. (2010). The beam size of the instrument is 33", which corresponds to a spatial resolution of ~ 8 pc at the distance of the LMC.

The two giant molecular clouds of N159 (referred to as N159E and N159W in Fig. 7.5) as well as its southern region (referred to as N159S) are thus already mapped at high resolution in many transitions. N159W is the strongest region in the CO(1-0) transition. The eastern region breaks into 3 independent peaks. Compared to the other giant molecular clouds, the southern region does not show any heating source and little star formation activity. Bolatto et al. (2000) also note the detection of diffuse low level emission in CO(2-1).

N159E and N159W are associated with embedded star clusters with temperatures that were determined to be 70-80K while N159S shows a nearly uniform temperature estimated to be $\sim$30K by (Mizuno et al. 2010). They also compare the spatial distribution of CO with *Spitzer* bands and found a fairly good correlation between the maps. The *Spitzer*/IRAC 4 (8 μm) observation is shown in Fig. 7.10 with overlaid ^{12}CO(3-2) contours. The spatial correlation is very good except for N159S. Indeed, a small amount of emission at 8 μm is detected on the east side of N159S, shifted by ~ 30 pc.

Figure 7.10 also shows the LABOCA image with ^{12}CO(3-2) contours overlaid. The spatial correlation is again very good, N159S included. Mizuno et al. (2010) note that the molecular peak of the N159E region is showing an elongated structure. This extension is very well resolved at 870 μm with LABOCA. They also note a slight shift between the peak of ^{12}CO(4-3) in N159W and the 8 and 24 μm peaks. The bright peak of the LABOCA emission in N159W does not seem to show any shift with the ASTE ^{12}CO(3-2) map. Finally, the east-west elongated structure of N159S as well as the south extension at 870 μm follow the CO map structure of N159S.

In Fig. 7.10, we also show the H I contours on both 8 and 870 μm maps. We clearly see that while the southern H I peak seems to be spatially correlated with the diffuse 8 μm emission in the south of N159, it is shifted compared to the 870 μm peak. Fukui et al. (2009) already noted the offset between the H I and CO peak for N159. They showed than H I and CO distributions correlate well on 40-100 pc scales and argued that the H I envelopes are gravitationally bound by giant molecular clouds. They also explain that the correlation between the H I and CO distribution becomes less clear at smaller scales. They interprete it as an illustration of the conversion of warmer, low-opacity H I to colder high-opacity H I from which H_2 could form, as suggested in Ott et al. (2008) and Wong et al. (2009).

7.7 Further studies to come

This is only an introduction to the observations existing for this study. We plan to quantify the atomic and molecular gas across the complex to improve the study of the variation of the D/G across the complex. More precisely, we would like to answer the questions: can the D/G be considered as constant across the complex. 1- If not, how is it evolving when the molecular cloud is taken into account in the gas mass? 2- If yes, are molecular observations consistent with what should be expected from the gas mass derived with dust masses or can we detect local variations in the X_{CO} (=$N(H_2)/I_{CO}$) conversion factor.

Our LABOCA map will be an important constraint on the submm slope for any attempt of
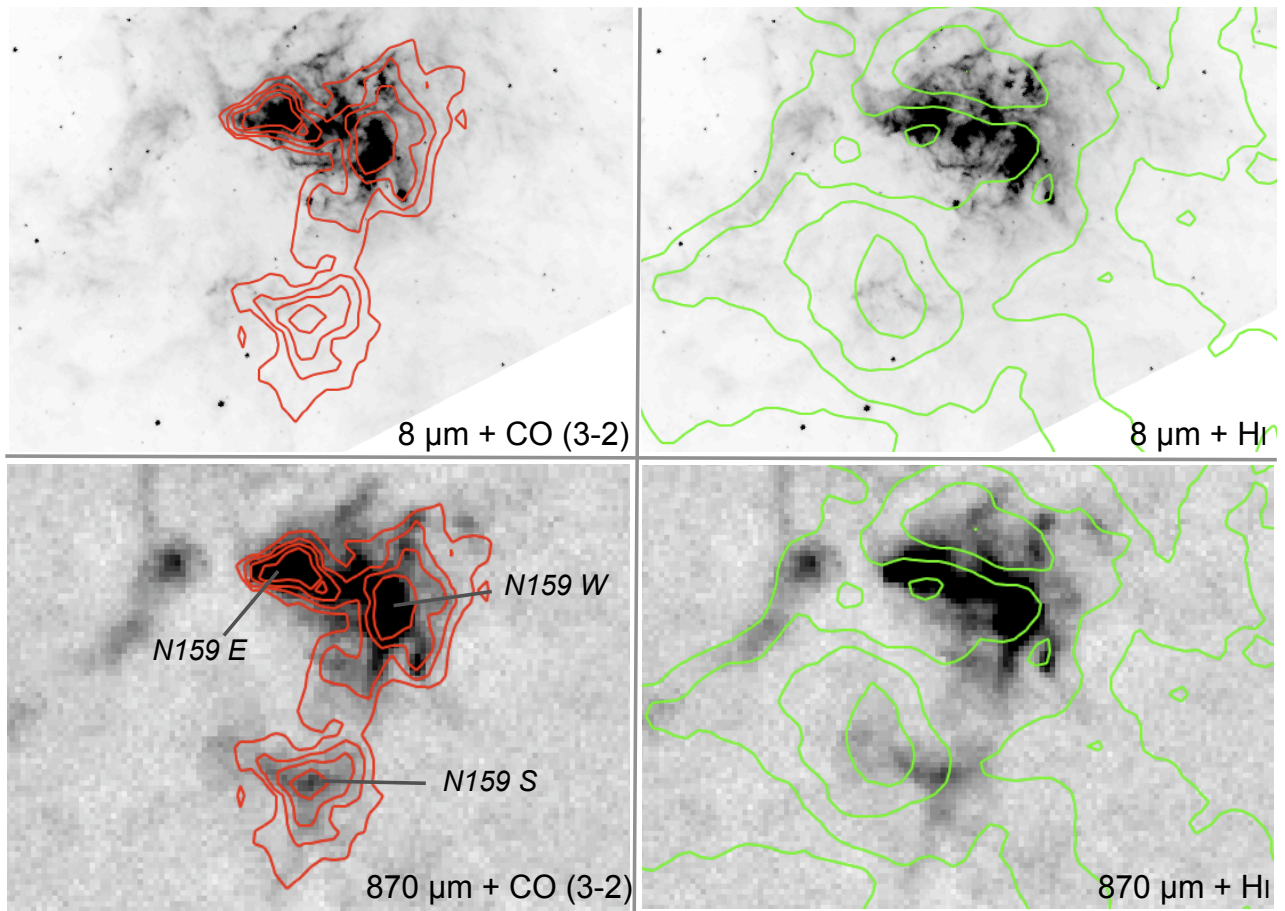
Figure 7.10. IRAC4 (8 μm) and LABOCA (870 μm) images with ASTE ^{12}CO(J = 3 $\rightarrow$ 2) and H I contours overlaid. The H I contours are 5 $\times$ 10^{21}, 6 $\times$ 10^{21} and 7 $\times$ 10^{21} atom cm^{-2}. The CO contours are 2, 8, 14, 27 K km s^{-1}. We thank Akiko Kawamura for the CO map.

SED modelling of the complex since only observations up to 160 μm are available for the moment. *Herschel* observations of the LMC for the HERITAGE (HERschel Inventory of The Agents of Galaxy Evolution) consortium to which I belong will, this year, complete the far-IR coverage from 70 to 500 μm.

Part III

The Local Universe revealed by Herschel

Chapter 8

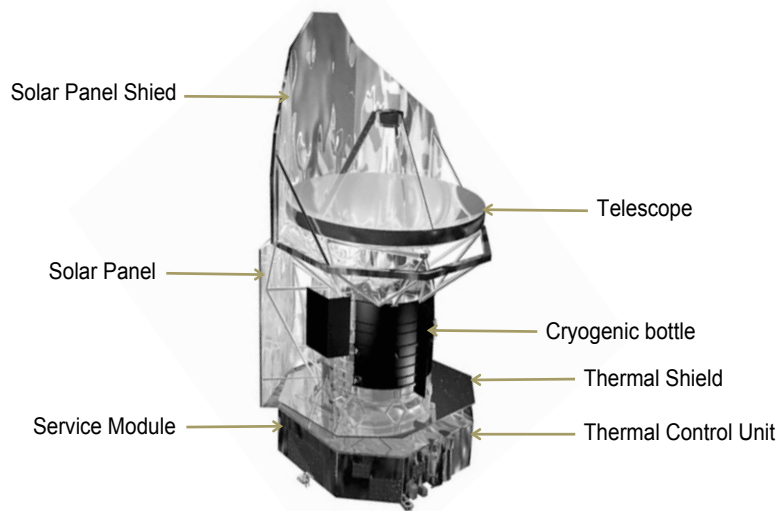# The Herschel Space Observatory and the SAG2/DGS programme

Contents

8.1 General Description

8.1.1 The telescope

The European Space Agency's *Herschel* Space Observatory (formerly called Far Infrared and Sub-millimetre Telescope or FIRST) has the largest single mirror ever built for a space telescope. At 3.5-metres in diameter the mirror will collect long-wavelength radiation from some of the coldest and most distant objects in the Universe. In addition, *Herschel* is the only space telescope that covers a spectral range from the far-IR to submm. It was successfully launched on 14 May 2009 at 13:12 UTC from Kourou, French Guyana, sharing the launching rocket with the Planck satellite, exactly at the middle of my PhD. In the last months of my thesis, we had access to the first Science Demonstration data of the Dwarf Galaxy Survey key program (see section 8.2) taken with two of the three instruments of the spacecraft, PACS (Photodetector Array Camera and Spectrometer for Herschel) and SPIRE (Spectral and Photometric Imaging Receiver). To reach the desired sensitivity, the instruments onboard have to be cooled to a cryogenic temperature of 0.3° above absolute zero. The necessity to cool down the instruments and thus the capacity of its main reservoir of superfluid helium will limit Herschel's lifetime to ~3 years. A description of the *Herschel* Observatory is given in Fig. 8.1.

Figure 8.1. Description of the Herschel Space Observatory

8.1.2 The PACS instrument

PACS (Poglitsch et al. 2010) has been designed and built by a large consortium of institutes and university departments from across Europe under the leadership of Principal Investigator Albrecht Poglitsch. The consortium members are MPE and MPIA (Germany); UVIE (Austria); KU Leuven, CSL and IMEC (Belgium); CEA and LAM (France); INAF-IFSI/OAA/OAP/OAT, LENS and SISSA (Italy) and IAC (Spain).

PACS possesses an integral field spectrometer and an imaging photometer. The spectrometer simultaneously observes 57-105 and 105-210 μm. The field of view covers 47" × 47" rearranged via an image slicer on a 16 × 25 pixel Ge:Ga detector array, leading to a theorical sensitivity of ~2-9 × 10^{-18} W m^{-2} (5-sigma limit in 1 hour). The photometer observes two-bands simultaneously (70-160 and 100-160 μm). The fields of view are 3.2' × 3.2' and 6.4' × 6.4' on sky, with focal plane arrays made of 64 × 32 (4 by 2 matrices of 16 × 16 pixels) and 32 × 16 pixels (2 matrices of 16×16

pixels) for the blue/green (70 or 100 μm) and red (160 μm) photometers respectively (see Fig. 8.2). Small gaps remain between the subarrays of the PACS detector. These gaps have to be filled by mapping methods. The main charateristics of the PACS photometer are summarized in Table 8.1. The spectral response function of PACS spectral bands are shown in Fig. 8.4.
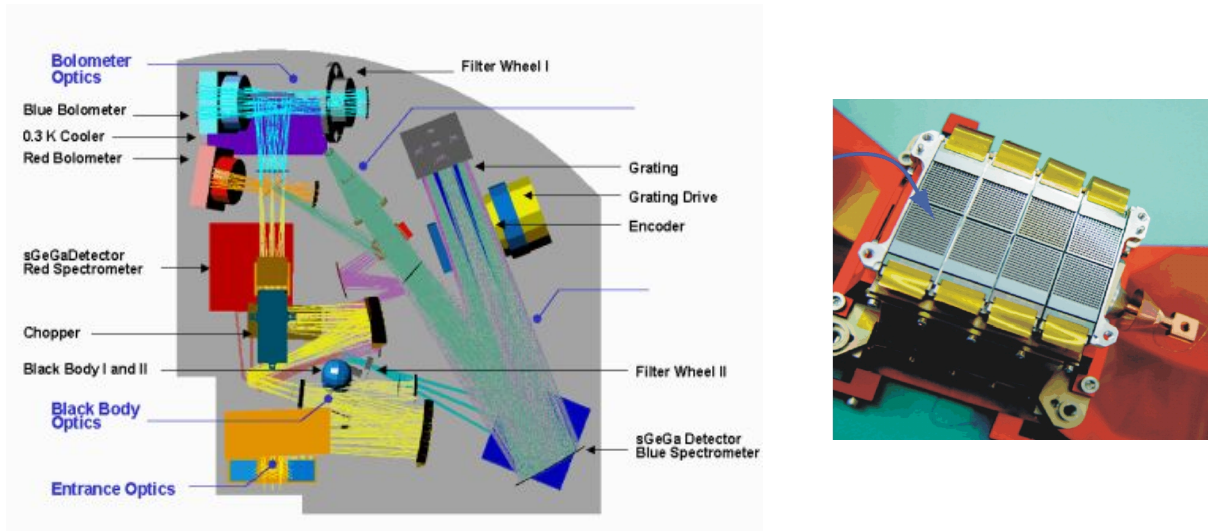
Figure 8.2. Optical layout of the PACS instrument and the blue bolometer array unit

8.1.3 The SPIRE instrument

SPIRE (Griffin et al. 2010) has been developed by a consortium of international institutes under the leadership of Principal Investigator Matt Griffin. Consortium members are Cardiff University (UK); the University of Lethbridge (Canada); NAOC (China); CEA, LAM (France); IFSI, the University of Padua (Italy); IAC (Spain); SNSB (Sweden); Imperial College London, RAL, UCL-MSSL, UKATC, the University of Sussex (UK) and Caltech, JPL, NHSC and the University of Colorado (USA).

SPIRE possesses an imaging Fourier Transform Spectrometer (FTS) and a three-band imaging photometer. The FTS has an approximate circular field of view with a diameter of 2.5' on the sky. Two bolometer arrays cover 200-325 μm and 315-670 μm. The spectral resolution can be adjusted between 0.04 and 2 cm^{-1}, corresponding to $\lambda/\Delta\lambda = 1000$ - 20 in the PSW (250 μm) band. The photometer operates in three bands at 250, 350 and 500 μm observed simultaneously. The detectors are arrays of feedhorn-coupled NTD spider-web bolometers. The field of view of the photometer is a 4' $\times$ 8' in scan map. The main characteristics of the SPIRE photometer are summarized in Table 8.1. The spectral response function of SPIRE spectral bands are shown in Fig. 8.4.

Table 8.1. PACS and SPIRE channels characteristics

	PACS			SPIRE		
	ch1	ch2	ch3	ch1	ch2	ch3
	blue	green	red	PSW	PMW	PLW
Wavelength (μm)	70	100	160	250	350	500
FWHM (arsec)	5.2	7.7	12	18	25	36
Nominal Fields	3.2' $\times$ 3.2'		6.4' $\times$ 6.4'	4' $\times$ 8' in scan map		
Number of detectors	64 $\times$ 32		32 $\times$ 16	139	88	43
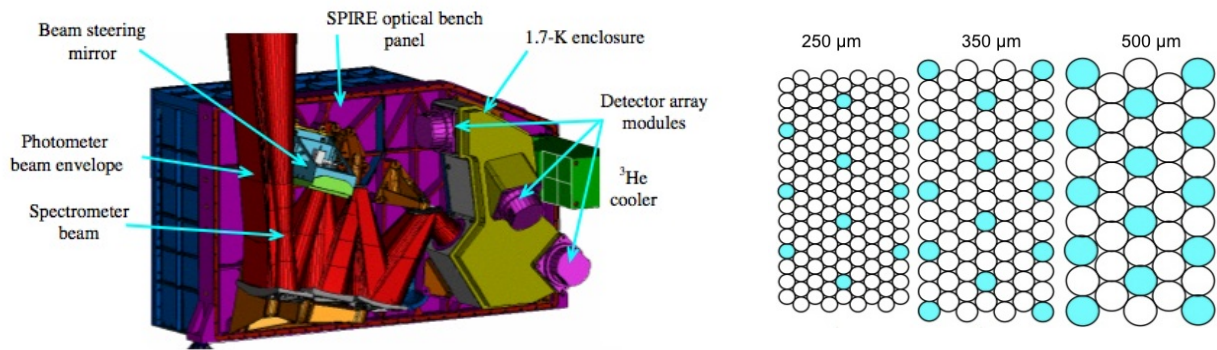
Figure 8.3. SPIRE photometer layout and photometer arrays. The colored detectors indicate those for which there is exact overlap on the sky for the three bands.
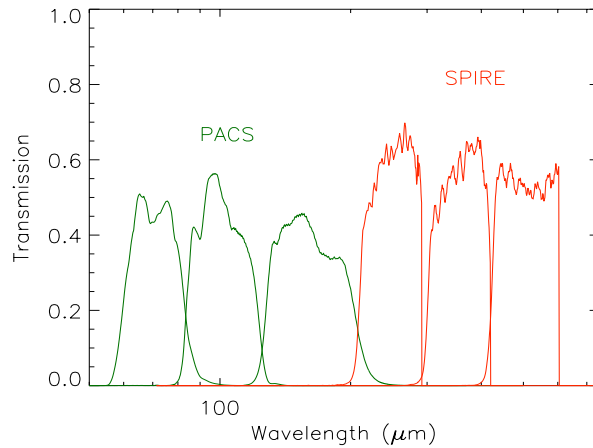
Figure 8.4. Spectral Response of the PACS (70, 100, 160 μm) and SPIRE (250, 350, 500 μm) instruments.

8.2   The SAG2 / Dwarf Galaxy Survey

I am a member of the SPIRE Local Galaxies Working Group (SPIRE Specialist Astronomy Group 2 or SAG2) consortium (coordinated by S. Madden and W. Gear) that aims to study galaxies of the Nearby Universe using the PACS and SPIRE instruments. The project includes three different *Herschel* Guaranteed time key programs: the HRS (Herschel Reference Survey, PI: S. Eales), the VNGS (Very Nearby Galaxy Survey, PI: C. Wilson) and the DGS (Dwarf Galaxy Survey, PI: S. Madden). I have been working on the DGS observations. Additionally, my PhD home institute, the CEA at Saclay, contributed to the development of the PACS instrument so we also have access to PACS Guaranteed Time observations in a key program SHINING (PI: E.Sturm), for which we are the PI team of the program that surveys the gas in dwarf galaxies as well as metal-rich starbursts using PACS and SPIRE spectroscopy.

   The DGS group was granted time (110 hours) to obtain 60-500 μm photometry of a large sample of 55 low-metallicity galaxies. This sample covers a wide range of ISM physical conditions with a large range of star formation activity (0.1 to 10 $M_\odot$/yr, see Fig. 8.5). The metallicity range of the sample is also the largest possible for dwarf galaxies in the Local Universe, from $Z_\odot$ down to 1/50 $Z_\odot$. Our spectroscopic observations between 60 and 200 μm with PACS will complement the photometric observations for a subset of this sample. These combined observations will enable us:

1- to access to unprecedented detail the ISM dust and gas (HII regions, diffuse emission) of low-metallicity galaxies with PACS photometry.

2- to constrain the submm regime of SEDs up to 500 μm with a high sensitivity and good resolution with SPIRE (FWHM of SPIRE 500 μm : 36").

3- to have access to the important far-IR fine-structure cooling lines such as [CII] 158 μm or [OI] 63 μm and 145 μm as well as tracers of the dense and diffuse ionised gas such as [OIII] 88 μm, [NIII] 57 μm and [NII] 122 and 205 μm with PACS spectroscopy.
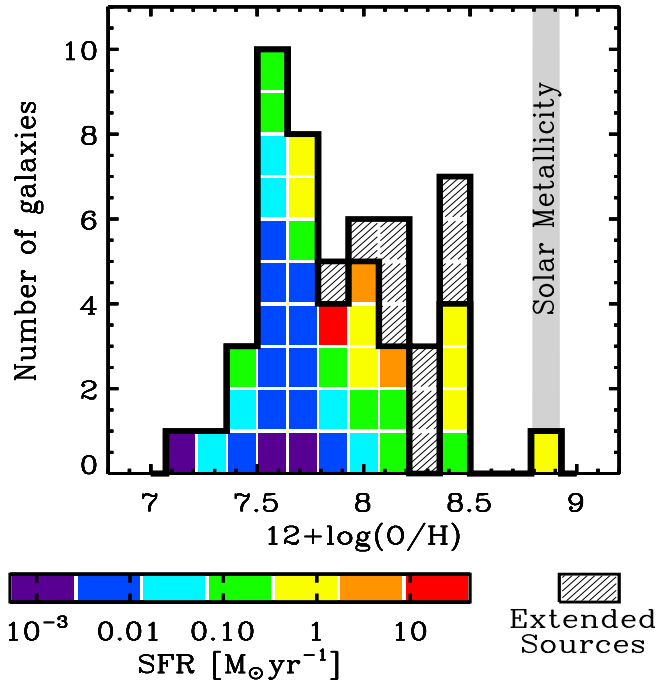
Figure 8.5. The SAG2 / Dwarf Galaxy Survey sample

I am responsible for the reduction of the PACS photometric observations for the Dwarf Galaxy Survey. I will describe in the following paragraphs the steps of the PACS reduction of both scan-map and chop-nod observations. Rather technical, these sections nevertheless aim to introduce the main concepts of the PACS data reduction pipelines (which are still in the process of improvement) and should be reproducible by the reader.

8.3 Observations in the scan mapping mode of PACS

8.3.1 Description of the mode

This mode is the default mode for PACS observations of large areas of the sky and was selected for the observations of our extragalactic sources (see Fig. 8.6). Scan maps are performed by slewing the spacecraft at a constant speed of 20 arcsec s^{-1}, along parallel lines to cover a large area. The lines follow great circles on the sphere which approximates parallel lines over short distances. When completing a scan leg, the spacecraft must perform a turn manoeuvre and continue observations along the next scan leg in the opposite direction. The time required for this turn is about half a minute. The sensitivity on point sources and the shape of the PSF are degraded by the increase

of the scanning speed. Cross-scans are necessary for PACS observations to remove the 1/f drifts in the maps.

Map reconstruction can be performed with photProject, which is a simple projection of the data cube on the map grid. A more sophisticated method is MADmap (Cantalupo et al. 2010), a maximum likelihood method which produces the best-fit solution for the final projected maps. MADmap, in principle, does not require the use of a high-pass filter to mitigate the 1/f noise and thus minimizes the removal of extended emission). This method requires pre-treatment of the data (correlated signal drift correction for instance).
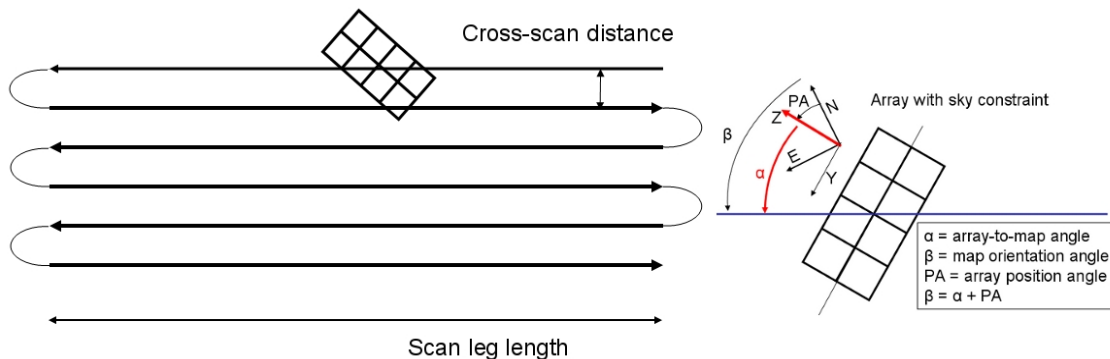
Figure 8.6. *Left:* Schematic view of a PACS scan map (6 scan lines). *Right:* Scheme of the reference angles of the array in sky constraint.

8.3.2 Data reduction

The data reduction of PACS observations taken in the scan map mode can be performed using HIPE (Herschel Interactive Processing Environment). This working environment (see Fig. 8.7) enables the user to directly access his/her data through the Herschel Science Archive, to import them in the HIPE environment, to reduce data using reduction pipelines calling HIPE or user-developed routines, manipulate and analyse reduced data (maps, spectra etc.).

During this PhD, we used the version 3.0 (versions 3.0.4.55 and 3.0.1134) of HIPE to reduce the observations of the SAG2/Dwarf Galaxy Survey (see Chapter 9). We are reducing data that were taken in two different modes: the scan mapping mode and chop-nod mode. We will separate the description of how data are reduced for these two different modes.

Our reduction pipeline starts from the level 0 data and produced maps with a standard pixel size of 3.2", 3.2" and 6.4" at 70, 100 and 160 μm (see Table. 8.1 for a reminder of the PACS PSF FWHM values).

The following lines describe the main steps of the PACS reduction. For extended sources, masking the sources is necessary to avoid dark artefacts around the bright structures of the map. This particular masking process is described in the script below.

Steps of the reduction pipeline:

\# Access to data corresponding to the observation identification (obsid) number XX. Data are stored in the 'store' called here Mygalaxy. We remind the reader that observations are taken in pairs for PACS (70-160 μm or 100-160 μm). In this example, we want to reduce the blue band.
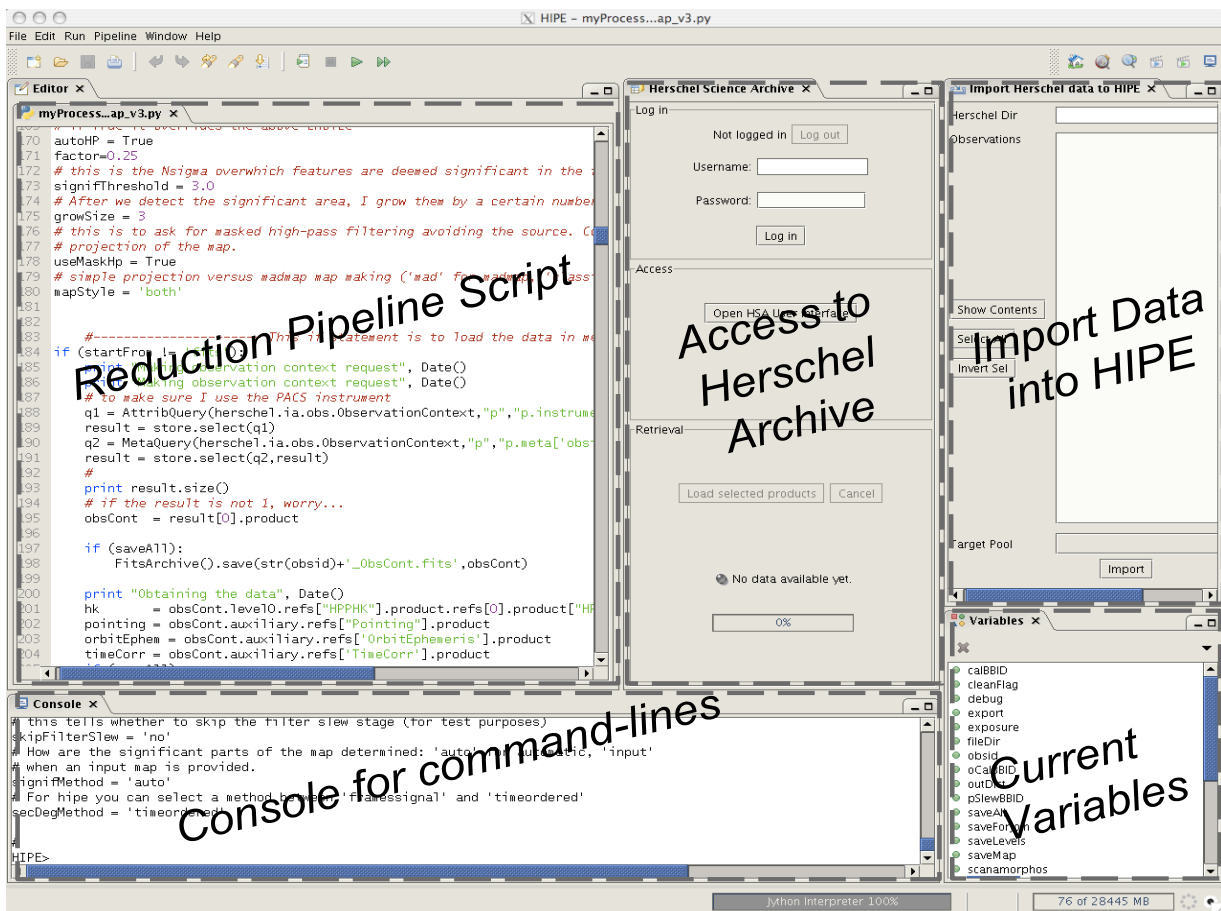
Figure 8.7. Example of an HIPE workbench with the most commonly used windows

(Note: In Herschel data, both 70 or 100 μm bands are called 'blue'. The real wavelength of this 'blue' observation has to be carefully checked beforehand.)

```
obsid = XX
store = ProductStorage(LocalStoreFactory.getStore(''Mygalaxy'))
side='blue'
q1 = AttribQuery(herschel.ia.obs.ObservationContext,''p",
                p.instrument=='PACS')
result = store.select(q1)
q2 = MetaQuery(herschel.ia.obs.ObservationContext,''p",
               ''p.meta['obsid'].value=="+str(obsid)+''L")
result = store.select(q2,result)
obsCont = result[0].product
```

Read the instrument housekeeping parameters or auxiliary information (pointings, orbit ephemeris, time correlation products) and save the data in the variable *frames*

```
hk = obsCont.level0.refs[''HPPHK"].product.refs[0].product['HPPHKS"]
pointing = obsCont.auxiliary.refs[''Pointing"].product
orbitEphem = obsCont.auxiliary.refs['OrbitEphemeris'].product
timeCorr = obsCont.auxiliary.refs['TimeCorr'].product
```

```
frames = obsCont.level0.refs[''HPPAVGB"].product.refs[0].product
```

Define the high-pass filtering width from the scan length. The keyword *factor* enables us to play with the filtering window to apply.

```
legLength = obsCont.meta.get('mapSize1').value * 60.
scanSpeed = obsCont.meta.get('mapScanRate').value
imPerSec = 10
if (scanSpeed == 'low'):
        leg_width = imPerSec * (legLength / 10.)
elif (scanSpeed == 'medium') or (scanSpeed == 'slow'):
        leg_width = imPerSec * (legLength / 20.)
else:
        leg_width = imPerSec * (legLength / 60.)
leg_width = int(leg_width * factor)
```

Initialize the Calibration Tree

```
calTree = getCalTree(''FM")
```

Detect, extract and process the calibration block - Add the result to the frames and remove the calibration block from the data

```
frames = findBlocks(frames)
frames = detectCalibrationBlock(frames)
calBlock = photCSExtraction(frames)
calBlock = photCSProcessing(calBlock,hk,calTree)
frames = photCSClean(frames,calBlock,cleanFlag)
```

Detect the bad pixels and those affected by saturation - Convert the data in Jy.pixel^{-1}

```
frames = photFlagBadPixels(frames, calTree=calTree)
frames = photFlagSaturation(frames, calTree=calTree, hkdata=hk,
                check='full')
frames = photConvDigit2Volts(frames, calTree=calTree)
```

Convert the digital chopper postions to angle on the sky and assign the pointing - Mask frames affected by chopper movements

```
frames = convertChopper2Angle(frames,calTree=calTree)
frames = photAddInstantPointing(frames, pointing, calTree=calTree,
                orbitEphem = orbitEphem)
frames = cleanPlateauFrames(frames, calTree=calTree)
```

Perform a flatfield correction and calibrate the flux

```
frames = photRespFlatfieldCorrection(frames, calTree = calTree)
```

Here, a few masks are built (mask to flag the frames taken before the first scanleg, those where the satellite is not scanning, mask to absorb the photometer time constant after the chopper motion from the CS position etc.). I will not enter into the details of how these masks are created here.

Save a copy of the frames before deglitching (will be used later) and perform a multiresolution median transform deglitching of the data

```
origSignal = frames.signal.copy()
frames = photMMTDeglitching(frames, copy=False, scales=3.,
            incr_fact=2, mmt_mode='multiply', onlyMask=False)
```

We now want to perform high pass filtering to remove the stripping within the map in the scanning direction but this treatment introduces dark artefacts along the scanning directions close to bright structures. We thus chose to mask the bright sources during the treatment. To proceed, a first naive map built in which significant structures are isolated and protected in a mask :
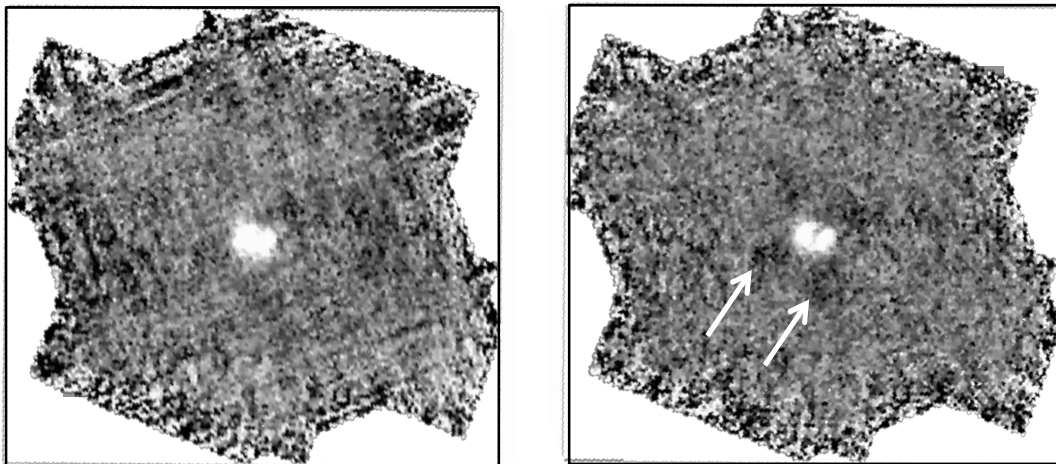
Figure 8.8. *Left:* Map of the galaxy NGC1705 affected by stripping due to a (too) large HP fitering window. *Right:* Map of the galaxy NGC1705 with HP filtering performed on half a scanleg. The stripping is significantly reduced but the surrounndings of the source are affected by dark artefacts linked with the HP filtering

Make a copy of the frames and perform a first high-pass filtering of the data (we chose to perform it on a scan leg to be conservative) - Mask the slews to produce the naive map 'map1'

```
framesC = frames.copy()
framesC = highpassFilter(framesC,leg_width/2)
framesC.setMask('UNCLEANCHOP',slewMask.or(ucl))
map1 = photProject(framesC,calibration=True,calTree=calTree)
```

Select pixels that are covered enough by observations

```
mapCov = map1['coverage'].data.copy()
selCov = mapCov.where(mapCov != 0)
```

```
medCov = MEDIAN(mapCov[selCov])
meanCov = MEAN(mapCov[selCov])
threshCov = meanCov - ABS(medCov - meanCov)
selCov = mapCov.where(mapCov > threshCov)

  # Isolate the pixels that are above a chosen sigma threshold (here we choose 3-sigma)

image = map1['image'].data.copy()
medFlux = MEDIAN(image[selCov])
sigFlux = STDDEV(image[selCov])
selSignif = image[selCov].where(image[selCov] > (medFlux + 3*sigFlux))

  # Create a mask. Pixels above the threshold are set to 1, the rest to 0

imaMask = map1['image'].data.copy()*0.0
tmp = imaMask[selCov]
tmp[selSignif] = 1.0
imaMask[selCov] = tmp

  # Display the map of the mask

map1 = photProject(framesC,calibration=True,calTree=calTree)
mapMask = map1.copy()
mapMask['image'].data = imaMask
Display(mapMask)
```

  # Flag the pixels of the cube corresponding to the bright regions isolated in the mask. Figure 8.9 shows an example of masking for the galaxy NGC6822 (red contours).

```
framesC = photReadMaskFromImage(framesC,mapMask,threshold=0.7,
           calTree=calTree, \extendedMasking=False)
objectMask = framesC.getMask('Highpassmask').copy()

  # Detect pixels that are both on source and masked

mmtMask = frames.getMask('MMT_Glitchmask')
objectGlitchMask = objectMask.copy().and(mmtMask)
objectGlitchPix = objectGlitchMask.where(objectGlitchMask == True)

  # Replace the interpolated signal of these pixels by the original signal

signal=frames.signal.copy()
signal[objectGlitchPix] = origSignal[objectGlitchPix]
frames.setSignal(signal)

  # Also cancel the masking of these pixels

mmtMask[objectGlitchPix] = False
frames.setMask('MMT_Glitchmask',mmtMask)
```

The map is now used to perform a second order deglitching of the data. So first, re-update the mask and high-pass filter the data

```
framesC = frames.copy()
framesC.setMask('UNCLEANCHOP',slewMask.or(ucl))
framesC = highpassFilter(framesC,leg_width/2)
```

Create the map-to-cube index

```
mi = MapIndexTask()
mapToCubeIdx = mi(framesC,slimindex=False)
```

Do sigma-clipping : thus detect isolated values that are above a given threshold and replace them by a 'comparator' (here the median value) - Perform the second order deglitching of the data

```
s = Sigclip(10, secondnsigma, behavior=``clip", outliers=``both",
            mode=Sigclip.MEDIAN)
iind = IIndLevelDeglitchTask()
map3 = iind(mapToCubeIdx, framesC, map=True, mask=True, maskname=
mask = framesC.getMask('SecondGlitchmask')
            'SecondGlitchmask', algo=s, \deglitchvector=secDegMethod)
```

Add this 2nd order deglitching mask to the frames

```
frames.addMaskType('SecondGlitchmask','Second level degtlitching')
frames.setMask('SecondGlitchmask',mask)
```

We will now build the final maps: We start again from 'frames'. Two techniques can be used: a simple projection of the data or the madmap procedure that is producing maximum likelihood sky maps from time ordered instrument data. Madmap is partly designed to remove 1/f noise effects.

—> *Classical projection*

Add the mask to the frames and high-pass filter the frames with a user-defined length HP_width

```
frames.addMaskType('OBJECT','Pixels that see the object')
frames.setMask('OBJECT',objectMask)
frames = highpassFilter(frames,HP_width,maskname='OBJECT',
            interpolateMaskedValues=True)
```

Saved the reduced frames - Project, display and save the final map

```
FitsArchive().save(str(obsid)+'_'+side+'_classicSavedForJoin.fits', frames)
mapClassic = photProject(framesC,calibration=True,calTree=calTree)
d = Display(mapClassic)
FitsArchive().save('mygalaxy_' + str(obsid)+'_'+ side +'_classicmap.fits',
mapClassic)
```
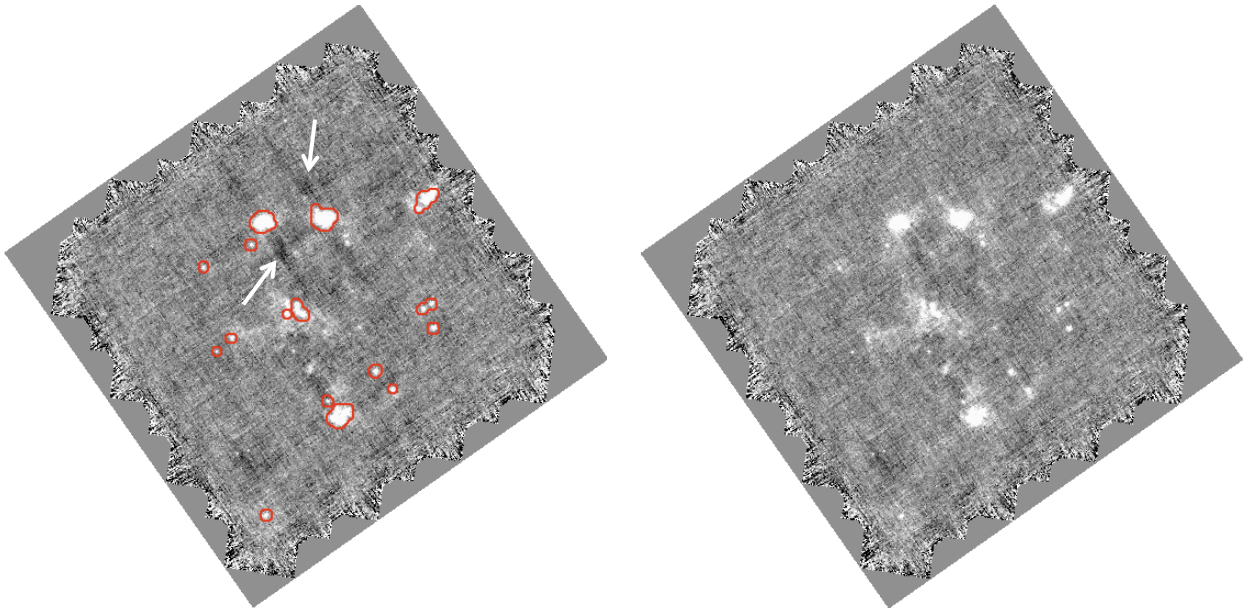
Figure 8.9. *Left:* Map of the galaxy NGC6822 in the blue band of PACS (70 μm). The reduction is performed in half a scan leg. The map is affected by dark artefacts (examples are indicated by white arrows) in the scanning direction of bright structures. The red contours show the mask, i.e. the data (bright structures) removed to perform the HP filtering and second deglitching processes. *Right:* Final map of NGC6822 when the mask is applied.

$\longrightarrow$ *Madmap method*

 # Assign (RA, Dec) coordinates to the data

```
frames = photAssignRaDec(frames, calTree=calTree)
```

 # Add the mask to the frames and high-pass filter the frames with a user-defined length HP_width

```
frames.addMaskType('OBJECT','Pixels that see the object')
frames.setMask('OBJECT',objectMask)
frames = highpassFilter(frames,HP_width, maskname='OBJECT',
            interpolateMaskedValues=True)
```

 # Saved the reduced frames - Create Time ordered data - Project, display and save the final map

```
FitsArchive().save(str(obsid)+'_'+side+'_madSavedForJoin.fits',frames)
scale = 1
crota2 = 0.0
tod = makeTodArray(frames, 1 , 0.0 ,optimizeOrientation=True)
maxRelError = 1.e-10
maxIterations = 500
mapMad = runMadMap(tod,calTree, maxRelError = ,maxIterations,False)
Display(mapMad)
```

```
FitsArchive().save('mygalaxy_' + str(obsid) + _'+ side +'_madmap.fits',
mapMad)
```

8.4 Observations in the chop-nod mode of PACS

8.4.1 Description of the mode

The chop-nod mode uses the PACS chopper to move the source by about 50" with a chopper frequency of 1.25 Hz. The nodding is performed by a satellite movement of the same amplitude but perpendicular to the chopping direction. On each nod-position, the chopper executes 3×25 chopper cycles, completed in less than 1 minute and the pattern is then repeated on the second nod-position (consecutive nod cycles in ABBA pattern). The 3 sets of chopper patterns can be on 3 different array positions (option: dither) or on the same array positions (no dithering).

8.4.2 Data reduction

We also used the environment HIPE to reduce chop-nod observations of extragalactic sources. The reduction pipeline we used is close to the default pipeline available in HIPE. We describe the different steps in the following lines. The pipeline starts with the level 0.5 data cube.

Steps of the reduction pipeline:

```
#Access to data corresponding to the obsid number XX.

obsid = XX
store = ProductStorage(LocalStoreFactory.getStore(``Mygalaxy"))
camera = 'blue'
q = MetaQuery (herschel.ia.obs.ObservationContext , ``p" ,
              ``p.meta['obsid'].value=="+str(obsid)+``L")
result = store.select(q)
obsCont = result[0].product
```

```
# Read the pointing, orbit ephemeris, time correlation products

hk = obsCont.level0.refs[``HPPHK"].product.refs[0].product[``HPPHKS"]
pointing = obsCont.auxiliary.pointing
orbitEphem = obsCont.auxiliary.orbitEphemeris
timeCorr = obsCont.auxiliary.timeCorrelation
```

```
# Initialize the Calibration Tree

calTree=getCalTree()
```

Get the level 0.5 data cube. Blue and red channel frames data are sliced in packets of one ABBA nodding cycle.

```
level0_5 = PacsContext(obs.level0_5)
slicedFrames = level0_5.averaged.getCamera(camera).product
pacsPropagateMetaKeywords(obs,'0.5',slicedFrames)
```

From here, a loop is initiated. The following lines are applied for each nod cycle.

```
noofsciframes=slicedFrames.numberOfScienceFrames

for i in range(noofsciframes):
```

  # Extract one slice, process and remove the calibration block

```
    framesnod = slicedFrames.getCal(0).copy()
    sciframesnod = slicedFrames.getScience(i).copy()
    framesnod.join(sciframesnod)
    framesnod = detectCalibrationBlock(framesnod)
    calBlock = photCSExtraction(framesnod)
    calBlock = photCSProcessing(calBlock,photHK,calTree)
    framesnod = photCSClean(framesnod,calBlock)
    framesnod = removeCalBlocks(framesnod)
```

  # Flag bad pixels and saturation and convert digital values to volts

```
    framesnod = photFlagBadPixels(framesnod,calTree=calTree
    framesnod = photFlagSaturation(framesnod,calTree=calTree,
                  hkdata=photHK,check='full')
    framesnod = photConvDigit2Volts(framesnod,calTree=calTree)
```

   # Adding UTC reference time frame - Convert chopper readout to angles and assign the
pointing - Mask frames affected by chopper movements

```
    framesnod = addUtc(framesnod, timeCorr)
    framesnod = convertChopper2Angle(framesnod,calTree=calTree)
    framesnod = photAddInstantPointing(framesnod,pp, calTree=calTree,
                  horizons=horizons)
    framesnod = cleanPlateauFrames(framesnod)
```

   # Determine readout frames per dither position - Correct pointing information and assign
(RA, DEC) coordinates

```
    framesnod = photMakeDithPos(framesnod)
    framesnod = photMakeRasPosCount(framesnod)
    framesnod = photAvgPlateau(framesnod,skipFirst=True,copy=1)
    framesnod = photAddPointings4PointSource(framesnod)
    framesnod = photAssignRaDec(framesnod,calTree=calTree)
```

   # Produce differentiated chopped signal - Average detector readouts per dither position and
subtract nodded signal - Average detectors readouts per nod position

```
framesnod = photDiffChop(framesnod)
framesnod = photAvgDith(framesnod,sigclip=3.)
framesnod = photDiffNod(framesnod)
framesnod = photCombineNod(framesnod)

# Perform a flatfield correction and calibrate the flux

framesnod = photRespFlatfieldCorrection(framesnod,calTree=calTree)

# Project all images onto a map and save maps into fits files

map = photProjectPointSource(framesnod, calTree=calTree,
             allInOne=1, calibration=True)
product = simpleFitsWriter(map,dir+'/PSmap_'+str(obsid)+'_'+
             camera+'_nod' + str(i) + '.fits')
```

```
# We will finally combine all the NOD cycles, mosaic, display and save the maps

for i in range(slicedFrames.numberOfScienceFrames):

   ima = simpleFitsReader(dir+'/PSmap_'+str(obsid)+'_'+camera+'_nod'
             +str(i)+'.fits'
   ima.exposure = ima.coverage
   images.add(ima)
   mosaic=MosaicTask()(images=images,oversample=0)
   Display(mosaic)
   simpleFitsWriter(mosaic,dir+''/PSmosaic_map_"+str(obsid)+''_"+
             camera+''.fits")
```
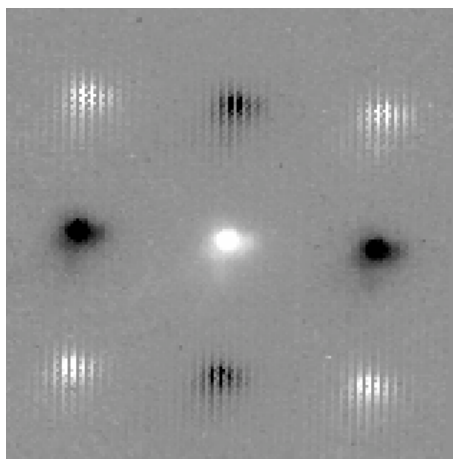

Figure 8.10. Chopped-nodded observation of the galaxy IIZw40 in the blue band

8.5   Buiding convolution kernels between PACS bands

As mentionned previously in this report, the PACS and SPIRE fluxes will be used to sample the SED of the galaxies we want to study. The different images have to share a common resolution so each map has to be convolved to the lowest common resolution. Gaussian kernels can be used to 'degrade' the resolution of maps to lower resolution. We want to construct convolution kernels to convolve PACS bands to the lowest PACS resolution (PACS 160 μm - 12"). If the PSFs of the different bands are correctly defined, you can try to build the real convolution kernels.

We obtained observations of Vesta in the three bands of PACS which shows that PACS PSFs are more complex than gaussians. We used the technique described in Gordon et al. (2008) for *Spitzer* bands but applied to PACS bands. This process is based on two-dimensional fast Fourier transforms (FFT). To avoid high-frequency numerical noise polluting the convolution kernel, the FFT of the initial PSFs is 'windowed' by a clamping function. The Hanning function H(ω) is thus used to filter high-frequencies and is defined as:

$$H(\omega) = \begin{cases} \frac{1}{2}\left[1 - cos(\frac{2\pi\omega}{\omega_0})\right] & \omega \leq \omega_0 \\ 0 & \omega > \omega_0 \end{cases} \tag{8.1}$$

with ω the radial spatial frequency and ω_0 the cuttoff radial spatial frequency.

The convolution kernel K(x,y) is thus defined as:

$$K(x,y) = FFT^{-1}\left[\frac{FFT[PSF_2(x,y)]}{H(\omega)FFT[PSF_1(x,y)]}\right] \tag{8.2}$$

with PSF_1 the initial PSF, PSF_2 the desired common resolution PSF, H(ω) the Hanning function defined above.

The value of ω_0 has to be optimized to suppress as much high-frequency noise as possible. The following lines describe how the process was implemented in IDL to build a convolution kernel from PACS 70 μm (blue) to PACS 160 μm (red).

IDL script :

```
; Define the speed of the telescope during your observations (the PSFs depend on this speed)
and the cutoff radial frequency of the hanning window we want to use.

speed = 20
N = 40
Initial_PACS = readfits('./vestapsf' + string(speed, format='I2.0') + 'blue.fits' , header_int )
Desired_PACS = readfits('./vestapsf' + string(speed, format='I2.0') + 'red.fits' , header_des )

; Normalize the PSFs - Calculate the FFTs

Initial_PACS = Initial_PACS / total (Initial_PACS)
Desired_PACS = Desired_PACS / total (Desired_PACS)
fft_Initial_PACS = dft (Initial_PACS)
```

```
fft_Desired_PACS = dft (Desired_PACS)

; Define the Hanning function

size = size (fft_Initial_PACS)
o = origin (fft_Initial_PACS)
conv_function = fltarr(size[1],size[2])
conv_function ( o[0]-N : o[0]+N , o[1]-N : o[1]+N ) = hanning ( 2*int+1 , 2*int+1 )
hanning = conv_function

; Build the convolution kernel (apply the formula 8.2) and save the result.

inv_fft_Initial_PACS = 1 / fft_Initial_PACS
inv_fft_Initial_PACS_H=inv_fft_Initial_PACS*hanning
FFT_K = fft_Desired_PACS * inv_fft_Initial_PACS_H
K = (dftinv_SP(FFT_K))
PACSconv = convolve(PACSint,K1)
Result_fits = './kernel_PACS1_to_PACS3_speed'+ string(speed, format='I2.0')+'_N'+ string(N,
format='I2.0').fits'

writefits , Result_fits , real_part(K) , header_int
```

Figure 8.11 shows an example of a convolution kernel obtained to convolve a PACS 70 μm band to the PACS 160 μm resolution. The windowing parameter of the Hanning function (N in our script) is 40 in this example. Radial profiles of the different PSFs, of the convolution kernels and on the convolution of PACS 70 μm PSF convolved with our convolution kernel are also shown. The PACS 70 μm PSF convolved with the kernel (red dashed line) is optimized, playing with the parameter N, to be close to the PSF of PACS 160 μm (black line).
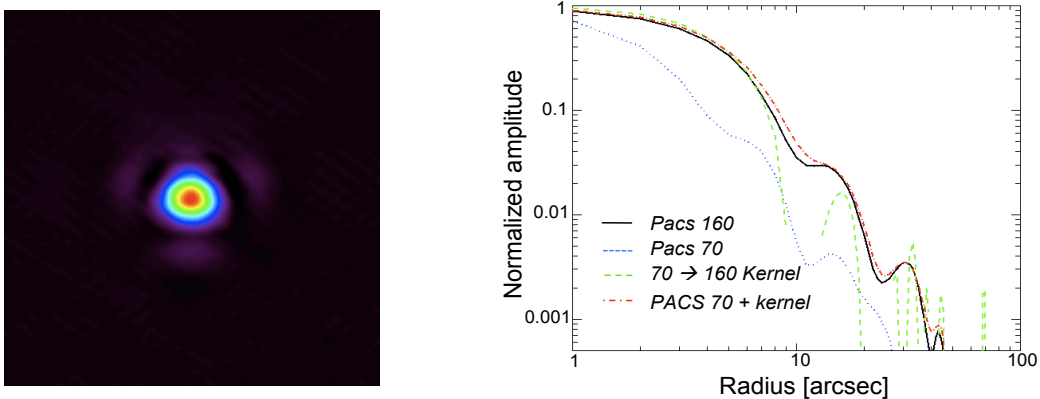
Figure 8.11. *Left:* Convolution kernel between PACS 70 and PACS 160 μm (windowing: N=40). *Right:* Radial profiles of the 70 and 160 μm PACS PSFs, the 70-to-160 μm kernel and the PACS 70 μm convolved with this kernel.

In our analysis, we mainly used kernels to convolve PACS and SPIRE bands to the lowest resolution of our data, namely that of MIPS 160 μm (40"). The kernels to 'degrade' PACS images to the

MIPS 160 μm resolution were built by G. Bendo, from Imperial College, for the SAG2 consortium. We finally used Gaussian kernels to convolve the SPIRE maps to the MIPS 160 μm resolution. The latest convolution kernels between *Spitzer* and *Herschel* bands are available on Karl Gordon's website: http://dirty.as.arizona.edu/~kgordon/mips/conv_psfs/conv_psfs.html.

These data treatment techniques allow us to take data from the ESA archive and apply complete data treatment on PACS and SPIRE data and to create a harmonious data set sampling the area. Now, we can study the full dust SEDs with *Spitzer* and *Herschel* observations.

Chapter 9

# A new glance on the irregular low-metallicity NGC 6822

Contents

9.1 NGC 6822

NGC6822 is one of our closest (490 kpc; Mateo 1998) metal-poor galaxy neighbours ($\sim 30\% \ Z_\odot$) beyond the Magellanic Clouds and possesses isolated star forming regions at different evolutionary stages (Fig. 9.1). The galaxy is a perfect candidate to study the feedback of star formation on the low-metallicity ISM by analysing the spatial variations of its SEDs, as we started to do in Chapter 7 in the LMC.
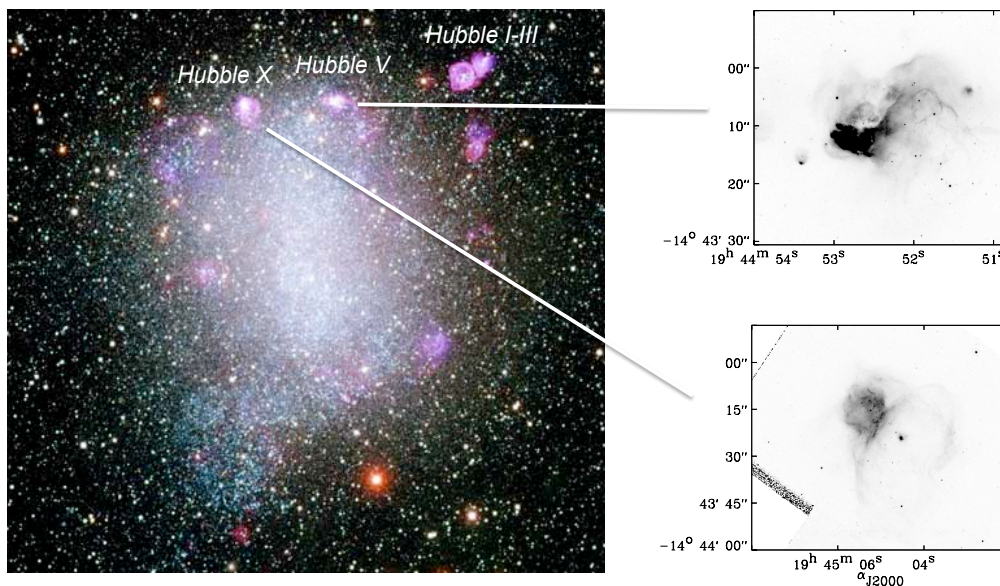
Figure 9.1. 8-Color image of NGC6822: U in violet, B in blue, V in green, R in orange, I in red, Hα in red and Oxygen [OIII] in green (Credits to NOAO/AURA/NSF). A few Hɪɪ regions are indicated. The two brightest Hɪɪ regions Hubble V and X observed with HST F656 are plotted on the right.

NGC6822 has low star formation throughout the disk but very bright star forming regions associated with strong Hα emission (Hunter & Elmegreen 2004). de Blok & Walter (2006) estimated the Hα flux to be 2×10^{39} ergs s^{-1}. The early star formation has been quite smooth until ~ 1 Gyr ago (Wyder 2003). Bianchi & Efremova (2006) focuses on the youngest stellar population of NGC 6822 and found, however, that the recent current star formation seems to occur episodically, showing extreme variations spatially and in time.

The galaxy also possesses an intriguing rotating Hɪ disk of $1.34 \times 10^8 \ M_\odot$ (de Blok & Walter 2000), that extends far beyond the optical disk (Mateo 1998) and has one of the largest Hɪ holes ever observed in a dwarf galaxy (Fig. 9.2). de Blok & Walter (2006) indicate that the old and intermediate stellar populations extend outside the Hɪ disk of the galaxy while younger stars seem to follow this HI disk . They also found evidence that the properties of the giant Hɪ hole observed in NGC 6822 are consistent with it being created by the past star formation activity (color gradients in the stellar population).

NGC 6822 was observed for the first time in the IR by *IRAS*. Using these observations, Gallagher et al. (1991) noted a good spatial correlation between the far-IR and the Hα emission. They found that the far-IR-to-Hα emission varies significantly between the different Hɪɪ regions, up to a factor of 5.

The main structures of the ISM of NGC 6822 have then been observed and resolved by *Spitzer* more than a decade later as part of the SINGS project, producing images with a resolution of ∼130 pc at 160 μm. The *Spitzer* images are shown and described in detail in Cannon et al. (2006a). They
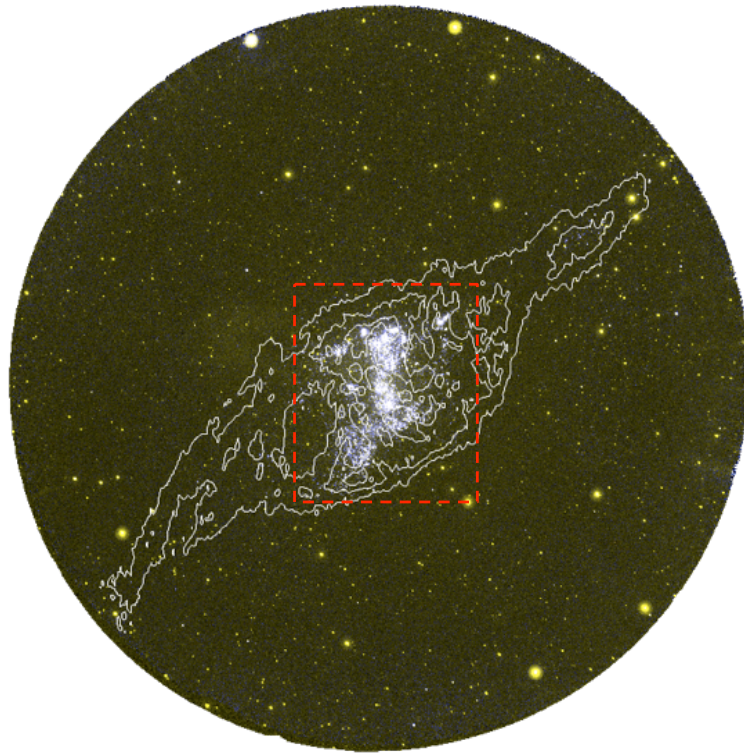
Figure 9.2. NGC6822 observed in UV with GALEX. The far-UV band (1539 $\mathring{A}$) appears in blue and the near-UV (2316 $\mathring{A}$) band appears in yellow. GALEX images have been reduced and provided by Luca Cortese. The extended H I contours of NGC 6822 at 3.1, 7.8 and 13 $\times 10^{20}$ atom cm^{-2} are overlaid in white (de Blok & Walter 2000). The H I covers 1° $\times$ 24'. The red box indicates the central region mapped by *Herschel*.

performed a global and local study of the dust properties within the galaxy. They, in particular, found that 50 % of the L$_{TIR}$ ($\sim$4.3 $\times 10^7$ $L_\odot$) was emitted in the form of discrete far-IR sources.

They also suggest that the galaxy, like other resolved low-metallicity galaxies, could follow a different 24 μm versus Hα luminosity trend than normal spirals. They explained this result by 1- a lack of metals that could prevent the galaxy to form the same quantity of dust as spiral galaxies 2- a massive amount of cold dust not heated by the current star formation. They also performed SED modelling of the galaxy (using the Dale et al. (2001) and Draine & Li (2001) models) and estimated the local D/G across the galaxy. The global D/G was found to be $\sim$ 25 times lower than in spiral galaxies. They derived a global D/G of 8 $\times 10^{-4}$ but also note uncertainties of a factor $\sim$ 2 level. These uncertainties are partly linked with the lack of submm constraints on the SEDs and thus the difficulty to quantify the total dust mass of the galaxy and its substructures. *Herschel* observations were thus crucial to complete the far-IR to submm coverage of the SED of NGC 6822 and locally resolve the dust coldest phases.

In our SAG2/DGS sample of low-metallicity galaxies (see section 8.2), NGC 6822 was thus an obvious target to point at first during the *Herschel* Science Demonstration phase. A letter describing this study was accepted for publication in the A&A Special Issue on *Herschel* first results (Galametz et al. 2010).

9.2 PACS observations

The PACS observations of NGC 6822 were performed as part of the Science Demonstration phase in October 2009. Observations were taken in scan mapping mode in the three bands of *Herschel*/PACS (70, 100 and 160 μm). The observations cover a region of 18' × 18' around the center of the galaxy where its IR emission resides, a region which is similar to the area mapped by *Spitzer*.

The steps of the PACS data reduction are described in § 8.3. The basic reduction leads to the emergence of dark artefacts close to the bright structures of the galaxy in the scanning directions (see Fig. 8.9). Data corresponding to these bright sources are masked in the data cube beforehand to avoid these numerical effects. The maps we use have standard pixel sizes of 3.2", 3.2" and 6.4" at 70, 100 and 160 μm with PSF FWHM values of 5.2", 7.7" and 12" respectively (corresponding to <30 pc structures). The absolute flux calibration uncertainties are estimated to be of the order of ± 10%.

Figure 9.3 shows detailed views of bright H<small>II</small> regions of the galaxy observed with PACS at 70 and 160 μm. The FWHM of the PSFs of both MIPS 70 and 160 μm and PACS 70 and 160 μm are overlaid. The MIPS images are also shown in Fig. 9.4 along with the final PACS maps of NGC 6822. We clearly observe how PACS resolves the different structures of the ISM compared to the resolution that MIPS could reach for the same wavelengths. Substructures are separated with PACS and diffuse emission is detected. A median baseline filtering technique was used during the PACS data reduction to diminish the striping but this process may remove some of the diffuse emission.

9.3 The SPIRE images

The SPIRE observations of NGC 6822 were also carried out as part of the Science Demonstration observations. They have been taken in scan mapping mode and are covering a region of 26' × 26' in the three bands of *Herschel*/SPIRE (250, 350 and 500 μm). At SPIRE 500 μm (36"), ISM structures down to ∼ 85 pc can be resolved. This will permit us to accurately probe the distribution of dust temperature throughout the galaxy down to very cold dust phases.

During my PhD, I directly used the SPIRE images generated by Michael Pohlen for the SAG2 team. Data have been reprocessed from the level 1 cube following the different steps described in Pohlen et al. (2010) and Bendo et al. (2010). The overall absolute calibration accuracy of the final SPIRE maps is estimated to be ± 15% (Swinyard et al. 2010). The maps we use have pixel sizes of 6", 10" and 14" at 250, 350 and 500 μm with PSF FWHM values of 18", 25" and 36" respectively (corresponding to <85 pc structures). The ICC has released preliminary multiplying factors to correct the calibration of the SPIRE fluxes: 1.02, 1.05 and 0.94 at 250, 350 and 500 μm.

The final SPIRE maps are shown in Fig. 9.4.

9.3.1 Estimation of the Cirrus contamination

The three SPIRE maps look very similar and resolve the structures already detected with *Spitzer*/MIPS and *Herschel*/PACS bands. As previously detected in *IRAS* and MIPS maps by Gallagher et al. (1991) and Cannon et al. (2006a) respectively, foreground emission from the Milky Way is significant in the line of sight of the galaxy (due to the low Galactic latitude of NGC 6822) and SPIRE maps are thus strongly affected by Galactic emission of highly non-homogeneous cirrus.

To estimate the contamination due to cirrus emission, we first mask the emission that we associate with the galaxy in each map. We model the cirrus emission by fitting a plane to the rest of
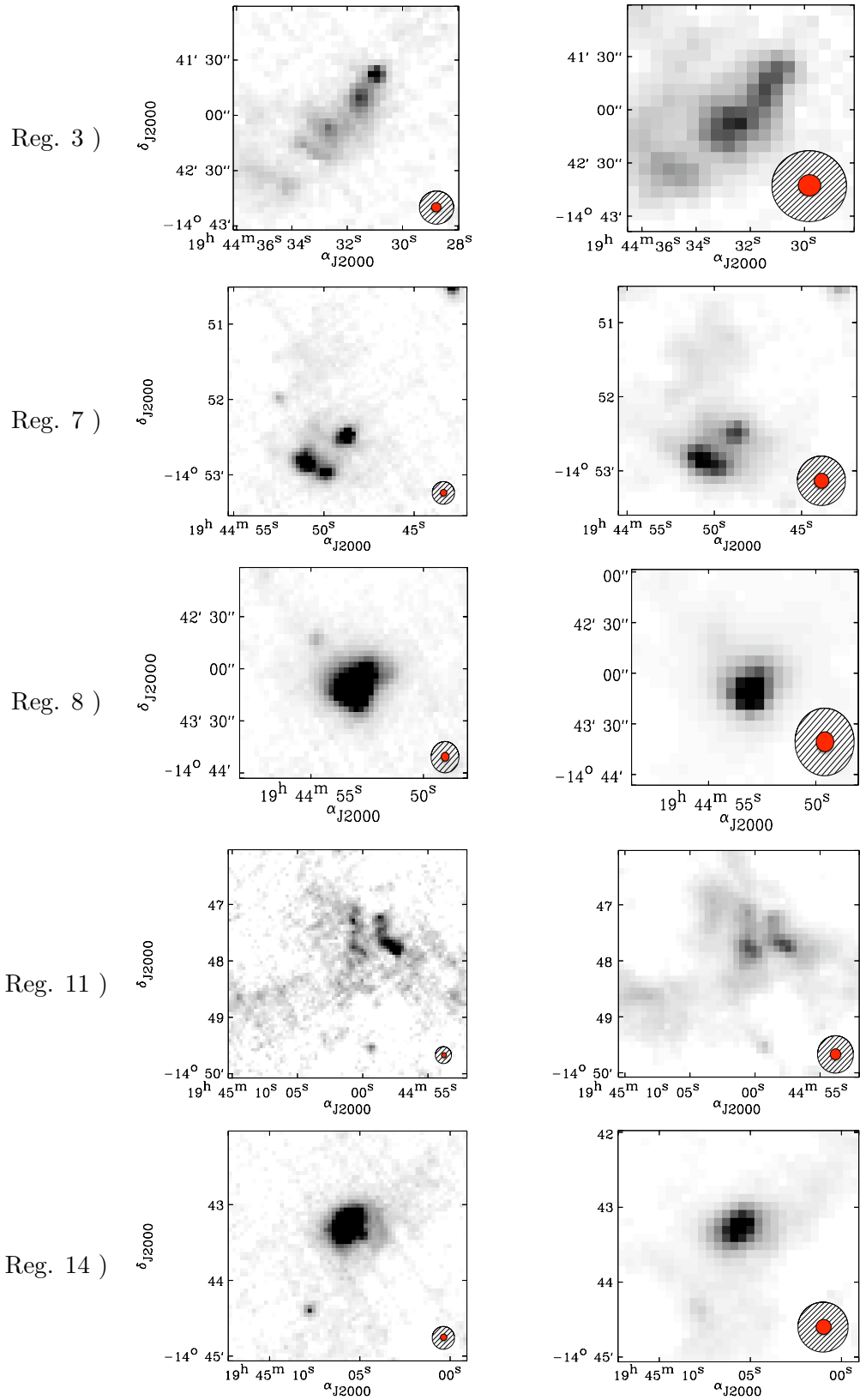
Figure 9.3. PACS 70 μm (left) and 160 μm (right) observations of bright star-forming regions of NGC 6822. These regions are numbered (from top to bottom) 3, 7, 8 (Hubble V), 11 and 14 (Hubble X) in Fig. 9.6. The FWHM of *Spitzer*/MIPS 70 and 160 μm PSFs (black striped circles) and those of PACS 70 and 160 μm (red circles) are overlaid for comparison.

151
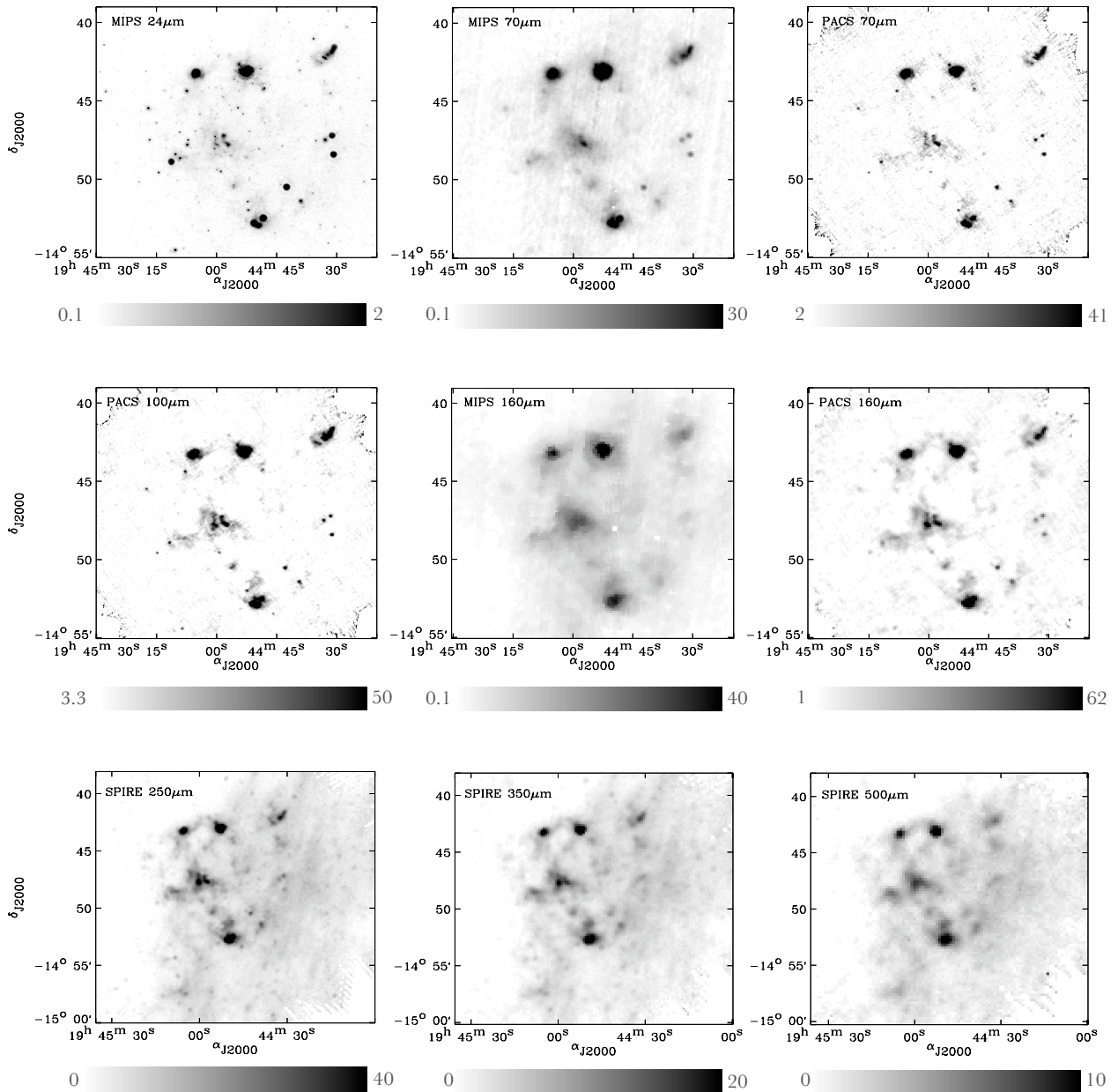
Figure 9.4. NGC 6822 observed by *Spitzer*/MIPS, *Herschel*/PACS and SPIRE. Fluxes are in MJy/sr.

the map and interpolate it across the area of the galaxy. We finally subtract this 'modelled' cirrus emission from the SPIRE maps. Figure 9.5 summarizes the technique with images.

The cirrus contamination is estimated to be less than 10% of the flux densities of the bright star-forming regions at 250 and 350 μm. It is inferior to 15% and 25 % on the less active regions respectively at 250 μm and 350 μm. The contamination is finally estimated to be $\sim$ 25 % on the bright regions at 500 μm but can be as high as $\sim$ 50 % of the emission in the diffuse ISM, which constitutes the main source of uncertainties on the 500 μm flux estimates of these regions. Taking all the uncertainties into account, we adopted an overall conservative error estimate of $\sim$ 30% for all SPIRE bands.

Image with Cirrus

Isolate the structures that belong to the galaxy

Fitting plane

Image with cirrus removed
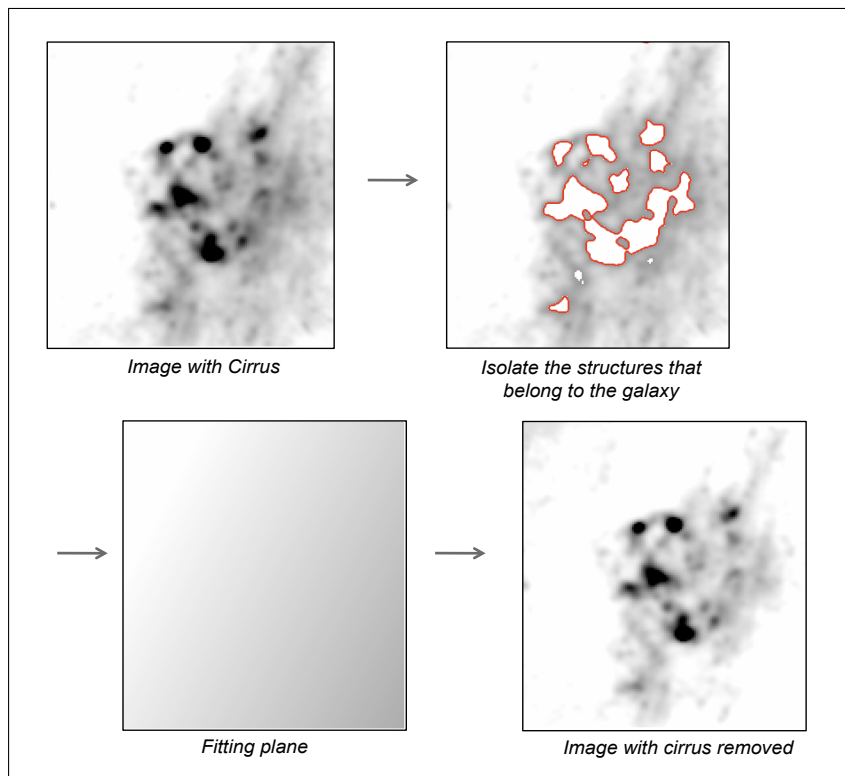
Figure 9.5. Scheme of the cirrus estimation process. The structures that are associated with the galaxy are isolated. A plane is then fitted to what is considered to be cirrus emission. The plane is then subtracted from the data.

9.3.2 SPIRE Ratio maps

From the maps corrected for cirrus contamination, we built the ratio maps of the three different SPIRE bands of NGC 6822. These ratio maps are used to diagnose the local variations of the submm regime of the SEDs and thus the cold dust temperature distribution within the galaxy.

The 250 μm SPIRE map was deconvolved and regridded to the resolution and grid of the SPIRE 500 μm map (FWHM of the PSF: 36") . Figure 9.6a shows the 250 / 500 flux density ratio map. We clearly observe that the 250 / 500 flux density ratio is higher in the H ii regions than in the fainter regions, with Hubble V (Reg. 8) showing the highest ratio. This ratio map, as mentioned previously, permits us to observe the evolution of the dust temperature distribution across the galaxy: Dust seems to be warmer toward the bright star forming regions and reaches lower temperatures in the diffuse extended medium between these regions.

To better understand the processes contributing to the heating of dust, we examine how the submm part of the SED evolves with star formation. We select individual regions and estimate the SPIRE 250 and 500 μm flux densities of these regions in apertures of 57" radius. The circles overlaid in Fig. 9.6b indicate these photometric apertures (Cannon et al. 2006a). In Fig. 9.7, we plot the 250 / 500 flux density ratio of the selected regions as a function of their 24 μm surface brightness as well as all of the points throughout the galaxy. Indeed, the 24 μm flux is commonly used as a tracer of star formation (Calzetti 2007).

The submm ratio seems to correlate with the 24 μm surface brightness across NGC 6822, which could imply that the cold dust temperature distribution varies with star formation activity of the
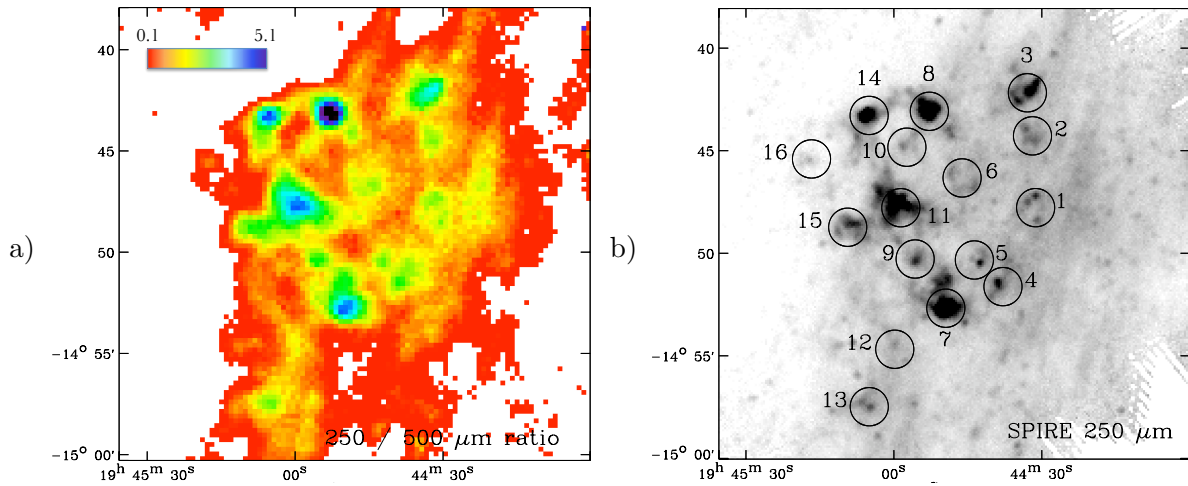
Figure 9.6. *a)* 250 / 500 μm flux density ratio map of NGC 6822 with cirrus removed. *b)* NGC 6822 observed at 250 μm. Circles indicate our selected regions (circles have the size of the photometric apertures (57" radius) we used. These regions correspond to the regions of interest defined in Cannon et al. (2006a). Hubble V and X are numbered 8 and 14 respectively.

region, with dust grains having higher temperatures where the star formation activity dominates (Boselli et al. 2010). Bendo et al. (2010) find that the SPIRE ratios in M81 depend on radius, and that the old stellar population of the bulge and disk could be the primary source for the dust emission seen by SPIRE. In their paper, their submm ratios do not show any strong correlation with surface brightness. This difference with NGC 6822 suggests that the dust heating processes may differ from normal dusty spirals to dwarf galaxies. Indeed, the ISM of dwarfs is less opaque than spirals, with dense SF regions usually influencing the whole galaxy. Moreover, these galaxies usually contain less evolved stars. The SF history of M81 and NGC 6822 are also radically different.
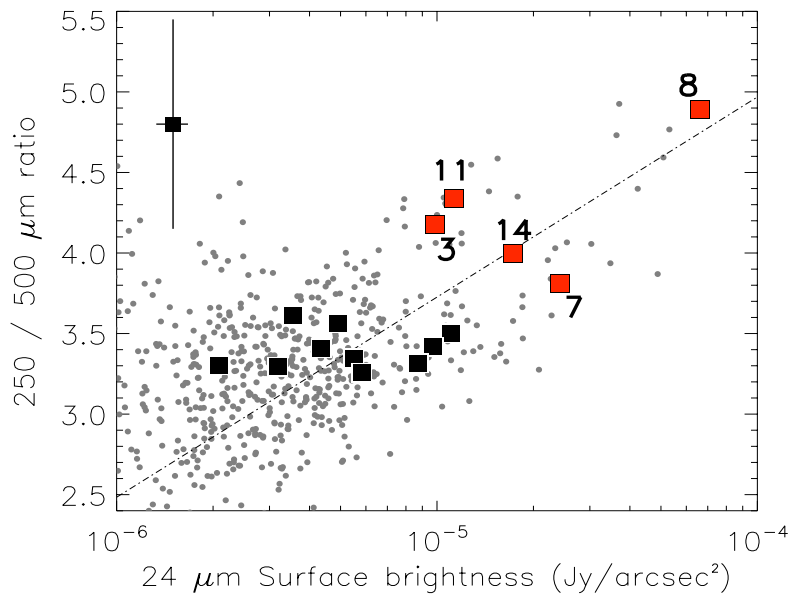
Figure 9.7. $F_\nu(250) / F_\nu(500)$ μm ratio as a function of the 24 μm surface brightness for our 16 selected regions across NGC 6822. The bright star forming regions are plotted as red squares. Since the uncertainties in the SPIRE fluxes are preliminary at this stage, we give an indication of the error bars in the upper left corner.

9.4 Individual SEDs and dust masses

To study the variations of the local SEDs, we select two H II regions (Hubble V and X, numbered 8 and 14 in Fig. 9.6b) and three less active regions (Reg. 6, 9 and 13 in Fig. 9.6b). As mentioned previously, we suspect that the median filtering technique applied during the PACS reduction may have removed some of the diffuse emission. It is consistent with the fact that we systematically find lower PACS fluxes than MIPS fluxes at the same wavelength for the faintest regions for this analysis. PACS fluxes were thus not used yet in the modelling of the less active regions or in the total SED. IRAC and MIPS observations (SINGS 5th release; Kennicutt et al. 2003) complete the SED coverage. We convolve the images to the MIPS 160 μm resolution (40") and estimate the flux densities within 57" radius apertures.

Table 9.1. Integrated flux densities of total and individual regions of NGC6822 measured with *Herschel* and *Spitzer*.

			Total	8	14	6	9	13
IRAC	3.6 μm	*(mJy)*	2062.7	64.5	32.8	56.2	62.9	10.9
IRAC	4.5 μm	*(mJy)*	1352.6	50.7	24.3	38.1	42.7	-
IRAC	5.8 μm	*(mJy)*	1349.2	58.0	30.1	35.5	38.8	7.4
IRAC	8.0 μm	*(mJy)*	1382.7	84.9	34.6	29.0	34.3	-
MIPS	24 μm	*(mJy)*	1859.8	674.8	176.0	44.5	50.0	30.0
MIPS	70 μm	*(Jy)*	39.5	5.7	3.0	0.7	1.2	0.05
PACS	70 μm	*(Jy)*	-	7.9	3.4	-	-	-
PACS	100 μm	*(Jy)*	-	10.4	4.5	-	-	-
MIPS	160 μm	*(Jy)*	100.7	6.7	3.7	1.9	2.3	1.7
PACS	160 μm	*(Jy)*	-	9.0	4.0	-	-	-
SPIRE	250 μm	*(Jy)*	70.4	7.0	3.6	2.0	2.1	1.9
SPIRE	350 μm	*(Jy)*	38.1	3.3	1.8	1.1	1.1	1.0
SPIRE	500 μm	*(Jy)*	20.9	1.4	0.9	0.6	0.6	0.05

We use our SED model described in Chapter 2 to analyse the dust properties in the galaxy. One of the first points to note here is that no submm excess seems to be detected (neither locally nor globally) in NGC 6822, contrary to other dwarf galaxies observed with *Herschel* (O'Halloran et al. 2010; Grossi et al. 2010). We find that the SEDs of the two bright H II regions show warmer dust temperatures than the less active regions. The total SED of NGC 6822 (see Fig.9.9) does not show a high 24/70 ratio, indicating that it may not be dominated by the IR emission of bright H II regions.

The dust masses derived are quite high compared to what was derived in the study of Cannon et al. (2006a) based on *Spitzer* data with constraints up to 160 μm only. As mentioned in Chapter 7, we tried to use amorphous carbons to model carbon dust. Fig. 9.9 presents the new global SED of NGC 6822 along with the individual SEDs of the 5 selected regions obtained now with amorphous carbon dust. The dust masses using graphites are 2.2 to 2.8 times higher than those using amorphous carbons (Table 9.2), due to their lower emissivity at submm wavelengh. The same technique was applied in the LMC by Meixner et al. (2010) since a dust emissivity index of β=2 was not sufficient to explain the SPIRE fluxes they obtained without leading to incoherent D/G compared

to the elemental abundances of the LMC.
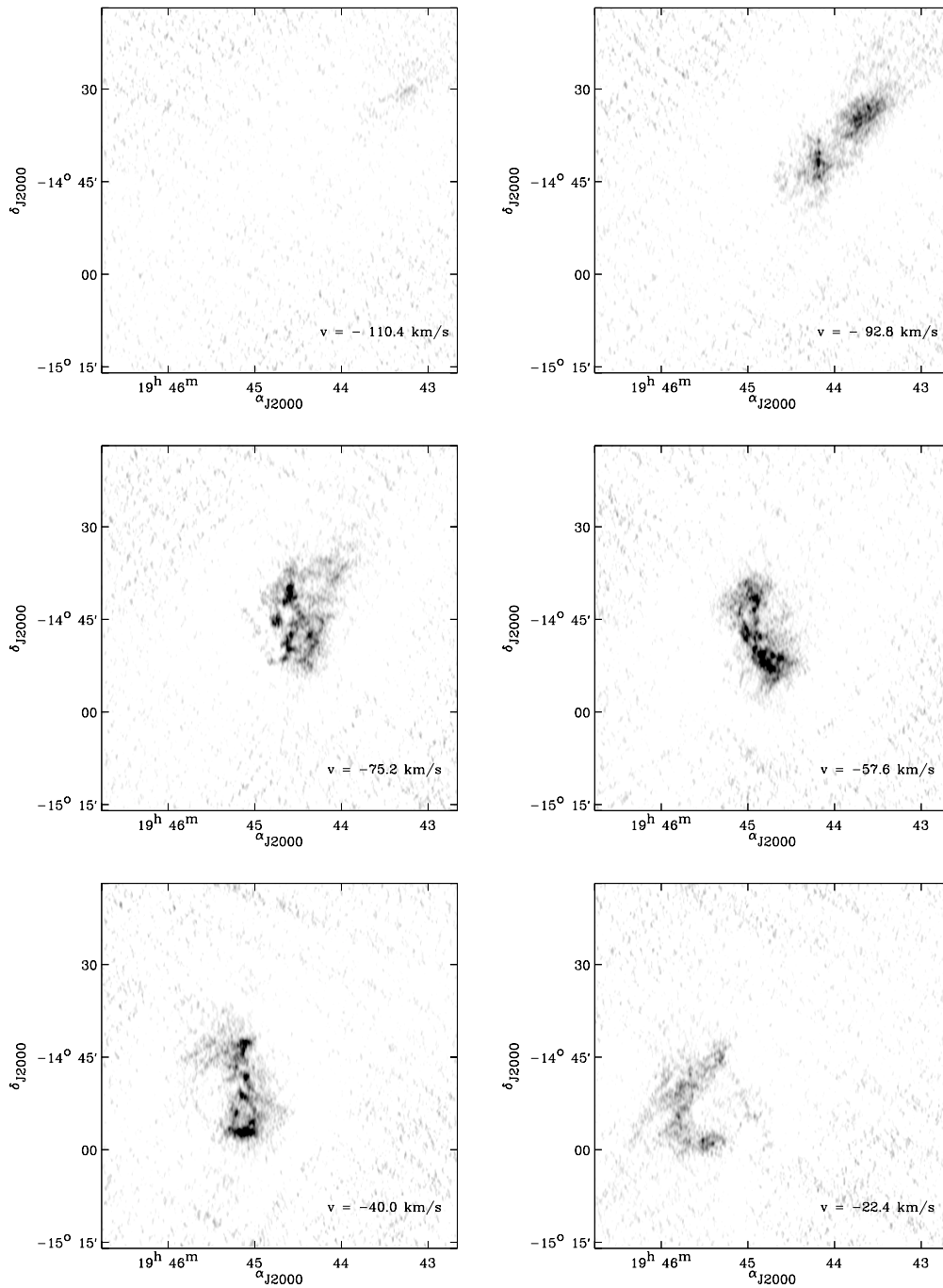
Figure 9.8. Examples of individual channel maps of the H I data cube of NGC 6822. We thank Prof. Erwin de Blok for his H I data cube. The heliocentric velocities are indicated in the bottom right corner.

9.5 The gas mass in NGC6822

Individual channel maps of the H I data cube of NGC 6822 are shown in Fig. 9.8. We derive the H I mass of our regions from the integrated map of de Blok & Walter (2000). Our original map is in Jy/beam km s^{-1}.

We convert our numbers in K km s^{-1} using the correspondance 1Jy/beam = 1190.5 K (Cannon et al. 2006a). The column density is then obtained using:

$$N_H^{HI,thin} \ (Hcm^{-2}) = 1.82 \times 10^{18} \ W_{HI} \ (K \ km \ s^{-1}) \tag{9.1}$$

We then convert the number of atoms in solar mass. We finally multiply the gas masses by 1.4 to take the helium contribution into account, as described in Cannon et al. (2006a). The H I mass can be found in Table 9.2.

Gratier et al. (2010) found that H_2 derived from CO observations in NGC 6822 should not represent more than 10^7 $M_\odot$. Weak emission from warm H_2 is detected in Hubble V (Hunter & Kaufman 2007). Cannon et al. (2006a) note that the mid-IR major H II regions correspond to the strongest Hα sources of the galaxy. From their Hα fluxes, we derive an Hα mass inferior to 10^5 $M_\odot$ in the H II regions (Storey & Hummer 1995, assuming T=10^4 K and N$_e$=100). We conclude that the H I mass should thus dominate the total gas mass in NGC 6822.

9.6 Graphite versus amorphous carbon ?

The Dwek (1998) models, presented in Galliano et al. (2008), predicts a D/G of $\sim 2 \times 10^{-3}$ for galaxies with the metallicity of NGC 6822 (~ 30 %). We find high D/G (Table 9.2) for the individual regions compared to what can be expected from chemical evolution models, especially when graphite grains are used in the modelling. As mentionned in Chapter 7, using amorphous carbon (AC) lead to a flatter submm slope and thus require less mass to produce the same emission. The dust masses derived using amorphous carbon to describe the carbon dust in our model thus systematically lead to lower dust masses. These results, along with similar results found by Meixner et al. (2010) for the LMC could be the last evidence to herald new dust grain properties (especially emissivity) and abandon graphite in our future SED models.

The total dust mass of the central region of NGC 6822 mapped with *Herschel* is $\sim 2.7 \times 10^5$ $M_\odot$ using amorphous carbon. We estimate the H I mass contained in the same region to be $\sim 5 \times 10^7$ $M_\odot$. These two values lead to total D/G value of 5×10^{-3}, more consistent (but high by a factor of 2) with that expected by current chemical models. These results suggest that standard graphite and maybe also the silicate grains used in our model, may not be the most appropriate description of the dust properties of NGC 6822.

9.7 Conclusions

I was very lucky to lead the *Herschel* Special Issue paper on NGC6822, one of the most intruiguing low-metallicity galaxies of the Local Group. Its proximity enables *Herschel* to resolve ISM structures up to the SPIRE 500 μm band. We obtained PACS and SPIRE observations of the galaxy at 70, 100, 160, 250, 350 and 500 μm. This paper and the short deadline of the Special Issue papers enabled me to quickly get up to speed with *Herschel* and more especially the PACS reduction pipelines with the software HIPE and the issues linked with the reduction of extended sources and diffuse emission similar to what is encountered by researchers working on Galactic regions.
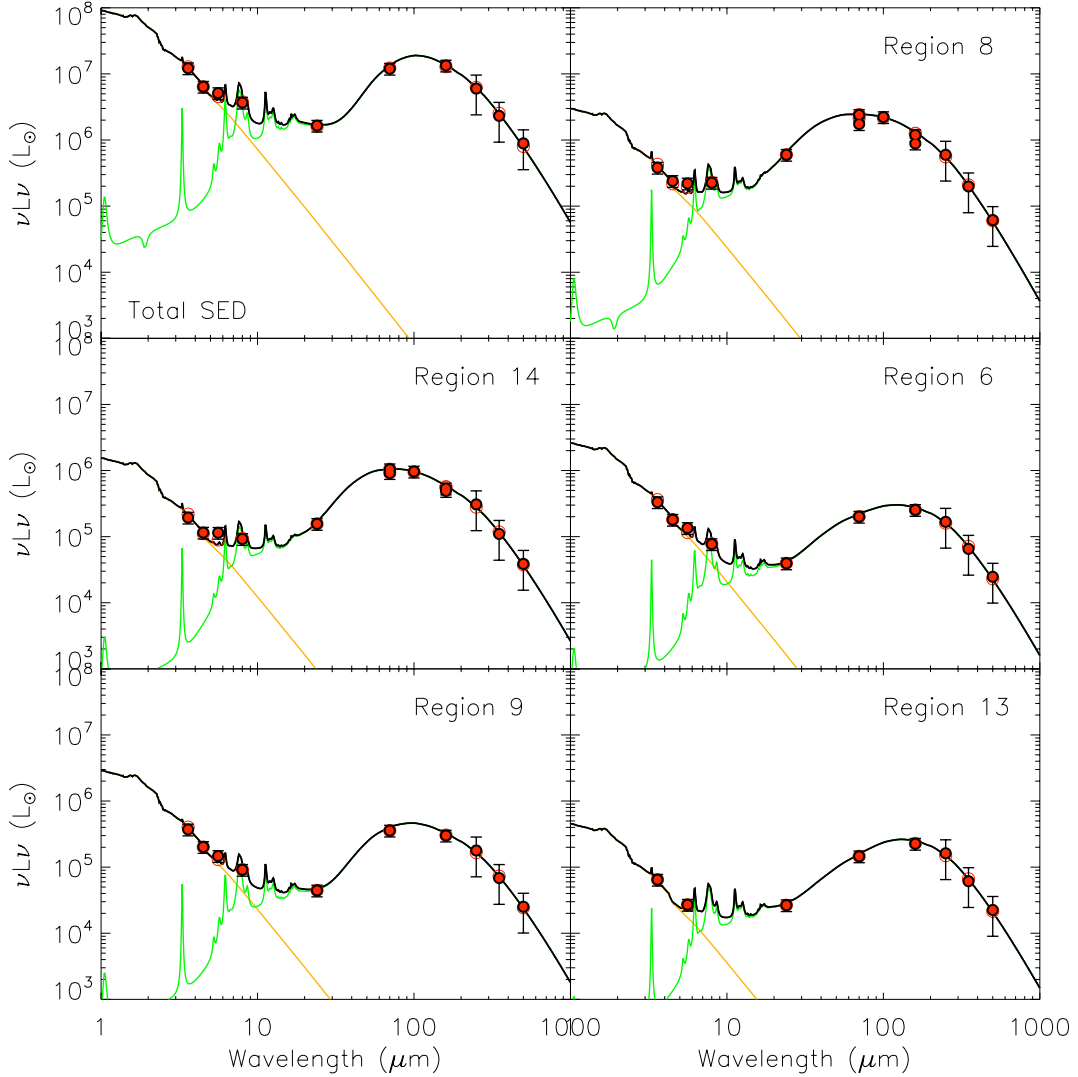
Figure 9.9. Total SED of NGC 6822 and SEDs of individual regions among which bright H II regions (Region 8 and 14) and less active regions (Regions 6, 9 and 13). Our SED models using amorphous carbon instead of graphite are plotted in black. Observational constraints are overlaid in red circles. The orange and green lines distinguish the stellar and the dust contribution. The 30% uncertainties are conservatively estimated for the SPIRE bands.

We completed the coverage with *Spitzer* data to constrain the near to mid-IR part of the SED. The SPIRE maps are contaminated with Galactic cirrus emission that had to be modeled and removed from the maps. We first find that the 250-to-500 flux density ratio, which is tracing the cold dust temperature range, may depend on the 24 μm surface brightness and thus could be a good tracer of star forming activity, in contrast to spiral galaxies. We model individual SEDs across NGC6822 and show that the SED shape is evolving significantly from H II regions to less active regions, with H II regions having a warmer dust temperature range, as first noticed in Chapter 7 in the N158/N159/N160 complex. We derive very high dust masses using graphite to describe carbon dust and find that the use of amorphous carbon decreases the dust masses, indicating that SED models including *Herschel* constraints require different dust properties, namely higher emissivity grains. *Herschel* may provide the data that finally herald the arrival of amorphous carbon dust in

Table 9.2. Derived properties

Id	M_{HI} $(10^5\ M_\odot)$	$M_{dust\ Gr}$ [a] $(10^3\ M_\odot)$	$M_{dust\ Gr}$ / M_{HI}	$M_{dust\ AC}$ [a] $(10^3\ M_\odot)$	$M_{dust\ AC}$ / M_{HI}
8	7.6	22.2^{+7}_{-6}	2.9×10^{-2}	7.8^{+3}_{-3}	10^{-2}
14	9.1	23.0^{+8}_{-7}	2.5×10^{-2}	10.2^{+4}_{-4}	1.1×10^{-2}
6	5.8	14.1^{+5}_{-4}	2.4×10^{-2}	5.3^{+2}_{-2}	9×10^{-3}
9	7.7	22.1^{+5}_{-5}	2.9×10^{-2}	8.5^{+3}_{-4}	10^{-2}
13	7.8	12.9^{+5}_{-3}	1.7×10^{-2}	4.7^{+3}_{-3}	6×10^{-3}
Total	500 [b]	612^{+105}_{-182}	1.2×10^{-2}	269^{+143}_{-145}	5.3×10^{-3}

[a] Dust mass derived using graphite (Gr) or amorphous carbon (AC).

[b] HI mass corresponding to the region mapped with *Herschel*.

models and the demise of graphite, which we have used for decades in our dust description of the Galaxy.

We would like, in the future, to observe the external regions (HI disk extension) of NGC 6822 that has never been mapped with any IR-instruments similar to what is offered by *Herschel*. We would like to study the diffuse emission of the galaxy far from its star forming regions and see if any IR emission is detected close to the HI hole. We would also like to obtain a bigger submm map to improve our model of the cirrus emission across the galaxy, contamination that is currently the main source of uncertainty of our flux densities and thus on our dust masses. The galaxy was also observed with LABOCA. The 870 μm constraints would help us to completely sample the submm slope and thus constrain the grain properties (e.g. emissivity) and to explore the coldest dust phase.

The following chapter briefly describes the study we perform on the *Herschel* data of another low-metallicity galaxy, NGC 1705, that was first addressed in this report in Chapter 5.

# Chapter 10

NGC 1705 observed with *Herschel*

Contents

In this Chapter, I will briefly present the new observations of NGC 1705 observed by *Herschel*.
This study was performed with Brian O'Halloran, from Imperial College, London (UK), who is
the PI of the A&A Special Issue paper on NGC 1705 (O'Halloran et al. 2010). My contribution
resides in the reduction of the PACS observations and the SED modelling of the galaxy.

10.1   *Herschel* images
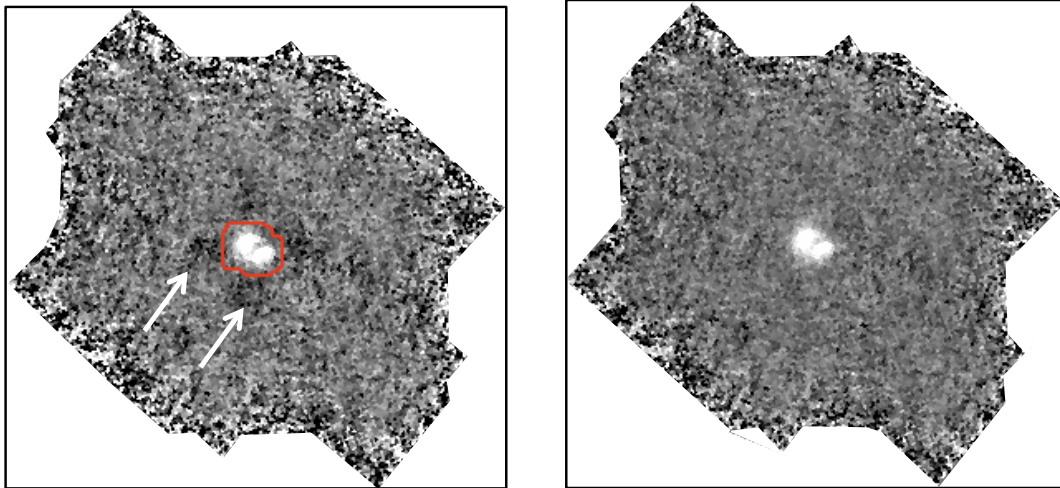
Figure 10.1. *Left:* Map of NGC 1705 observed in the blue band (70 μm) affected by dark artefacts in the
scanning direction. The red contour indicates the data (bright emission) we removed from the cube in the
HP filtering steps. *Right:* Final map of NGC 1705 with masking.

NGC 1705 was already presented in Chapter 5 in which we were studying the LABOCA obser-
vations of the galaxy (Galametz et al. 2009). It was observed with the PACS instrument in the
three bands (70, 100 and 160 μm) in scan-map mode on October, 24th and 25th, 2009 as part of
the Science Demonstration Phase. The observations cover a region of 7 by 6 arcmin. We refer to
Chapter 8 for a complete description of the data reduction process of the PACS data. The main
problem of the PACS reduction of the NGC 1705 observations was similar to that of NGC 6822,
that is to say, the emergence of dark artefacts during median noise filtering processes when the
window (we chose half a scan leg) is too short (Fig. 10.3). This issue was solved by masking the
bright structures during the reduction as described in Chapter 8.

NGC 1705 was also observed with SPIRE in its three bands (250, 350, 500 μm) in scan-map
mode on October, 19th, 2009, as part of the SAG2 / Dwarf Galaxy Survey in the Science Demon-
stration Phase. The observations cover a region of 16 by 16 arcmin. The reduction was performed
by Michael Pohlen, from the SAG2 team (see Pohlen et al. 2010; Bendo et al. 2010 for details on
the reduction). The measured 1σ noise level are 5, 6 and 7mJy beam^{-1} at 250, 350 and 500 μm
respectively.

Figure 10.2 gathers observations of *Spitzer* and *Herschel*. The three top panels show NGC 1705
observed by IRAC at 3.6 and 8 μm and MIPS at 24 μm. The middle panels show the three bands of
PACS (70, 100 and 160 μm) and the bottom panels the three bands of SPIRE (250, 350, 500 μm).
The evolution in the morphology of the galaxy as a function of wavelength was already described
in Chapter 5. The figure clearly highlights the progressive decrease of the stellar emission from the
SSC with the emergence of two bright off-nuclear H$_{II}$ regions in the mid-IR and above.

Two first new results can be deduced from these new images compared to what was observed with *Spitzer*. *1-* The MIPS images did not resolve the galaxy beyond 70 μm (see Fig. 10.2). PACS images, on the contrary, enable us to resolve the two IR structures for the first time at these wavelengths. They also clearly show that the central SSC does not seem to have any emission beyond ~ 24 μm and completely disappears, highlighting the extreme nature of this region with an SED peaking at much shorter wavelength than the other two star forming regions. *2-* SPIRE is observing NGC 1705 for the first time above 160 μm with such sensitivity. An assymetry in the far-IR emission at 250 μm is observed and indicates that the easternmost off-nuclear HII region (D1 in the nomenclature of Cannon et al. 2006b) dominates the system in the far-IR and submm (~ 1.15 to 1.45 times brighter than the western source D2).
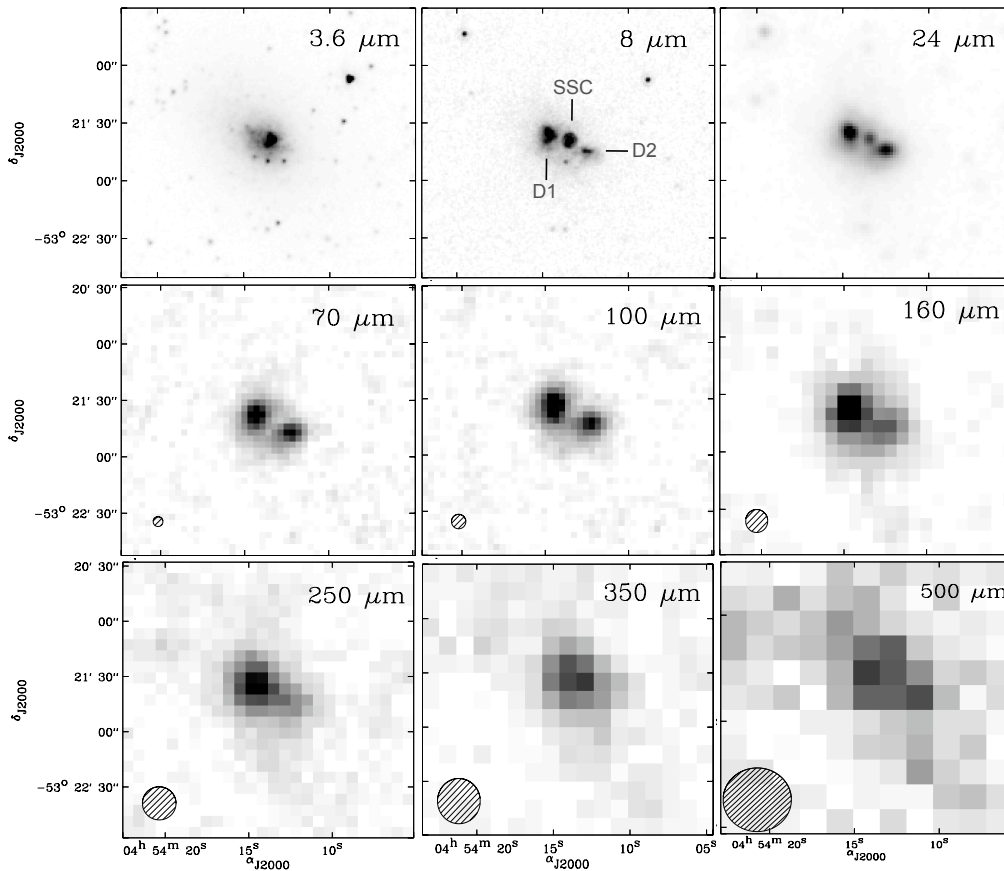
Figure 10.2. NGC 1705 observed by *Spitzer*/IRAC (3.6 and 8 μm), *Spitzer*/MIPS (24 μm), *Herschel*/PACS (70, 100 and 160 μm) and *Herschel*/SPIRE (250, 350 and 500 μm). The central SSC and the eastern (D1) and western (D2) IR components presented in Chapter 5 are indicated on the IRAC 8 μm map. Beam FWHM are overlaid.

10.2 SED modelling and results

Using an aperture of 72" (and the IRAF package apphot) that encompass the full galaxy, we find final global fluxes of 1.05 ± 0.12, 1.22 ± 0.13 and 1.18 ± 0.12 Jy at 70, 100 and 160 μm respectively. We apply our SED model (described in detail in Chapter 4) to the data, completing the wavelength coverage with *Spitzer* fluxes given in Chapter 5. The fiducial model does not fit the IR and submm

fluxes without a submm excess (Fig. 10.3). We decided to use an independant modified-blackbody and let its temperature or emissivity vary.

We find that when β is allowed to vary with the temperature of the cold dust fixed to 10K, the SED fit had a tendancy to find β values less than 0.5. These values of β are unrealistic (β is commonly thought to reside between 1 and 2; Bolatto et al. (2000)) and probably reflects instead a distribution of dust temperatures. We thus fix the emissivity index to 1 and let the temperature vary. Our best-fit model leads to a cold dust mass (mass of the modified blackbody) of $4 \times 10^5 \ M_\odot$, with a temperature of the cold dust of 5.8 K, thus extremely cold. We tried to fix the temperature to span the range between 20 and 5K. We obtained reasonable fits when the temperature reaches less than 10K. In terms of obtaining a reasonable lower limit for the dust mass, fitting a cold dust component of 10K leads to an acceptable χ^2 value of 1.1 and a total dust mass of $1.8 \times 10^5 \ M_\odot$, with a cold dust (10K) mass accounting for more than 60% of the total dust mass.
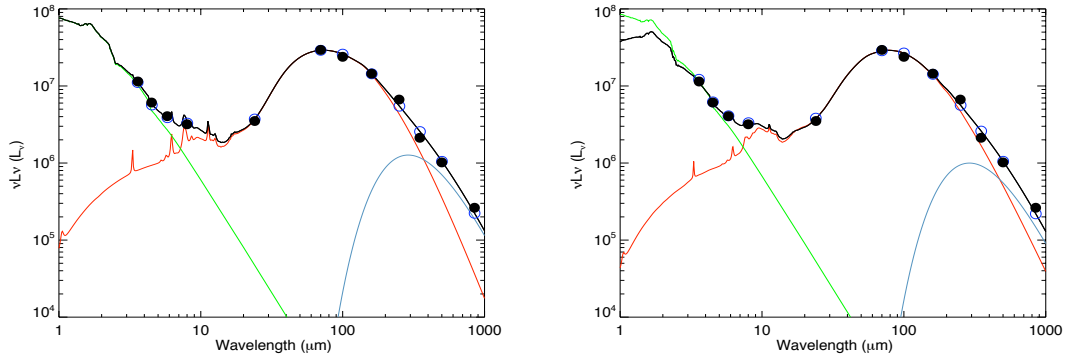
Figure 10.3. *Left:* SED of NGC 1705 using the SED modelling technique described in Chapter 4 and a cold blackbody of 10K (β=1) to model the submm excess detected at 500 and 870 μm. We use graphite to describe the carbon dust in this model. *Right:* SED of NGC 1705.

As for NGC 6822 (see Chapter 9), we also tried to replace graphite by amorphous carbon to model the carbon dust. We obtain a reduced total dust mass of 1.2×10^5 (cold dust masses of $8 \times 10^4 \ M_\odot$). This reduced dust mass leads to a reduced D/G estimate ($\sim 2.3 \times 10^{-3}$), a value that is much closer to that expected for a dwarf of such metallicity.

The precise nature of the submm excess and the dust composition will be studied in great detail with these new *Herschel* data.

Conclusions and prospects

This thesis is based on a multi-wavelength approach (from optical to submm observations) to study nearby galaxies. For a few decades now, IR astronomy has revolutionized our understanding of the properties of galaxies. The *Spitzer* telescope enables us to have access to the PAH features and the near to mid-IR wavelengths. Many issues are still unanswered, especially linked with the fact that *Spitzer* observations stop at 160 μm. The thesis took place at a turning point in IR astronomy. The *Herschel* observatory was launched in 2009 to observe wavelengths from 70 to 500 μm and thus observe the far-IR regime. These observations are constraining both the peak and the beginning of the submm slope of SEDs and thus increase our knowledge on how dust temperatures are distributed in galaxies and on the processes of star formation and recycling in the ISM.

In this PhD thesis, we primarily focused on the study of nearby low-metallicity galaxies, intriguing objects and ideal laboratories to investigate the physical properties in conditions mimicking those of the early Universe. The main questions we want to address surround the evolution of physical properties and how they evolve with the metal enrichment history of galaxies. Dwarf galaxies usually show very different SED properties than normal spirals. Most of them exhibit a submm excess that is still debated nowadays, as is the origin of this possible excess. Researchers are also thus more and more convinced of the importance of probing submm wavelengths in addition to IR observations to properly constrain the coldest dust phases.

Studying the dust and gas budget in global galaxies

We have analysed submm LABOCA observations of 4 low-metallicity galaxies to probe a possible submm excess and study the spatial distribution of cold dust in those galaxies. The study described in Chapter 5 is the first reduction, detection and interpretation of observations of faint low-metallicity galaxies with the APEX/LABOCA instrument at 870 μm. We developed a SED model that combined realistic dust optical properties, distributions of grains and radiation field intensities to investigate and quantify the dust temperature distribution in these different environments.

We found that adding submm constraints to our sample leads to an increase of the total dust mass of our 4 low-metallicity galaxies. A submm excess was detected in two of them, confirming that submm observations were necessary to constrain the submm regime of SEDs and investigate the coldest phases of dust. The submm excess, in this study, was treated as a cold dust component but we also discuss other possible explanations. The low-metallicity galaxy Haro 11 possesses an incredible dust mass, and thus D/G, compared to what could be expected by current chemical evolution models. That could suggest that a lot of gas is actually not detected by current observations. There could be a large reservoir of molecular gas not detected by current CO observations. This is consistent with the fact that CO is a poor tracer of molecular hydrogen in low-metallicity environments. A paper published in 2009 (Galametz et al. 2009) presents these results.

We then enlarged our study to a wider range of metallicities to study how the addition of submm constraints influences the dust mass estimates as a function of metallicity. We found that submm observations are crucial to properly sample the submm regime of SEDs, especially when only *Spitzer*

70 and 160 μm data are available to constrain the dust SED peak. Submm constraints are also essential to model the SEDs of metal-rich galaxies. They usually peak at long wavelengths, which means that *Spitzer* observations are not sufficient to sample the peak and the submm slope of the SED. The modelling of those galaxies without submm constraints (if they are not available) would require *a priori* assumptions to avoid overestimating the total dust mass.

In the study of Chapter 6, we also study the relation between D/G and metallicities (12+log(O/H)). We obtain a tighter correlation compared to previous studies while using submm constraints in the estimation of the dust masses. We are nevertheless lacking very low-metallicity (12+log(O/H)<7.9) constraints for these relations. We have also investigated the conditions for a submm excess in galaxies. A paper presenting these results (Galametz et al.) was submitted to A&A.

Studying the cold dust in star forming complexes

We initiated a study of the dust and gas budget of the hot, warm and cold dust spatial distribution in a bright and resolved star forming complex of the nearby Large Magellanic Cloud. Like previous studies, we found a very good spatial correlation between the 8 and 870 μm observations except for the region named N159S which shows an interesting huge reservoir of molecular gas and a high level of 870 μm emission. We modeled the SEDs of individual regions across the complex. We note significant variations in the shape of SEDs, the SEDs of HII regions showing far warmer temperature ranges than the SEDs of less active regions. We found significant variations in the dust-to-HI ratio across the complex. We also observed a decrease of the dust masses derived from our modelling when amorphous carbons are used to describe carbon dust instead of graphite. We finally investigated the molecular gas in the region. This study will enable us to investigate variations of the conversion factor X_{CO} (=I_{CO}/M(H$_2$)) in low-metallicity conditions. A paper presenting these results is in preparation.

A new vision with Herschel

We presented the first results derived from the Science Demonstration Phase observations for the SAG2/Dwarf Galaxy Survey of two low-metallicity galaxies NGC 6822 and NGC 1705. I led the A&A Special Issue paper on NGC 6822 and was second author on that of NGC 1705 (PI: B. O'Halloran). I came up to speed on the reduction of *Herschel* scan-map and chop-nod observations using the reduction interface HIPE.

We performed an SED modelling of individual regions across NGC 6822. The SPIRE maps of the galaxy are covered by cirrus emission that had to be modelled and removed. We found that the 250-to-500 flux density ratio seems to depend on the 24 μm surface brightness, linking the cold dust temperature range with star forming activity. This correlation was not observed in spiral galaxies such as M81. We suggest that dust heating processes may differ from normal dusty spirals to dwarf galaxies. Using graphite, we obtain high dust masses and a local D/G inconsistent with the metallicity of NGC 6822. The dust masses, here again, decrease when using amorphous carbon. We conclude that *Herschel* constraints require different dust properties than those commonly used in current SED models.

The proposals

Part of my time during this PhD was dedicated to the preparation of proposals both as Principal Investigator (PI) and co-Investigator (co-I). We proposed to observe low-metallicity galaxies with APEX/LABOCA, P-ArTéMiS, SCUBA-2 or APEX/SABOCA. I was PI of an accepted proposal to observe NGC 625 with LABOCA (083.B-0119: "Constraining the cold dust phase in low-metallicity

galaxies"). Data still have to be analysed. We were also granted time (co-I) to observe low-metallicity sources with P-ArTéMiS (see *the observations*).

The conferences

I was very fortunate to go to the conference "Far-Infrared and submillimeter emission of the interstellar medium: Models meet extragalactic and galactic observations" in Bad Honnef in Germany during the first month of the PhD (October 2007). This conference enabled me to quickly be informed on the problems currently discussed in the ISM community at local scales as well as more distant scales, from modelling and observational point of view.

I presented the first results obtained during this thesis (Chapter 5 and 6) during "IAU Symposium 255: Low-Metallicity Star formation : From the First Stars to Dwarf Galaxies" in Rapallo, Italy (June 2008 - poster). I also gave a talk on that subject at the "Nearby Dwarf Galaxy Conference" at the Special Astrophysical Observatory in Nizhnij Arkhyz, Russia (September 2009). I finally presented the new *Herschel* observations of NGC 6822 at the ESLAB Herschel First Results conference at ESTEC in Noordwijk, the Netherlands (May 2010 - poster).

The observations

We were granted time to observe low-metallicity galaxies with the instrument P-ArTéMiS, a prototype of the instrument ArTéMiS observing at 450 μm and developed at CEA. I participated to the installation of P-ArTéMiS as a visitor instrument, at APEX, in the Atacama Desert in Chile, in May 2009. Observations of a part of our sample of dwarf galaxies (e.g. Haro 11) and of the LMC/N159 complex were performed.

What's next

We plan to continue our analysis of the star forming complex N158/N159/N160. We especially want to investigate the relation between dust, molecular and atomic gas and to probe the variations of the D/G across the regions. How does the D/G evolve when taking the molecular gas into account? How can we estimate the X_{CO} factor for this region? Is this factor evolving across the region? This will help zoom in the long-standing issue of the conversion of CO to H_2 and the question of just how much molecular gas is residing in low-metallicity environments.

A large number of *Herschel* images have been taken for the Dwarf Galaxy Survey and I am partly in charge of their reduction. This dataset will enable us to constrain in an unbiased fashion the submm slope and peak of dust SEDs in low-metallicity galaxies. I furthermore obtained a post-doc at the Institute of Astronomy of Cambridge, UK, to work with Rob Kennicutt on the Kingfish (Key Insights on Nearby Galaxies: a Far-Infrared Survey with Herschel; http://www.ast.cam.ac.uk/research/kingfish/) programme, an imaging and spectroscopic survey of 62 nearby (d < 30 Mpc) galaxies, chosen to cover a wide range of integrated properties in the nearby Universe. This programme is the natural follow-up of the *Spitzer*/SINGS survey. Combined with the observations of the DGS, this broad sample will cover a wide range of metallicities and offer a complete and unbiased sample to observe the coldest dust phases in nearby galaxies.

I would also want to improve the SED modelling technique we used in this thesis to adapt it to the study of individual regions within galaxies or to global galaxies presenting different physical conditions than the simple assumptions we used (radiation field etc.).

Appendix A - List of publications

❑ Galametz M., Hony S., Madden S.C., Galliano F., Albrecht M., "Studying the dust in the N159 region with SAGE and LABOCA", in preparation

❑ Galametz M., Madden S.C., Galliano F., Hony S., Bendo G., Sauvage M., "Probing the Dust Properties of Galaxies up to Submillimetre Wavelengths. II. Submm excess and dust-to-gas mass ratio trend with metallicity", submitted to A&A

❑ Galametz M., Madden S.C., Galliano F., Hony S., Sauvage M., Pohlen M., Bendo G. and the SAG2 team, "Herschel photometric observations of the nearby low metallicity irregular galaxy NGC 6822", in press, accepted for publication for the Herschel A&A Special Issue.

❑ Galametz M., Madden S.C., Galliano F., Hony S., Schuller F., Beelen A., Bendo G., Sauvage M., Lundgren A., Billot N., "Probing the Dust Properties of Galaxies up to Submillimetre Wavelengths. I. The Spectral Energy Distribution of dwarf galaxies using LABOCA", Astronomy and Astrophysics, Volume 508, Issue 2, 2009, pp.645-664

❑ O'Halloran B., Galametz M., Madden S.C. and the SAG2 team, "Herschel photometric observations of the low metallicty dwarf galaxy NGC 1705", in press, submitted for the Herschel A&A Special Issue.

Appendix

Bibliography

Aguirre, J. E. et al. 2003, ApJ, 596, 273

Aller, L. H., ed. 1984, Astrophysics and Space Science Library, Vol. 112, Physics of thermal gaseous nebulae

Aloisi, A., Savaglio, S., Heckman, T. M., et al. 2003, ApJ, 595, 760

Aloisi, A. et al. 1998, in European Southern Observatory Astrophysics Symposia, Vol. 55, European Southern Observatory Astrophysics Symposia, ed. W. Freudling & R. N. Hook, 154–+

Anderson, N. & Watson, W. D. 1993, A&A, 270, 477

Aparicio, A., Dalcanton, J. J., Gallart, C., & Martinez-Delgado, D. 1997, AJ, 114, 1447

Appleton, P. N., Davies, R. D., & Stephenson, R. J. 1981, MNRAS, 195, 327

Bakes, E. L. O. & Tielens, A. G. G. M. 1994, ApJ, 427, 822

Barone, L. T., Heithausen, A., Hüttemeister, S., Fritz, T., & Klein, U. 2000, MNRAS, 317, 649

Bazell, D. & Dwek, E. 1990, ApJ, 360, 142

Bendo, G. et al. 2006, ApJ, 652, 283

Bendo, G. J. et al. 2010, ArXiv e-prints

Benford, D. J. 1999, PhD thesis, CALIFORNIA INSTITUTE OF TECHNOLOGY

Bergin, E. A., Hartmann, L. W., Raymond, J. C., & Ballesteros-Paredes, J. 2004, ApJ, 612, 921

Bergvall, N., Masegosa, J., Östlin, G., & Cernicharo, J. 2000, A&A, 359, 41

Bergvall, N. & Östlin, G. 2002, A&A, 390, 891

Bernard, J.-P. et al. 2008, AJ, 136, 919

Bernloehr, K. 1993, A&A, 270, 20

Bettoni, D., Galletta, G., & García-Burillo, S. 2003, A&A, 405, 5

Bianchi, L. & Efremova, B. V. 2006, AJ, 132, 378

Bigiel, F., Leroy, A., Walter, F., et al. 2008, AJ, 136, 2846

Billett, O. H., Hunter, D. A., & Elmegreen, B. G. 2002, AJ, 123, 1454

Blum, J. 2004, in Astronomical Society of the Pacific Conference Series, Vol. 309, Astrophysics of Dust, ed. A. N. Witt, G. C. Clayton, & B. T. Draine, 369–+

Bolatto, A. D., Jackson, J. M., Israel, F. P., Zhang, X., & Kim, S. 2000, ApJ, 545, 234

Bonatto, C. J. & Pastoriza, M. G. 1990, ApJ, 353, 445

Boselli, A., Gavazzi, G., Lequeux, J., & Pierini, D. 2002a, A&A, 385, 454

Boselli, A., Lequeux, J., & Gavazzi, G. 2002b, A&A, 384, 33

Boselli, A. et al. 2010, in press

Bot, C., Boulanger, F., Lagache, G., Cambrésy, L., & Egret, D. 2004, A&A, 423, 567

Böttner, C., Klein, U., & Heithausen, A. 2003, A&A, 408, 493

Boulanger, F. et al. 1996, A&A, 312, 256

Bowen, D. V., Jenkins, E. B., Tripp, T. M., et al. 2008, ApJS, 176, 59

Bresolin, F., Garnett, D. R., & Kennicutt, Jr., R. C. 2004, ApJ, 615, 228

Brinks, E., Oh, S., Bagetakos, I., et al. 2008, in IAU Symposium, Vol. 255, IAU Symposium, ed. L. K. Hunt, S. Madden, & R. Schneider, 265–273

Burke, J. R. & Hollenbach, D. J. 1983, ApJ, 265, 223

Calzetti, D. 2007, Nuovo Cimento B Serie, 122, 971

Calzetti, D., Kennicutt, R. C., Dale, D. A., et al. 2010, ArXiv e-prints

Cannon, J. M. et al. 2006a, ApJ, 652, 1170

Cannon, J. M. et al. 2006b, ApJ, 647, 293

Cantalupo, C. M., Borrill, J. D., Jaffe, A. H., Kisner, T. S., & Stompor, R. 2010, ApJS, 187, 212

Cardelli, J. A., Clayton, G. C., & Mathis, J. S. 1989, ApJ, 345, 245

Casoli, F., Sauty, S., Gerin, M., et al. 1998, A&A, 331, 451

Chen, H.-W. et al. 2009, ApJ, 691, 152

Chini, R., Kreysa, E., Kruegel, E., & Mezger, P. G. 1986, A&A, 166, L8

Chokshi, A., Tielens, A. G. G. M., & Hollenbach, D. 1993, ApJ, 407, 806

Cohen, R. S., Dame, T. M., Garay, G., et al. 1988, ApJ, 331, L95

Condon, J. J. et al. 1998, AJ, 115, 1693

Conti, P. S. 1991, ApJ, 377, 115

Conti, P. S., Leitherer, C., & Vacca, W. D. 1996, ApJ, 461, L87+

Contursi, A., Kaufman, M. J., Helou, G., et al. 2002, AJ, 124, 751

Dahlem, M., Ehle, M., & Ryder, S. D. 2001, A&A, 373, 485

Dahlem, M. et al. 1990, A&A, 240, 237

Dalcanton, J. 1995, PhD thesis, PRINCETON UNIVERSITY.

Dalcanton, J. J., Spergel, D. N., Gunn, J. E., Schmidt, M., & Schneider, D. P. 1997, AJ, 114, 635

Dale, D. A. & Helou, G. 2002, ApJ, 576, 159

Dale, D. A. et al. 2001, ApJ, 549, 215

Dale, D. A. et al. 2005, ApJ, 633, 857

Dale, D. A. et al. 2007, ApJ, 655, 863

Dame, T. M., Hartmann, D., & Thaddeus, P. 2001, ApJ, 547, 792

Dartois, E., Muñoz Caro, G. M., Deboffle, D., & d'Hendecourt, L. 2004, A&A, 423, L33

de Blok, W. J. G. & Walter, F. 2000, ApJ, 537, L95

de Blok, W. J. G. & Walter, F. 2006, AJ, 131, 343

Dean, J. F. & Davies, R. D. 1975, MNRAS, 170, 503

Deharveng, L., Zavagno, A., & Caplan, J. 2005, A&A, 433, 565

Demyk, K., Carrez, P., Leroux, H., et al. 2001, A&A, 368, L38

Dennison, B., Simonetti, J. H., & Topasna, G. A. 1998, Publications of the Astronomical Society of Australia, 15, 147

Desert, F., Boulanger, F., & Puget, J. L. 1990, A&A, 237, 215

Dickel, J. R., McIntyre, V. J., Gruendl, R. A., & Milne, D. K. 2005, AJ, 129, 790

Disney, M., Davies, J., & Phillipps, S. 1989, MNRAS, 239, 939

Dominik, C. & Dullemond, C. P. 2008, A&A, 491, 663

Dopita, M. A., Groves, B. A., Fischera, J., et al. 2005, Astronomische Nachrichten, 326, 526

Draine, B. T. 1989, in ESA Special Publication, Vol. 290, Infrared Spectroscopy in Astronomy, ed. E. Böhm-Vitense, 93–98

Draine, B. T. 2003, ARA&A, 41, 241

Draine, B. T. & Anderson, N. 1985, ApJ, 292, 494

Draine, B. T. & Lazarian, A. 1998, ApJ, 508, 157

Draine, B. T. & Lee, H. M. 1984, ApJ, 285, 89

Draine, B. T. & Li, A. 2001, ApJ, 551, 807

Draine, B. T. & Li, A. 2007, ApJ, 657, 810

Draine, B. T. & Malhotra, S. 1993, ApJ, 414, 632

Draine, B. T. et al. 2007, ApJ, 663, 866

Duc, P., Mirabel, I. F., & Brinks, E. 1997, in IAU Joint Discussion, Vol. 2, IAU Joint Discussion

Dudley, C. C. & Wynn-Williams, C. G. 1997, ApJ, 488, 720

Dufour, R. J., Shields, G. A., & Talbot, Jr., R. J. 1982, ApJ, 252, 461

Duley, W. W. & Williams, D. A. 1981, MNRAS, 196, 269

Dultzin-Hacyan, D., Masegosa, J., & Moles, M. 1990, A&A, 238, 28

Dumke, M., Krause, M., & Wielebinski, R. 2004, A&A, 414, 475

Dunne, L. & Eales, S. A. 2001, MNRAS, 327, 697

Dunne, L. et al. 2000, MNRAS, 315, 115

Dupac, X. et al. 2003, A&A, 404, L11

Dutil, Y. & Roy, J.-R. 1999, ApJ, 516, 62

Dwek, E. 1998, ApJ, 501, 643

Dwek, E. 2005, in American Institute of Physics Conference Series, Vol. 761, The Spectral Energy Distributions of Gas-Rich Galaxies: Confronting Models with Data, ed. C. C. Popescu & R. J. Tuffs, 103–122

Eales, S. A. et al. 2010, ArXiv e-prints

Edmunds, M. G. 2001, MNRAS, 328, 223

Ehle, M. 2005, in The Magnetized Plasma in Galaxy Evolution, ed. K. T. Chyzy, K. Otmianowska-Mazur, M. Soida, & R.-J. Dettmar , 31–38

Elias, J. H. et al. 1978, ApJ, 220, 25

Ellis, R. S. 1997, ARA&A, 35, 389

Elmegreen, B. G. 1998, in Astronomical Society of the Pacific Conference Series, Vol. 148, Origins, ed. C. E. Woodward, J. M. Shull, & H. A. Thronson Jr., 150–+

Engelbracht, C. W. et al. 2005, ApJ, 628, L29

Engelbracht, C. W. et al. 2007, PASP, 119, 994

Engelbracht, C. W. et al. 2008, ApJ, 678, 804

Favata, F., Micela, G., Sciortino, S., & Morale, F. 1997, A&A, 324, 998

Fazio, G. G. et al. 2004, ApJS, 154, 10

Ferland, G. J. 1996, Hazy, A Brief Introduction to Cloudy 90, ed. G. J. Ferland

Ferrara, A. & Dettmar, R. 1994, ApJ, 427, 155

Ferriere, K. 1998, ApJ, 503, 700

Fioc, M. & Rocca-Volmerange, B. 1997, A&A, 326, 950

Fitzpatrick, E. L. 2004, in Astronomical Society of the Pacific Conference Series, Vol. 309, Astrophysics of Dust, ed. A. N. Witt, G. C. Clayton, & B. T. Draine, 33–+

Franco, J. & Cox, D. P. 1986, PASP, 98, 1076

Fukui, Y., Kawamura, A., Wong, T., et al. 2009, ApJ, 705, 144

Fukui, Y., Mizuno, N., Yamaguchi, R., et al. 1999, PASJ, 51, 745

Gaensler, B. M., Madsen, G. J., Chatterjee, S., & Mao, S. A. 2008, Publications of the Astronomical Society of Australia, 25, 184

Galametz, M. et al. 2009, A&A, 508, 645

Galametz, M. et al. 2010, ArXiv e-prints

Gallagher, III, J. S., Hunter, D. A., Gillett, F. C., & Rice, W. L. 1991, ApJ, 371, 142

Galliano, F., Dwek, E., & Chanial, P. 2008, ApJ, 672, 214

Galliano, F. et al. 2003, A&A, 407, 159

Galliano, F. et al. 2005, A&A, 434, 867

Gatley, I., Becklin, E. E., Hyland, A. R., & Jones, T. J. 1981, MNRAS, 197, 17P

Gaustad, J. E., McCullough, P. R., Rosing, W., & Van Buren, D. 2001, PASP, 113, 1326

Genzel, R., Tacconi, L. J., Rigopoulou, D., Lutz, D., & Tecza, M. 2001, ApJ, 563, 527

Gerin, M., Combes, F., & Nakai, N. 1988, A&A, 203, 44

Giammanco, C. & Beckman, J. E. 2005, A&A, 437, L11

Gil de Paz, A., Madore, B. F., & Pevunova, O. 2003, ApJS, 147, 29

Glassgold, A. E., Huggins, P. J., & Langer, W. D. 1985, ApJ, 290, 615

Glassgold, A. E., Meijerink, R., & Najita, J. R. 2009, ApJ, 701, 142

Goldsmith, P. F. & Langer, W. D. 1978, ApJ, 222, 881

Gonzalez-Delgado, R. M. et al. 1995, ApJ, 439, 604

Gordon, D. & Gottesman, S. T. 1981, AJ, 86, 161

Gordon, K. D., Clayton, G. C., Misselt, K. A., Landolt, A. U., & Wolff, M. J. 2003, ApJ, 594, 279

Gordon, K. D. et al. 2005, PASP, 117, 503

Gordon, K. D. et al. 2008, ApJ, 682, 336

Gordon, K. D. et al. 2009, ApJ, 690, L76

Gorenstein, P. 1975, ApJ, 198, 95

Gratier, P. et al. 2010, A&A, 512, A68+

Grebel, E. K. 2001, in Dwarf galaxies and their environment, ed. K. S. de Boer, R.-J. Dettmar, & U. Klein, 45–+

Greve, A., Becker, R., Johansson, L. E. B., & McKeith, C. D. 1996, A&A, 312, 391

Griffin, M. et al. 2010, A&A, in press

Grimes, J. P. et al. 2007, ApJ, 668, 891

Grossi, M. et al. 2010, A&A, in press

Guhathakurta, P. & Draine, B. T. 1989, ApJ, 345, 230

Guseva, N. G., Izotov, Y. I., & Thuan, T. X. 1998, Kinematics and Physics of Celestial Bodies, 14, 41

Haas, M., Klaas, U., & Bianchi, S. 2002, A&A, 385, L23

Haffner, L. M. et al. 2009, Reviews of Modern Physics, 81, 969

Haser, S. M., Pauldrach, A. W. A., Lennon, D. J., et al. 1998, A&A, 330, 285

Heckman, T. M., Lehnert, M. D., Strickland, D. K., & Armus, L. 2000, ApJS, 129, 493

Heckman, T. M. & Leitherer, C. 1997, AJ, 114, 69

Heckman, T. M., Robert, C., Leitherer, C., Garnett, D. R., & van der Rydt, F. 1998, ApJ, 503, 646

Heisler, C. A. & Vader, J. P. 1995, AJ, 110, 87

Helfer, T. T. et al. 2003, ApJS, 145, 259

Helou, G. et al. 2004, in Bulletin of the American Astronomical Society, Vol. 36, Bulletin of the American Astronomical Society, 701–+

Henize, K. G. 1956, ApJS, 2, 315

Hickson, P. 1982, ApJ, 255, 382

Hildebrand, R. H. 1983, QJRAS, 24, 267

Hildebrand, R. H., Whitcomb, S. E., Winston, R., et al. 1977, ApJ, 216, 698

Hill, A. S., Benjamin, R. A., Kowal, G., et al. 2008, ApJ, 686, 363

Hirashita, H., Kaneda, H., Onaka, T., & Suzuki, T. 2008, PASJ, 60, 477

Hirashita, H. & Omukai, K. 2009, MNRAS, 399, 1795

Hoang, T., Draine, B. T., & Lazarian, A. 2010, ApJ, 715, 1462

Hodge, P. & Lee, M. G. 1990, PASP, 102, 26

Hoefner, S. 2009, Cosmic Dust - Near and far, Th. Henning, E. Grün, J. Steinacker (eds.) ASP Conf Ser., in press (arXiv:0903.5280)

Hollenbach, D. J. & Tielens, A. G. G. M. 1999, Reviews of Modern Physics, 71, 173

Hong, S. A., Rosenberg, J. L., Ashby, M. L. N., & Salzer, J. J. 2010, ApJ, 717, 503

Hopkins, A. M., Schulte-Ladbeck, R. E., & Drozdovsky, I. O. 2002, AJ, 124, 862

Horellou, C., Booth, R. S., & Karlsson, B. 1999, Ap&SS, 269, 629

Houck, J. R. et al. 2004, ApJS, 154, 18

Huchtmeier, W. K. & Bohnenstengel, H.-D. 1981, A&A, 100, 72

Hughes, A., Wong, T., Ott, J., et al. 2010, MNRAS, 873

Hunt, L., Bianchi, S., & Maiolino, R. 2005, A&A, 434, 849

Hunter, D. A., Brinks, E., Elmegreen, B., et al. 2007, in Bulletin of the American Astronomical Society, Vol. 38, Bulletin of the American Astronomical Society, 895–+

Hunter, D. A. & Elmegreen, B. G. 2004, AJ, 128, 2170

Hunter, D. A., Hawley, W. N., & Gallagher, III, J. S. 1993, AJ, 106, 1797

Hunter, D. A. & Kaufman, M. 2007, AJ, 134, 721

Hunter, D. A., van Woerden, H., & Gallagher, III, J. S. 1994, ApJS, 91, 79

Hurwitz, M. & Bowyer, S. 1996, ApJ, 465, 296

Iglesias-Páramo, J. & Vílchez, J. M. 1997, ApJ, 479, 190

Israel, F. 2000, in Molecular Hydrogen in Space, ed. F. Combes & G. Pineau Des Forets, 293–+

Israel, F. P. 1997, A&A, 328, 471

Israel, F. P. 2005, A&A, 438, 855

Israel, F. P. et al. 1993, A&A, 276, 25

Issa, M. R., MacLaren, I., & Wolfendale, A. W. 1990, A&A, 236, 237

Izotov, Y. I. & Thuan, T. X. 1998, ApJ, 500, 188

Izotov, Y. I. et al. 1999, ApJ, 527, 757

James, A., Dunne, L., Eales, S., & Edmunds, M. G. 2002, MNRAS, 335, 753

Jarrett, T. H., Chester, T., Cutri, R., Schneider, S. E., & Huchra, J. P. 2003, AJ, 125, 525

Jerjen, H., Kalnajs, A., & Binggeli, B. 2000, A&A, 358, 845

Johnson, K. E. & Conti, P. S. 2000, AJ, 119, 2146

Johnson, K. E., Hunt, L. K., & Reines, A. E. 2009, AJ, 137, 3788

Johnson, K. E. et al. 2007, AJ, 134, 1522

Jones, A. 2009, in EAS Publications Series, Vol. 34, EAS Publications Series, ed. L. Pagani & M. Gerin, 107–118

Jones, A. P., Tielens, A. G. G. M., & Hollenbach, D. J. 1996, ApJ, 469, 740

Jones, T. J., Woodward, C. E., Boyer, M. L., Gehrz, R. D., & Polomski, E. 2005, ApJ, 620, 731

Kapferer, W., Kronberger, T., Weratschnig, J., & Schindler, S. 2007, A&A, 472, 757

Kaufman, M. J., Wolfire, M. G., Hollenbach, D. J., & Luhman, M. L. 1999, ApJ, 527, 795

Kemper, F., Vriend, W. J., & Tielens, A. G. G. M. 2004, ApJ, 609, 826

Kenney, J. D. P. & Young, J. S. 1989, ApJ, 344, 171

Kennicutt, Jr., R. C. 1998, ARA&A, 36, 189

Kennicutt, Jr., R. C., Tamblyn, P., & Congdon, C. E. 1994, ApJ, 435, 22

Kennicutt, Jr., R. C. et al. 2003, PASP, 115, 928

Kennicutt, Jr., R. C. et al. 2007, ApJ, 671, 333

Kim, S., Martin, P. G., & Hendry, P. D. 1994, ApJ, 422, 164

Kim, S., Staveley-Smith, L., Dopita, M. A., et al. 2003, ApJS, 148, 473

Klaas, U. et al. 2001, A&A, 379, 823

Kobulnicky, H. A. & Johnson, K. E. 1999, ApJ, 527, 154

Kobulnicky, H. A. & Skillman, E. D. 1997, ApJ, 489, 636

Kormendy, J. 1989, ApJ, 342, L63

Kormendy, J. & Sanders, D. B. 1992, ApJ, 390, L53

Krügel, E. 2003, The physics of interstellar dust, ed. E. Kruegel

Krügel, E. 2008, An introduction to the physics of interstellar dust, ed. E. Krügel

Kunth, D., Lequeux, J., Sargent, W. L. W., & Viallefond, F. 1994, A&A, 282, 709

Kunth, D. & Östlin, G. 2000, A&A Rev., 10, 1

Kunth, D. & Schild, H. 1986, A&A, 169, 71

Kwok, S. 2007, Physics and Chemistry of the Interstellar Medium, ed. Kwok, S.

Laor, A. & Draine, B. T. 1993, ApJ, 402, 441

Lawton, B. et al. 2010, ApJ, 716, 453

Le Bourlot, J. 2000, in ESA Special Publication, Vol. 456, ISO Beyond the Peaks: The 2nd ISO Workshop on Analytical Spectroscopy, ed. A. Salama, M. F. Kessler, K. Leech, & B. Schulz, 309–+

Le Petit, F., Nehmé, C., Le Bourlot, J., & Roueff, E. 2006, ApJS, 164, 506

Lebouteiller, V., Brandl, B., Bernard-Salas, J., Devost, D., & Houck, J. R. 2007, ApJ, 665, 390

Lee, H., Skillman, E. D., & Venn, K. A. 2006, ApJ, 642, 813

Lee, H., Zucker, D. B., & Grebel, E. K. 2007, MNRAS, 376, 820

Lee, J. C., Kennicutt, R. C., José G. Funes, S. J., Sakai, S., & Akiyama, S. 2009, ApJ, 692, 1305

Lee, M. G. & Geisler, D. 1993, in Astronomical Society of the Pacific Conference Series, Vol. 48, The Globular Cluster-Galaxy Connection, ed. G. H. Smith & J. P. Brodie, 576–+

Leger, A. & Puget, J. L. 1984, A&A, 137, L5

Leroy, A., Bolatto, A., Stanimirovic, S., et al. 2007, ApJ, 658, 1027

Leroy, A., Bolatto, A. D., Simon, J. D., & Blitz, L. 2005, ApJ, 625, 763

Leroy, A. K., Walter, F., Bigiel, F., et al. 2009, AJ, 137, 4670

Leroy, A. K., Walter, F., Brinks, E., et al. 2008, AJ, 136, 2782

Li, A. & Draine, B. T. 2001, ApJ, 554, 778

Lilly, S. J., Carollo, C. M., & Stockton, A. N. 2003, ApJ, 597, 730

Lilly, S. J., Tresse, L., Hammer, F., Crampton, D., & Le Fevre, O. 1995, ApJ, 455, 108

Lisenfeld, U. & Ferrara, A. 1998, ApJ, 496, 145

Lisenfeld, U., Sievers, A., Israel, F., & Stil, J. 2001, Astrophysics and Space Science Supplement, 277, 105

Lundgren, A. A., Olofsson, H., Wiklind, T., & Rydbeck, G. 2004, A&A, 422, 865

Madau, P., Ferguson, H. C., Dickinson, M. E., et al. 1996, MNRAS, 283, 1388

Madden, S. C. 2000, New Astronomy Review, 44, 249

Madden, S. C. 2005, in American Institute of Physics Conference Series, Vol. 761, The Spectral Energy Distributions of Gas-Rich Galaxies: Confronting Models with Data, ed. C. C. Popescu & R. J. Tuffs, 223–+

Madden, S. C., Galliano, F., Jones, A. P., & Sauvage, M. 2006, A&A, 446, 877

Madden, S. C., Poglitsch, A., Geis, N., Stacey, G. J., & Townes, C. H. 1997, ApJ, 483, 200

Maier, C., Meisenheimer, K., & Hippelein, H. 2004, A&A, 418, 475

Malhotra, S., Kaufman, M. J., Hollenbach, D., et al. 2001, ApJ, 561, 766

Marleau, F. R. et al. 2006, ApJ, 646, 929

Martin, P. G. & Whittet, D. C. B. 1990, ApJ, 357, 113

Mas-Hesse, J. M. & Kunth, D. 1999, A&A, 349, 765

Massa, D. & Savage, B. 1989, in IAU Symposium, Vol. 135, Interstellar Dust, ed. L. J. Allamandola & A. G. G. M. Tielens, 3–+

Mateo, M. L. 1998, ARA&A, 36, 435

Mathis, J. S. 1990, in Astronomical Society of the Pacific Conference Series, Vol. 12, The Evolution of the Interstellar Medium, ed. L. Blitz, 63–77

Mathis, J. S., Mezger, P. G., & Panagia, N. 1983, A&A, 128, 212

Mathis, J. S., Rumpl, W., & Nordsieck, K. H. 1977, ApJ, 217, 425

Mauch, T. et al. 2003, MNRAS, 342, 1117

McGaugh, S. S. 1991, ApJ, 380, 140

McKee, C. F. & Williams, J. P. 1997, ApJ, 476, 144

Mehlert, D., Noll, S., Appenzeller, I., et al. 2002, A&A, 393, 809

Meier, D. S., Turner, J. L., & Beck, S. C. 2002, AJ, 124, 877

Meier, D. S., Turner, J. L., Crosthwaite, L. P., & Beck, S. C. 2001, AJ, 121, 740

Meijerink, R., Tilanus, R. P. J., Dullemond, C. P., Israel, F. P., & van der Werf, P. P. 2005, A&A, 430, 427

Meixner, M. et al. 2006, AJ, 132, 2268

Meixner, M. et al. 2010, A&A, in press

Meny, C., Gromov, V., Boudet, N., et al. 2007, A&A, 468, 171

Meurer, G. R., Freeman, K. C., Dopita, M. A., & Cacciari, C. 1992, AJ, 103, 60

Meurer, G. R., Staveley-Smith, L., & Killeen, N. E. B. 1998, MNRAS, 300, 705

Micelotta, E. R., Jones, A. P., & Tielens, A. G. G. M. 2010, A&A, 510, A36+

Miller, B. W. & Lotz, J. M. 2007, ApJ, 670, 1074

Mirabel, I. F. & Sanders, D. B. 1989, ApJ, 340, L53

Misselt, K. A., Gordon, K. D., Clayton, G. C., & Wolff, M. J. 2001, ApJ, 551, 277

Mizuno, Y. et al. 2010, PASJ, 62, 51

Moles, M., Marquez, I., Masegosa, J., et al. 1994, ApJ, 432, 135

Morfill, G. E. & Scholer, M., eds. 1987, Physical processes in interstellar clouds; Proceedings of the NATO Advanced Study Institute, Irsee, Federal Republic of Germany, Aug. 18-28, 1986

Moshir, M. & et al. 1990, in IRAS Faint Source Catalogue, version 2.0 (1990), 0–+

Moustakas, J. & Kennicutt, Jr., R. C. 2006, ApJ, 651, 155

Muñoz-Mateos et al. 2009a, ApJ, 703, 1569

Muñoz-Mateos et al. 2009b, ApJ, 701, 1965

Nomura, H., Aikawa, Y., Nakagawa, Y., & Millar, T. J. 2009, A&A, 495, 183

Obreschkow, D. & Rawlings, S. 2009, ApJ, 696, L129

Oey, M. S., Clarke, C. J., & Massey, P. 2001, in Dwarf galaxies and their environment, ed. K. S. de Boer, R.-J. Dettmar, & U. Klein, 181–+

O′Halloran, B., Madden, S. C., & Abel, N. P. 2008, ApJ, 681, 1205

O′Halloran, B., Satyapal, S., & Dudik, R. P. 2006, ApJ, 641, 795

O′Halloran, B. et al. 2010, A&A, in press

Olofsson, J., Augereau, J., van Dishoeck, E. F., et al. 2009, A&A, 507, 327

Ondrechen, M. P., van der Hulst, J. M., & Hummel, E. 1989, ApJ, 342, 39

Ormel, C. W., Paszun, D., Dominik, C., & Tielens, A. G. G. M. 2009, A&A, 502, 845

Östlin, G., Amram, P., Masegosa, J., Bergvall, N., & Boulesteix, J. 1999, A&AS, 137, 419

Östlin, G. & Mouhcine, M. 2005, A&A, 433, 797

Ott, J. et al. 2008, Publications of the Astronomical Society of Australia, 25, 129

Otte, B., Reynolds, R. J., Gallagher, III, J. S., & Ferguson, A. M. N. 2001, ApJ, 560, 207

Pagel, B. E. J., Edmunds, M. G., Blackwell, D. E., Chun, M. S., & Smith, G. 1979, MNRAS, 189, 95

Palla, F., Salpeter, E. E., & Stahler, S. W. 1983, ApJ, 271, 632

Palme, H. & Jones, A. 2005, Solar System Abundances of the Elements, ed. Davis, A. M., Holland, H. D., & Turekian, K. K. (Elsevier B), 41–+

Paradis, D., Bernard, J., & Mény, C. 2009, A&A, 506, 745

Peeters, E., Allamandola, L. J., Tielens, A. G. G. M., & Wolfire, M. G. 2010, in Bulletin of the American Astronomical Society, Vol. 41, Bulletin of the American Astronomical Society, 435–+

Peeters, E., Mattioda, A. L., Kemper, F., Hudgins, D. M., & Allamandola, L. J. 2006, in Astronomical Society of the Pacific Conference Series, Vol. 357, Astronomical Society of the Pacific Conference Series, ed. L. Armus & W. T. Reach, 95–+

Pérez-Montero, E. & Díaz, A. I. 2003, MNRAS, 346, 105

Petrosian, A. R. & Burenkov, A. N. 1993, A&A, 279, 21

Pettini, M., Smith, L. J., King, D. L., & Hunstead, R. W. 1997, ApJ, 486, 665

Phillipps, S. & Edmunds, M. G. 1991, MNRAS, 251, 84

Pier, E. A. & Krolik, J. H. 1992, ApJ, 401, 99

Pilyugin, L. S., Mattsson, L., Vílchez, J. M., & Cedrés, B. 2009, MNRAS, 398, 485

Pilyugin, L. S. & Thuan, T. X. 2005, ApJ, 631, 231

Pilyugin, L. S., Vílchez, J. M., & Contini, T. 2004, A&A, 425, 849

Pineda, J. L. et al. 2008, A&A, 482, 197

Poglitsch, A. et al. 1995, ApJ, 454, 293

Poglitsch, A. et al. 2010, A&A, in press

Pohlen, M. et al. 2010, A&A, in press

Popescu, C. C. & Tuffs, R. J., eds. 2005, American Institute of Physics Conference Series, Vol. 761, The Spectral Energy Distributions of Gas-Rich Galaxies: Confronting Models with Data

Popescu, C. C., Tuffs, R. J., Völk, H. J., Pierini, D., & Madore, B. F. 2002, ApJ, 567, 221

Ravindranath, S. & Prabhu, T. P. 2001, Ap&SS, 276, 593

Reach, W. T. et al. 1995, ApJ, 451, 188

Reach, W. T. et al. 2005, PASP, 117, 978

Reddy, N. A., Erb, D. K., Pettini, M., Steidel, C. C., & Shapley, A. E. 2010, ApJ, 712, 1070

Reif, K., Mebold, U., Goss, W. M., van Woerden, H., & Siegman, B. 1982, A&AS, 50, 451

Relaño, M. & Kennicutt, R. C. 2009, ApJ, 699, 1125

Relaño, M., Lisenfeld, U., Pérez-González, P. G., Vílchez, J. M., & Battaner, E. 2007, ApJ, 667, L141

Reynolds, R. J. 1984, ApJ, 282, 191

Richer, M. G. et al. 2003, A&A, 397, 99

Rieke, G. H. & Lebofsky, M. J. 1985, ApJ, 288, 618

Rieke, G. H. et al. 2004, ApJS, 154, 25

Röllig, M., Ossenkopf, V., Jeyakumar, S., Stutzki, J., & Sternberg, A. 2006, A&A, 451, 917

Rouleau, F. & Martin, P. G. 1991, ApJ, 377, 526

Roussel, H., Helou, G., Hollenbach, D. J., et al. 2007, ApJ, 669, 959

Rubin, D. et al. 2009, A&A, 494, 647

Rubin, V. C. & Ford, Jr., W. K. 1983, ApJ, 271, 556

Rubin, V. C., Hunter, D. A., & Ford, W. K. J. 1990, ApJ, 365, 86

Sage, L. J., Salzer, J. J., Loose, H.-H., & Henkel, C. 1992, A&A, 265, 19

Sage, L. J., Welch, G. A., & Young, L. M. 2007, ApJ, 657, 232

Salzer, J. J. & MacAlpine, G. M. 1988, AJ, 96, 1192

Sanders, D. B., Mazzarella, J. M., Kim, D.-C., Surace, J. A., & Soifer, B. T. 2003, AJ, 126, 1607

Sauty, S., Gerin, M., & Casoli, F. 1998, A&A, 339, 19

Sauvage, M., Thuan, T. X., & Lagage, P. O. 1997, A&A, 325, 98

Sauvage, M., Tuffs, R. J., & Popescu, C. C. 2005, Space Science Reviews, 119, 313

Sauvage, M., Vigroux, L., & Thuan, T. X. 1990, A&A, 237, 296

Savage, B. D., Sembach, K. R., Jenkins, E. B., et al. 2000, ApJ, 538, L27

Schaefer, B. E. 2008, AJ, 135, 112

Schombert, J. M., Pildis, R. A., Eder, J. A., & Oemler, Jr., A. 1995, AJ, 110, 2067

Scoville, N. & Young, J. S. 1983, ApJ, 265, 148

Serra Díaz-Cano, L. & Jones, A. P. 2008, A&A, 492, 127

Shetrone, M. D., Bolte, M., & Stetson, P. B. 1998, AJ, 115, 1888

Shetty, R., Kauffmann, J., Schnee, S., Goodman, A. A., & Ercolano, B. 2009, ApJ, 696, 2234

Shields, J. C. & Kennicutt, Jr., R. C. 1995, ApJ, 454, 807

Silsbee, K., Ali-Haimoud, Y., & Hirata, C. M. 2010, ArXiv e-prints

Skillman, E. D. 1998, in Stellar astrophysics for the local group: VIII Canary Islands Winter School of Astrophysics, ed. A. Aparicio, A. Herrero, & F. Sánchez, 457–+

Skillman, E. D., Terlevich, E., & Terlevich, R. 1998, Space Science Reviews, 84, 105

Skillman, E. D., Terlevich, R., Teuben, P. J., & van Woerden, H. 1988, A&A, 198, 33

Smecker-Hane, T. A., Stetson, P. B., Hesser, J. E., & Vandenberg, D. A. 1996, in Astronomical Society of the Pacific Conference Series, Vol. 98, From Stars to Galaxies: the Impact of Stellar Physics on Galaxy Evolution, ed. C. Leitherer, U. Fritze-von-Alvensleben, & J. Huchra, 328–+

Smith, M. W. L. et al. 2010, ArXiv e-prints

Smith, P. A., Brand, P. W. J. L., Puxley, P. J., Mountain, C. M., & Nakai, N. 1990, MNRAS, 243, 97

Smoker, J. V., Davies, R. D., Axon, D. J., & Hummel, E. 2000, A&A, 361, 19

Sodroski, T. J. et al. 1997, ApJ, 480, 173

Sofue, Y. & Wakamatsu, K. 1992, PASJ, 44, L23

Spitzer, Jr., L. 1978, JRASC, 72, 349

Stansberry, J. A. et al. 2007, PASP, 119, 1038

Staveley-Smith, L. & Davies, R. D. 1987, MNRAS, 224, 953

Staveley-Smith, L., Kim, S., Calabretta, M. R., Haynes, R. F., & Kesteven, M. J. 2003, MNRAS, 339, 87

Steidel, C. C., Giavalisco, M., Pettini, M., Dickinson, M., & Adelberger, K. L. 1996, ApJ, 462, L17+

Stepnik, B., Abergel, A., Bernard, J., et al. 2001, in Astronomical Society of the Pacific Conference Series, Vol. 243, From Darkness to Light: Origin and Evolution of Young Stellar Clusters, ed. T. Montmerle & P. André, 47–+

Stepnik, B., Jones, A. P., Abergel, A., et al. 2002, in EAS Publications Series, Vol. 4, EAS Publications Series, ed. M. Giard, J. P. Bernard, A. Klotz, & I. Ristorcelli, 31–31

Stevens, J. A., Amure, M., & Gear, W. K. 2005, MNRAS, 357, 361

Stil, J. M. & Israel, F. P. 2002, A&A, 392, 473

Storchi-Bergmann, T., Kinney, A. L., & Challis, P. 1995, ApJS, 98, 103

Storey, P. J. & Hummer, D. G. 1995, MNRAS, 272, 41

Strong, A. W. & Mattox, J. R. 1996, A&A, 308, L21

Strong, A. W., Moskalenko, I. V., Reimer, O., Digel, S., & Diehl, R. 2004, A&A, 422, L47

Struck, C. & Smith, B. J. 2003, ApJ, 589, 157

Surace, J. A., Sanders, D. B., & Mazzarella, J. M. 2004, AJ, 127, 3235

Swinyard, B. et al. 2010, A&A, in press

Szewczyk, O., Pietrzyński, G., Gieren, W., et al. 2009, AJ, 138, 1661

Tacconi, L. J., Neri, R., Chapman, S. C., et al. 2006, ApJ, 640, 228

Taylor, C. L., Kobulnicky, H. A., & Skillman, E. D. 1998, AJ, 116, 2746

Terlevich, R., Melnick, J., Masegosa, J., Moles, M., & Copetti, M. V. F. 1991, A&AS, 91, 285

Thuan, T. X., Hibbard, J. E., & Lévrier, F. 2004, AJ, 128, 617

Tielens, A. G. G. M. 2005, The Physics and Chemistry of the Interstellar Medium, ed. Tielens, A. G. G. M.

Tielens, A. G. G. M. & Hollenbach, D. 1985, ApJ, 291, 722

Tielens, A. G. G. M., McKee, C. F., Seab, C. G., & Hollenbach, D. J. 1994, ApJ, 431, 321

Tielens, A. G. G. M., Meixner, M. M., van der Werf, P. P., et al. 1993, Science, 262, 86

Tilanus, R. P. J. & Allen, R. J. 1993, A&A, 274, 707

Tosi, M. 2003, Ap&SS, 284, 651

Tremonti, C. A., Heckman, T. M., Kauffmann, G., et al. 2004, ApJ, 613, 898

Urry, C. M. & Padovani, P. 1995, PASP, 107, 803

van den Bergh, S. 2009, ApJ, 702, 1502

van Gorkom, J. 1992, in Astrophysics and Space Science Library, Vol. 178, Morphological and Physical Classification of Galaxies, ed. G. Longo, M. Capaccioli, & G. Busarello, 233–+

van Zee, L., Westpfahl, D., Haynes, M. P., & Salzer, J. J. 1998, AJ, 115, 1000

Wada, K., Spaans, M., & Kim, S. 2000, ApJ, 540, 797

Walter, F., Brinks, E., de Blok, W. J. G., et al. 2008, AJ, 136, 2563

Walter, F., Weiss, A., & Scoville, N. 2002, ApJ, 580, L21

Webster, B. L. & Smith, M. G. 1983, MNRAS, 204, 743

Weingartner, J. C. & Draine, B. T. 2001, ApJ, 548, 296

Welty, D. E., Jenkins, E. B., Raymond, J. C., Mallouris, C., & York, D. G. 2002, ApJ, 579, 304

Whaley, C. H., Irwin, J. A., Madden, S. C., Galliano, F., & Bendo, G. J. 2009, MNRAS, 395, 97

Whittet, D. C. B. 1988, in Dust in the Universe, ed. M. E. Bailey & D. A. Williams, 25–53

Whittet, D. C. B., ed. 2003, Dust in the galactic environment

Whittet, D. C. B., Martin, P. G., Fitzpatrick, E. L., & Massa, D. 1993, ApJ, 408, 573

Wilcots, E. M. 2001, in Astronomical Society of the Pacific Conference Series, Vol. 240, Gas and Galaxy Evolution, ed. J. E. Hibbard, M. Rupen, & J. H. van Gorkom, 167–+

Williams, B. A., McMahon, P. M., & van Gorkom, J. H. 1991, AJ, 101, 1957

Wilson, C. D. 1995, ApJ, 448, L97+

Witt, A. N. & Gordon, K. D. 1996, ApJ, 463, 681

Witt, A. N., Thronson, Jr., H. A., & Capuano, Jr., J. M. 1992, ApJ, 393, 611

Wolfire, M. G., Hollenbach, D., & McKee, C. F. 2010, ApJ, 716, 1191

Wong, T. et al. 2009, ApJ, 696, 370

Worthey, G. 1994, ApJS, 95, 107

Wu, H., Zhu, Y.-N., Cao, C., & Qin, B. 2007, ApJ, 668, 87

Wyder, T. K. 2003, AJ, 125, 3097

Xilouris, E. M., Madden, S. C., Galliano, F., Vigroux, L., & Sauvage, M. 2004, A&A, 416, 41

Xu, C. & Buat, V. 1995, A&A, 293, L65

Xue, R. & Huang, M. 2009, Research in Astronomy and Astrophysics, 9, 457

Young, J. S. & Knezek, P. M. 1989, ApJ, 347, L55

Young, J. S. & Scoville, N. Z. 1991, ARA&A, 29, 581

Young, L. M. & Lo, K. Y. 1997, ApJ, 476, 127

Ysard, N. & Verstraete, L. 2010, A&A, 509, A12+

Yun, M. S. & Hibbard, J. E. 2001, ApJ, 550, 104

Yun, M. S., Verdes-Montenegro, L., del Olmo, A., & Perea, J. 1997, ApJ, 475, L21+

Zavagno, A. et al. 2010, ArXiv e-prints

Zhao, Y., Gao, Y., & Gu, Q. 2010, ApJ, 710, 663

Zhu, M., Papadopoulos, P. P., Xilouris, E. M., Kuno, N., & Lisenfeld, U. 2009, ApJ, 706, 941

Zhu, Y.-N., Wu, H., Cao, C., & Li, H.-N. 2008, ApJ, 686, 155

Zubko, V., Dwek, E., & Arendt, R. G. 2004, ApJS, 152, 211